# Principles of Nanophotonics

# SERIES IN OPTICS AND OPTOELECTRONICS

Series Editors: **E. Roy Pike**, Kings College, London, UK
**Robert G. W. Brown**, University of Nottingham, UK

*Recent titles in the series*

**The Quantum Phase Operator: A Review**
Stephen M. Barnett, John A. Vaccaro (Eds.)

**An Introduction to Biomedical Optics**
R Splinter, B A Hooper

**High-Speed Photonic Devices**
Nadir Dagli

**Lasers in the Preservation of Cultural Heritage: Principles and Applications**
C Fotakis, D Anglos, V Zafiropulos, S Georgiou, V Tornari

**Modeling Fluctuations in Scattered Waves**
E Jakeman, K D Ridley

**Fast Light, Slow Light and Left-Handed Light**
P W Milonni

**Diode Lasers**
D Sands

**Diffractional Optics of Millimetre Waves**
I V Minin, O V Minin

**Handbook of Electroluminescent Materials**
D R Vij

**Handbook of Moire Measurement**
C A Walker

**Next Generation Photovoltaics**
A Martí, A Luque

**Stimulated Brillouin Scattering**
M J Damzen, V Vlad, A Mocofanescu, V Babin

**Laser Induced Damage of Optical Materials**
R M Wood

**Optical Applications of Liquid Crystals**
L Vicari

**Optical Fibre Devices**
J P Goure, I Verrier

# Principles of Nanophotonics

**Motoichi Ohtsu**
*The University of Tokyo, Japan*

**Kiyoshi Kobayashi**
*Tokyo Institute of Technology, Japan*

**Tadashi Kawazoe**
*The University of Tokyo, Japan*

**Takashi Yatsui**
*The University of Tokyo, Japan*

**Makoto Naruse**
*National Institute of Information &*
*Communications Technology, Japan*

CRC Press
Taylor & Francis Group
Boca Raton London New York

CRC Press is an imprint of the
Taylor & Francis Group, an **informa** business
A TAYLOR & FRANCIS BOOK

CRC Press
Taylor & Francis Group
6000 Broken Sound Parkway NW, Suite 300
Boca Raton, FL 33487-2742

© 2008 by Taylor & Francis Group, LLC
CRC Press is an imprint of Taylor & Francis Group, an Informa business

No claim to original U.S. Government works
Printed in the United States of America on acid-free paper
10 9 8 7 6 5 4 3 2 1

International Standard Book Number-13: 978-1-58488-972-4 (Hardcover)

This book contains information obtained from authentic and highly regarded sources. Reprinted material is quoted with permission, and sources are indicated. A wide variety of references are listed. Reasonable efforts have been made to publish reliable data and information, but the author and the publisher cannot assume responsibility for the validity of all materials or for the consequences of their use.

Except as permitted under U.S. Copyright Law, no part of this book may be reprinted, reproduced, transmitted, or utilized in any form by any electronic, mechanical, or other means, now known or hereafter invented, including photocopying, microfilming, and recording, or in any information storage or retrieval system, without written permission from the publishers.

For permission to photocopy or use material electronically from this work, please access www.copyright.com (http://www.copyright.com/) or contact the Copyright Clearance Center, Inc. (CCC) 222 Rosewood Drive, Danvers, MA 01923, 978-750-8400. CCC is a not-for-profit organization that provides licenses and registration for a variety of users. For organizations that have been granted a photocopy license by the CCC, a separate system of payment has been arranged.

**Trademark Notice:** Product or corporate names may be trademarks or registered trademarks, and are used only for identification and explanation without intent to infringe.

**Library of Congress Cataloging-in-Publication Data**

Principles of nanophotonics / Motoichi Ohtsu ... [et al.].
p. cm. -- (Series in optics and optoelectronics)
Includes bibliographical references.
ISBN 978-1-58488-972-4 (alk. paper)
1. Nanophotonics. I. Ohtsu, Motoichi. II. Title. III. Series.

TA1530.P75 2007
621.36--dc22 2007044308

**Visit the Taylor & Francis Web site at**
**http://www.taylorandfrancis.com**

**and the CRC Press Web site at**
**http://www.crcpress.com**

# Contents

# *Preface*

This book outlines physically intuitive concepts of *nanophotonics* using a novel theoretical framework that differs from conventional wave optics. In the early 1980s, M. Ohtsu commenced his pioneering research into optical near-fields, because he understood that future optical science and technology would require breaking the diffraction limit of light. One decade later, a reliable technology was established for fabricating high-quality fiber probes. This led to the development of near-field optical microscopy and spectroscopy, with high-resolution, beyond the diffraction limit of conventional optical microscopy.

Immediately after establishing the fiber probe technology, Ohtsu tried to describe the nature of optical near-fields in a physically intuitive manner, as the nanometric subsystem (nanometric material systems interacting via optical near-fields) under study is always buried in a macroscopic subsystem consisting of the macroscopic substrate material and the macroscopic electromagnetic fields of the incident and scattered light. In the nanometric subsystem, the optical near-field should be regarded as an electromagnetic field that mediates the interaction between nanometric materials. After starting to develop a novel theory to describe this interaction, he found that it could be applied to realize novel photonic devices, fabrication techniques, and systems. Therefore, in 1993, the idea of *nanophotonics* was proposed. It is a novel technology that utilizes the optical near-field to realize novel devices, fabrications, and systems.

Following elaboration of the idea of nanophotonics, much theoretical and experimental work has been carried out, and several novel functions and phenomena that originated from the intrinsic optical near-field interaction have been discovered. Examples include device operation via the optical near-field energy transfer between the optically forbidden energy levels of excitons and subsequent relaxation, and a fabrication technique using a non-adiabatic process with optically inactive molecules. These constitute examples of *qualitative innovation* in optical science and technology because they were impossible to realize as long as conventional propagating light was used. The true nature of *nanophotonics* is to realize this *qualitative innovation*. After reading this note, it may be surmised that the advantage of going beyond the diffraction limit, that is, *quantitative innovation*, is no longer essential but is simply a secondary aspect of *nanophotonics*. One of the objectives in publishing this book was to review this *qualitative innovation* for the students, engineers, and scientists who will be engaged in *nanophotonics*.

In conventional optical science and technology, light and matter have been discussed separately, and the flow of optical energy in a photonic integrated circuit or system has been unidirectional from a light source to a photodetector. By contrast, in *nanophotonics*, light and matter have to be regarded as being coupled to each other, and the energy flow between nanometric particles is bidirectional. This means that *nanophotonics* should be regarded as a *technology fusing optical fields and matter*.

The term *nanophotonics* is occasionally used for photonic crystals, plasmonics, metamaterials, silicon photonics, and QD lasers using conventional propagating lights. Here, as will be described in Section 1.4, the stern warning from C. Shannon on the casual use of the term *information theory*, which was a trend in the study of information theory during the 1950s, should be considered. The term *nanophotonics* has been used in a similar way, although some work in *nanophotonics* is not based on optical near-field interactions. For the development of *nanophotonics*, far-reaching physical insights into the local electromagnetic interaction in the nanometric subsystem composed of electrons and photons is required.

Chapter 1 of this book reviews the background, history, and present status of research and development in *nanophotonics* and related technologies. It explains why *qualitative innovation* lies at the heart of *nanophotonics*. Chapter 2 presents a novel theoretical model and a new approach that describes the interaction between nanometric material systems via optical near-fields in a physically intuitive manner. Nanophotonic devices and systems are designed and their performances are analyzed using this model. A non-adiabatic fabrication process is also evaluated using this model. Chapters 3 and 4 deal with nanophotonic devices and fabrication techniques, and present examples of *qualitative innovation*. Chapter 5 presents a novel nanophotonic system realized by assembling nanophotonic devices. Its performance is also an example of *qualitative innovation* in optical information technology.

Chapters 1 and 2 were written by M. Ohtsu and K. Kobayashi, respectively. Chapters 3 and 4 were coauthored by T. Kawazoe and T. Yatsui. Chapter 5 is by M. Naruse. All of the authors checked the entire manuscript under the supervision of M. Ohtsu.

The authors gratefully acknowledge Prof. H. Hori (Yamanashi University) for his collaboration in conducting the authors' research on *nanophotonics*, and for his critical comments on the manuscript.

**Motoichi Ohtsu**
Bunkyo, Tokyo
September 2007

# Authors

**Motoichi Ohtsu** received the B.E., M.E., and D.E. degrees in electronics engineering from the Tokyo Institute of Technology, Tokyo, Japan, in 1973, 1975, and 1978, respectively. In 1978, he was appointed a Research Associate, and in 1982, he became an Associate Professor at the Tokyo Institute of Technology. From 1986 to 1987, while on leave from the Tokyo Institute of Technology, he joined the Crawford Hill Laboratory, AT&T Bell Laboratories, Holmdel, NJ. In 1991, he became a Professor at the Tokyo Institute of Technology. In 2004, he moved to the University of Tokyo as a Professor. He has been the leader of the "Photon Control" project (1993–1998: the Kanagawa Academy of Science and Technology, Kanagawa, Japan), the "Localized Photon" project (1998–2003: ERATO [Exploratory Research for Advanced Technology], JST [Japan Science and Technology Corporation], Japan), "Terabyte Optical Storage Technology" project (2002–2006: NEDO [New Energy and Industrial Technology Development Organization], Japan), and "Near-Field Optical Lithography System" project (2004–2006: Ministry of Education, Japan). He is concurrently the leader of the "Nanophotonics" team (2003–present: SORST [Solution Oriented Research for Science and Technology], JST, Japan), "Innovative Nanophotonics Components Development" project (2006–present: NEDO, Japan), and "Nanophotonics Total Expansion: Industry-University Cooperation and Human Resource Development" project (2006–present: NEDO, Japan). He has written over 380 papers and received 87 patents. He is the author, coauthor, and editor of 51 books, with 22 in English, including *Near-Field Nano/Atom Optics and Technology* (Springer-Verlag, Berlin, 1998), *Near-Field Nano-Optics* (Kluwer Academic/Plenum Publishers, New York, 1999), *Optical and Electronic Properties of Nano-matters* (Kluwer Academic/KTK Scientific Publishers, Dordrecht/Tokyo, 2001), *Progress in Nano Electro-Optics* I-V (Springer Verlag, Berlin, 2002–present), and *Optical Near Fields* (Springer–Verlag, Berlin, 2004). In 1999, he was Vice-President of the IEEE/LEOS Japan Chapter, and in 2000, he was appointed President of the chapter. He was an executive director of the Japan Society of Applied Physics (2000–2001). He served as a Technical Program Co-chair for the 4th Pacific Rim Conference on Lasers and Electro-Optics (CLEO/PR01), 2001. He has been a tutorial lecturer to the SPIE and the OSA. His main fields of interests are nanophotonics and atom-photonics. Dr. Ohtsu is a Fellow of the Optical Society of America, a Fellow of the Japan Society of Applied Physics, a senior member of IEEE, a member of the Institute of Electronics, Information and Communication Engineering of Japan, and a member of the

American Physical Society. He is also a Tandem Member of the Science Council of Japan. He has been awarded 14 prizes from academic institutions, including the Issac Koga Gold Medal of URSI in 1984, the Japan IBM Science Award in 1988, two awards from the Japan Society of Applied Physics in 1982 and 1990, the Inoue Science Foundation Award in 1999, the Japan Royal Medal with a Purple Ribbon from the Japanese Government in 2004, H. Inoue Award from JST in 2005, and the Distinguished Achievement Award from the Institute of Electronics, Information and Communication Engineering of Japan in 2007.

**Kiyoshi Koayashi** received the Ph.D. degree in Physics from the University of Tsukuba, Japan, in 1982. After receiving the degree, he joined IBM Japan as a Researcher at Tokyo Research Laboratory, Tokyo, Japan. In 1998, he became a theoretical group leader of the "Localized Photon" project for the Exploratory Research for Advanced Technology (ERATO) at the Japan Science and Technology Agency (JST). Since 2004, he has been a Professor with the 21 Century Center of Excellence Program, Nanometer-Scale Quantum Physics, Department of Physics, Tokyo Institute of Technology, Japan. Prof. Kobayashi is also a member of the Core Research for Evolutional Science and Technology (CREST) at JST.

His main fields of interest are quantum optical near-field theory and its application to nano/atom photonics. He is the coauthor of *Optical Near Fields* (Springer-Verlag, Berlin, 2003), *Progress in Nano-Electro-Optics I* (Springer-Verlag, Berlin, 2003), *Near-Field Nano/Atom Optics and Technology* (Springer-Verlag, Tokyo, 1998). He is a member of the Japan Society of Applied Physics, the Physical Society of Japan, and the American Physical Society.

**Tadashi Kawazoe** was born in Kochi, Japan, on April 5, 1967. He received B.E., M.E., and Ph.D. degrees in physics from University of Tsukuba, Tsukuba, Japan, in 1990, 1993, and 1996, respectively. He has studied optical nonlinearities in semiconductor QDs at the Institute of Physics, University of Tsukuba. In 1996, he joined the faculty of Engineering, Yamagata University, Japan, as a research associate, engaged in research on nonlinear optical materials and devices. In 2000, he has been with Japan Science and Technology Corporation, Japan. Since 2000, He has studied optical devices and fabrication based on an optical near-field interaction. In 2007, he joined the University of Tokyo as a Project Associate Professor. His current research interests are in the nanophotonic device.

Dr. Kawazoe is a member of the Japan Society of Applied Physics and the Physical Society of Japan.

**Takashi Yatsui** was born in Tokyo, Japan, on January 21, 1972. He received the B.E. degree from Keio University, Tokyo, Japan, in 1995, and M.E. and D.E. degrees from Tokyo Institute of Technology, Tokyo, Japan, in 1997 and 2000, respectively.

From 1999 to 2000, he was a Research Fellow of the Japan Society for the Promotion of Science. From 2000 to 2003, he was a Researcher at the Japan Science and Technology Corporation, Tokyo. Since 2003, he has been a Researcher at the Japan Science and Technology Agency, Tokyo. In 2008, he joined the University of Tokyo as an Associate Professor. His current research interests include nanofabrication using optical near-field and its application to nanophotonics.

Dr. Yatsui is a Member of the Japan Society of Applied Physics. Dr. Yatsui received 1st prize in Paper Contest from IEEE Student Branch at Tokyo Institute of Technology in 1998, and the excellent research presentation award from the Japan Society of Applied Physics in 2000, and Tejima Doctoral Dissertation Award from Tejima Foundation in 2001**.**

**Makoto Naruse** received B.E., M.E., and D.E. degrees from the University of Tokyo in 1994, 1996, and 1999, respectively.

From 1999 to 2000, he was a Postdoctoral Researcher of the Japan Society for the Promotion of Science. From 2000 to 2002, he was a Research Associate at the University of Tokyo. In 2002, he joined the National Institute of Information and Communications Technology. Since 2003, he has been a senior researcher. From 2001 to 2005, he served concurrently as a researcher of the PRESTO program of the Japan Science and Technology Agency (JST). Since 2006, he has also served as a Project Associate Professor at the University of Tokyo.

Dr. Naruse is a member of the OSA. He received the Inoue Research Award for Young Scientists from the Inoue Foundation for Science and the Research Award from Research Foundation for Opto-Science and Technology in 2000, and the Optics Prize for Excellent Papers from the Japan Society of Applied Physics in 2008.

# 1

# Introduction

## 1.1 Modern Optical Science and Technology and the Diffraction Limit

As a major step forward in quantum theory and its applications, the laser, a novel light source, was invented in 1960 [1]. The use of lasers has dramatically changed optical science and technology, and it is considered to be one of the biggest scientific achievements of the 20th century, on a par with the invention of transistors. Lasers have a variety of applications because of the high controllability of their amplitude, phase, frequency, and polarization. Their industrial applications are known as photonics or optoelectronics, with examples including optical disk memory, optical fiber communication systems, and optical fabrication, including photolithography.

A compact disk (CD), popularly used as read-only memory, is an example of an optical disk memory. It has numerous small pits on its surface for storing digital signals, such that one pit corresponds to one bit, and to read these signals, the disk surface is illuminated by a laser beam focused by a convex lens. Detection of the laser light reflected from the disk surface corresponds to the readout operation. Random access memories, such as digital versatile disks (DVDs), have also been developed, in which a focused laser beam is used to store and rewrite information by locally heating the disk surface. A report on future trends in the photonics industry recently estimated that the storage density of the optical disk memory should be as high as 1 Tb/inch$^2$ in the year 2010 (see Figure. 1.1) [2], but the diameter of a circular pit corresponding to 1 Tb/inch$^2$ is 25 nm, which cannot be fabricated or read due to the diffraction limit of light. As an alternative storage technology, a hard disk drive system using magnetic storage technology has realized a storage density much higher than that of optical disk memory. However, this system also has an upper limit of storage density due to thermal instability of the magnetic domain. As a result of this limit, densities higher than 300 Gb/inch$^2$ are difficult to realize, and 1 Tb/inch$^2$ is a much higher value.

Long-distance optical fiber communication systems have been established by installing submarine optical communication cables in the Pacific and Atlantic oceans. These systems have also been used for local area networks. These technical trends mean that the electronics technology in these systems has been replaced by optical technology. Furthermore, this

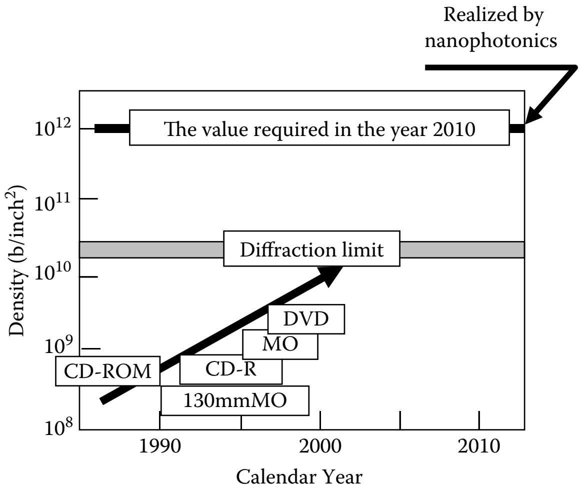

**FIGURE 1.1**
Technical road map showing the increase in storage density of optical disk systems. The storage density already realized by nanophotonics is also shown.

replacement is required for very short-distance communication systems, such as board–board, chip–chip, and device–device systems in electronic circuits to increase the degree of integration and decrease the power consumption (see Figure. 1.2) [3]. It is thus advantageous to replace some electronic devices with photonic devices to facilitate connecting with optical fibers. Consequently, the

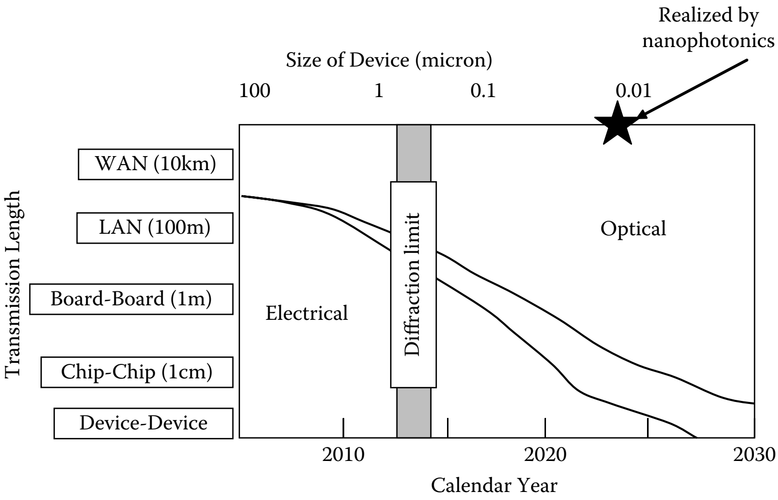

**FIGURE 1.2**
Technical road map showing the requirement to reduce the size of photonic devices for shorter-distance optical fiber communication systems. The device size already realized by nanophotonics is also shown.

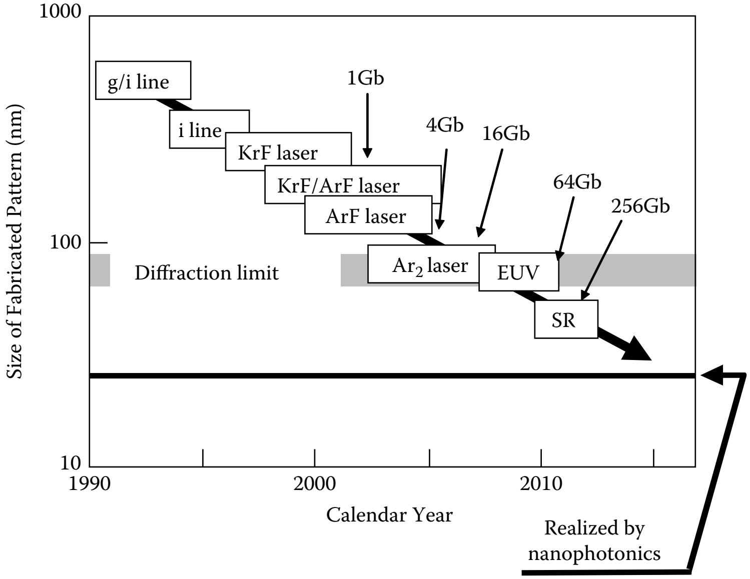

**FIGURE 1.3**
Technical road map of the line width reduction of patterns fabricated by photolithography. The names of light sources and DRAM capacities are also shown. EUV and SR stand for extreme ultraviolet light and synchronous radiation, respectively. The line width already realized by nanophotonics is also shown.

size of the photonic device (e.g., lasers and modulators) must be reduced to be as small as electronic devices for greater integration, which, however, is impossible because of the diffraction limit of light.

Optical fabrication technology has been developed for fabricating a variety of devices. For example, photolithography is popularly used for fabricating semiconductor dynamic random access memories (DRAMs). It uses focused light to process the material surface, and fabricated sizes have been reduced using shorter wavelength light. It is estimated that 64–256-Gb DRAMs will be required in the near future, and the linear pattern in these devices must be as narrow as 35–70 nm (see Figure 1.3) [4]. However, such narrow patterns cannot be fabricated because of the diffraction limit of light. To narrow the pattern to within the diffraction limit, various light sources emitting extreme ultraviolet light, synchrotron radiation, and X-rays, as well as electron beams, are under development, but they may not be feasible in mass production because of their large size, high energy consumption, and high cost. Thus, novel, inexpensive, and practical fabrication tools are required for fabricating semiconductor devices and advanced photonic devices.

The examples presented here indicate that 21st-century society requires novel optical science and technology to meet the measurement, fabrication, control, and function requirements on the scale of several tens of nanometers because conventional optical science and technology cannot overcome the diffraction limit of light waves.

After a light wave passes through a small aperture on a plate, it is converted into a diverging spherical wave. Such divergence is called diffraction, an intrinsic characteristic of waves. For a circular aperture, the divergence angle is about $\lambda/a$, where $\lambda$ and $a$ are the wavelength of the incident light and the aperture radius, respectively. Due to diffraction, the spot size of the light cannot be zero, even if it is focused with a convex lens. The spot size on the focal plane is as large as $\lambda/NA$, where $NA$ is the numerical aperture, which is smaller than unity for a conventional convex lens. Therefore, when two point sources of light are located closer together than $\lambda/NA$, their images formed by a convex lens cannot be resolved on the focal plane.

This also holds true for imaging under an optical microscope, and the smallest size resolvable with an optical microscope (i.e., the resolution) is $\lambda/NA$, which is called the diffraction limit. Consequently, for optical disk memory, the storage and readout of pits smaller than $\lambda/NA$ are impossible. Shorter wavelength lasers have been developed to decrease the diffraction-limited pit size, but the upper limit of the storage density achieved using visible light is several 10 Gb/inch$^2$, while the value required in the year 2010 is 1 Tb/inch$^2$.

Semiconductor lasers, optical waveguides, and related integrated photonic devices must confine the light within them for effective operation, and the active layer of a semiconductor laser has to exceed the diffraction-limited volume, that is, $\lambda^3$, for this confinement. The core diameter of an optical fiber must exceed $\lambda$. These examples indicate that photonic devices cannot be smaller than the wavelength of light, which is the diffraction-limited size of photonic devices, but photonic devices for optical fiber communication systems in the year 2015 must be even smaller.

The narrowest line width of a pattern fabricated using photolithography is also limited by diffraction. The progress in reducing the pattern size has been the result of effort to use a shorter wavelength light to decrease the diffraction-limited value. However, further shortening of the wavelength requires gigantic, expensive light sources, which can become prohibitive when developing practical microfabrication systems. For visible light sources, the 35–70 nm line width required for 64–256-Gb DRAMs is far beyond the diffraction limit.

To summarize, the miniaturization of optical science and technology is impossible as long as conventional propagating light is used. This is the deadlock imposed by the diffraction of light. We must go beyond the diffraction limit to open up a new field of optical science and technology. This field is called *nanophotonics,* and will be reviewed in this book.

## 1.2 Breaking Through the Diffraction Limit

Novel or nanometer-sized materials may be used for future advanced photonic devices. However, the size of these devices cannot be reduced beyond the diffraction limit as long as propagating light is used for their operation. This also applies to improvements in the resolution of optical fabrication and for increasing the storage density of optical disk memories. To go beyond the diffraction limit, we need nonpropagating nanometer-sized light to induce primary excitation in a nanometer-sized material in such a manner that the spatial phase of excitation is independent of that of the incident light.

The use of optical near fields has been proposed as a way to transcend the diffraction limit [5]. This proposal holds that an optical near field can be generated on a sub-wavelength-sized aperture by irradiating the propagating light. It also holds that the size of the spatial distribution of the optical near-field energy depends not on the wavelength of the incident light, but on the aperture size. Although these claims are no more than those in the framework of primitive wave optics, optical near fields have been applied to realize diffraction-free, high-resolution optical microscopy (i.e., near-field optical microscopy), which achieved rapid progress after high-resolution, high-throughput fiber probes were invented and fabricated in a reproducible manner [6, 7]. In the early stage of such studies, however, the concept of optical near fields was not clearly discriminated from that of an evanescent wave on a planar material surface (i.e., a two-dimensional topographical material) or that of a guided wave in a sub-wavelength-sized cross-sectional waveguide (i.e., a one-dimensional topographical material).

To distinguish these clearly, note that an evanescent wave is generated by the primary excitations, that is, electronic dipoles, induced near the two-dimensional material surface, which align periodically depending on the spatial phase of the incident light (see Table 1.1). In contrast, the guided wave in a sub-wavelength-sized cross-sectional waveguide is generated by the electronic dipoles induced along the one-dimensional waveguide axis. They align periodically depending on the spatial phase of the incident light. Examples are the silicon and metallic waveguides used for silicon photonics and plasmonics, respectively. The two-dimensional evanescent wave and one-dimensional guided wave are both light waves, and are generated by the periodic alignment of electric dipoles depending on the spatial phase of the incident light. Because of this dependence, the two components of the evanescent wave

**TABLE 1.1**

Comparison of an Evanescent Wave and an Optical Near Field

| | Evanescent Wave | Optical Near Field |
|---|---|---|
| Alignment of electric dipole moments | Depends on the spatial phase of the incident light | Depends on the size, conformation, and structure of the particle |
| Decay length | The wavelength of the incident light | The size of the particle |
| Generated propagating light | Reflected light(total reflection) | Scattered light |

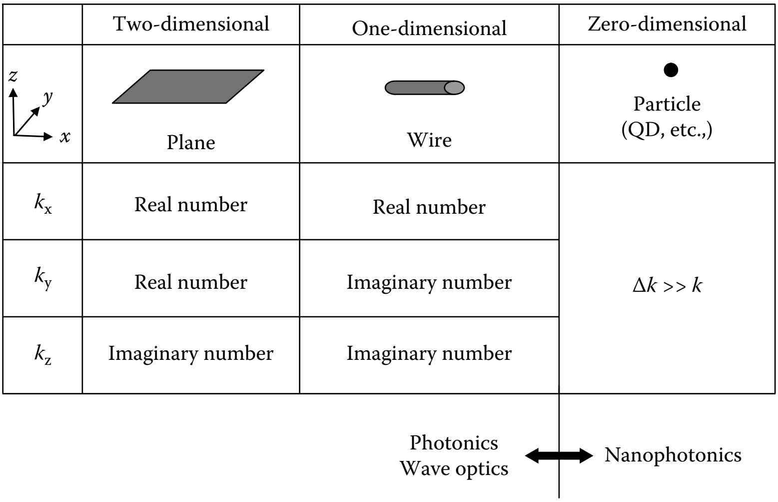

| | Two-dimensional | One-dimensional | Zero-dimensional |
|---|---|---|---|
| $z$ $y$ $x$ | Plane | Wire | Particle<br>(QD, etc.,) |
| $k_x$ | Real number | Real number | $\Delta k >> k$ |
| $k_y$ | Real number | Imaginary number | |
| $k_z$ | Imaginary number | Imaginary number | |

**FIGURE 1.4**
Relationship between the profile of a material surface and the wave number of the light. $k_x$, $k_y$, and $k_z$: $x$-, $y$-, and $z$-axis components of the wave number. $\Delta k$: uncertainty of the wave number. $k$: absolute value of the wave number. The dimensions in the $y$–$z$ plane and along the three axes are sub-wavelength.

vector along the material surface take real numbers. The component along the waveguide axis takes a real number in the case of a guided wave. These real numbers limit evanescent and guided waves to the category of diffraction-limited light waves.

Unlike these waves, an optical near field is generated by the electronic dipoles induced in a nanometric particle (i.e., a sub-wavelength-sized zero-dimensional topographical material). Their alignment is independent of the spatial phase of the incident light because the particles are much smaller than the wavelength of the incident light. Instead, it depends on the size, conformation, and structure of the particle. In other words, because of the uncertainty principle for the wave number ($\Delta k$) and position ($\Delta x$) of the light, that is, $\Delta k \Delta x \geq 1$, the wave number and consequently the wave vector are not defined accurately in a sub-wavelength-sized area ($\Delta x < \lambda$). Thus, the optical near field is free of diffraction, and as a result, optical science and technology beyond the diffraction limit can be realized only by using optical near fields, and not evanescent or guided waves (see Figure 1.4).

Classical electromagnetics explains the mechanisms of optical near-field generation described above (see Figure 1.5). Electric dipoles are induced by irradiating a nanometric particle with incident light. Among the electric lines of forces originating from these electric dipoles, the optical near field is represented by those that originate from the positive charge of the electric dipole and terminate on the negative charge. This does not propagate to the

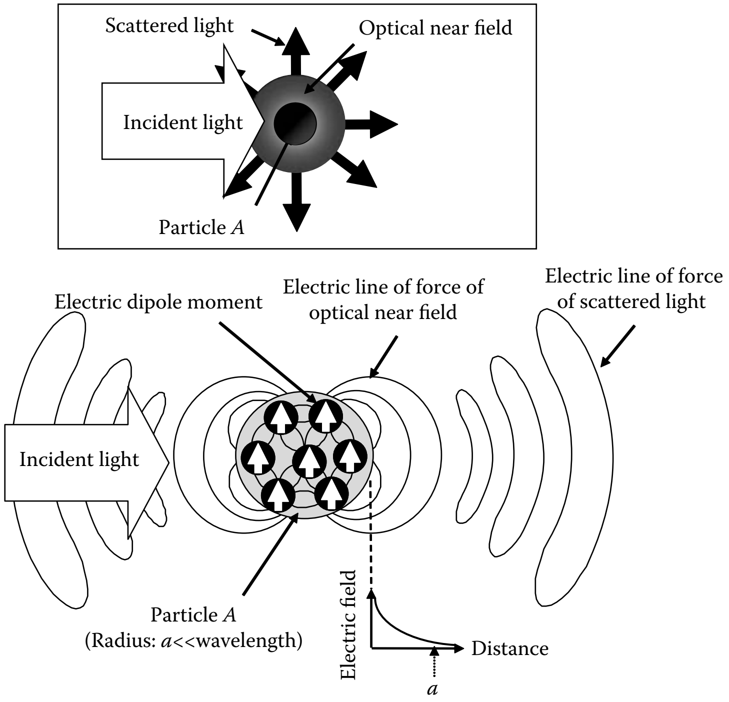

**FIGURE 1.5**
Generation of optical near fields.

far field. Because the particle is much smaller than the wavelength of the incident light, the alignment of the electric dipoles is determined independently of the spatial phase of the incident light. Therefore, the spatial distribution and decay length of the optical near-field energy depend not on the wavelength of the light, but on the size, conformation, and structure of the particle. Moreover, the scattered light is represented by the closed loop of the electric line of forces, and propagates to the far field.

Methods such as Green's function, a calculation using the finite-difference time domain (FDTD) method, and so on have been developed to describe the optical near field based on conventional optics theories [8]. However, conventional optics theories do not provide any physically intuitive pictures of nonpropagating nanometric optical near fields because these theories were developed to describe the light waves propagating through macroscopic space or materials. A novel theory has been developed based on a framework that is completely different from those of the conventional theories. It will be reviewed in Chapter 2.

This novel theory is based on how one observes an optical near field, that is, the interaction and energy transfer between nanometric particles via

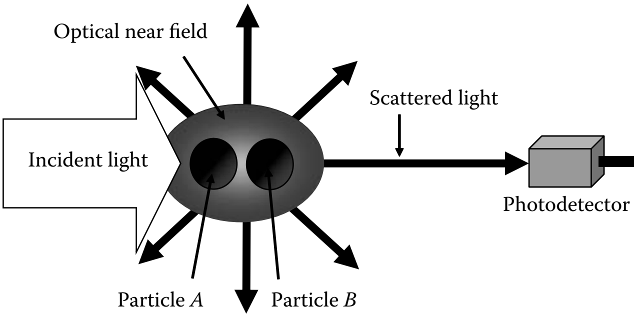

**FIGURE 1.6**
Observation of optical near fields.

an optical near field. This perspective is essential because the interaction and energy transfer are indispensable for nanophotonic devices and nanophotonic fabrications. That is, to observe a nonpropagating optical near field, a second particle is inserted (see Figure 1.6) to generate observable scattered light by disturbing the optical near field. However, the real system is more complicated than that shown in Figure 1.6 because the "nanometric subsystem" (the two particles and the optical near field) is buried in the "macroscopic subsystem" consisting of the macroscopic substrate material and the macroscopic electromagnetic fields of the incident and scattered light (see Figure 1.7).

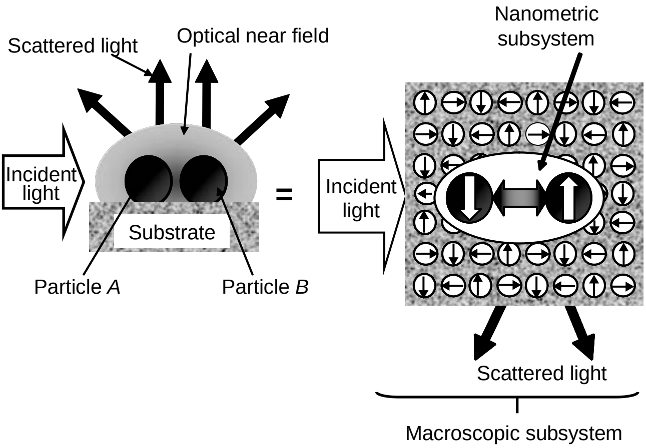

**FIGURE 1.7**
A nanometric subsystem composed of two particles and an optical near field; this is buried in a macroscopic subsystem.

The premise behind the novel theory is to avoid the complexity of describing all of the behaviors of nanometric and macroscopic subsystems rigorously, because we are interested only in the behavior of the nanometric subsystem. The macroscopic subsystem is expressed as an exciton–polariton, which is a mixed state of material excitation and electromagnetic fields. Because the nanometric subsystem is excited by an electromagnetic interaction with the macroscopic subsystem, the projection operator method is effective for describing the quantum mechanical states of these systems [9]. Under this treatment, the nanometric subsystem is regarded as being isolated from the macroscopic subsystem, whereas the functional form and magnitude of effective interactions between the elements of the nanometric subsystem are influenced by the macroscopic subsystem. In other words, the two nanometric particles can be considered as being isolated from the surrounding macroscopic system and as interacting by exchanging exciton–polariton energies.

Because the time required for this local electromagnetic interaction is very short, the uncertainty principle allows the exchange of a virtual exciton–polariton between the two nanometric particles, as well as that of a real exciton–polariton (see Figure 1.8). The former exchange corresponds to the nonresonant interaction between the two particles. The optical near field mediates this interaction, which is represented by a Yukawa function. The Yukawa function represents the localization of the optical near-field energy around the nanometric particles, like an electron cloud around an atomic nucleus whose decay length is equivalent to the material size [9]. The latter corresponds to the resonant interaction mediated by the conventional propagating scattered light, which is represented by a conventional spherical wave function.

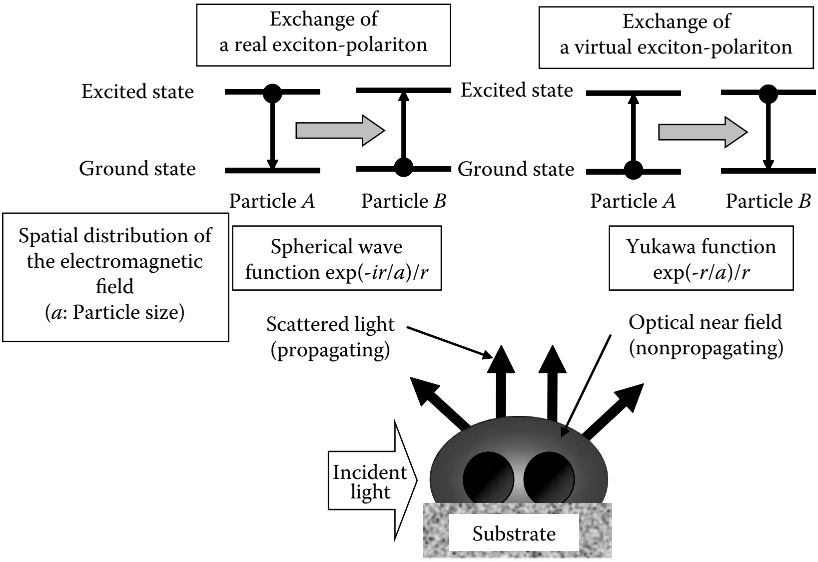

**FIGURE 1.8**
Real and virtual exciton–polaritons.

## 1.3 Nanophotonics and Its True Nature

As described in Section 1.2, the optical near field is an electromagnetic field that mediates the interaction between nanometric particles located in close proximity to each other. Nanophotonics utilizes this field to realize novel devices, fabrications, and systems, as proposed by M. Ohtsu [10]. That is, a photonic device with a novel function can be operated by transferring the optical near-field energy between nanometric particles and subsequent dissipation. In such a device, the optical near field transfers a signal and carries the information. Novel photonic systems become possible by using these novel photonic devices. Furthermore, if the magnitude of the transferred optical near-field energy is sufficiently large, structures or conformations of nanometric particles can be modified, which suggests the feasibility of novel photonic fabrications.

Note that the true nature of nanophotonics is to realize "qualitative innovation" in photonic devices, fabrications, and systems by utilizing novel functions and phenomena caused by optical near-field interactions, which are impossible as long as conventional propagating light is used (see Figure 1.9). On reading this note, one may understand that the advantage of going beyond the diffraction limit, that is, "quantitative innovation," is no longer essential, but only a secondary nature of nanophotonics. In this sense, one should also note that optical near-field microscopy, that is, the methodology

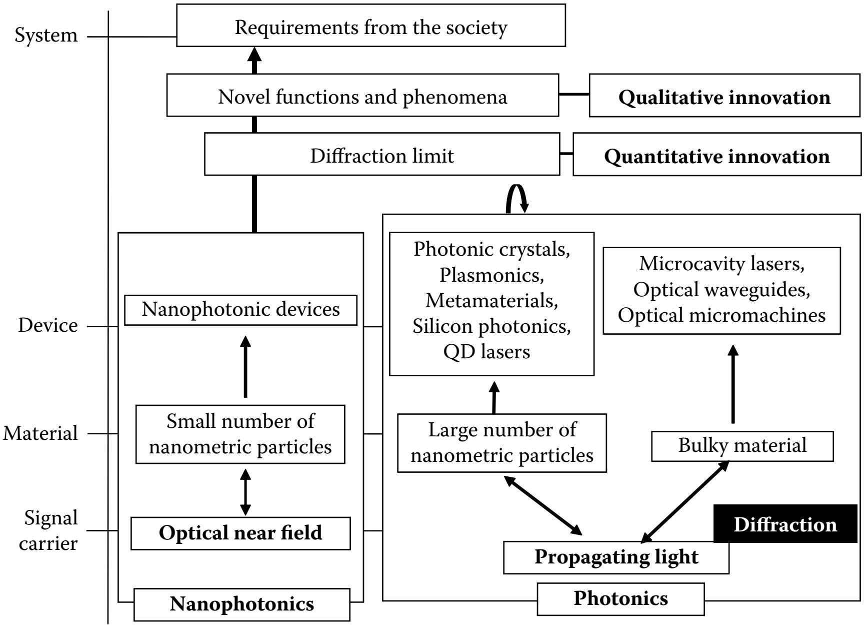

**FIGURE 1.9**
Nanophotonics for realizing qualitative innovation.

used for image acquisition and interpretation in a nondestructive manner, is not an appropriate application of nanophotonics because the magnitude of the optical near-field energy transferred between the probe and sample must be extrapolated to zero to avoid destroying the sample.

Quantitative innovation has already been realized by breaking the diffraction limit. Examples include the following:

1. Optical–magnetic hybrid disk storage systems: The optical near field is used to heat the surface of the magnetic storage medium locally to decrease the coercivity. Immediately after heating, the magnetic field writes the pit. The Japanese National Project (METI-NEDO Program entitled "Terabyte Optical Storage Technology") has realized 1 Tb/inch$^2$ storage density, which is higher than the diffraction limit of optical storage and the limit imposed by the thermal fluctuations of a hard disk drive system (see Figure 1.10) [11].
2. Nanophotonic devices and systems: The operation of novel photonic devices has been demonstrated by utilizing the optical near-field energy transfer between closely located quantum dots (QDs) and the subsequent dissipation. These devices are much smaller than the wavelength of light (see Figure 1.11). A novel router system was also demonstrated using several nanophotonic devices to show that the system size is much smaller than that of a conventional system (Figure 1.12) [12].
3. Photochemical vapor deposition and photolithography: An optical near field is used to excite molecules for fabrication with nanometer-sized resolution (Figure 1.13) [13].

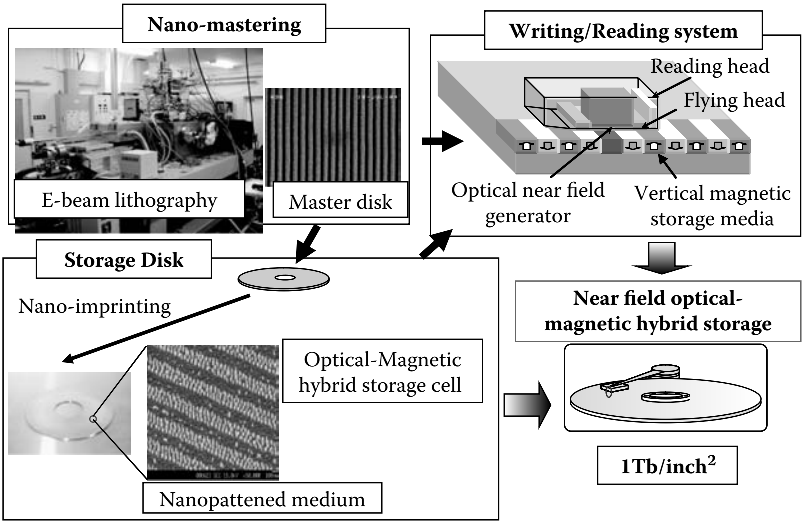

**FIGURE 1.10**
A high-density optical–magnetic hybrid disk storage system.

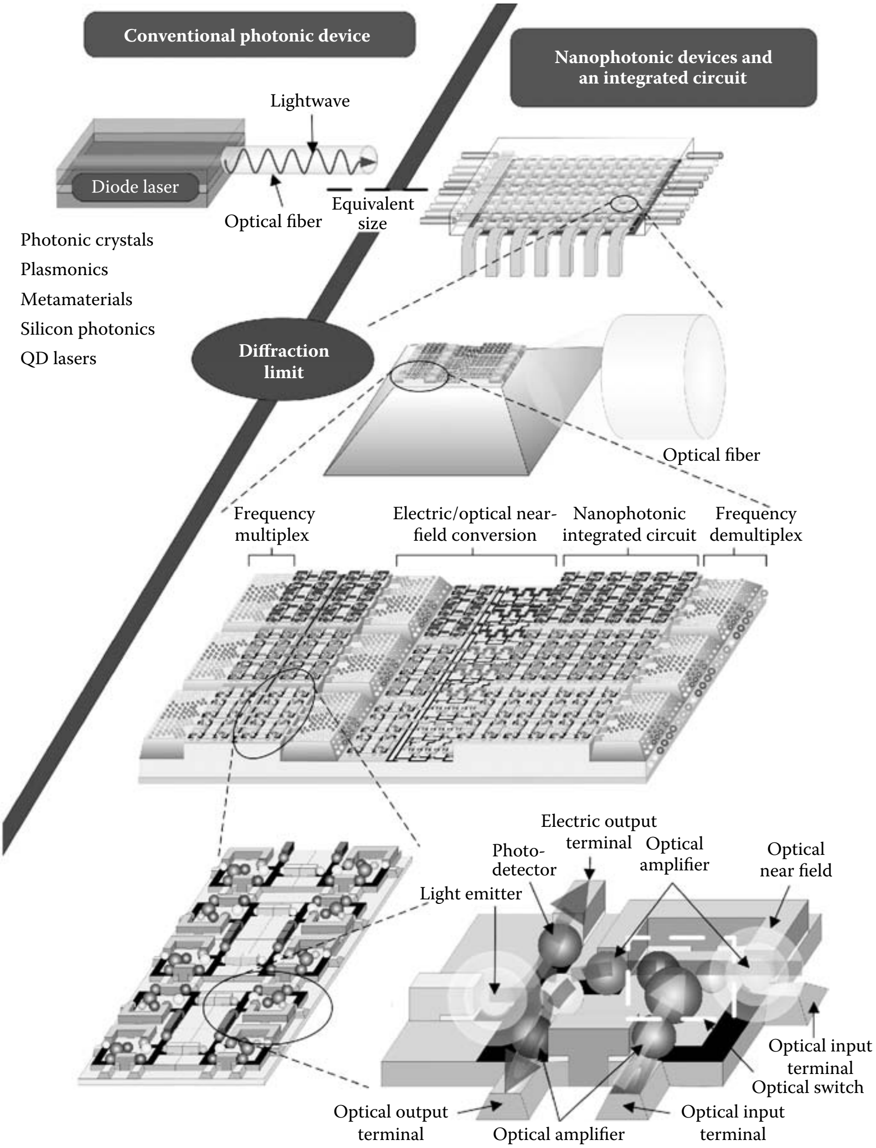

**FIGURE 1.11**
Nanophotonic devices and an integrated circuit.

Figures 1.1–1.3 show the status of these quantitative innovations. For microscopy and spectroscopy using optical near fields, a near-field spectrometer has been developed for diagnosing single semiconductor QDs [14], semiconductor devices [15], single organic molecules [16], and biological specimens [17]. Numerous experimental results for spatially resolved photoluminescence and Raman spectra with a 10-nm resolution have accumulated [18].

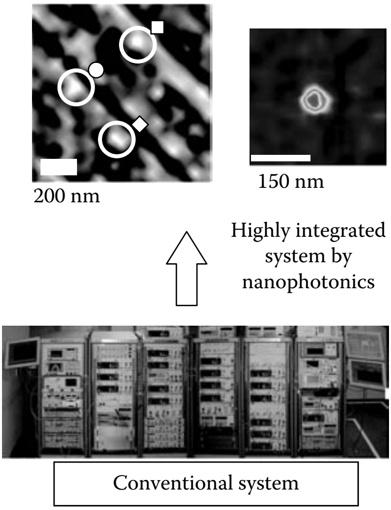

**FIGURE 1.12**
A conventional router system and its improvement using nanophotonics.

Commercial near-field photoluminescence spectrometers have been produced for operation at the ultraviolet–infrared and liquid helium–room temperature ranges [19]. These are popularly used in different areas of nano-science and technology.

However, it is important to note that these examples also realize qualitative innovation. Examples include the following:

1. An optical storage system containing an optical disk and optical–magnetic hybrid disk: By utilizing the inherent hierarchical nature of optical near fields, a multilayer memory system has been demonstrated [20]. In addition, by using near-field optical energy transfer and subsequent dissipation, a traceable memory system has been developed [21].

**FIGURE 1.13**
Nanophotonic lithography. Right: Appearance of the system. Left: A scanning electron microscopic image of a fabricated corrugated pattern.

2. Nanophotonic devices and systems: To operate the above-mentioned nanophotonic devices, optical near-field energy transfer is utilized between the forbidden optical transition energy levels of adjacent QDs, which is impossible as long as propagating light is used. Subsequent energy dissipation in a QDs can fix the position and magnitude of the transferred near-field optical energy. Assembling these devices, the optical router system has established qualitative innovation in its novel performance [22].
3. Photochemical vapor deposition and photolithography: A nonadiabatic process that does not follow the Franck–Condon principle has been demonstrated [23], which is attributable to the exchange of a virtual exciton–phonon–polariton via an optical near field. This process has enabled deposition and lithography using a long wavelength light source, which suggests that large, expensive ultraviolet light sources are no longer required. It also suggests that harmless, chemically stable molecules can be dissolved and resist films can be carved, even if they are optically inactive.

Details of these examples will be reviewed in Chapters 3–5. Nanophotonics has also led to innovative growth in related sciences. One example is atom photonics, which controls the thermal motions of neutral atoms in a vacuum using optical near fields [24]. Theoretical studies have examined the manipulation of a single atom based on the virtual exciton–polariton model [25], and in an experimental study, an atom was successfully guided through a hollow optical fiber [26]. Recent studies have examined atom-detecting devices [27], atom deflectors [28], and an atomic funnel [29]. Atom photonics will open a new field of science that examines the interaction between virtual exciton–polaritons and a single atom. Furthermore, it can be applied to novel technologies for fabricating atomic-level materials.

Basic research to further the field of nanophotonics is being carried out actively. An optical near-field problem has been formulated in terms of the Carniglia–Mandel model as a complete and orthogonal set that satisfies the infinite planar boundary conditions between the dielectric and a vacuum. This approach has revealed interesting atomic phenomena occurring near the surface, which have been analyzed based on angular spectrum representation [30, 31]. For example, optical radiation from an excited molecule on the substrate surface has been analyzed [32], and a self-consistent, nonlocal, semiclassical theory on light–matter interactions has been developed to reveal the optical response in a variety of nanostructures [33]. In particular, the size dependence and allowance of a dipole-forbidden transition in a nanometric QDs system were noted [34, 35]. The optical manipulation of nanometric objects in superfluid $^4$He has been investigated based on the nonlocal semiclassical theory [36]. Electron transport through molecular bridges connecting nanoscale electrons has been formulated [37], and a unified method has been proposed for treating extended and polaron-like localized states coupled with molecular vibrations.

A one-dimensional molecular bridge made of thiophene molecules has been analyzed numerically. The study of optical near fields associated with molecular bridges is now in progress. In addition, as basic experimental work, desorption and ionization have been carried out assisted by optical near fields, and their application to mass spectroscopy has been proposed [38, 39].

Thus far, the general opinion concerning modern technology is that "the light should be used for communication because it is fast" while "the electron should be used for computers because it is small." This means that light cannot be used for computers because it is large. However, the miniaturization of electronic devices is reaching the fundamental limit due to electric current leaking through ultrathin films. Nevertheless, nanophotonics has already demonstrated the possibility of miniaturizing photonic devices beyond the diffraction limit (quantitative innovation), as well as novel functions and phenomena (qualitative innovation). This means that nanophotonics has great potential to open novel fields of technology, which are impossible with conventional photonics, and deviates from the general opinion. In addition to communication, fabrication, and storage, this may include information security.

## 1.4 Some Remarks

Nanophotonics now exists as a novel field of optical technology in nanometric space. However, the name "nanophotonics" is occasionally used for photonic crystals [40], plasmonics [41], metamaterials [42, 43], silicon photonics [44], and QD lasers [45] using conventional propagating lights. For example, plasmonics utilizes the resonant enhancement of the light in a metal by exciting free electrons. The letters "on" in the word "plasmon" represent the quanta, or the quantum mechanical picture of the plasma oscillation of free electrons in a metal. However, plasmonics utilizes the classical wave optical picture using conventional terminology, such as the refractive index, wave number, and guided mode. Even when a metal is irradiated with light that obeys the laws of quantum mechanics, the quantum mechanical property is lost because the light is converted into the plasma oscillation of electrons, which has a short phase relaxation time. To reduce device size and heat generation, it is still insufficient to quantize the plasma oscillation because the position of the photon is defined only in a space larger than the wavelength of light, which is the consequence of the uncertainty principle. That is, the wave function of a photon cannot be defined in sub-wavelength space. However, if a sub-wavelength-sized nanometric particle is used to absorb the light, it works as a photodetector, and consequently, the photon can be detected and its position determined by the size of the particles with high spatial accuracy. This means that a local interaction between nanometric particles and photons is required to go beyond the diffraction limit.

Furthermore, the energy transferred via this interaction must be dissipated in the nanometric particles or adjacent macroscopic materials to fix the position and magnitude of the transferred energy. Because plasmonics does not deal with this local dissipation of energy, it is irrelevant for quantitative innovation by breaking the diffraction limit, or for qualitative innovation. Local energy transfer and its subsequent dissipation have become possible only in nanophotonics by using optical near fields [46, 47].

Here, we should consider the stern warning by C. Shannon on the casual use of the term "information theory," which was a trend in the study of information theory during the 1950s [48]. The term "nanophotonics" has been used in a similar way, although some work in "nanophotonics" is not based on optical near-field interactions. For the true development of nanophotonics, one needs deep physical insights into the virtual exciton–polariton and the nanometric subsystem composed of electrons and photons.

## References

1. Townes, C.H. 1999. *How the Laser Happened.* London: Oxford University Press.
2. Optoelectronics Industry and Technology Development Association. 1998. *Report on Photonics Technology Road Map: Information Storage.*
3. MIT Microelectronics center. 2005. *Communication Technology Roadmap.*
4. Semiconductor Industry Association. 2006. *International Technology Roadmap for Semiconductors.*
5. Synge, E.A. 1928. A suggested method for extending microscopic resolution into the ultra-microscopic region. *Phil. Mag.* 6: 356–362.
6. Ohtsu, M. 1998. *Near-Field Nano/Atom Optics and Technology,* 31–69. Spinger-Verlag.
7. Ohtsu, M. and Hori, H. 1999. *Near-Field Nano-Optics,* 113–142. New York: Kluwer Academic/Plenum Publishers.
8. Ohtsu, M. and Kobayashi, K. 2004. *Optical Near Fields,* 88–108. Berlin: Springer-Verlag.
9. Ohtsu, M. and Kobayashi, K. 2004. *Optical Near Fields,* 109–120. Berlin: Springer-Verlag.
10. Ohtsu, M.(ed). 2006. *Progress in Nano-Electro-Optics V,* Spinger-Verlag, Preface to Volume V: Based on "nanophotonics" proposed by Ohtsu in 1993, OITDA (Optical Industry Technology Development Association, Japan) organized the nanophotonics technical group in 1994, and discussions on the future direction of nanophotonics were started in collaboration with academia and industry.
11. Nishida, T., Matsumoto, T., Akagi, F., Hieda, H., Kikitsu, A., Naito, K., Koda, T., Nishida, N., Hatano, H., and Hirata, M. 2007. Hybrid recording on bit-patterned media by using a near-field optical head. *J. Nanophotonics* 2: to be published.
12. Naruse, M, Miyazaki, T., Kawazoe,T., Sangu,S., Kobayashi,K., Kubota, F., and Ohtsu, M. 2005. Nanophotonic Computing Based on Optical Near-Field Interactions between QDs. *IEICE Transaction. Electron.* E88-C: 1817–1823.
13. Inao, Y., Nakasato, S., Kuroda, R., and Ohtsu, M. 2007. Nonadiabatic photochemical reaction and application to photolithography. *Microelectronic Engineering* 84: 705–710.

14. Matsuda, K., Saiki, T., Saito, H., and Nishi, K. 2000. Room temperature photoluminescence spectroscopy of a single $In_{0.5}Ga_{0.5}As$ QDs by using highly sensitive near-field scanning optical microscope. *Appl. Phys. Lett.* 76: 73–75.
15. Fukuda, H., Saiki, T., and Ohtsu, M. 2001. Diagnostics of Semiconductor Devices beyond the Diffraction Limit of Light. *Sensors and Materials* 13: 445–460.
16. Hosaka, N. and Saiki, T. 2001. Near-field fluorescence imaging of single molecules with a resolution in the range of 10 nm. *J. Microscopy* 202: 362–364.
17. Ushiki, T. 2005. Scanning near-field optical/atomic force microscopy in biology. *Abstracts of the 5th Asia-Pacific Conference on Near-Field Optics,* 5. Optical Society of Japan.
18. Narita, Y., Tadokoro, T., Ikeda, T., Saiki, T., Mononobe, S., and Ohtsu, M. 1998. Near-Field Raman Spectral Measurement of Polydiacetylene. *Appl. Spectrocopy* 52: 1141–1144.
19. Sato, F. 2004. Development of a time-resolved near field scanning optical microscope by time-correlated single photon measurement. *Jasco Report* 46: 34–38.
20. Naruse, M., Yatsui, T., Nomura, W., Hirose, N., and Ohtsu, M. 2005. Hierarchy in optical near-fields and its application to memory retrieval. *Opt. Express* 13: 9265–9271.
21. Naruse, M., Hori, H., Kobayashi, K., and Ohtsu, M. 2007. Tamper resistance in optical excitation transfer based on optical near-field interactions. *Optics Letters* 32: 1761–1763.
22. Naruse, M., Kawazoe, T., Yatsui, T., Sangu, S., Kobayashi, K., and Ohtsu, M. 2006. Architectural Approach in Nanophotonics for Information and Communication Systems. In *Progress in Nano-Electro-Optics V,* ed. M. Ohtsu, 163–182. Berlin: Springer-Verlag.
23. Kawazoe, T., Kobayashi, K., Takubo, S., and Ohtsu, M. 2005. Nonadiabatic photodissociation process using an optical near field. *J. Chem. Phys.* 122: 024715 1–5.
24. Ohtsu, M. 1998. *Near-Field Nano/Atom Optics and Technology,* 218–293. Springer-Verlag.
25. Kobayashi, K., Sangu, S., Ito, H., and Ohtsu, M. 2001. Near-field optical potential for a neutral atom. *Phys. Rev. A* 63: 013806 1–9.
26. Ito, H., Nakata, T., Sakaki, K., Ohtsu, M., Lee, K.I., and Jhe, W. 1996. Laser Spectroscopy of Atoms Guided by Evanescent Waves in Micron-Sized Hollow Optical Fibers. *Phys. Rev. Lett.* 76: 4500–4503.
27. Totsuka, K., Ito, H., Kawamura, T., and Ohtsu, M. 2003. High spatial resolution atom detector with two-color optical near fields. *Jpn. J. Appl. Phys.* 41: 1566–1571.
28. Totsuka, K., Ito, H., Suzuki, K., Yamamoto, K., Ohtsu, M., and Yatsui, T. 2003. A slit-type atom deflector with near-field light. *Appl. Phys. Lett.* 82: 1616–1618.
29. Takamizawa, A., Ito, H., Yamada, S., and Ohtsu, M., 2004. Observation of cold atom output from an evanescent-light funnel. *Appl. Phys. Lett.* 85: 1790–1792.
30. Inoue, T. and Hori, H. 2001. Quantization of evanescent electromagnetic waves based on detector modes. *Physical Review A* 63: 063805 1–16.
31. Inoue, T. and Hori, H. 2005. Quantum Theory of Radiation in Optical Near Field Based on Quantization of Evanescent Electromagnetic Waves Using Detector Mode. In *Progress in Nano-Electro Optics IV,* ed. M. Ohtsu, 127–199. Berlin: Springer-Verlag.
32. Inoue, T., and Hori, H. 2005. Theory of transmission and dissipation of radiation near a metallic slab based on angular spectrum representation. *IEICE Trans. Electron.* E88-C: 1836–1844.

33. Cho, K. 1991. Nonlocal theory of radiation-matter interaction: Boundary-condition-less treatment of Maxwell equation. *Progress of Theoretical Physics Supplement* 106: 225–233.
34. Ishihara, H., and Cho, K. 1993. Nonlocal theory of the third-order nonlinear optical response of confined excitons. *Physical Review B.* 48: 7960–7974.
35. Cho, K., Ohfuti, Y., and Arima, K. 1996. Theory of resonant SNOM (scanning near-field optical microscopy): breakdown of the electric dipole selection rule in the reflection mode. *Surface Science* 363: 378–384.
36. Iida, T., and Ishihara, H. 2005. Optical manipulation of nano materials under quantum mechanical resonance conditions. *IEICE Transactions on Electronics* E88-C: 1809–1816.
37. Mitsutake, K., and Tsukada, M. 2006. Theoretical study of electron-vibration coupling on carrier transfer in molecular bridges. *e-J. Surface Science and Nanotechnology* 4: 311–318.
38. Chen, L.C., Yonehama, J., Ueda, T., Hori, H., and Hiraoka, K. 2007. Visible-laser desorption/ionization on gold nanostructures. *J. Mass Spectrometry* 42: 346–353.
39. Chen, L.C., Ueda, T., Sagisaka, M., Hori, H., and Hiraoka, K. 2007. Visible laser desorption/ionization mass spectrometry using gold nanorods. *J. Phys. Chemistry* 111: 2409–2415.
40. Ho, K. M. , Chan, C. T., and Soukoulis, C. M. 1990. Existence of a photonic gap in periodic dielectric structures. *Phys. Rev. Lett.* 65: 3152–3155.
41. Podolskiy, V. A., Sarychev, A. K. , and Shalaev. V. M. 2003. Plasmon modes and negative refraction in metal nanowire composites. *Optics Express* 11: 735–745.
42. Shelby, R.A., Smith, D.R., and Shultz, S. 2001. Experimental verification of a negative index of refraction. *Science* 292: 77–79.
43. Pendry, J. B. 2000. Negative refraction makes a perfect lens. *Phys. Rev. Lett.* 85: 3966–3969.
44. Rong, H., Liu, A., Nicolaescu, R., and Paniccia, M. 2004. Raman gain and nonlinear optical absorption measurements in a low-loss silicon waveguide. *Appl. Phys. Lett.* 85: 2196–2198.
45. Arakawa, Y., and Sakaki, H. 1982. Multidimensional quantum well laser and temperature-dependence of its threshold current. *Appl. Phys. Lett.* 40: 939–941.
46. Ohtsu, M. and Kobayashi, K. 2003. *Optical Near Fields,* 109–150. Springer-Verlag.
47. Ohtsu, M. 2007. Nanooptics. In *Handbook of Lasers and Optics,* ed.F. Träger, 1079–1090. Berlin: Springer-Verlag.
48. Shannon, C. 1956. The bandwagon. *IEEE Trans. Information Theory* 2: 3.

# 2

# *Basis of Nanophotonics*

In Section 2.1, as a base for nanophotonics, we provide a quantum theoretical description of optical near fields and related problems that puts matter excitation such as electronic and vibrational ones on an equal footing with photons. With the help of the projection operator method, we derive effective interactions exerted in the nanometric material (nanomaterial) system surrounded by an incident light and a macroscopic material system, which are called optical near-field interactions. They are essential to understand the topics of the following sections, that is, the principles of operations of nanophotonic devices and those of nanofabrication using optical near fields.

Section 2.2 discusses the principles of operations of nanophotonic devices that are based on the control of the excitation (energy) transfer between nanomaterials via optical near fields, or optical near-field interactions. In an example of nanomaterials, we describe the fundamentals of a semiconductor quantum dot (QD) such as energy levels, electron or hole states, and electron-hole pair states in a QD. After the outline of basic ideas of nanophotonic devices, a quantum master equation for the relevant system (a typical open system) is described in some depth, which is then utilized for a discussion of the temporal evolution of the excitation transfer and the relaxation of an electron-hole pair between adjacent QDs driven by an optical near field.

In Section 2.3, we deal with nanostructure fabrication, in particular, photochemical vapor deposition (CVD) with optical near fields. Before the detail, we briefly show that the steep gradient fields lead a molecule to a nonadiabatic transition. Experimental illustration is then outlined, and unique features found in the experimental results are explained by using a simple quasiparticle model. Finally, the mechanism of photon localization in a nanometer space is discussed in detail, focusing on the phonon's role to the elementary process of photochemical reactions with optical near fields.

## 2.1 Optical Near-Fields and Effective Interactions as a Base for Nanophotonics

Several theoretical approaches to optical near-field problems, different from each other in viewpoints, have been proposed for these two decades. The optical near-field problems including its application to nanophotonics are ultimately how one should formulate a separated (more than two) composite system, each of which consists of a photon-electron-phonon interacting system on a nanometer scale and at the same time is connected with a macroscopic matter system as a source or a detector system. It must be inevitable toward realization of nanophotonics to clearly answer those issues. In order to provide a base for a variety of discussions in this research field, we will develop a new formulation within a quantum theoretical framework, putting mater excitations (electronic and vibrational) on an equal footing with photons.

It is well known that a "photon," whose concept has been established as a result of quantization of a free electromagnetic field [1], corresponds to a discrete excitation of electromagnetic modes in a virtual cavity. Different from an electron, a photon is massless, and it is difficult to construct a wave function in the coordinate representation that gives a photon picture as a spatially localized point particle as an electron [2]. However, if there is a detector such as an atom to absorb a photon in an area whose linear dimension is much smaller than the wave length of light, it would be possible to detect energy of a photon with the same precision as the detector size [3,4]. In optical near-field problems, it is required to consider the interactions between light and nanomaterials and detection of light by another nanomaterial on a nanometer scale. Then it is more serious for quantization of the field how to define a virtual cavity, or which normal modes to be used, since there exist more than two systems composed of an arbitrary shape, size, and material on the nanometer region, and still connected with a macroscopic material system such as a source or a detector system.

In this section, we describe a model and a theoretical approach to address the issue, which is essential to understand principles of operations of nanophotonic devices and that of nanofabrication using optical near fields.

Let us consider a nanomaterial system surrounded by an incident light and a macroscopic material system, which is electromagnetically interacting with one another in a complicated way, as schematically shown in Figure 2.1. Using the projection operator method (refer to Appendix A), we can derive an effective interaction (refer to appendix B) between the relevant nanomaterials in which we are interested, after renormalizing the other effects [5–8]. It corresponds to an approach to describe "photons localized around nanomaterials" as if each nanomaterial would work as a detector and light source in a self-consistent way. The effective interaction related to optical near fields is hereafter called an optical near-field interaction [5–8]. As it will be discussed in detail in this section, the optical near-field interaction potential between nanomaterials separated by $R$ is given as follows:

$$V_{\mathrm{eff}} = \frac{\exp(-aR)}{R}, \tag{2.1}$$

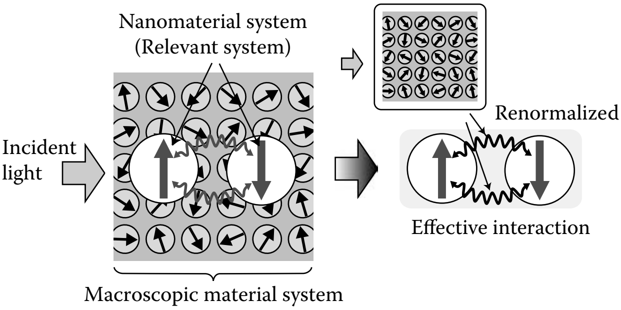

**FIGURE 2.1**
Schematic drawing of the effective interaction between nanomaterials after renormalizing the effects of the macroscopic material and incident light field system.

where $a^{-1}$ is the interaction range that represents the characteristic size of nanomaterials, does not depend on the wavelength of light. It indicates that photons are localized around the nanomaterials as a result of the interaction with matter fields, from which a photon, in turn, can acquire a finite mass. Therefore, we might consider that the optical near-field interaction is produced via the localized photon hopping [9–11] between nanomaterials.

On the basis of the projection operator method introduced in Appendix A, we will investigate formulation of an optical near-field system that was briefly mentioned earlier. Moreover, explicit functional forms of the optical near-field interaction will be obtained by using either the effective interaction $\hat{V}_{\text{eff}}$ in Eq. (B14), or its approximation with Eq. (B23) [5,6].

### 2.1.1 Relevant Nanometric Subsystem and Irrelevant Macroscopic Subsystem

As illustrated in Figure 2.1, the optical near-field system consists of two subsystems: one is a macroscopic subsystem including the incident light, whose typical dimension is much larger than the wavelength of the incident light. The other is a nanometric subsystem whose constituents are, for example, a nanometric aperture or a protrusion at the apex of the near-field optical probe, and a nanometric sample. We call such an aperture or a protrusion a probe tip. As a nanometric sample we mainly suppose a single atom/molecule, or QD (QDs). Subdivision of the total system is schematically illustrated in Figure 2.2. Two subsystems are interacting with each other, and it is very important to formulate the interaction consistently and systematically.

Let us call the nanometric subsystem as relevant subsystem n, and the macroscopic subsystem as irrelevant subsystem M. We are interested in

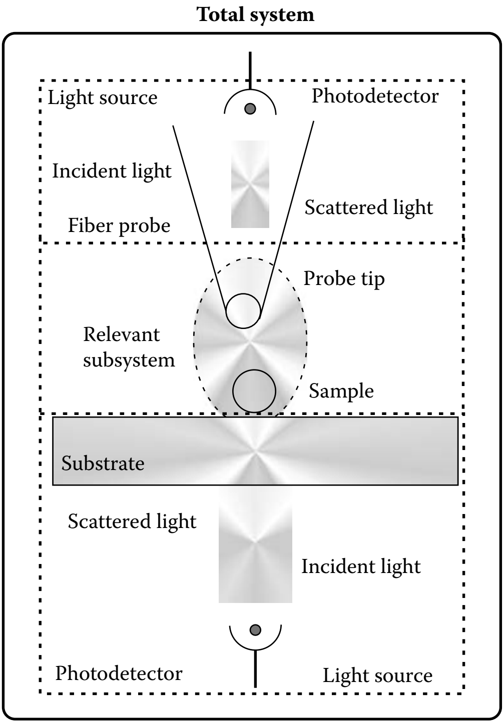

**FIGURE 2.2**
Subdivision of the optical near-field system into a relevant nanometric subsystem and an irrelevant macroscopic subsystem.

the subsystem n, in particular, the interaction induced to the subsystem n. Therefore, it is a key to renormalize the effects originating from the subsystem M in a consistent and systematic way. Now we show a formulation based on the projection operator method described in Appendix A.

### 2.1.2 P Space and Q Space

It is preferable to express exact states $|\psi\rangle$[*] for the total system in terms of a small number of bases of a small number of degrees of freedom as possible, which span P space. In the following let us assume two states as the

---

[*] This notation is the bra and ket notation developed by P. A. M. Dirac. In quantum mechanics a physical state is represented by a state vector in a complex vector space. Following Dirac, such a state is called a ket and denoted by $|\psi\rangle$. We also introduce the notation of a bra vector, denoted by $\langle\psi|$. There is a one-to-one correspondence between a ket vector and a bra vector. An observable, such as energy and momentum, can be expressed by an operator, such as $\hat{H}$ and $\hat{\vec{p}}$, in the vector space, and quite generally an operator acts on a ket vector from the left as $\hat{H}|\psi\rangle$ [1, 12, 13].

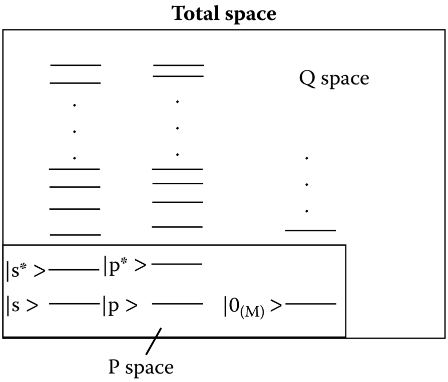

**FIGURE 2.3**
Schematic illustration of P space and its complementary space, Q space. The P space is spanned by a small number of bases of a small number of degrees of freedom, while the Q space is spanned by a huge number of bases of a large number of degrees of freedom.

P-space components: $|\phi_1\rangle = |s^*\rangle\,|p\rangle \otimes |0_{(M)}\rangle$ and $|\phi_2\rangle = |s\rangle\,|p^*\rangle \otimes |0_{(M)}\rangle$. Here $|s\rangle$ and $|s^*\rangle$ are eigenstates[*] of the sample that is isolated from the others, whereas $|p\rangle$ and $|p^*\rangle$ are eigenstates of the probe tip that is also isolated[†]. In addition, exciton polariton states as bases discussed in Appendix C are used to describe the macroscopic subsystem M, and thus $|0_{(M)}\rangle$ represents the vacuum for exciton polaritons. Note that there exist photons and electronic matter excitations even in the vacuum state $|0_{(M)}\rangle$. The direct product[‡] is denoted by the symbol ⊗. The complementary space to the P space is called Q space, which is spanned by a huge number of bases of a large number of degrees of freedom not included in the P space, as schematically shown in Figure 2.3.

---

[*] When an operator $\hat{A}$ acts on a ket vector $|\alpha\rangle$, there are particular kets of importance so that $a_\alpha\,|\alpha\rangle$ is a constant $a_\alpha$ times $|\alpha\rangle$. They are known as eigenkets of operator $\hat{A}$. If the eigenkets are particularly denoted by $|1\rangle, |2\rangle, \ldots, |j\rangle, \ldots$, then the following property is satisfied $\hat{A}\,|1\rangle = a_1\,|1\rangle, \hat{A}\,|2\rangle = a_2\,|2\rangle, \cdots, \hat{A}\,|j\rangle = a_j\,|j\rangle, \cdots,$ where $a_1, a_2, \ldots, a_j, \ldots,$ are just numbers and the set of numbers $\{a_1, a_2, \ldots, a_j, \ldots\}$ is called eigen values of operator $\hat{A}$. The physical state corresponding to an eigenket is called an eigenstate. The eigenstates in the text, for example, $|s\rangle$ and $|p\rangle$ are eigenkets of the Hamiltonian describing the isolated sample and probe, $\hat{H}_s$ and $\hat{H}_p$, respectively.

[†] Here a two-level system is assumed for each material system, but can be easily extended to a multilevel system by introducing another projection operators.

[‡] Let **A** and **B** be a 2 by 2 matrix, respectively, and expressed as $\mathbf{A} = \begin{pmatrix} a_{11} & a_{12} \\ a_{21} & a_{22} \end{pmatrix}, \mathbf{B} = \begin{pmatrix} b_{11} & b_{12} \\ b_{21} & b_{22} \end{pmatrix}$, in order to understand the concept of the direct product. Then the direct product, $\mathbf{C} = \mathbf{A} \otimes \mathbf{B}$, is given by $\mathbf{C} = \begin{pmatrix} a_{11}\mathbf{B} & a_{12}\mathbf{B} \\ a_{21}\mathbf{B} & a_{22}\mathbf{B} \end{pmatrix}$ with $a_{ij}\mathbf{B} = \begin{pmatrix} a_{ij}b_{11} & a_{ij}b_{11} \\ a_{ij}\mathrm{b}_{21} & a_{ij}b_{11} \end{pmatrix}$ for $(i, j) = 1,2$.

### 2.1.3 Effective Interaction Exerted in the Nanometric Subsystem

When we evaluate the effective interaction in the P space given by

$$\hat{V}_{\mathrm{eff}} = (P\hat{J}^{\dagger}\hat{J}P)^{-1/2}(P\hat{J}^{\dagger}\hat{V}\hat{J}P)(P\hat{J}^{\dagger}\hat{J}P)^{-1/2} \tag{2.2}$$

(see Appendix B, especially Eq. (B14)), and trace out the other degrees of freedom, the result gives an effective interaction potential of the nanometric subsystem n after renormalizing the effects from the macroscopic subsystem M. Using the effective interaction potential, one can forget the subsystem M as if the subsystem n were isolated and separated from the subsystem M.

As the first step of the procedure, let us employ the bare interaction between the two subsystems in a dipole approximation as

$$\hat{V} = -\left\{\hat{\vec{\mu}}_s \cdot \hat{\vec{D}}^{\perp}(\vec{r}_s) + \hat{\vec{\mu}}_p \cdot \hat{\vec{D}}^{\perp}(\vec{r}_p)\right\} \tag{2.3}$$

(see Appendix D for the derivation and physical meanings). It should be noted that there are no interactions, that is, $\hat{V} = 0,$ without incident photons in the macroscopic subsystem M. The electric dipole operator is denoted by $\hat{\vec{\mu}}_{\alpha}(\alpha = s, p)$. The subscript s and p represent physical quantities related to the sample and the probe tip, respectively. Representative positions of the sample and the probe tip are chosen for simplicity by the vectors $\vec{r}_s$ and $\vec{r}_p$, respectively, but may be composed of several positions. In that case the quantities inside curly brackets in Eq. (3) should be read as summation. The transverse component of the electric displacement operator*, $\vec{D}^{\perp}(\vec{r})$, is expressed in terms of the vector potential $\hat{\vec{A}}(\vec{r})$ and its conjugate momentum $\hat{\vec{\Pi}}(\vec{r})$ as

$$\hat{\vec{\Pi}}(\vec{r}) = \frac{1}{4\pi c^2}\frac{\partial\hat{\vec{A}}}{\partial t} - \frac{1}{c}\hat{\vec{P}}^{\perp}(\vec{r}) = -\frac{1}{4\pi c}\hat{\vec{E}}^{\perp}(\vec{r}) - \frac{1}{c}\hat{\vec{P}}^{\perp}(\vec{r}) = -\frac{1}{4\pi c}\hat{\vec{D}}^{\perp}(\vec{r}), \tag{2.4}$$

according to Appendix D. Here $c$ is light speed in vacuum, while $\hat{\vec{P}}^{\perp}(\vec{r})$ and $\hat{\vec{E}}^{\perp}(\vec{r})$ are the transverse components of the polarization and electric fields, respectively.

With the help of the mode expansion of $\hat{\vec{A}}(\vec{r})$ and $\hat{\vec{\Pi}}(\vec{r})$ as

$$\hat{\vec{A}}(\vec{r}) = \sum_{\vec{k}}\sum_{\lambda=1}^{2}\left(\frac{2\pi\hbar c^2}{V\omega_{\vec{k}}}\right)^{1/2}\vec{e}_{\lambda}(\vec{k})\left\{\hat{a}_{\lambda}(\vec{k})e^{i\vec{k}\cdot\vec{r}} + \hat{a}_{\lambda}^{\dagger}(\vec{k})e^{-i\vec{k}\cdot\vec{r}}\right\} \tag{2.5}$$

and

$$\hat{\vec{\Pi}}(\vec{r}) = \frac{1}{4\pi c^2}\frac{\partial\hat{\vec{A}}}{\partial t} = -\frac{i}{4\pi c}\sum_{\vec{k}}\sum_{\lambda=1}^{2}\left(\frac{2\pi\hbar\omega_{\vec{k}}}{V}\right)^{1/2}\vec{e}_{\lambda}(\vec{k})\left\{\hat{a}_{\lambda}(\vec{k})e^{i\vec{k}\cdot\vec{r}} - \hat{a}_{\lambda}^{\dagger}(\vec{k})e^{-i\vec{k}\cdot\vec{r}}\right\}, \tag{2.6}$$

---

* The transverse component is defined by $\nabla\cdot\vec{F}^{\perp} = 0$, while the longitudinal component is defined by $\nabla\times\vec{F}^{\parallel} = 0$, for an arbitrary vector field $\vec{F}(\vec{r})$.

we can rewrite the transverse component of the electric displacement operator as

$$\hat{\vec{D}}^{\perp}(\vec{r}) = i\sum_{\vec{k}}\sum_{\lambda=1}^{2}\left(\frac{2\pi\hbar\omega_{\vec{k}}}{V}\right)^{1/2}\vec{e}_{\lambda}(\vec{k})\left\{\hat{a}_{\lambda}(\vec{k})e^{i\vec{k}\cdot\vec{r}} - \hat{a}_{\lambda}^{\dagger}(\vec{k})e^{-i\vec{k}\cdot\vec{r}}\right\}, \tag{2.7}$$

where the plane waves are used for the mode functions, and the creation and annihilation operators of a photon with wave vector $\vec{k}$, angular frequency $\omega_{\vec{k}}$, and polarization component $\lambda$ are designated by $\hat{a}_{\lambda}^{\dagger}(\vec{k})$ and $\hat{a}_{\lambda}(\vec{k})$, respectively. The quantization volume is V, and the unit vector related to the polarization direction is shown by $\vec{e}_{\lambda}(\vec{k})$.

Because exciton polariton states as bases are employed to describe the macroscopic subsystem M, the creation and annihilation operators of a photon in Eq. (7) are rewritten by the exciton polariton operators $\xi^{\dagger}(\vec{k})$, and $\hat{\xi}^{\dagger}(\vec{k})$, and then they are substituted into Eq. (3). Using the electric dipole operator defined by

$\hat{\vec{\mu}}_{\alpha}$ = with creation and annihilation operators $\hat{B}(\vec{r}_{\alpha})$ and $\hat{B}^{\dagger}(\vec{r}_{\alpha})$
and dipole moment $\vec{\mu}_{\alpha}$, (2.8)

we obtain the bare interaction in the exciton polariton picture as

$$\hat{V} = -i\sum_{\alpha=s}^{p}\sum_{\vec{k}}\left(\frac{2\pi\hbar}{V}\right)^{1/2}\left(\hat{B}(\vec{r}_{\alpha}) + \hat{B}^{\dagger}(\vec{r}_{\alpha})\right)\left(K_{\alpha}(\vec{k})\hat{\xi}(\vec{k}) - K_{\alpha}^{*}(\vec{k})\hat{\xi}^{\dagger}(\vec{k})\right). \tag{2.9}$$

Here $K_{\alpha}(\vec{k})$ is the coupling coefficient between the exciton polariton and the nanometric subsystem n, and given by

$$K_{\alpha}(\vec{k}) = \sum_{\lambda=1}^{2}\left(\vec{\mu}_{\alpha}\cdot\vec{e}_{\lambda}(\vec{k})\right)f(k)e^{i\vec{k}\cdot\vec{r}_{\alpha}} \tag{2.10}$$

with

$$f(k) = \frac{ck}{\sqrt{\Omega(k)}}\sqrt{\frac{\Omega^{2}(k) - \Omega^{2}}{2\Omega^{2}(k) - \Omega^{2} - (ck)^{2}}}\,. \tag{2.11}$$

The asterisk stands for the complex conjugate, whereas c, $\Omega(k)$ and $\Omega$ are eigenfrequencies of both exciton polariton and electronic polarization of the macroscopic subsystem M, respectively (refer to Appendix E for the derivation). The dispersion relation for a free photon, $\omega_{\vec{k}} = ck$ is used in Eq. (11). Note that the wave-number dependence of $f(k)$ characterizes a typical interaction range of exciton polaritons coupled to the nanometric subsystem n.

Next step is to evaluate the amplitude of effective interaction exerted in the nanometric subsystem, for example, effective sample-probe tip interaction in the P space

$$V_{\text{eff}}(2,1) \equiv \langle\phi_{2}|\hat{V}_{\text{eff}}|\phi_{1}\rangle. \tag{2.12}$$

Using Eq. (2) as $\hat{V}_{\text{eff}}$ with first-order approximation of $\hat{J}^{(1)}$ Eq. (B23) in Appendix B, we can explicitly write down Eq. (12) in the following form:

$$\begin{aligned} V_{\text{eff}}(2,1) &= \langle \phi_2 | P\hat{V}Q\hat{V}\left(E_P^0 - E_Q^0\right)^{-1} P | \phi_1 \rangle + \langle \phi_2 | P\left(E_P^0 - E_Q^0\right)^{-1} \hat{V}Q\hat{V}P | \phi_1 \rangle \\ &= \sum_m \langle \phi_2 | P\hat{V}Q | m \rangle \langle m | Q\hat{V}P | \phi_1 \rangle \left( \frac{1}{E_{P1}^0 - E_{Qm}^0} + \frac{1}{E_{P2}^0 - E_{Qm}^0} \right), \end{aligned} \tag{2.13}$$

The second line shows that a virtual transition from the initial state $|\phi_1\rangle$ in the P space to an intermediate state $|m\rangle$ in the Q space is followed by subsequent virtual transition from the intermediate state $|m\rangle$ to the final state $|\phi_2\rangle$ in the P space. Here $E_{P1}^0$ $E_{P2}^0$ and $E_{Qm}^0$ denote eigenenergies of $|\phi_1\rangle$ $(|\phi_2\rangle)$ in the *P* space and that of $|\phi_m\rangle$ in the Q, respectively. Now we can proceed to further process by substituting the explicit bare interaction $\hat{V}$ in Eq. (9) with Eqs. (10) and (11) into Eq. (13). First of all, note that the one-exciton polariton state among arbitrary intermediate states $|m\rangle$, can only contribute to nonzero matrix elements. Therefore Eq. (13) can be transformed into

$$V_{\text{eff}}(2,1) = -\frac{\hbar}{(2\pi)^2} \int d^3k \left[ \frac{K_p(\vec{k})K_s^*(\vec{k})}{\Omega(k) - \Omega_0(s)} + \frac{K_s(\vec{k})K_p^*(\vec{k})}{\Omega(k) + \Omega_0(p)} \right], \tag{2.14}$$

where the summation over $\vec{k}$ is replaced by $\vec{k}$- integration, that is, $\frac{V}{(2\pi)^3}\int d^3k$ in a usual manner. Excitation energies of the sample (between $|s^*\rangle$ and $|s\rangle$) and the probe tip (between $|p^*\rangle$ and $|p\rangle$) are assumed as $E_s = \hbar\Omega_0(s)$ and $E_p = \hbar\Omega_0(p)$, respectively.

Exchanging the arguments 1 and 2, or the role of the sample and probe tip, we can similarly calculate $V_{\text{eff}}(1,2) \equiv \langle \phi_1 | \hat{V}_{\text{eff}} | \phi_2 \rangle$ as

$$V_{\text{eff}}(1,2) = -\frac{\hbar}{(2\pi)^2} \int d^3k \left[ \frac{K_s(\vec{k})K_p^*(\vec{k})}{\Omega(k) - \Omega_0(p)} + \frac{K_p(\vec{k})K_s^*(\vec{k})}{\Omega(k) + \Omega_0(s)} \right]. \tag{2.15}$$

Therefore, the total amplitude of the effective sample-probe tip interaction is given by the sum of Eqs. (14) and (15), which includes the effects from the macroscopic subsystem M. We write this effective interaction potential for the nanometric subsystem n as $V_{\text{eff}}(\vec{r})$ as follows:

$$V_{\text{eff}}(\vec{r}) = -\frac{1}{4\pi^2} \sum_{\lambda=1}^{2} \sum_{\alpha=p,s} \int d^3k [(\vec{\mu}_p \cdot \vec{e}_\lambda(\vec{k}))(\vec{\mu}_s \cdot \vec{e}_\lambda(\vec{k}))] \hbar f^2(k) \left( \frac{e^{i\vec{k}\cdot\vec{r}}}{E(k) + E_\alpha} + \frac{e^{-i\vec{k}\cdot\vec{r}}}{E(k) - E_\alpha} \right), \tag{2.16}$$

where we have set $E(k) = \hbar\Omega(k)$, and $E_\alpha = \hbar\Omega_0(\alpha^*) - \hbar\Omega_0(\alpha)$ for $\alpha = \mathrm{p}$ and $\alpha = \mathrm{s}$. The summation over polarization λ is performed as

$$\sum_{\lambda=1}^{2} \vec{e}_{\lambda i}(\vec{k})\vec{e}_{\lambda j}(\vec{k}) = \delta_{ij} - \hat{k}_i\hat{k}_j, \tag{2.17}$$

and thus the summation of $(\vec{\mu}_p \cdot \vec{e}_\lambda(\vec{k}))(\vec{\mu}_s \cdot \vec{e}_\lambda(\vec{k}))$ over $\lambda$ can be reduced as follows:

$$\sum_{\lambda=1}^{2} (\vec{\mu}_p \cdot \vec{e}_\lambda(\vec{k}))(\vec{\mu}_s \cdot \vec{e}_\lambda(\vec{k})) = \sum_{\lambda=1}^{2}\sum_{i,j} (\mu_{pi}\vec{e}_{\lambda i}(\vec{k}))(\mu_{sj}\vec{e}_{\lambda j}(\vec{k})) = \sum_{i,j} \mu_{pi}\mu_{sj}(\delta_{ij} - \hat{k}_i\hat{k}_j) \tag{2.18}$$

with the unit vector $\hat{k} \equiv \vec{k}/k$. Noticing $d^3k = k^2 dk d\Omega = k^2 dk \sin\theta d\theta d\varphi$ and

$$\begin{aligned} \delta_{ij}\int e^{\pm i\vec{k}\cdot\vec{r}} d\Omega &= \delta_{ij}\int_0^{2\pi}\int_{-1}^{1} e^{\pm ikr\cos\theta} d(\cos\theta) d\varphi = \delta_{ij}\frac{2\pi}{ikr}(e^{ikr} - e^{-ikr}), \\ -\int \hat{k}_i\hat{k}_j e^{\pm i\vec{k}\cdot\vec{r}} d\Omega &= \frac{1}{k^2}\nabla_i\nabla_j \int e^{\pm i\vec{k}\cdot\vec{r}} d\Omega = \frac{2\pi}{ik^3}\nabla_i\nabla_j\left(\frac{e^{ikr} - e^{-ikr}}{r}\right), \end{aligned} \tag{2.19}$$

we find

$$\begin{aligned} \int (\delta_{ij} - \hat{k}_i\hat{k}_j) e^{\pm i\vec{k}\cdot\vec{r}} d\Omega &= \delta_{ij}\frac{2\pi}{ik}\left(\frac{e^{ikr} - e^{-ikr}}{r}\right) + \frac{2\pi}{ik^3}\nabla_i\nabla_j\left(\frac{e^{ikr} - e^{-ikr}}{r}\right) \\ &= 2\pi\left[\delta_{ij}\frac{(e^{ikr} - e^{-ikr})}{ikr} + (\delta_{ij} - 3\hat{r}_i\hat{r}_j)\left\{\frac{(e^{ikr} + e^{-ikr})}{k^2r^2} - \frac{(e^{ikr} - e^{-ikr})}{ik^3r^3}\right\}\right. \\ &\quad \left. - \frac{(e^{ikr} - e^{-ikr})}{ikr}\hat{r}_i\hat{r}_j\right], \end{aligned} \tag{2.20}$$

where $\hat{r}$ is the unit vector defined by $\hat{r} \equiv \vec{r}/r$, and the $j$-th component is denoted by $\hat{r}_j$ Hence the effective interaction potential can be rewritten as

$$\begin{aligned} V_{\text{eff}}(\vec{r}) = &-\frac{1}{2\pi}\int_{-\infty}^{\infty} k^2 dk \hbar f^2(k) \sum_{\alpha=s,p}\left(\frac{1}{E(k)+E_\alpha} + \frac{1}{E(k)-E_\alpha}\right) \\ &\times\left\{(\vec{\mu}_s\cdot\vec{\mu}_p)e^{i\vec{k}\cdot\vec{r}}\left(\frac{1}{ikr} + \frac{1}{k^2r^2} - \frac{1}{ik^3r^3}\right) - (\vec{\mu}_s\cdot\hat{r})(\vec{\mu}_p\cdot\hat{r})e^{i\vec{k}\cdot\vec{r}}\left(\frac{1}{ikr} + \frac{3}{k^2r^2} - \frac{3}{ik^3r^3}\right)\right\}, \end{aligned} \tag{2.21}$$

where the integration range is extended from $(0, \infty)$ to $(-\infty, \infty)$. When the dispersion relation of exciton polaritons, which have been chosen as a basis describing the macroscopic subsystem M, is approximated as

$$E(k) = \hbar\Omega + \frac{(\hbar k)^2}{2m_{\mathrm{pol}}} = E_m + \frac{(\hbar ck)^2}{2E_{\mathrm{pl}}}, \tag{2.22}$$

in terms of the effective mass of exciton polaritons, $m_{\mathrm{pol}}$, or $E_{\mathrm{pl}} = m_{\mathrm{pol}}c^2$ and the electronic excitation energy of the macroscopic subsystem M, $E_m = \hbar\Omega$, Eq. (21) is further simplified as follows:

$$\begin{aligned} V_{\mathrm{eff}}(\vec{r}) = & -\frac{1}{2\pi}\int_{-\infty}^{\infty} k^2 dk \hbar f^2(k) \sum_{\alpha=s,p} \frac{2E_{\mathrm{pl}}}{(\hbar c)^2}\left\{\frac{1}{(k+i\Delta_{\alpha+})(k-i\Delta_{\alpha+})} + \frac{1}{(k+i\Delta_{\alpha-})(k-i\Delta_{\alpha-})}\right\} \\ & \times\left\{(\vec{\mu}_s\cdot\vec{\mu}_p)e^{i\vec{k}\cdot\vec{r}}\left(\frac{1}{ikr}+\frac{1}{k^2r^2}-\frac{1}{ik^3r^3}\right) - (\vec{\mu}_s\cdot\hat{r})(\vec{\mu}_p\cdot\hat{r})e^{i\vec{k}\cdot\vec{r}}\left(\frac{1}{ikr}+\frac{3}{k^2r^2}-\frac{3}{ik^3r^3}\right)\right\} \\ & \equiv \sum_{\alpha=s,p}[V_{\mathrm{eff},\alpha+}(\vec{r}) + V_{\mathrm{eff},\alpha-}(\vec{r})] \end{aligned} \tag{2.23}$$

with

$$\Delta_{\alpha\pm} \equiv \frac{1}{\hbar c}\sqrt{2E_{\mathrm{pl}}(E_m \pm E_\alpha)}, \quad (E_m > E_\alpha). \tag{2.24}$$

The $k$-integration can be performed with the residues evaluated at $k = i\Delta_{\alpha\pm}$ and we have

$$\begin{aligned} V_{\mathrm{eff},\alpha\pm}(\vec{r}) = \mp\frac{1}{2}\Bigg[ & (\vec{\mu}_s\cdot\vec{\mu}_p)\left\{\frac{(\Delta_{\alpha\pm})^2}{r}+\frac{\Delta_{\alpha\pm}}{r^2}+\frac{1}{r^3}\right\}W_{\alpha\pm}e^{-\Delta_{\alpha\pm}r} \\ & -(\vec{\mu}_s\cdot\hat{r})(\vec{\mu}_p\cdot\hat{r})\left\{\frac{(\Delta_{\alpha\pm})^2}{r}+\frac{3\Delta_{\alpha\pm}}{r^2}+\frac{3}{r^3}\right\}W_{\alpha\pm}e^{-\Delta_{\alpha\pm}r}\Bigg], \end{aligned} \tag{2.25}$$

where the constants $W_{\alpha\pm}$ is defined by

$$W_{\alpha\pm} \equiv \frac{E_{\mathrm{pl}}}{E_\alpha}\frac{E_m^2 - E_\alpha^2}{(E_m \pm E_\alpha)(E_m - E_{\mathrm{pl}} \mp E_\alpha) - E_m^2/2}. \tag{2.26}$$

If the angular average of $(\vec{\mu}_s\cdot\hat{r})(\vec{\mu}_p\cdot\hat{r})$ is taken, the following expression

$$V_{\mathrm{eff}}(r) = -\frac{(\vec{\mu}_s\cdot\vec{\mu}_p)}{3}\sum_{\alpha=s,p}\left\{W_{\alpha+}(\Delta_{\alpha+})^2\frac{e^{-\Delta_{\alpha+}r}}{r} - W_{\alpha-}(\Delta_{\alpha-})^2\frac{e^{-\Delta_{\alpha-}r}}{r}\right\} \tag{2.27}$$

is obtained for the effective interaction potential, or the optical near-field interaction potential $V_{\text{eff}}(r)$, which consists of the sum of the Yukawa functions $Y(\Delta_{\alpha\pm} r) \equiv e^{-\Delta_{\alpha\pm} r}/r.$ with a shorter interaction range $\Delta_{\alpha+}$ (heavier effective mass) and a longer interaction range $\Delta_{\alpha-}$ (lighter effective mass).

To sum up, we find that the major part of the effective interaction exerted in the nanometric subsystem n is the Yukawa potential after renormalizing the effects from the macroscopic subsystem. This interaction comes from the mediation of massive virtual photons, or polaritons, where exciton polaritons have been employed in an explicit formulation, but in principle other type of polaritons would be applicable. In this section, we have mainly focused on the effective interaction of the nanometric subsystem n, after tracing out the other degrees of freedom. It is certainly possible to have a formulation with the projection onto the P space that is spanned in terms of the degrees of freedom of the massive virtual photons. This kind of formulation emphasizes a "dressed photon" picture, in which photons are not massless but massive as a result of light-matter interactions.

## 2.2 Principles of Operations of Nanophotonic Devices Using Optical Near-Fields

This section discusses the principles of operations of nanophotonic devices that are based on the control of the excitation energy transfer between nanomaterials by using the characteristics of optical near fields described in the preceding section, and then shows how to formulate them. To begin with we choose a semiconductor QDs in an example of nanomaterials to explain the fundamentals such as energy levels, electron or hole states, and electron-hole pair states in a QD. Using such fundamentals, we briefly outline the basic ideas and principles of operation of nanophotonic devices. Then by introducing the density operator, a quantum master equation for an open system is described in detail, in order to discuss the temporal evolution of the excitation energy transfer and the relaxation of an electron-hole pair between adjacent QDs driven by an optical near field, which is the heart of the problem.

### 2.2.1 Energy States of a Semiconductor QD

Because a QD is a nanomaterial confined in all the three dimensions, it has unique properties that cannot be fulfilled in bulk semiconductor materials; for example, an electron or an electron-hole pair created by light in a QD has discrete energy eigenvalues originating from the fact that wave functions of the electron or electron-hole are confined in the material. It is called a quantum confinement effect. In the following subsections, we summarize fundamental aspects of a semiconductor QD whose confinement geometry is spherical or cubic [34–38].

### *One-Particle States*

Even in a nanometric QD, the property is determined by a lot of electrons. In such a many-particle problem, it is useful to employ the envelope function and effective mass approximation on the assumption that the energy eigenvalues of the electron in the periodic lattice, that is, the energy bands, are not appreciably modified through the quantum confinement. This approximation allows us to determine a ground state and excited states of one-particle (electron or hole) problem, and a ground state of many-particle problem by successively placing particles into lowest energy levels that are not already occupied. The one-particle wavefunction in a QD can be given by a product of the one-particle wavefunction in a bulk material and the envelope function that satisfies the boundary conditions of the QD. Thus the eigenstate vector $|\psi_\mathrm{e}\rangle$ for a single electron in the QD is expressed as

$$|\psi_\mathrm{e}\rangle = \int d^3r\, \xi_\mathrm{e}(\vec{r})\hat{\psi}_\mathrm{e}^\dagger(\vec{r})\,|\Phi_\mathrm{g}\rangle, \tag{2.28}$$

in terms of the crystal ground state $|\Phi_g\rangle$ operated by the field operator for electron creation $\hat{\psi}_\mathrm{e}^\dagger(\vec{r})$, and multiplied by the envelope function $\xi_\mathrm{e}(\vec{r})$. Since no electrons in the conduction band exist in the crystal ground state, the field operator for electron annihilation $\hat{\psi}_\mathrm{e}(\vec{r})$ operated on $|\Phi_\mathrm{g}\rangle$ gives the following relation:

$$\hat{\psi}_\mathrm{e}(\vec{r})\,|\Phi_\mathrm{g}\rangle = 0. \tag{2.29}$$

The field operators for electron creation and annihilation satisfy the anticommutation relation for a fermion as

$$\left\{\hat{\psi}_\mathrm{e}(\vec{r}\,'), \hat{\psi}_\mathrm{e}^\dagger(\vec{r})\right\} \equiv \hat{\psi}_\mathrm{e}(\vec{r}\,')\hat{\psi}_\mathrm{e}^\dagger(\vec{r}) + \hat{\psi}_\mathrm{e}^\dagger(\vec{r})\hat{\psi}_\mathrm{e}(\vec{r}\,') = \delta(\vec{r} - \vec{r}\,'), \tag{2.30}$$

where $\delta(\vec{r} - \vec{r}\,')$ is the Dirac delta function. The equation for the envelope function $\xi_\mathrm{e}(\vec{r})$ can be obtained from the Schrödinger equation

$$\hat{H}_\mathrm{e}\,|\psi_\mathrm{e}\rangle = E_\mathrm{e}\,|\psi_\mathrm{e}\rangle \tag{2.31}$$

with the Hamiltonian $\hat{H}_\mathrm{e}$ for a single electron in the QD as

$$\hat{H}_\mathrm{e} = \int d^3r\,\hat{\psi}_\mathrm{e}^\dagger(\vec{r})\left[-\frac{\hbar^2}{2m_\mathrm{e}}\nabla^2\right]\hat{\psi}_\mathrm{e}(\vec{r}) + E_\mathrm{g}\int d^3r\,\hat{\psi}_\mathrm{e}^\dagger(\vec{r})\hat{\psi}_\mathrm{e}(\vec{r}), \tag{2.32}$$

and the energy eigenvalue $E_\mathrm{e}$. Here $m_\mathrm{e}$ and $E_\mathrm{g}$ denote the effective mass of an electron and the band gap energy of the bulk semiconductor, respectively

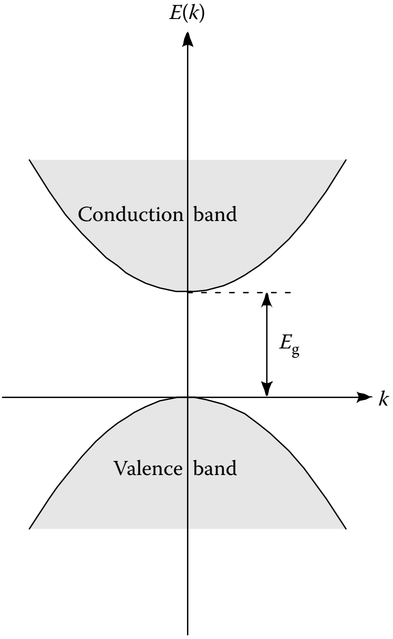

**FIGURE 2.4**
Band structure and energy gap $E_g$ of bulk semiconductor. The electron energy in the bulk semiconductor, $E(k)$, is plotted as a function of wave number $k$.

(see Figure 2.4). Substituting the explicit expressions into the Schrödinger equation, we have

$$\begin{aligned}\hat{H}_{\mathrm{e}}\,|\psi_{\mathrm{e}}\rangle &= \int d^3r'\,\hat{\psi}_{\mathrm{e}}^{\dagger}(\vec{r}\,')\left[-\frac{\hbar^2}{2m_{\mathrm{e}}}\nabla^2\right]\hat{\psi}_{\mathrm{e}}(\vec{r}\,')\int d^3r\,\xi_{\mathrm{e}}(\vec{r})\hat{\psi}_{\mathrm{e}}^{\dagger}(\vec{r})\,|\Phi_{\mathrm{g}}\rangle \\ &\quad + E_{\mathrm{g}}\int d^3r'\,\hat{\psi}_{\mathrm{e}}^{\dagger}(\vec{r}\,')\hat{\psi}_{\mathrm{e}}(\vec{r}\,')\int d^3r\,\xi_{\mathrm{e}}(\vec{r})\hat{\psi}_{\mathrm{e}}^{\dagger}(\vec{r})\,|\Phi_{\mathrm{g}}\rangle \\ &= -\frac{\hbar^2}{2m_{\mathrm{e}}}\int d^3r'\int d^3r\,\delta(\vec{r}-\vec{r}\,')\nabla^2\xi_{\mathrm{e}}(\vec{r})\hat{\psi}_{\mathrm{e}}^{\dagger}(\vec{r}\,')\,|\Phi_{\mathrm{g}}\rangle \\ &\quad + E_{\mathrm{g}}\int d^3r'\int d^3r\,\delta(\vec{r}-\vec{r}\,')\xi_{\mathrm{e}}(\vec{r})\hat{\psi}_{\mathrm{e}}^{\dagger}(\vec{r}\,')\,|\Phi_{\mathrm{g}}\rangle \\ &= \int d^3r\left[-\frac{\hbar^2}{2m_{\mathrm{e}}}\nabla^2\xi_{\mathrm{e}}(\vec{r})\right]\hat{\psi}_{\mathrm{e}}^{\dagger}(\vec{r})\,|\Phi_{\mathrm{g}}\rangle + E_{\mathrm{g}}\int d^3r\,\xi_{\mathrm{e}}(\vec{r})\,\hat{\psi}_{\mathrm{e}}^{\dagger}(\vec{r})\,|\Phi_{\mathrm{g}}\rangle\end{aligned} \tag{2.33}$$

and

$$E_{\mathrm{e}}\,|\psi_{\mathrm{e}}\rangle = E_{\mathrm{e}}\int d^3r\,\xi_{\mathrm{e}}(\vec{r})\,\hat{\psi}_{\mathrm{e}}^{\dagger}(\vec{r})|\Phi_{\mathrm{g}}\rangle, \tag{2.34}$$

where we used the anticommutation relation and the ground state property. It follows from these equations that the envelope function must satisfy the eigenvalue equation as

$$-\frac{\hbar^2}{2m_\mathrm{e}}\nabla^2\xi_\mathrm{e}(\vec{r}) = (E_\mathrm{e} - E_\mathrm{g})\xi_\mathrm{e}(\vec{r}). \tag{2.35}$$

Replacing the subscript of the envelope function, e by h, we similarly obtain the eigenvalue equation for the one-hole state

$$-\frac{\hbar^2}{2m_\mathrm{h}}\nabla^2\xi_\mathrm{h}(\vec{r}) = E_\mathrm{h}\xi_\mathrm{h}(\vec{r}), \tag{2.36}$$

where $E_g = 0$ is used.

Now let us solve the equation for the envelope function, assuming the spherical boundary conditions as $\xi_\mathrm{e}(\vec{r}) = \xi_\mathrm{h}(\vec{r}) = 0$ for $|\vec{r}| > R$. Noticing that the Laplace operator is written in the spherical coordinates as

$$\begin{aligned} \nabla^2 &= \frac{1}{r}\frac{\partial^2}{\partial r^2}r - \frac{\mathbf{L}^2}{r^2}, \\ \mathbf{L}^2 &= -\left(\frac{1}{\sin\theta}\frac{\partial}{\partial\theta}\sin\theta\frac{\partial}{\partial\theta} + \frac{1}{\sin^2\theta}\frac{\partial^2}{\partial\phi^2}\right), \end{aligned} \tag{2.37}$$

we can divide the envelope function $\xi(\vec{r})$ into the radial and angular parts as $\xi(\vec{r}) = f_l(r)Y_{lm}(\theta,\phi)$. Here **L** denotes the operator of the orbital angular momentum, and obey the following eigenvalue equation

$$\mathbf{L}^2 Y_{lm}(\theta,\phi) = l(l+1)Y_{lm}(\theta,\phi) \tag{2.38}$$

with $|m| \le l$, where the functions $Y_{lm}(\theta,\phi)$ are the spherical harmonics with $l =$ 0.1,2, … and $m = 0, \pm 1, \pm 2, \ldots$. The radial part $f_l(r)$ should satisfy

$$\frac{d^2 f_l}{dr^2} + \frac{2}{r}\frac{df_l}{dr} + [\alpha^2 - l(l+1)]f_l = 0 \tag{2.39}$$

with

$$\alpha^2 \equiv \frac{2m_e}{\hbar^2}(E_e - E_g), \quad \text{or} \quad \frac{2m_h E_h}{\hbar^2}, \tag{2.40}$$

and the solution has the form of $f_{nl}(r) = \sqrt{\frac{2}{R^3}}\frac{j_l(\alpha_{nl}r/R)}{j_{l+1}(\alpha_{nl})}$, where the spherical Bessel function of order $l$ is denoted as $j_l$, and $\alpha_{nl}$ is determined from the boundary conditions as

$$j_l(\alpha_{nl}) = 0, \quad \text{for} \quad (n = 1,2,3,\cdots), \quad \text{and} \quad \alpha_{n0} = n\pi, \alpha_{11} = 4.4934, \ \cdots \tag{2.41}$$

Note that the envelope function depends only on $R$ and not on specific parameters for the electron and hole. It is because we dropped the suffix e and h from $\xi(\vec{r})$. The energy eigenvalues are discrete and given by

$$E_{e,nlm} = E_g + \frac{\hbar^2}{2m_e}\left(\frac{\alpha_{nl}}{R}\right)^2 \tag{2.42}$$

and

$$E_{h,nlm} = \frac{\hbar^2}{2m_h}\left(\frac{\alpha_{nl}}{R}\right)^2 \tag{2.43}$$

Next we consider the cubic boundary conditions that an electron or a hole is confined in a cubic QD with side length $L$. Let us begin with a one-dimensional case illustrated in Figure 2.5, where the following one-dimensional well potential

$$V(x) = \begin{cases} 0 & \text{for } |x| \le \dfrac{L}{2} \\ \infty & \text{for } |x| > \dfrac{L}{2} \end{cases} \tag{2.44}$$

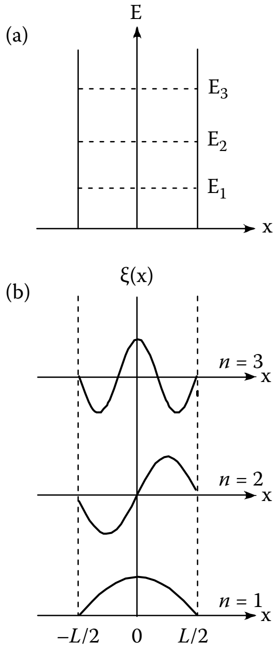

**FIGURE 2.5**
(a) One-dimensional well potential with infinite height and several energy eigenstates represented by dashed lines, (b) corresponding envelope functions.

is assumed. The envelope function $\xi(x)$ obeys the Schrödinger equation as

$$\left[-\frac{\hbar^2}{2m}\frac{d^2}{dx^2}+V(x)\right]\xi(x)=E_x\xi(x), \tag{2.45}$$

and the boundary conditions as

$$\xi\left(\frac{L}{2}\right)=\xi\left(-\frac{L}{2}\right)=0 \tag{2.46}$$

are satisfied. The solutions of the equation are given by

$$\begin{cases}\xi_{\text{even}}(x)=\sqrt{\dfrac{2}{L}}\cos(k_x x)\\[2ex] \xi_{\text{odd}}(x)=\sqrt{\dfrac{2}{L}}\sin(k_x x)\end{cases} \tag{2.47}$$

and it follows from the boundary conditions that $k_x$ has the following discrete values:

$$\begin{cases}k_x^{\text{even}}=\dfrac{\pi}{L}(2n-1)\\[2ex] k_x^{\text{odd}}=\dfrac{\pi}{L}(2n)\end{cases}\quad (n=1,2,3,\cdots). \tag{2.48}$$

Therefore, the energy eigenvalues are also discrete as $E_x=\frac{\hbar^2k_x^2}{2m}=\frac{\hbar^2}{2m}\left(\frac{\pi}{L}n_x\right)^2$, with $n_x=1,2,3,\cdots$, where we set $n_x=2n-1$ for $k_x^{\text{even}}$, while $n_x=2n$ for $k_x^{\text{odd}}$. Similarly, the envelope functions $\xi(y)$ and $\xi(z)$ can be obtained by replacing $x$ by its corresponding $y$ and $z$, respectively, and thus the envelope functions for an electron or a hole confined in the three-dimensional well potential have the form of $\xi(x)\ \xi(y)\ \xi(z)$. The energy eigenvalues specified by a set of quantum numbers $(n_x, n_y, n_z)$ are given as follows:

$$E_{n_x,n_y,n_z}=\frac{\hbar^2}{2m}\left(\frac{\pi}{L}\right)^2\left(n_x^2+n_y^2+n_z^2\right)\quad\text{for}\quad (n_x,n_y,n_z)=1,2,3,\cdots. \tag{2.49}$$

If we assume that the energy eigenvalues of an electron in a periodic potential, or the conduction and valence bands, and the energy gap are not changed drastically, the energies of an electron in the conduction or valence bands are given by

$$E_{\text{c}}=E_{\text{g}}+\frac{\hbar^2k^2}{2m_{\text{c}}}=E_{\text{g}}+\frac{\hbar^2}{2m_{\text{c}}}\left\{\left(\frac{\pi}{L_x}n_x\right)^2+\left(\frac{\pi}{L_y}n_y\right)^2+\left(\frac{\pi}{L_z}n_z\right)^2\right\} \tag{2.50a}$$

and

$$E_{\text{v}}=\frac{\hbar^2k^2}{2m_{\text{v}}}=\frac{\hbar^2}{2m_{\text{v}}}\left\{\left(\frac{\pi}{L_x}n_x\right)^2+\left(\frac{\pi}{L_y}n_y\right)^2+\left(\frac{\pi}{L_z}n_z\right)^2\right\}, \tag{2.50b}$$

respectively. The relation between energy and momentum is called the dispersion relation. The energy-dispersion relation of either $E_c$ or $E_v$ cannot be measured in semiconductor materials, because an electron excited by light, from the valence band to the conduction band, is simultaneously followed by a hole generation in the valence band. It requires a measurement of the energy dispersions of both an electron and a hole, $E_c$ and $E_v$. In order to discuss such energy dispersions, we will examine the electron-hole pair states in the next subsection.

### *Electron-Hole Pair States in a QD*

Let us consider the following eigenstate vectors for an electron-hole pair

$$|\psi_{\text{eh}}\rangle = \iint d^3r_e d^3r_h \; \psi(\vec{r}_e,\vec{r}_h)\hat{\psi}_e^\dagger(\vec{r}_e)\hat{\psi}_h^\dagger(\vec{r}_h)\,|\Phi_g\rangle, \tag{2.51}$$

where the crystal ground state mentioned before is represented by $|\Phi_g\rangle$, and the field operators of an electron creation in the conduction and those of a hole creation in the valence band are designated by $\hat{\psi}_e^\dagger(\vec{r}_e)$ and $\hat{\psi}_h^\dagger(\vec{r}_h)$, respectively. The envelope function for an electron-hole pair is denoted by $\psi(\vec{r}_e,\vec{r}_h)$, which obeys the following equation:

$$\left[-\frac{\hbar^2}{2m_e}\nabla_e^2 - \frac{\hbar^2}{2m_h}\nabla_h^2 + V_c + V_{\text{conf}}\right]\psi_{\text{eh}}(\vec{r}_e,\vec{r}_h) = (E - E_g)\psi_{\text{eh}}(\vec{r}_e,\vec{r}_h) \tag{2.52}$$

with the Coulomb interaction potential $V_c$ and the confinement potential $V_{\text{conf}}$. When the confinement region is a sphere with a radius $R$, $V_{\text{conf}}(r) = 0$ for $|\vec{r}| = r \le R$, while $V_{\text{conf}}(x,y,z) = 0$ for $-L/2 \le x,y,z \le L/2$ when it is a cube with a side-length $L$. Here it might be useful to qualitatively examine the electron-hole pair states by comparing the confinement size ($R$ or $L$) with the Bohr radius $a_0$ that represents the average distance of the electron and the hole in the pair. Noting that the confinement potential is proportional to $1/R^2$ ($1/L^2$) while the Coulomb interaction potential is proportional to $1/R$ ($1/L$), let us consider three cases: (a) $R << a_0$, (b) $R >> a_0$, and (c) intermediate region.

(a) $R << a_0$

In this region, the Coulomb interaction between an electron and a hole is weak, and each electron (hole) in a pair independently moves in the corresponding electron (hole) confinement potential. In particular, when both the Coulomb and confinement potentials are zero in a perfectly confined area, the lowest energy of an electron-hole pair is given, in terms of energy eigenvalues in the one-particle problem already discussed, as follows.

$$E = E_g + \frac{\pi^2\hbar^2}{2m_e R^2} + \frac{\pi^2\hbar^2}{2m_h R^2} = E_g + \frac{\pi^2\hbar^2}{2m_r R^2} \tag{2.53}$$

where $m_r$ is the reduced mass for an electron-hole pair defined by

$$\frac{1}{m_r}=\frac{1}{m_\mathrm{e}}+\frac{1}{m_\mathrm{h}}. \tag{2.54}$$

(b) R >> $a_0$

Because the Coulomb interaction between an electron and a hole becomes strong in this case, it is a good approximation to treat an electron-hole pair as a single particle (an exciton). Then the center of mass motion of the exciton is confined within the area of $R$ ($L$). Defining the mass of the exciton as $M = m_\mathrm{e} + m_\mathrm{h}$, the center of mass coordinates as $\vec{r}_\mathrm{CM}=\frac{m_\mathrm{e}\vec{r}_\mathrm{e}+m_\mathrm{h}\vec{r}_\mathrm{h}}{M}$, and the relative coordinates between an electron and a hole as $\vec{\beta}=\vec{r}_\mathrm{e}-\vec{r}_\mathrm{h}$, respectively, we can write the envelope functions of the exciton as

$$\psi(\vec{r}_\mathrm{e},\vec{r}_\mathrm{h})=\phi_\mu(\vec{\beta})F_\nu(\vec{r}_\mathrm{CM}), \tag{2.55}$$

where we have, in particular,

$$F_\nu(\vec{r}_\mathrm{CM})=\sqrt{\frac{2}{R^3}}\,\frac{j_\ell\left(\frac{\alpha_{n\ell}r_\mathrm{CM}}{R}\right)}{j_{\ell+1}(\alpha_{n\ell})}Y_{\ell m}(\Omega_\mathrm{CM}) \tag{2.56}$$

and

$$\phi_{\mu=1s}(\vec{\beta})=\frac{1}{\sqrt{\pi a_0^3}}\exp\left(-\frac{\beta}{a_0}\right). \tag{2.57}$$

for the spherical boundary conditions, as similarly obtained in the one-particle problem. Here the solid angle $\Omega_\mathrm{CM}$ for $\vec{r}_\mathrm{CM}$ is used, and $\phi_\mu(\vec{\beta})$ is assumed to be the lowest (1s) form. The energy eigenvalues of the states specified by the quantum numbers $(n,l)$ are

$$E_{n\ell}=E_\mathrm{g}+E_\mathrm{ex}+\frac{\hbar^2\alpha_{n\ell}^2}{2MR^2}\quad(n=1,2,3,\cdots), \tag{2.58}$$

and discretized as expected, where $E_\mathrm{ex}$ is the exciton binding energy in he bulk system. Similarly for the cubic boundary conditions, we have the envelope functions for the center for mass motion as

$$F_\nu(\vec{r}_\mathrm{CM})=\sqrt{\frac{8}{L^3}}\begin{cases}\cos\left(\frac{\pi}{L}(2n_x-1)x_\mathrm{CM}\right)\cos\left(\frac{\pi}{L}(2n_y-1)y_\mathrm{CM}\right)\cos\left(\frac{\pi}{L}(2n_z-1)z_\mathrm{CM}\right),\\ \sin\left(\frac{2\pi}{L}n_x x_\mathrm{CM}\right)\sin\left(\frac{2\pi}{L}n_y y_\mathrm{CM}\right)\sin\left(\frac{2\pi}{L}n_z z_\mathrm{CM}\right),\end{cases} \tag{2.59}$$

and Eq. (57) for the relative motion.

The energy eigenvalues are expressed in a similar way as

$$E_{n_x,n_y,n_z}=E_\mathrm{g}+E_\mathrm{ex}+\frac{\pi^2\hbar^2}{2ML^2}\left(n_x^2+n_y^2+n_z^2\right)\ (n_x,n_y,n_z=1,2,3,\cdots) \tag{2.60}$$

and are also discretized. Note that the center of mass motion is confined to a sphere of radius $R - \eta a_0$ or a cubic of side length $L - \eta a_0$ where the factor $\eta$ is of the order of unity and depends on the electron-hole mass ratio [37]. This is called dead-layer correction, indicating a finite size of the exciton whose center of mass coordinates is limited to be smaller than the actual size of a QD.

(c) Intermediate region

The situation in this region is more complicated than those in (a) and (b). Let Bohr radii of an electron and a hole be $a_\mathrm{e}$ and $a_\mathrm{h}$, respectively, and suppose that the confinement size $R$ is larger than $a_\mathrm{h}$, and smaller than $a_\mathrm{e}$. Then one may assume that a hole can move in an average potential generated by a free-electron confined within a QD, and approximate the envelope functions of the exciton as

$$\psi(\vec{r}_\mathrm{e}, \vec{r}_\mathrm{h}) \simeq \xi_{n\ell m}(\vec{r}_\mathrm{e})\psi_\mathrm{h}(\vec{r}_\mathrm{h}). \tag{2.61}$$

Using the orthonormalization of $\xi_{n\ell m}(\vec{r}_\mathrm{e})$, we can write down the equation for the envelop functions of the hole as follows:

$$\left[-\frac{\hbar^2}{2m_\mathrm{h}}\nabla_\mathrm{h}^2 - \int d\vec{r}_\mathrm{e}\, |\xi_{n\ell m}(\vec{r}_\mathrm{e})|^2 V_\mathrm{c}\right]\psi_\mathrm{h}(\vec{r}_\mathrm{h}) = \left(E - E_\mathrm{g} - \frac{\hbar^2}{2m_\mathrm{e}}\frac{\alpha_{n\ell}^2}{R^2}\right)\psi_\mathrm{h}(\vec{r}_\mathrm{h}), \tag{2.62}$$

where the spherical confinement is assumed and $V_\mathrm{conf} = 0$ within the confinement. When the cubic boundary conditions are used, the envelope functions of an electron $\xi(\vec{r}_\mathrm{e}) = \xi_{n\ell m}(\vec{r}_\mathrm{e})$ and the discrete energy $\frac{\hbar^2}{2m_\mathrm{e}}\frac{\alpha_{n\ell}^2}{R^2}$ should be replaced by $\xi(\vec{r}_\mathrm{e}) = \xi_{n_x n_y n_z}(\vec{r}_\mathrm{e})$ and $\frac{\hbar^2}{2m}\left(\frac{\pi}{L}\right)^2\left(n_x^2 + n_y^2 + n_z^2\right)$, respectively. In both cases, the second term on the left hand side shows the Coulomb potential for the hole averaged by the electron. The equations can be numerically solved on a case by case basis.

### 2.2.2 Dipole-Forbidden Transition

On the basis of the above discussion, let us examine the behavior of an electron-hole pair excited by an optical near field, or by a propagating far field. In order to make the difference clear, we consider the case (b) in an example. It is then convenient to use a Wannier function basis, a complete set of orthogonal functions representing that electrons are localized at an atomic site $\vec{R}$, as schematically shown in Figure 2.6. The Wannier functions $w_{b\vec{R}}(\vec{r})$ are defined by

$$w_{b\vec{R}}(\vec{r}) \equiv \frac{1}{\sqrt{N}}\sum_{\vec{k}} \exp(-i\vec{k}\cdot\vec{R})\psi_{b\vec{k}}(\vec{r}), \tag{2.63}$$

with the Bloch functions $\psi_{b\vec{k}}(\vec{r})$ that are plane waves modulated with the periodicity of the lattice and are obtained from a linear combination of

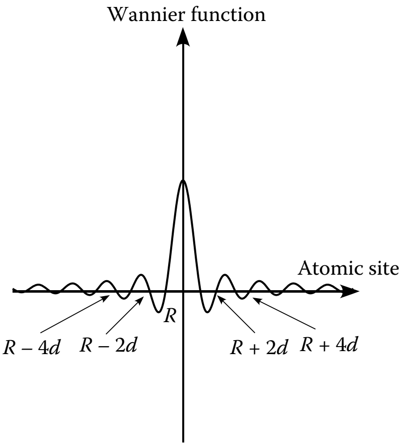

**FIGURE 2.6**
Wannier function at an atomic site *R* is schematically shown. The lattice constant is assumed to be *d*.

electron wavefunctions in an isolated atom at arbitrary site. Here $N$ is the number of constituent atoms, The Wannier functions for different bands (index b) and different site $\vec{R}$ are orthogonal, which follow from

$$\begin{aligned}\int w^*_{b\vec{R}}(\vec{r})w_{b'\vec{R}'}(\vec{r})\,d^3r &= \frac{1}{N}\sum_{\vec{k},\vec{k}'}\exp[i(\vec{k}\cdot\vec{R}-\vec{k}'\cdot\vec{R}')]\int \psi^*_{b\vec{k}}(\vec{r})\,\psi_{b'\vec{k}'}(\vec{r})\,d^3r\\ &= \frac{1}{N}\sum_{\vec{k},\vec{k}'}\exp[i(\vec{k}\cdot\vec{R}-\vec{k}'\cdot\vec{R}')]\,\delta_{bb'}\delta_{\vec{k}\vec{k}'} \qquad (2.64)\\ &= \frac{1}{N}\sum_{\vec{k}}\exp[i\vec{k}\cdot(\vec{R}-\vec{R}')]\,\delta_{bb'} = \delta_{bb'}\delta_{\vec{R}\vec{R}'}\end{aligned}$$

We express the field operator of an electron creation in the conduction and that of a hole creation in the valence band in terms of the Wannier basis. In case (b), where an electron-hole pair (an exciton) is confined within a QD, the exciton state $|\Phi_\nu\rangle$ specified by the quantum numbers $\nu=(\mathbf{m},\mu)$ are represented as a superposition of a variety of electron states at $\vec{R}$ and hole states at $\vec{R}'$ as

$$|\Phi_\nu\rangle = \sum_{\vec{R},\vec{R}'} F_{\mathbf{m}}(\vec{R}_{\text{C.M.}})\varphi_\mu(\vec{\beta})\hat{c}^\dagger_{c\vec{R}}\hat{c}_{v\vec{R}'}\,|\Phi_g\rangle. \qquad (2.65)$$

Here $F_{\mathbf{m}}(\vec{R}_{\text{C.M.}})$ is the center of mass motion of the exciton specified by a set of quantum numbers $\mathbf{m}=(m_x,m_y,m_z)$ while $\varphi_\mu(\vec{\beta})$ is the relative motion specified by the quantum number $\mu$, and the product of them represents the envelope function of the exciton. The creation operator of an electron at $\vec{R}$ in the conduction band is denoted by $\hat{c}^{\dagger}_{\mathrm{c}\vec{R}'}$ and the annihilation operator of an electron at $\vec{R}'$ in the valence band is represented by $\hat{c}_{\mathrm{v}\vec{R}'}$. The crystal ground state is designated by $|\Phi_{\mathrm{g}}\rangle$ as before.

In order to derive the optical near-field interaction based on Eq. (13) in Section 2.1, or the effective interaction between a QD pair, we first calculate the transition matrix elements from the exciton state $|\Phi_v\rangle$ to the crystal ground state $|\Phi_{\mathrm{g}}\rangle$ as

$$\langle\Phi_g|\hat{V}|\Phi_v\rangle = \sum_{\vec{k},\lambda}\sum_{\vec{R},\vec{R}'} F_{\mathbf{m}}(\vec{R}_{\mathrm{C.M.}})\varphi_\mu(\vec{\beta})\left(\hat{\xi}(\vec{k})g_{\mathrm{v}\vec{R}'\mathrm{c}\vec{R},\vec{k}\lambda} - \hat{\xi}^{\dagger}(\vec{k})g_{\mathrm{v}\vec{R}'\mathrm{c}\vec{R},-\vec{k}\lambda}\right) \qquad (2.66)$$

with

$$g_{\mathrm{v}\vec{R}'\mathrm{c}\vec{R},\vec{k}\lambda} = -i\sqrt{\frac{2\pi\hbar}{V}}f(k)\int w^{*}_{\mathrm{v}\vec{R}'}(\vec{r})\,\vec{\mu}(\vec{r})\,w_{\mathrm{c}\vec{R}}(\vec{r})\cdot\vec{e}_{\lambda}(\vec{k})\,\mathrm{e}^{\mathrm{i}\vec{k}\cdot\vec{r}}d^3r \qquad (2.67)$$

where we used the fact that the expectation values of $\langle\Phi_g|\hat{c}^{\dagger}_{\mathrm{v}\vec{R}_1}\hat{c}_{\mathrm{c}\vec{R}_2}\hat{c}^{\dagger}_{\mathrm{c}\vec{R}}\hat{c}_{\mathrm{v}\vec{R}'}|\Phi_g\rangle$ are not zero only if $\vec{R}' = \vec{R}_1$ and $\vec{R} = \vec{R}_2$ hold. In Eq. (67), the transformation of the spatial integral into the sum of the unit cells and the spatial locality of the Wannier functions provide $\delta_{\vec{R}\vec{R}'}$. Defining the transition dipole moment for each unit cell as

$$\vec{\mu}_{\mathrm{cv}} = \int_{\mathrm{UC}} w^{*}_{\mathrm{v}\vec{R}}(\vec{r})\vec{\mu}(\vec{r})w_{\mathrm{c}\vec{R}}(\vec{r})d^3r, \qquad (2.68)$$

and noticing that it is the same as that of the bulk material, independent of the site $\vec{R}$, we obtain the final form of

$$\langle\Phi_g|\hat{V}|\Phi_v\rangle = -i\sqrt{\frac{2\pi\hbar}{\mathrm{V}}}\sum_{\vec{k}}\sum_{\lambda=1}^{2}\sum_{\vec{R}} f(k)[\vec{\mu}_{\mathrm{cv}}\cdot\vec{e}_{\lambda}(\vec{k})]F_{\mathbf{m}}(\vec{R})\varphi_\mu(0)\left\{\hat{\xi}(\vec{k})\mathrm{e}^{\mathrm{i}\vec{k}\cdot\vec{R}} - \hat{\xi}^{\dagger}(\vec{k})\mathrm{e}^{-\mathrm{i}\vec{k}\cdot\vec{R}}\right\}. \qquad (2.69)$$

Here it should be noted that the exciton-polariton field expanded by the plane wave with the wave vector $\vec{k}$ depends on the site $\vec{R}$ in the QDs because the long-wave approximation $\mathrm{e}^{\pm\mathrm{i}\vec{k}\cdot\vec{R}} \approx 1$ is not applied, which is usually used for far-field light. According to the formulation described in Section 2.1, we have the optical near-field interaction energy between a pair of QDs, in the lowest order, as

$$V_{\mathrm{eff}} = \sum_m \left\langle\Psi^P_{\mathrm{f}}\middle|P\hat{V}Q\middle|m^{\mathrm{Q}}\right\rangle\left\langle m^{\mathrm{Q}}\middle|Q\hat{V}P\middle|\Psi^P_{\mathrm{i}}\right\rangle\left(\frac{1}{E^P_{0\mathrm{i}} - E^{\mathrm{Q}}_{0m}} + \frac{1}{E^P_{0\mathrm{f}} - E^{\mathrm{Q}}_{0m}}\right), \qquad (2.70)$$

where $E^{\mathrm{P}}_{0\mathrm{i}}$, $E^{\mathrm{P}}_{0\mathrm{f}}$ and $E^{\mathrm{Q}}_{0m}$ represent the eigenenergies of the unperturbed Hamiltonian for the initial and final states in $P$ space and the intermediate state in $Q$ space, respectively. Since we focus on the interdot interaction of Eq. (70), we set the initial and final states in $P$ space to $|\Psi_{\mathrm{i}}^{P}\rangle = |\Phi_{\mathbf{m}\mu}^{A}\rangle|\Phi_{g}^{B}\rangle|0\rangle$ and $|\Psi_{\mathrm{f}}^{P}\rangle = |\Phi_{g}^{A}\rangle|\Phi_{\mathbf{m}'\mu'}^{B}\rangle|0\rangle$. Then the intermediate states in $Q$ space that involve an exciton-polariton with the wave vector $\vec{k}$ are utilized for intermediating from one QD to the other, according to $|m^{Q}\rangle = |\Phi_{g}^{A}\rangle|\Phi_{g}^{B}\rangle|\vec{k}\rangle$ and $|m^{Q}\rangle = |\Phi_{\mathbf{m}\mu}^{A}\rangle|\Phi_{\mathbf{m}'\mu'}^{B}\rangle|\vec{k}\rangle$. The superscripts A and B are used to label two QDs. Using Eq. (69), one can rewrite Eq. (70) as

$$V_{\mathrm{eff}} = \varphi_{\mu}^{A}(0)\varphi_{\mu'}^{B*}(0)\iint F_{\mathbf{m}}^{A}(\vec{R}_A)F_{\mathbf{m}'}^{B*}(\vec{R}_B)\,[Y_A(\vec{R}_A - \vec{R}_B) + Y_B(\vec{R}_A - \vec{R}_B)]\,d^3R_A d^3R_B, \tag{2.71a}$$

where the sum of $\vec{R}_\alpha\,(\alpha = A, B)$ in Eq. (69) is transformed to the integral form. The integral Kernels $Y_\alpha(\vec{R}_{AB})\ (\alpha = A, B)$ with $\vec{R}_{AB} = \vec{R}_A - \vec{R}_B$, which connect the spatially isolated two envelope functions $F_{\mathrm{m}}^{A}(\vec{R}_A)$ and $F_{\mathrm{m}'}^{B}(\vec{R}_B)$, are defined by

$$\begin{aligned} Y_\alpha(\vec{R}_{AB}) = -\frac{1}{4\pi^2}\sum_{\lambda=1}^{2}\int \left[\vec{\mu}_{\mathrm{cv}}^{\mathrm{A}}\cdot\vec{e}_\lambda(\vec{k})\right]\left[\vec{\mu}_{\mathrm{cv}}^{\mathrm{B}}\cdot\vec{e}_\lambda(\vec{k})\right]\hbar f^2(k) \\ \times\left\{\frac{e^{i\vec{k}\vec{R}_{AB}}}{E(k)+E_\alpha} + \frac{e^{-i\vec{k}\vec{R}_{AB}}}{E(k)-E_\alpha}\right\}d^3k. \end{aligned} \tag{2.71b}$$

Here the transition dipole moments for QD$\alpha$ ($\alpha$= A, B), $\vec{\mu}_{\mathrm{cv}}^{\alpha}$, are defined by Eq. (68), and $E_\alpha$ denotes the exciton energy in QD$\alpha$. Then Eq. (71b) can be rewritten in the same way as described in Section 2.1, for example, corresponding to Eq. (27) in Section 2.1

$$Y_\alpha(\vec{R}_{AB}) = -\frac{\mu_{\mathrm{cv}}^{A}\mu_{\mathrm{cv}}^{B}}{3R_{AB}}\left(W_{\alpha+}\Delta_{\alpha+}^{2}\mathrm{e}^{-\Delta_{\alpha+}R_{AB}} - W_{\alpha-}\Delta_{\alpha-}^{2}\mathrm{e}^{-\Delta_{\alpha-}R_{AB}}\right), \tag{2.72}$$

where $R_{AB} = |\vec{R}_{AB}|$ is used. This is valid for the optical near-field excitation.

For far-field excitation, the displacement vector fields in the QDs are spatially homogeneous and the long-wave approximation $\mathrm{e}^{\pm i\vec{k}\cdot\vec{R}} \approx 1$ is applied. Then the transition matrix elements can be written in the separated form in terms of $\vec{R}$ and $(\vec{k}, \lambda)$ as

$$\begin{aligned} \langle\Phi_g|\hat{V}|\Phi_\nu^\alpha\rangle &= -i\sqrt{\frac{2\pi\hbar}{\mathrm{V}}}\sum_{\vec{R}}F_{\mathbf{m}}^{\alpha}(\vec{R})\,\varphi_{\mu}^{\alpha}(0)\sum_{\vec{k}}\sum_{\lambda=1}^{2}f(k)[\vec{\mu}_{\mathrm{cv}}\cdot\vec{e}_\lambda(\vec{k})]\left\{\hat{\xi}(\vec{k}) - \hat{\xi}^{\dagger}(\vec{k})\right\} \\ &= -i\sqrt{\frac{2\pi\hbar}{\mathrm{V}}}\left[\int F_{\mathbf{m}}^{\alpha}(\vec{R})\,d\vec{R}\right]\varphi_{\mu}^{\alpha}(0)\sum_{\vec{k}}\sum_{\lambda=1}^{2}f(k)\,[\vec{\mu}_{\mathrm{cv}}\cdot\vec{e}_\lambda(\vec{k})]\left\{\hat{\xi}(\vec{k}) - \hat{\xi}^{\dagger}(\vec{k})\right\}. \end{aligned} \tag{2.73}$$

The intergral $\int F_{\mathbf{m}}^{\alpha}(\vec{R})d\vec{R}$ as well as $\vec{\mu}_{\mathrm{cv}}$ provide the criterion whether the electric dipole transition is allowed or forbidden between the crystal ground state $|\Phi_g\rangle$ and the exciton state $|\Phi_\nu^\alpha\rangle$ in the QD α(=A, B) specified by the quantum number $\nu = (\mathbf{m}, \mu)$. Thus it follows that the electric dipole transition is forbidden if the spatial integral of the envelope function $F_{\mathbf{m}}^{\alpha}(\vec{R})$ representing the center of mass motion of the exciton is zero, $\int F_{\mathbf{m}}^{\alpha}(\vec{R})\,d\vec{R} = 0$, while it is allowed if the integral is not zero as $\int F_{\mathbf{m}}^{\alpha}(\vec{R})d\vec{R} \neq 0$. For example, let us calculate the spatial integral for a spherical QD. Since we have

$$\begin{aligned}\int d^3r\, F_{\mathbf{m}}(\vec{r}) &= \sqrt{\frac{2}{R^3}}\int_0^R r^2 dr \frac{j_\ell\left(\dfrac{\alpha_{n\ell} r}{R}\right)}{j_{\ell+1}(\alpha_{n\ell})}\iint \sin\vartheta d\vartheta d\varphi Y_{\ell m}(\vartheta\varphi) \\ &= \frac{1}{n}\sqrt{\frac{2R^3}{\pi^2}}\delta_{\ell 0}\delta_{m0},\end{aligned} \tag{2.74}$$

the transition to the state specified by $\ell = m = 0$ is only allowed. Similarly when all the integrand are even functions, we obtain the nonzero result as

$$\begin{aligned}\int d^3r\, F_{\mathbf{m}}(\vec{r}) &= \sqrt{\frac{8}{L^3}}\int_{-\frac{L}{2}}^{\frac{L}{2}} dx \cos\left(\frac{(2n_x-1)\pi x}{L}\right)\int_{-\frac{L}{2}}^{\frac{L}{2}} dx \cos\left(\frac{(2n_y-1)\pi y}{L}\right) \\ &\quad\times \int_{-\frac{L}{2}}^{\frac{L}{2}} dx \cos\left(\frac{(2n_z-1)\pi z}{L}\right) \\ &= \sqrt{\frac{512L^3}{\pi^6}}\frac{1}{(2n_x-1)}\frac{1}{(2n_y-1)}\frac{1}{(2n_z-1)}\sin\left(\frac{(2n_x-1)\pi}{2}\right) \\ &\quad\times \sin\left(\frac{(2n_y-1)\pi}{2}\right)\sin\left(\frac{(2n_z-1)\pi}{2}\right) \\ &= \sqrt{\frac{512L^3}{\pi^6}}\frac{1}{(2n_x-1)}\frac{1}{(2n_y-1)}\frac{1}{(2n_z-1)}\end{aligned} \tag{2.75}$$

for a cubic QD, and thus the transitions are allowed if all of $(n_x, n_y, n_z)$ are odd, while they are forbidden if either of $(n_x, n_y, n_z)$ is even. It follows from these results that the center of mass motion of the exciton in a QD is spatially modulated and the even or odd properties of the envelope function are mixed in the near-field case, which results in the violation of the forbidden conditions.

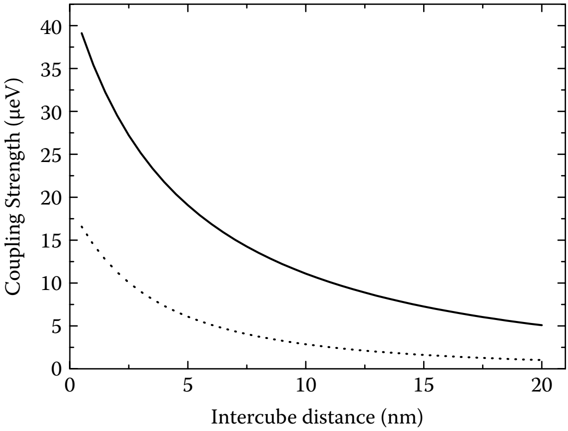

**FIGURE 2.7**
Optical near-field coupling strength as a function of the intercube distance. The solid curve shows the coupling strength between two dipole-allowed levels (1,1,1) of QDs with a width of 5 nm, while the dotted curve is the result for the (1,1,1) level of QD with a width of 5 nm and the (2,1,1) level of QD with a width of 7 nm.

For later use, we give typical values of the coupling strength, $|V_{\text{eff}}|$ in Eq. (71a), using an example of CuCl quantum cubes embedded in a NaCl matrix [39, 40]. In Figure 2.7, the calculation results are plotted as a function of the intercube distance, where the solid curve represents the coupling strength between two dipole-allowed levels $\mathbf{m} = \mathbf{m}' = (1,1,1)$ of QDs with a width of 5 nm, while the dotted curve is the result for $\mathbf{m} = (1,1,1)$ of QD with a width of 5 nm and $\mathbf{m}' = (2,1,1)$ of QD with a width of 7 nm. For conventional far-field light, $\mathbf{m}' = (2,1,1)$ is the dipole-forbidden exciton level, but it is allowed via an optical near-field interaction, as described earlier. Alternatively, a propagating far field constructs a symmetric state (cf. Eq. (77)) from two resonant exciton levels of inter-QDs by global coupling, while an optical near field allows producing an antisymmetric state (cf. Eq. (77)) by its steep gradient field to excite either one of QDs individually. The antisymmetric coupling strength is estimated as $|V_{\text{eff}}| \equiv \hbar U' = 5.05\ \mu\text{eV}\ \ (U'^{-1} = 130\text{ ps})$ for intercube distance of 6.1 nm, which is approximately a quarter of the symmetric case at the same intercube distance.

### 2.2.3 Coupled States Originating in Two Energy Levels

We have learned the fundamental properties of one-electron (or hole) states, electron-hole pair states in a QD, forming a variety of energy levels. Let us now consider what kind of coupled states are produced through the interaction between arbitrary two energy levels, regardless of a single or different QDs. In the following, for simplicity, we focus on two energy levels belonging to different QDs, and assume that state vector $|1\rangle$ in the QD 1 has the same energy $\varepsilon$ as state vector $|2\rangle$ in the QD 2 while the interaction energy

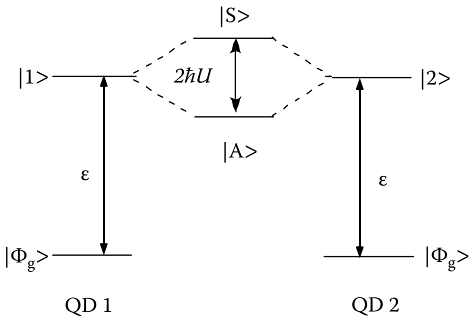

**FIGURE 2.8**
Symmetric and antisymmetric states, $|S\rangle$ and $|A\rangle$, generated by the interaction between energy levels $|1\rangle$ and $|2\rangle$ of QDs 1 and 2, respectively.

between them is $\hbar U$, as shown in Figure 2.8. The Hamiltonian for the system is given by

$$H = \varepsilon(\,|1\rangle\langle 1| + |2\rangle\langle 2|\,) + \hbar U(\,|1\rangle\langle 2| + |2\rangle\langle 1|\,). \tag{2.76}$$

Using the symmetric state $|S\rangle$ and antisymmetric state $|A\rangle$ respectively defined by

$$|S\rangle = \frac{1}{\sqrt{2}}(\,|1\rangle + |2\rangle),\quad |A\rangle = \frac{1}{\sqrt{2}}(\,|1\rangle - |2\rangle), \tag{2.77}$$

we evaluate the expectation value of the system energy as follows:

$$\begin{aligned}\langle \mathrm{S}|\,H\,|\mathrm{S}\rangle &= \frac{\varepsilon}{2}(\langle 1| + \langle 2|\,)[\,|1\rangle\langle 1| + |2\rangle\langle 2|\,](\,|1\rangle + |2\rangle)\\ &\quad + \frac{\hbar U}{2}(\langle 1| + \langle 2|\,)[\,|1\rangle\langle 2| + |2\rangle\langle 1|\,](\,|1\rangle + |2\rangle)\\ &= \varepsilon + \hbar U\end{aligned} \tag{2.78}$$

and

$$\begin{aligned}\langle \mathrm{A}|\,H\,|\mathrm{A}\rangle &= \frac{\varepsilon}{2}(\langle 1| - \langle 2|\,)[\,|1\rangle\langle 1| + |2\rangle\langle 2|\,](\,|1\rangle - |2\rangle)\\ &\quad + \frac{\hbar U}{2}(\langle 1| - \langle 2|)\big[|1\rangle\langle 2| + |2\rangle\langle 1|\big]\big(|1\rangle - |2\rangle\big)\\ &= \varepsilon - \hbar U.\end{aligned} \tag{2.79}$$

Here the orthogonality and normalization conditions of the state vectors, $\langle i\,|\,j\rangle = \delta_{ij}$ for $(i, j = 1,2)$, were used. It follows that these state vectors $|S\rangle$ and $|A\rangle$

are eigenstates of the Hamiltonian $H$, which indicates that the symmetric state $|S\rangle$ and the antisymmetric state $|A\rangle$ are produced after the interaction between the states $|1\rangle$ and $|2\rangle$ of the eigenstates of noninteracting two QDs. In particular, the state $|S\rangle$ corresponds to the bonding sate in a molecular case, whereas the state $|A\rangle$ corresponds to the antibonding state.

Now we then evaluate the scalar product of the transition dipoles $\vec{\mu}_1 \cdot \vec{\mu}_2$, in terms of the states $|S\rangle$ and $|A\rangle$. The transition dipole moment between $|\Phi_g\rangle$ and $|1\rangle$ of QD 1, for simplicity, is parallel to that between $|\Phi_g\rangle$ and $|2\rangle$ of QD 2, and set the magnitudes of them as $\mu_i = |\vec{\mu}_i| > 0$ $(i = 1, 2)$. Noticing that

$$\hat{\vec{\mu}}_i = \vec{\mu}_i\left(\hat{b}_i + \hat{b}_i^\dagger\right), \ \hat{b}_i^\dagger |\Phi_g\rangle = |i\rangle, \ \hat{b}_i |\Phi_g\rangle = 0 \tag{2.80}$$

we have

$$\begin{aligned}\langle S|\, \hat{\vec{\mu}}_1 \cdot \hat{\vec{\mu}}_2 \,|S\rangle &= \frac{\mu_1\mu_2}{2}(\langle 1| + \langle 2|\,)\left(\hat{b}_1 + \hat{b}_1^\dagger\right)\left(\hat{b}_2 + \hat{b}_2^\dagger\right)(\,|1\rangle + |2\rangle) \\ &= \frac{\mu_1\mu_2}{2}\left(\langle 1| + \langle 2|\right)\left(\hat{b}_1\hat{b}_2^\dagger + \hat{b}_1^\dagger\hat{b}_2\right)(|1\rangle + |2\rangle) \\ &= \frac{\mu_1\mu_2}{2}\left[\langle 2|\,\hat{b}_1\hat{b}_2^\dagger\,|1\rangle + \langle 1|\,\hat{b}_1^\dagger\hat{b}_2\,|2\rangle\right] \\ &= \mu_1\mu_2 > 0,\end{aligned} \tag{2.81}$$

which indicates that the transition dipole moments of $\vec{\mu}_1$ and $\vec{\mu}_2$ are parallel in the symmetric state $|S\rangle$. Similar calculation gives

$$\langle A|\, \vec{\mu}_1 \cdot \vec{\mu}_2 \,|A\rangle = -\mu_1\mu_2 < 0, \tag{2.82}$$

which shows that they are antiparallel in the antisymmetric state $|A\rangle$. It follows from these results that the excitation of two nanometric QDs with a far field light leads us to the symmetric state, that is, the state with parallel dipoles produced in QD 1 and 2, becausee two QDs cannot be distinguished spatially owing to the diffraction limit. By contrast, the near-field excitation of them can produce either one or both of the symmetric and antisymmetric states. In this sense, the symmetric state is called a bright state while the antisymmetric state is called a dark state. This is one of the major differences between the near-field and far-field excitations. In particular, the superposition or entangled sate of $|S\rangle$ and $|A\rangle$ are generated since the specific QD either 1 or 2, for example, dot 1 can be excited locally with an optical near field. Then the state $|1\rangle$ is expressed by

$$|1\rangle = \frac{1}{\sqrt{2}}(\,|S\rangle + |A\rangle) \tag{2.83}$$

which shows the quantum coherence. Since the state vectors $|S\rangle$ and $|A\rangle$ also form a complete and orthonormalized basis, state vectors $|\psi(t)\rangle$ of the system at an arbitrary time $t$ are expressed in terms of the basis by

$$|\psi(t)\rangle = \frac{1}{\sqrt{2}}\left\{\exp\left(-i\frac{\varepsilon + \hbar U}{\hbar}t\right)|\mathrm{S}\rangle + \exp\left(-i\frac{\varepsilon - \hbar U}{\hbar}t\right)|\mathrm{A}\rangle\right\}, \tag{2.84}$$

where we assumed that the state vectors $|\psi(t)\rangle$ are also normalized and $|\psi(0)\rangle = |1\rangle$ at time $t = 0$. Using the state vectors $|1\rangle$ and $|2\rangle$, we can rewrite Eq. (84) as follows:

$$\begin{aligned} |\psi(t)\rangle &= \frac{1}{\sqrt{2}}\left\{[\cos(Ut) - i\sin(Ut)]\exp\left(-i\frac{\varepsilon}{\hbar}t\right)|\mathrm{S}\rangle + [\cos(Ut) + i\sin(Ut)]\exp\left(-i\frac{\varepsilon}{\hbar}t\right)|\mathrm{A}\rangle\right\} \\ &= \frac{1}{\sqrt{2}}\exp\left(-i\frac{\varepsilon}{\hbar}t\right)\{\cos(Ut)(|\mathrm{S}\rangle + |\mathrm{A}\rangle) - i\sin(Ut)(|\mathrm{S}\rangle - |\mathrm{A}\rangle)\} \\ &= \exp\left(-i\frac{\varepsilon}{\hbar}t\right)\{\cos(Ut)|1\rangle - i\sin(Ut)|2\rangle\}. \end{aligned} \tag{2.85}$$

This expression shows that the occupation probability $\rho_{11}(t)$ is given by

$$\rho_{11}(t) = |\langle 1|\,\psi(t)\rangle|^2 = \cos^2(Ut) \tag{2.86a}$$

when a particle such as an electron, a hole, or an exciton occupies the state $|1\rangle$ of the QD 1 at time $t$, while the occupation probability $\rho_{22}(t)$ is provided by

$$\rho_{22}(t) = |\langle 2|\,\psi(t)\rangle|^2 = \sin^2(Ut) \tag{2.86b}$$

when a particle occupies the state $|2\rangle$ of the QD 2 at time $t$. As shown in Figure 2.9, they complementally vary with a period of $\pi/U$. It means that the excitation energy $\varepsilon$ of the system is periodically transferred between the resonant energy levels of two QDs, 1 and 2, which is called nutation. It should be noted that the nutation cannot be continued permanently unless the relevant QD pair system is perfectly isolated from the other systems. It usually stops through the relaxation process such as the energy dissipation caused by the interaction with other systems. For example, the initial population of QD 1 is transferred to the population of QD 2 at later time, and the nutation stops by the energy dissipation, which then establishes the energy transfer from QD 1 to 2. In fact, this kind of (excitation) energy transfer has been experimentally observed [41–43], and the analogy to the light-harvesting photosynthetic system [44–46] has been pointed out. The following section deals with theoretical treatment of temporal evolution of such energy transfer between nanomaterials triggered by an optical near field.

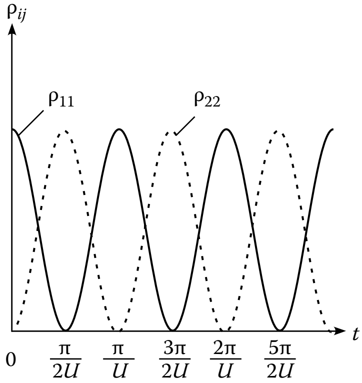

**FIGURE 2.9**
Temporal evolution of the occupation probability of the state |1⟩ in the QD 1, $\rho_{11}(t)$, and that of the state |2⟩ in the QD 2, $\rho_{22}(t)$. The solid curve represents $\rho_{11}(t)$, and the dashed curve shows $\rho_{11}(t)$.

### 2.2.4 Basic Ideas of Nanophotonic Devices

In the previous subsections, we have briefly described fundamental aspects on energy levels of an electron, a hole, and an exciton in a semiconductor QD that is one of constituent candidates of nanophotonic devices. The essential points, some of which are prerequisite for nanophotonic device operations, are summarized as follows:

- The energy levels are discretized in a QD.
- There are two kinds of energy levels, one of which can be excited by both near and far fields, while the others is excited only by a near field.
- A coupling of two discrete energy levels produces a symmetric state that is accessible with a far field, and an antisymmetric state that can be accessed only by a near field.
- Excitation energy in a QD can be transferred to another neighboring QD, via resonant or nearly resonant discrete energy levels.

Phenomena accessible only by an optical near field allow a new type of nanophotonic devices whose operations are hardly, or cannot be obtained with existing photonic devices using a wave nature of light. On the basis of such nanophotonic devices, a variety of functions (light source, signal transmission, control, operation, and interface) and systems are realized as will be discussed in the upcoming chapters, in detail. Moreover, it is possible to fabricate constituent elements and building blocks of nanophotonic devices by making use of novel properties of optical near fields that originate in their spatial localization, as will be described in Section 2.3.

As schematically shown in Figure 2.10(a), basic ideas and principles of operation of nanophotonic devices are to transmit quantum coherence generated

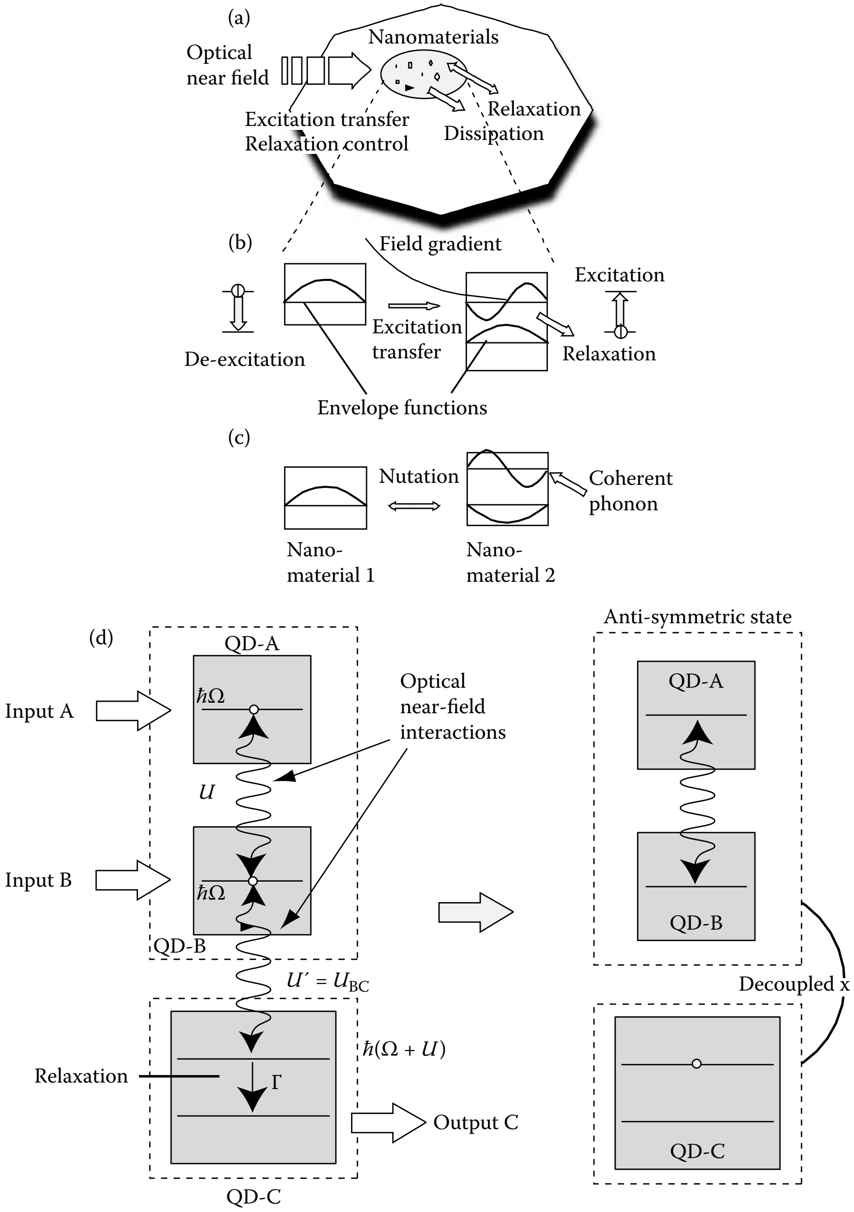

**FIGURE 2.10**
(a) Basic idea and principles of operation of nanophotonic devices, (b) use of excitation transfer between nanomaterials and energy dissipation via incoherent phonons, (c) use of nutation between nanomaterials and collective phenomena, control of phase relaxation and quantum coherence via coherent phonons, (d) use of antisymmetric state that prohibits interactions with incoherent phonons and propagating far field.

in discrete energy levels of a nanomaterial to neighboring nanomaterials, and to control the paths via interactions with a macroscopic matter system [8,11,39,40,47–49]. For example, unidirectional excitation energy transfer is performed with energy dissipation via incoherent phonons and destruction of quantum coherence occurred between nanomaterials that result in signal transmission from one to another nanomaterial, or between nanophotonic device components, as shown in Figure 2.10(b). It is also possible to suppress relaxation of quantum coherence and to continue the nutation between nanomaterials via coherent phonons or coherent photons, which promote a chance of occurrence of collective phenomena, as shown in Figure 2.10(c). In addition, a selective coupling between electric dipole-allowed levels by varying the size of two neighboring nanomaterials allows us to obtain an interface function of converting the transferred energy into a propagating light. Figure 2.10(d) schematically illustrates a way of converting an input signal of optical near fields into excitation of a nanomaterial and storing it, by selectively coupling with an antisymmetric state and suppressing the interactions with propagating light and incoherent phonons.

When nanomaterials are excited by a far (propagating) field, we selectively use energy levels resonant with incident photon energy, from electric dipole-allowed levels. On the other hand, when they are excited by an optical near field, electric dipole-forbidden levels as well as electric dipole-allowed levels are utilized, owing to the spatially local excitation of each nanomaterial, not the global excitation of whole nanomaterials. It can be performed by configuring nanomaterials asymmetrically in space. It is thus one of advantages of nanophotonic devices to make use of spatial information as well as frequency information of nanomaterial systems.

At the end of this section, let us summarize the goals, advantages, and future issues of nanophotonics by comparing with single molecular electronics. In the field of molecular electronics, one has a discussion on the subjects how to replace or complement the existing silicon devices (quantitative revolution), and how to construct a novel system such as a molecular computer based on a new concept and architecture towards new directions of molecular devices (qualitative revolution). This situation is valid for nanophotonics, as discussed in Chap. 1.

Here as an example of single molecular electronics, look at a single molecule cascade and cellular automaton. The single molecule cascade is a molecular configuration, where one of the molecules adsorbed and configured on the substrate with an atomic precision is first moved with a scanning tunneling microscope (STM). This operation is called a single molecule manipulation, and then the movement of the other molecules chain-react [50]. It is very important for fabrication and design of such molecular devices as well as for basic science to understand the mechanism of this molecular chain-reaction. It is also a key issue to clarify how the excitation energy from an initially excited molecule is transferred to another molecule and is converted to the energies of the internal degrees of freedom such as an electronic excitation, a vibrational/rotational excitation, and a translational motion. This kind of understanding might provide an important guideline to investigate a common process in the principles of operation of nanofabrication with optical near fields and those of nanophotonic devices.

Cellular automaton is a device that consists of a lot of cells with the same structure, and the cells are regularly allocated in space, each of which Coulombicly interacts with the surrounding cells, according to a set of rules [51]. Each state of the cells is determined by each local Coulomb interaction, and logic operations are performed by using a change in the states of the cells. Cellular automaton has the following advantages: parallel operation is possible. Wiring between all cells is not required, since local interactions are utilized. Total system is constructed with a repetition of single structure, and thus processing capability can increase according to the number of cells used. Currently molecular cellular automaton using a single molecule as a cell, and QD cellular automaton using a QD as a cell are investigated.

Figure 2.11 (a) illustrates a cell that consists of four molecules or QDs. When two excess electrons exist in a cell, electron's configuration on the diagonal leads us to a stable state because of Coulomb repulsion. As shown in Figure 2.11 (a), we assign two states relating to electron positions as "0" and "1," respectively. Now let us consider a case where two cells are configured and electron positions in one of them changes from "0" to "1." Then the other cell is immediately transformed to the state "1" via Coulomb interaction. In order to use this phenomenon, we arrange the cells along the line, as shown in Figure 2.11 (b), where the most left cell corresponds to the input cell. The stable states of the other cells take the same configuration of electrons as the input cell, and thus the input signal can be transmitted to the most right cell without electric current. This avoids a heating problem, which is one of

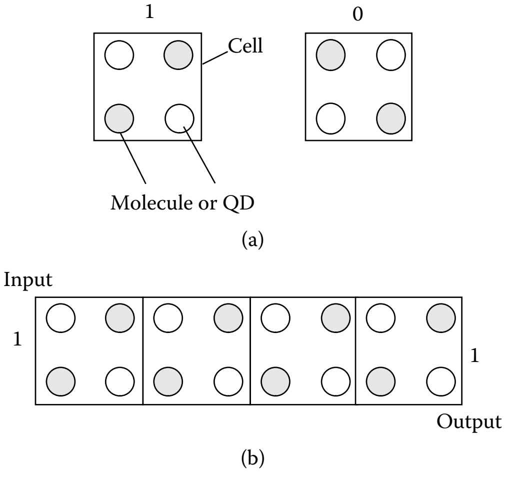

**FIGURE 2.11**
(a) Fundamental unit of cellular automaton: 0 and 1, (b) cells along the line, where the most left cell corresponds to the input cell and the most right cell is the output cell.

the essential issues in nanometer scale devices, as excitation energy transfer does in nanophotonic devices. The difference is that cellular automaton depends on the static (Coulomb) interactions between the elements of the cells while nanophotonics is based on the dynamic interactions that provide prompt response and controllability. Towards realizing cellular automaton, the following problems should be solved; the first is how to supply energies required for maintaining the states of the cells and for transitions. The second is how to synchronize each transition as a whole system because each state transition stochastically occurs in molecular systems. The third is how to initialize the system. The second and the third are common issues in nanophotonics and cellular automaton.

### 2.2.5 Fundamental Tool for Describing Temporal Behavior

In order to give a fundamental, but important theoretical tool for description of dynamic properties of nanophotonic devices, we introduce the density operator and derive a quantum master equation describing the temporal behavior [18,52–55]. Using perturbative solutions of the equation, we analytically examine behaviors of excitation energy transfer between nanomaterials via optical near fields [8,11,39,40,47,49].

#### *Density Operator and Density Matrix*

For a system isolated from the outside (which is called a closed system) the temporal evolution of the system can be described in terms of eigenstates $|\psi_q\rangle$ with eigenvalues $q$ for observable $Q$, or their eigenfunctions in the coordinate representation $\psi_q(\vec{r}) = \langle\vec{r}|\,\psi_q\rangle$. However, it is rather difficult to exactly describe the temporal evolution of an open system in terms of wave functions, where more than two systems are interacting each other and energy and phase relaxation take place via the interactions. It is well known that the density operator method is suitable to discuss the temporal evolution of such an open system.

Here we consider electronic states of multiple nanomaterials prepared on the substrate, which are superpositions of state vectors $|\psi_n\rangle$ with a variety of statistical (stochastic) weights $W_n$. The density operator $\hat{\rho}$ is then defined by

$$\hat{\rho} = \sum_n W_n \, |\psi_n\rangle \, \langle\psi_n| \, , \tag{2.87}$$

where the state vectors $|\psi_n\rangle$ are not necessarily orthogonalized nor normalized. Therefore we usually expand $|\psi_n\rangle$ as

$$|\psi_n\rangle = \sum_{m'} a_{m'}^{(n)} \, |\phi_{m'}\rangle, \tag{2.88}$$

in terms of complete orthonormalized state vectors $|\phi'_m\rangle$ specified by the quantum numbers $m'$ such as energy eigenstates, where $a_{m'}^{(n)}$ denote the expansion coefficients of the state vectors. Similarly we have the following expression for the Hermitean conjugates as

$$\langle\psi_n| = \sum_m a_m^{(n)*}\langle\phi_m|. \tag{2.89}$$

Substituting Eqs. (88) and (89) into Eq. (87), we obtain the density operator as

$$\hat{\rho} = \sum_{n,m,m'} W_n a_{m'}^{(n)} a_m^{(n)*}\,|\phi_{m'}\rangle\langle\phi_m| \tag{2.90}$$

and the matrix elements of $\hat{\rho}$ in terms of the state vectors $\langle\phi_i|$ and $|\phi_j\rangle$ as

$$\begin{aligned}\rho_{ij} \equiv \langle\phi_i|\,\hat{\rho}\,|\phi_j\rangle &= \sum_{n,m,m'} W_n a_{m'}^{(n)} a_m^{(n)*}\langle\phi_i|\,\phi_{m'}\rangle\,\langle\phi_m|\,\phi_j\rangle \\ &= \sum_n W_n a_i^{(n)} a_j^{(n)*},\end{aligned} \tag{2.91}$$

where the orthogonality and normalization of the state vectors $\langle\phi_i|\,\phi_{m'}\rangle = \delta_{im'}$ and $\langle\phi_m|\phi_j\rangle = \delta_{mj}$ are used. Since the statistical (stochastic) weights $W_n$ are real, the density operator is Hermitean, that is, $\hat{\rho}^\dagger = \hat{\rho}$ (the symbol † denoting the Hermitean conjugate), and thus the density matrix is a Hermitean matrix, or

$$\langle\phi_i|\,\hat{\rho}\,|\phi_j\rangle = \langle\phi_j|\,\hat{\rho}\,|\phi_i\rangle^*, \quad \rho_{ij} = \rho_{ji}^*. \tag{2.92}$$

In particular, using the energy eigenstates $|\phi_i\rangle$, we obtain the diagonal components as

$$\rho_{ii} = \sum_n W_n a_i^{(n)} a_i^{(n)*} = \sum_n W_n \left|a_i^{(n)}\right|^2 \geq 0, \tag{2.93}$$

which shows the incoherent superposition. The probability to find the state $|\psi_n\rangle$ in energy eigenstate $|\phi_i\rangle$ is given by $|a_i^{(n)}|^2$, and the diagonal components of the density matrix represent the probability that the system occupies the state $|\phi_i\rangle$. By contrast, the off-diagonal components $\rho_{ij}(i \neq j)$ is the coherent superposition and thus represent quantum coherence of the system. Both components are independent observables. Denoting a trace of $\hat{\rho}$ as tr $\hat{\rho}$, we have

$$\mathrm{tr}\hat{\rho} \equiv \sum_i \rho_{ii} = \sum_n W_n \sum_i \left|a_i^{(n)}\right|^2 = 1 \tag{2.94}$$

for any basis. Because the expectation value of an operator $\hat{O}$ corresponding to an arbitrary observable is given by

$$\langle \hat{O} \rangle = \sum_n W_n \langle \psi_n | \hat{O} | \psi_n \rangle, \tag{2.95}$$

substitution of Eqs. (88) and (89), with the help of Eq. (90), leads to

$$\begin{aligned} \langle \hat{O} \rangle &= \sum_{m,m',n} W_n a_{m'}^{(n)} a_m^{(n)*} \langle \phi_m | \hat{O} | \phi_{m'} \rangle \\ &= \sum_{m,m'} \langle \phi_{m'} | \hat{\rho} | \phi_m \rangle \langle \phi_m | \hat{O} | \phi_{m'} \rangle \\ &= \sum_{m'} \langle \phi_{m'} | \hat{\rho} \hat{O} | \phi_{m'} \rangle = \mathrm{tr}(\hat{\rho} \hat{O}), \end{aligned} \tag{2.96}$$

where completeness of the state vectors $|\phi_m\rangle$, $\Sigma_m |\phi_m\rangle \langle \phi_m| = 1$, is used. Note that all information about the system is involved in the density matrix.

### *Time Evolution Operator and Liouville Equation*

In order to study the temporal evolution of the system described by Hamiltonian $\hat{H}$, we introduce the time evolution operator that connects the state vectors at time $t = 0$ and at arbitrary time $t$. Then the equation for the density operator is derived by utilizing the time evolution operator. Let us consider the system interacting with the time-dependent external field, where the interaction explicitly depends on time as $\hat{V}(t)$, and thus the Hamiltonian is also time-dependent as $\hat{H}(t)$. The Schrödinger equation for the state vectors $|\psi(t)\rangle$ at arbitrary time $t$, is given by

$$i\hbar \frac{\partial}{\partial t} |\psi(t)\rangle = \hat{H}(t) |\psi(t)\rangle. \tag{2.97}$$

Defining the time evolution operator $\hat{U}(t)$ as

$$|\psi(t)\rangle = \hat{U}(t) |\psi(0)\rangle, \tag{2.98}$$

and its Hermitean conjugate $\hat{U}^{\dagger}(t)$ as

$$\langle \psi(t)| = \langle \psi(0)| \hat{U}^{\dagger}(t), \tag{2.99}$$

we rewrite the Schrödinger equation in the following form

$$i\hbar \frac{\partial U(t)}{\partial t} |\psi(0)\rangle = \hat{H}(t) \hat{U}(t) |\psi(0)\rangle \tag{2.100}$$

and

$$-i\hbar\langle\psi(0)|\frac{\partial U^{\dagger}(t)}{\partial t}=\langle\psi(0)|\,\hat{U}^{\dagger}(t)\hat{H}(t), \tag{2.101}$$

where the initial conditions for the time evolution operators, $\hat{U}(0)=\hat{U}^{\dagger}(0)=1$ are satisfied. Since they are valid for arbitrary state vectors, the time evolution operators satisfy the following equations:

$$i\hbar\frac{\partial\hat{U}(t)}{\partial t}=\hat{H}(t)\hat{U}(t) \tag{2.102}$$

and

$$-i\hbar\frac{\partial\hat{U}^{\dagger}(t)}{\partial t}=\hat{U}^{\dagger}(t)\hat{H}(t). \tag{2.103}$$

Multiplying $\hat{U}^{\dagger}(t)$ from the left side and $\hat{U}(t)$ from the right side, we easily obtain

$$i\hbar\left\{\hat{U}^{\dagger}(t)\frac{\partial\hat{U}(t)}{\partial t}+\frac{\partial\hat{U}^{\dagger}(t)}{\partial t}\hat{U}(t)\right\}=i\hbar\frac{\partial\hat{U}^{\dagger}(t)\hat{U}(t)}{\partial t}=0, \tag{2.104}$$

which shows that $\hat{U}^{\dagger}(t)\hat{U}(t)$ is constant with $\hat{U}^{\dagger}(0)\hat{U}(0)=1$. Therefore it follows that $\hat{U}^{\dagger}(t)\hat{U}(t)=1$, and that the time evolution operator $\hat{U}(t)$ is unitary. If the Hamiltonian does not explicitly depend on time, the operators $\hat{U}(t)$ and $\hat{U}^{\dagger}(t)$ can be written as

$$\hat{U}(t)=\exp\left(-\frac{\mathrm{i}\hat{H}t}{\hbar}\right),\ \hat{U}^{\dagger}(t)=\exp\left(\frac{\mathrm{i}\hat{H}t}{\hbar}\right). \tag{2.105}$$

Using the solution of Eq. (102) for the time evolution operator, we derive the equation describing the temporal evolution of the density operator. Noting that the density operator at time $t=0$ is expressed by

$$\hat{\rho}(0)=\sum_{n}W_{n}\,|\psi_{n}(0)\rangle\,\langle\psi_{n}(0)|, \tag{2.106}$$

we calculate

$$\begin{aligned}\hat{U}(t)\hat{\rho}(0)\hat{U}^{\dagger}(t)&=\sum_{n}W_{n}\hat{U}(t)\,|\psi_{n}(0)\rangle\,\langle\psi_{n}(0)|\hat{U}^{\dagger}(t)\\&=\sum_{n}W_{n}\,|\psi_{n}(t)\rangle\,\langle\psi_{n}(t)|=\hat{\rho}(t),\end{aligned} \tag{2.107}$$

where we used the definition of the time evolution operator in Eq. (98). If the Hamiltonian is time-independent, then the density operator at time *t* can be written as

$$\hat{\rho}(t) = \exp\left(-\frac{\mathrm{i}\hat{H}t}{\hbar}\right)\hat{\rho}(0)\exp\left(\frac{\mathrm{i}\hat{H}t}{\hbar}\right). \tag{2.108}$$

Differentiation of Eq. (107) in terms of *t* results in

$$\begin{aligned} \mathrm{i}\hbar\frac{\partial\hat{\rho}(t)}{\partial t} &= \mathrm{i}\hbar\frac{\partial\hat{U}(t)}{\partial t}\hat{\rho}(0)\hat{U}^{+}(t) + \mathrm{i}\hbar\hat{U}(t)\hat{\rho}(0)\frac{\partial\hat{U}^{+}(t)}{\partial t} \\ &= \hat{H}(t)\hat{U}(t)\hat{\rho}(0)\hat{U}^{+}(t) - \hat{U}(t)\hat{\rho}(0)\hat{U}^{+}(t)\hat{H}(t), \end{aligned} \tag{2.109}$$

and finally the Liouville equation is obtained as follows:

$$\mathrm{i}\hbar\frac{\partial\hat{\rho}(t)}{\partial t} = \hat{H}(t)\hat{\rho}(t) - \hat{\rho}(t)\hat{H}(t) \equiv [\hat{H}(t), \hat{\rho}(t)], \tag{2.110}$$

which is essential for discussion of the temporal evolution of observables.

In an example, let us consider a case where nanomaterials are interacting with a laser field as an external field. The unperturbative Hamiltonian $\hat{H}_0$ is assumed to be time-independent, whose eigenstate vectors are denoted by $|\phi_n^{(0)}\rangle$, and energy eigenvalues are designated by $E_n^{(0)}$, while the interaction depends on time *t* as $\hat{V}(t)$. Using the state vectors $|\phi_n^{(0)}\rangle$ as a basis, we derive the equation for the density matrix defined by

$$\rho_{m'm}(t) = \left\langle \phi_{m'}^{(0)} \middle| \hat{\rho}(t) \middle| \phi_m^{(0)} \right\rangle. \tag{2.111}$$

The left-hand side of Eq. (110) gives $i\hbar\partial\rho_{m'm}(t)/\partial t$ while the right-hand side reads

$$\begin{aligned} &\left\langle \phi_{m'}^{(0)} \middle| \hat{H}(t)\hat{\rho}(t) - \hat{\rho}(t)\hat{H}(t) \middle| \phi_m^{(0)} \right\rangle \\ &= \left\langle \phi_{m'}^{(0)} \middle| (\hat{H}_0 + \hat{V}(t))\rho(t) - \hat{\rho}(t)(\hat{H}_0 + \hat{V}(t)) \middle| \phi_m^{(0)} \right\rangle \\ &= \left(E_{m'}^{(0)} - E_m^{(0)}\right)\hat{\rho}_{m'm}(t) + \left\langle \phi_{m'}^{(0)} \middle| [\hat{V}(t), \hat{\rho}(t)] \middle| \phi_m^{(0)} \right\rangle. \end{aligned} \tag{2.112}$$

Therefore the Liouville equation is obtained as follows:

$$\mathrm{i}\hbar\frac{\partial\hat{\rho}_{m'm}(t)}{\partial t} = \left(E_{m'}^{(0)} - E_m^{(0)}\right)\hat{\rho}_{m'm}(t) + \left\langle \phi_{m'}^{(0)} \middle| [\hat{V}(t), \hat{\rho}(t)] \middle| \phi_m^{(0)} \right\rangle. \tag{2.113}$$

### *Interaction Representation*

It is rather difficult to solve the Liouville equation (110), or (113), but if the interaction $\hat{V}(t)$ is so weak that it can be treated as a perturbation, then the time-dependent perturbation theory can be applied. Here note that the rapidly varying time dependence of the state vectors $|\psi(t)\rangle$ is created by the unperturbed Hamiltonian $\hat{H}_0$ as $\hat{U}_0(t) \equiv \exp(-\mathrm{i}\hat{H}_0 t/\hbar)$. In order to explicitly express this dependence, let us write

$$|\psi(t)\rangle \equiv \hat{U}_0(t)\,|\tilde{\psi}(t)\rangle = \exp\left(-\frac{\mathrm{i}\hat{H}_0 t}{\hbar}\right)|\tilde{\psi}(t)\rangle, \tag{2.114}$$

where the state vectors $|\tilde{\psi}(t)\rangle$ are called the interaction representation while the state vectors $|\psi(t)\rangle$ are called the Schrödinger representation. Inserting Eq. (114) into the Schrödinger equation, we have

$$\mathrm{i}\hbar\frac{\partial(\hat{U}_0(t)\,|\tilde{\psi}(t)\rangle)}{\partial t} = [\hat{H}_0 + \hat{V}(t)]\hat{U}_0(t)\,|\tilde{\psi}(t)\rangle, \tag{2.115}$$

which can be rewritten as

$$\mathrm{i}\hbar\frac{\partial\,|\tilde{\psi}(t)\rangle}{\partial t} = \hat{U}_0{}^{\dagger}(t)\hat{V}(t)\hat{U}_0(t)\,|\tilde{\psi}(t)\rangle \equiv \tilde{V}(t)\,|\tilde{\psi}(t)\rangle \tag{2.116}$$

after performing the differentiation. Here $\hat{V}(t)$ is expressed in the interaction representation as

$$\tilde{V}(t) = \hat{U}_0^{\dagger}(t)\hat{V}(t)\hat{U}_0(t) = \exp\left(\frac{\mathrm{i}\hat{H}_0 t}{\hbar}\right)\hat{V}(t)\exp\left(-\frac{\mathrm{i}\hat{H}_0 t}{\hbar}\right), \tag{2.117}$$

from which it follows that if $\hat{V}(t) = 0$ is satisfied, then $\tilde{V}(t) = 0$ and $\frac{\partial|\tilde{\psi}(t)\rangle}{\partial t} = 0$ are obtained. It means that $\tilde{V}(t)$ completely governs the temporal evolution of $|\tilde{\psi}(t)\rangle$. Therefore if $\tilde{V}(t)$ is a small perturbation, $|\tilde{\psi}(t)\rangle$ vary slowly in time and the perturbation theory provides a reasonable solution in practice. Similarly an arbitrary operator $\hat{O}(t)$ is expressed in the interaction representation as follows:

$$\tilde{O}(t) = \hat{U}_0^{\dagger}(t)\hat{O}(t)\hat{U}_0(t) = \exp\left(\frac{\mathrm{i}\hat{H}_0 t}{\hbar}\right)\hat{O}(t)\exp\left(-\frac{\mathrm{i}\hat{H}_0 t}{\hbar}\right). \tag{2.118}$$

Because $\hat{U}_0(0) = 1$ and $|\tilde{\psi}(0)\rangle = |\psi(0)\rangle$ hold, the temporal evolution of $|\tilde{\psi}(t)\rangle$ can be determined by

$$\begin{aligned}|\tilde{\psi}(t)\rangle &= \hat{U}_0^{\dagger}(t)\,|\,\psi(t)\rangle = \hat{U}_0^{\dagger}(t)\hat{U}(t)\,|\psi(0)\rangle = \hat{U}_0^{\dagger}(t)\hat{U}(t)\,|\tilde{\psi}(0)\rangle \\ &\equiv \tilde{U}(t)\,|\tilde{\psi}(0)\rangle,\end{aligned} \tag{2.119}$$

that is, $\tilde{U}(t)$ completely governs the temporal evolution of the state vectors $|\tilde{\psi}(t)\rangle$ in the interaction representation. It follows from the definition that this operator $\tilde{U}(t)$ satisfies the following equation

$$\begin{aligned} \mathrm{i}\hbar\frac{\partial\tilde{U}(t)}{\partial t} &= \mathrm{i}\hbar\frac{\partial\hat{U}_0^\dagger(t)}{\partial t}\hat{U}(t)+\mathrm{i}\hbar\hat{U}_0^\dagger(t)\frac{\partial\hat{U}(t)}{\partial t} \\ &= -\hat{U}_0^\dagger(t)\hat{H}_0\hat{U}(t)+\hat{U}_0^\dagger(t)\hat{H}(t)\hat{U}(t) \\ &= \hat{U}_0^\dagger(t)\hat{V}(t)\hat{U}(t). \end{aligned} \tag{2.120}$$

Using $\hat{U}_0(t)\hat{U}_0^\dagger(t)=1$, we further rewrite $\hat{V}(t)$ and $\hat{U}(t)$ in the interaction representation as

$$\mathrm{i}\hbar\frac{\partial\tilde{U}(t)}{\partial t}=\hat{U}_0^\dagger(t)\hat{V}(t)\hat{U}_0(t)\hat{U}_0^\dagger(t)\hat{U}(t)=\tilde{V}(t)\tilde{U}(t), \tag{2.121}$$

from which the temporal evolution of $\tilde{U}(t)$ is wholly determined by $\tilde{V}(t)$, or $\hat{V}(t)$. under the condition of $\tilde{U}(0)=1$ It is justified, in this respect, to rely on the perturbation theory used in the interaction representation. This is true for the density operator and the density matrix. The density operator in the interaction representation is written in the form

$$\tilde{\rho}(t)=\hat{U}_0^\dagger(t)\hat{\rho}(t)\hat{U}_0(t)=\exp\left(\frac{\mathrm{i}\hat{H}_0 t}{\hbar}\right)\rho(t)\exp\left(-\frac{\mathrm{i}\hat{H}_0 t}{\hbar}\right). \tag{2.122}$$

Noticing that the temporal evolution of $\hat{\rho}(t)$ is given by Eq. (107) in terms of the time evolution operator $\hat{U}(t)$, we have

$$\tilde{\rho}(t)=\hat{U}_0^\dagger(t)\hat{U}(t)\hat{\rho}(0)\hat{U}^{+}(t)\hat{U}_0(t)=\tilde{U}(t)\hat{\rho}(0)\tilde{U}^{+}(t), \tag{2.123}$$

where the definition of $\tilde{U}(t)$ as $\tilde{U}(t)\equiv\hat{U}_0^\dagger(t)\hat{U}(t)$ was used. Finally we can thus transform the Liouville equation Eq. (110) into the interaction representation

$$\mathrm{i}\hbar\frac{\partial\tilde{\rho}(t)}{\partial t}=[\tilde{V}(t),\tilde{\rho}(t)]. \tag{2.124}$$

Here note that Eq. (124) plays a fundamental role, but it was derived, on the basis of the concept of the external field that cannot be affected by the response of the relevant system and can be treated in classical theory. Since we are interested in an open system, where the response of the relevant system affects the external system, we will discuss in the following how Eq. (124) is modified to describe the temporal evolution of an open system. Such an equation to be derived is called the quantum master equation.

### *Quantum Master Equation for an Open System*

Let us assume a closed system, which is described by the Hamiltonian $\hat{H}$ and is called a total system. Then we divide the total system into two subsystems: one is the open system S whose temporal evolution is paid attention to; the other is the reservoir system R interacting with the system S. Suppose that no interactions between them at time $t = 0$. Then the isolated systems $S$ and $R$ are described by the Hamiltonians $\hat{H}_S$ and $\hat{H}_R$, respectively. Taking the eigenstate vectors $|\varphi_i^{(\mathrm{S})}\rangle$ and $|\Phi_j^{(\mathrm{R})}\rangle$ as a basis, we express the matrix elements of the density operator for the total system (S + R) in the form

$$\left\langle \varphi_{i'}^{(\mathrm{S})}, \Phi_{j'}^{(\mathrm{R})} \middle| \hat{\rho}_{\mathrm{tot}}(t) \middle| \varphi_i^{(\mathrm{S})}, \Phi_j^{(\mathrm{R})} \right\rangle \tag{2.125}$$

where the suffix $i(j)$ and $i'(j')$ denote the quantum numbers to specify the system S (R). After time $t > 0$, the interaction between the systems S and R, $\hat{V}_{\text{S-R}}$, makes the state vectors of the system S different from $|\varphi_i^{(\mathrm{S})}\rangle$. Taking it into account, we define the reduced density operator $\hat{\rho}^{(\mathrm{S})}(t)$, and have to represent the density matrix in terms of a basis of $|\varphi_i^{(\mathrm{S})}\rangle$. Since $\hat{\rho}^{(\mathrm{S})}(t)$ is defined in the following form after taking a trace with respect to the system R, $\mathrm{tr}_{\mathrm{R}}$

$$\hat{\rho}^{(\mathrm{S})}(t) = \mathrm{tr}_{\mathrm{R}}[\hat{\rho}_{\mathrm{tot}}(t)] = \sum_j \left\langle \Phi_j^{(\mathrm{R})} \middle| \hat{\rho}_{\mathrm{tot}}(t) \middle| \Phi_j^{(\mathrm{R})} \right\rangle, \tag{2.126}$$

the density matrix is represented as

$$\left\langle \varphi_{i'}^{(\mathrm{S})} \middle| \hat{\rho}^{(\mathrm{S})}(t) \middle| \varphi_i^{(\mathrm{S})} \right\rangle = \left\langle \varphi_{i'}^{(\mathrm{S})} \middle| \mathrm{tr}_{\mathrm{R}} \left[ \hat{\rho}_{\mathrm{tot}}(t) \right] \middle| \varphi_i^{(\mathrm{S})} \right\rangle = \left\langle \varphi_{i'}^{(\mathrm{S})} \middle| \left[ \sum_j \left\langle \Phi_j^{(\mathrm{R})} \middle| \hat{\rho}_{\mathrm{tot}}(t) \middle| \Phi_j^{(\mathrm{R})} \right\rangle \right] \middle| \varphi_i^{(\mathrm{S})} \right\rangle, \tag{2.127}$$

and the expectation values of an arbitrary operator acting only on the state vectors that belong to the system S is written

$$\begin{aligned} \langle \hat{O}^{(\mathrm{S})} \rangle &= \mathrm{tr}_{\mathrm{S}}(\hat{\rho}^{(\mathrm{S})}(t)\, \hat{O}^{(\mathrm{S})}) = \sum_j \left\langle \varphi_j^{(\mathrm{S})} \middle| \hat{\rho}^{(\mathrm{S})}(t)\, \hat{O}^{(\mathrm{S})} \middle| \varphi_j^{(\mathrm{S})} \right\rangle \\ &= \sum_{i,j} \left\langle \varphi_j^{(\mathrm{S})} \middle| \hat{\rho}^{(\mathrm{S})}(t) \middle| \varphi_i^{(\mathrm{S})} \right\rangle \left\langle \varphi_i^{(\mathrm{S})} \middle| \hat{O}^{(\mathrm{S})} \middle| \varphi_j^{(\mathrm{S})} \right\rangle. \end{aligned} \tag{2.128}$$

From Eq. (124), the quantum master equation in the interaction representation is written

$$i\hbar \frac{\partial \tilde{\rho}_{\mathrm{tot}}(t)}{\partial t} = [\tilde{V}_{\text{S-R}}(t), \tilde{\rho}_{\mathrm{tot}}(t)], \tag{2.129}$$

and the temporal evolution of $\hat{\rho}^{(S)}(t)$ is given

$$\mathrm{i}\hbar\frac{\partial\tilde{\rho}^{(\mathrm{S})}(t)}{\partial t}=\mathrm{tr}_{\mathrm{R}}[\tilde{V}_{\text{S-R}}(t),\tilde{\rho}_{\mathrm{tot}}(t)] \tag{2.130}$$

by taking a trace with respect to the system R. Here $\tilde{\rho}^{(\mathrm{S})}(t)$ and $\tilde{V}_{\text{S-R}}(t)$ are respectively expressed in the interaction representation as

$$\tilde{\rho}^{(\mathrm{S})}(t)=\exp\left(\frac{\mathrm{i}\hat{H}_{\mathrm{S}}t}{\hbar}\right)\hat{\rho}^{(\mathrm{S})}(t)\exp\left(-\frac{\mathrm{i}\hat{H}_{\mathrm{S}}t}{\hbar}\right) \tag{2.131}$$

and

$$\tilde{V}_{\text{S-R}}(t)=\exp\left[\frac{\mathrm{i}(\hat{H}_{\mathrm{S}}+\hat{H}_{\mathrm{R}})t}{\hbar}\right]\hat{V}_{\text{S-R}}(t)\exp\left[-\frac{\mathrm{i}(\hat{H}_{\mathrm{S}}+\hat{H}_{\mathrm{R}})t}{\hbar}\right], \tag{2.132}$$

where both $\hat{H}_{\mathrm{S}}$ and $\hat{H}_{\mathrm{R}}$ are assumed to be time-independent. As mentioned earlier, the perturbative solutions are reasonable in practice if the interaction between the systems S and R, $\tilde{V}_{\text{S-R}}(t)$ is weak. Assuming such a case and using the perturbative expansion in terms of $\tilde{V}_{\text{S-R}}(t)$, we obtain the solutions of Eq. (130). It follows from Eq. (129),

$$\tilde{\rho}_{\mathrm{tot}}(t)=\tilde{\rho}_{\mathrm{tot}}(0)+\frac{1}{\mathrm{i}\hbar}\int_0^t dt'[\tilde{V}_{\text{S-R}}(t'),\tilde{\rho}_{\mathrm{tot}}(t')], \tag{2.133}$$

which is substituted into the right-hand side of Eq. (130). Then we have

$$\frac{\partial}{\partial t}\tilde{\rho}^{(\mathrm{S})}(t)=\frac{1}{\mathrm{i}\hbar}\mathrm{tr}_{\mathrm{R}}[\tilde{V}_{\text{S-R}}(t),\tilde{\rho}_{\mathrm{tot}}(0)]+\frac{1}{(\mathrm{i}\hbar)^2}\int_0^t dt'\mathrm{tr}_{\mathrm{R}}[\tilde{V}_{\text{S-R}}(t),[\tilde{V}_{\text{S-R}}(t'),\tilde{\rho}_{\mathrm{tot}}(t')]],. \tag{2.134}$$

which can be rewritten as

$$\begin{aligned}\frac{\partial\tilde{\rho}^{(\mathrm{S})}(t)}{\partial t}&=\frac{1}{\mathrm{i}\hbar}\mathrm{tr}_{\mathrm{R}}\left[\tilde{V}_{\text{S-R}}(t),\tilde{\rho}^{(\mathrm{S})}(0)\hat{R}_0\right]-\frac{1}{\hbar^2}\int_0^t dt'\,\mathrm{tr}_{\mathrm{R}}([\tilde{V}_{\text{S-R}}(t),[\tilde{V}_{\text{S-R}}(t'),\tilde{\rho}_{\mathrm{tot}}(t')]])\\&=-\frac{1}{\hbar^2}\int_0^t dt'\,\mathrm{tr}_{\mathrm{R}}([\tilde{V}_{\text{S-R}}(t),[\tilde{V}_{\text{S-R}}(t'),\tilde{\rho}_{\mathrm{tot}}(t')]]),\end{aligned} \tag{2.135}$$

where the density operators for the systems S and R at $t = 0$ are denoted by

$$\hat{\rho}_{\mathrm{tot}}(0)=\hat{\rho}^{(\mathrm{S})}(0)\hat{R}_0, \tag{2.136}$$

or

$$\tilde{\rho}_{\text{tot}}(0) = \tilde{\rho}^{(\text{S})}(0)\tilde{R}_0 = \tilde{\rho}^{(\text{S})}(0)\hat{R}_0 \tag{2.137}$$

in the interaction representation owing to no interactions between them. The right-hand side of Eq. (135) shows that both systems S and R have correlations between them at $t > 0$ after the interaction turns on.

Now let us adopt the Born approximation represented by

$$\tilde{\rho}_{\text{tot}}(t) = \tilde{\rho}^{(\text{S})}(t)\hat{R}_0 \tag{2.138}$$

which means the states belonging to the system R do not change from the initial ones at $t > 0$ while the states in the system S are largely affected by the interaction $\tilde{V}_{\text{S-R}}(t)$. Under the condition, Eq. (135) can be approximated

$$\frac{\partial \tilde{\rho}^{(\text{S})}(t)}{\partial t} = -\frac{1}{\hbar^2}\int_0^t dt' \,\text{tr}_{\text{R}}\left(\left[\tilde{V}_{\text{S-R}}(t), \left[\tilde{V}_{\text{S-R}}(t'), \tilde{\rho}^{(\text{S})}(t')\hat{R}_0\right]\right]\right), \tag{2.139}$$

from which it follows that $\tilde{\rho}^{(\text{S})}(t)$ to be solved depends on all $\tilde{\rho}^{(\text{S})}(t')$ in the past from the initial to current time $t$. Then we approximate $\tilde{\rho}^{(\text{S})}(t')$ on the right-hand side of Eq. (139) by $\tilde{\rho}^{(\text{S})}(t)$, which is called the Markov approximation, where the effects on the system S instantaneously occur and the interaction with the system R in the past time can be neglected. In Born-Markov approximation, Eq. (139) reads

$$\frac{\partial \tilde{\rho}^{(\text{S})}(t)}{\partial t} = -\frac{1}{\hbar^2}\int_0^t dt' \,\text{tr}_{\text{R}}\left(\left[\tilde{V}_{\text{S-R}}(t), \left[\tilde{V}_{\text{S-R}}(t'), \tilde{\rho}^{(\text{S})}(t)\hat{R}_0\right]\right]\right), \tag{2.140}$$

which is called the quantum master equation for an open system. It shows that $\tilde{\rho}^{(\text{S})}(t)$ in the open system cannot be obtained from $\tilde{\rho}^{(\text{S})}(0)$ via the time evolution operator $\hat{U}(t)$. This irreversibility is a result of the relaxation process occurred in the system S as a result of the interaction between the systems S and R.

In order to examine the correlation time of the reservoir and the meaning of the Markov approximation, let us take an example of the interaction in the form

$$\hat{V}_{\text{S-R}} = \hbar\sum_i \hat{s}_i\hat{\Gamma}_i, \tag{2.141}$$

where $\hat{s}_i$ and $\hat{\Gamma}_i$ denote the operators relating to the system S and R, respectively. Equation (141) can be easily expressed in the interaction representation

$$\begin{aligned}
\tilde{V}_{\text{S-R}}(t) &= \hbar\sum_i e^{\frac{i}{\hbar}(\hat{H}_{\text{S}}+\hat{H}_{\text{R}})t}(\hat{s}_i\hat{\Gamma}_i)e^{-\frac{i}{\hbar}(\hat{H}_{\text{S}}+\hat{H}_{\text{R}})t} \\
&= \hbar\sum_i \left(e^{\frac{i}{\hbar}\hat{H}_{\text{S}}t}\hat{s}_i e^{-\frac{i}{\hbar}\hat{H}_{\text{S}}t}\right)\left(e^{\frac{i}{\hbar}\hat{H}_{\text{R}}t}\hat{\Gamma}_i e^{-\frac{i}{\hbar}\hat{H}_{\text{R}}t}\right) \\
&= \hbar\sum_i \tilde{s}_i(t)\tilde{\Gamma}_i(t),
\end{aligned} \tag{2.142}$$

and Eq. (139) reads

$$\begin{aligned}\frac{\partial\tilde{\rho}^{(\mathrm{S})}(t)}{\partial t} &= -\sum_{i,j}\int_0^t dt'\,\mathrm{tr}_\mathrm{R}\left(\left[\tilde{s}_i(t)\tilde{\Gamma}_i(t),\left[\tilde{s}_j(t')\tilde{\Gamma}_j(t'),\tilde{\rho}^{(\mathrm{S})}(t')\hat{R}_0\right]\right]\right)\\ &= -\sum_{i,j}\int_0^t dt'\left\{\tilde{s}_i(t)\tilde{s}_j(t')\tilde{\rho}^{(\mathrm{S})}(t')\mathrm{tr}_\mathrm{R}\,[\tilde{\Gamma}_i(t)\tilde{\Gamma}_j(t')\hat{R}_0]\right.\\ &\quad -\tilde{s}_i(t)\tilde{\rho}^{(\mathrm{S})}(t')\tilde{s}_j(t')\mathrm{tr}_\mathrm{R}[\tilde{\Gamma}_i(t)\hat{R}_0\tilde{\Gamma}_j(t')]\\ &\quad -\tilde{s}_j(t')\tilde{\rho}^{(\mathrm{S})}(t')\tilde{s}_i(t)\mathrm{tr}_\mathrm{R}[\tilde{\Gamma}_j(t')\hat{R}_0\tilde{\Gamma}_i(t)]\\ &\quad \left.+\tilde{\rho}^{(\mathrm{S})}(t')\tilde{s}_j(t')\tilde{s}_i(t)\mathrm{tr}_\mathrm{R}[\hat{R}_0\tilde{\Gamma}_j(t')\tilde{\Gamma}_i(t)]\right\}.\end{aligned} \tag{2.143}$$

Using the properties of the trace that $\mathrm{tr}_\mathrm{R}(\hat{A}\hat{B}\hat{C}) = \mathrm{tr}_\mathrm{R}(\hat{B}\hat{C}\hat{A}) = \mathrm{tr}_\mathrm{R}(\hat{C}\hat{A}\hat{B})$ and the definition of the correlation functions

$$\langle\tilde{\Gamma}_i(t)\tilde{\Gamma}_j(t')\rangle_\mathrm{R} = \mathrm{tr}_\mathrm{R}[\hat{R}_0\tilde{\Gamma}_i(t)\tilde{\Gamma}_j(t')] \tag{2.144}$$

and

$$\langle\tilde{\Gamma}_j(t')\tilde{\Gamma}_i(t)\rangle_\mathrm{R} = \mathrm{tr}_\mathrm{R}[\hat{R}_0\tilde{\Gamma}_j(t')\tilde{\Gamma}_i(t)], \tag{2.145}$$

we rewrite Eq. (143)

$$\begin{aligned}\frac{\partial\tilde{\rho}^{(\mathrm{S})}(t)}{\partial t} = -\sum_{i,j}\int_0^t dt'&\left\{\left[\tilde{s}_i(t)\tilde{s}_j(t')\tilde{\rho}^{(\mathrm{S})}(t') - \tilde{s}_j(t')\tilde{\rho}^{(\mathrm{S})}(t')\tilde{s}_i(t)\right]\langle\tilde{\Gamma}_i(t)\tilde{\Gamma}_j(t')\rangle_\mathrm{R}\right.\\ &\left.+\left[\tilde{\rho}^{(\mathrm{S})}(t')\tilde{s}_j(t')\tilde{s}_i(t) - \tilde{s}_i(t)\tilde{\rho}^{(\mathrm{S})}(t')\tilde{s}_j(t')\right]\langle\tilde{\Gamma}_j(t')\tilde{\Gamma}_i(t)\rangle_\mathrm{R}\right\}.\end{aligned} \tag{2.146}$$

The effects of the system R are taken into account through the correlation functions (144) and (145), and if the correlation functions decay much faster than the time scale of the variation in $\tilde{\rho}^{(\mathrm{S})}(t)$ as

$$\langle\tilde{\Gamma}_i(t)\tilde{\Gamma}_j(t')\rangle_\mathrm{R} = \langle\tilde{\Gamma}_j(t')\tilde{\Gamma}_i(t)\rangle_\mathrm{R} \propto \delta(t-t'), \tag{2.147}$$

then it is allowed to replace $\tilde{\rho}^{(\mathrm{S})}(t')$ by $\tilde{\rho}^{(\mathrm{S})}(t)$. In other words, if the time constant of the temporal evolution of the system S is much slower than the decay time of the characteristic correlation function, the Markov approximation is justified. In the following discussions, we will use the Born-Markov approximation.

Let us now consider a damped oscillator model within the Born-Markov approximation, in order to investigate the quantum master equation including the relaxation process in detail. The Hamiltonian describing the model system is given by

$$\hat{H}_{\mathrm{S}} = \hbar\omega_0 \hat{a}^{\dagger}\hat{a}, \tag{2.148a}$$

$$\hat{H}_{\mathrm{R}} = \sum_j \hbar\omega_j \hat{r}_j^{\dagger}\hat{r}_j, \tag{2.148b}$$

$$\hat{V}_{\text{S-R}} = \sum_j \hbar\left(\kappa_j^{*}\hat{a}\,\hat{r}_j^{\dagger} + \kappa_j \hat{a}^{\dagger}\hat{r}_j\right) \equiv \hbar\left(\hat{a}\hat{\Gamma}^{\dagger} + \hat{a}^{\dagger}\hat{\Gamma}\right), \tag{2.148c}$$

where $\hat{H}_{\mathrm{S}}$ for the system S describes the harmonic oscillator with energy of $\hbar\omega_0$, and its creation and annihilation operators are $\hat{a}^{\dagger}$ and $\hat{a}$, respectively. The Hamiltonian $\hat{H}_{\mathrm{R}}$ for the system R describes a set of the harmonic oscillators with energy of $\hbar\omega_j$, creation and annihilation operators $\hat{r}_j^{\dagger}$ and $\hat{r}_j$. The interaction between the system S and R is denoted by $\hat{V}_{\text{S-R}}$ and the coupling constant is $\kappa_j$. Comparing with Eq. (141), we have the following correspondence: $\hat{s}_1 = \hat{a}$, $\hat{s}_2 = \hat{a}^{\dagger}$, $\hat{\Gamma}_1 = \hat{\Gamma}^{\dagger}$, $\hat{\Gamma}_2 = \hat{\Gamma}$, whose interaction representation can be easily obtained as follows.

$$\tilde{s}_1(t) = \mathrm{e}^{\mathrm{i}\omega_0 \hat{a}^{\dagger}\hat{a}t}\hat{a}\mathrm{e}^{-\mathrm{i}\omega_0 \hat{a}^{\dagger}\hat{a}t} = \hat{a}\mathrm{e}^{-\mathrm{i}\omega_0 t}, \tag{2.149a}$$

$$\tilde{s}_2(t) = \mathrm{e}^{\mathrm{i}\omega_0 \hat{a}^{\dagger}\hat{a}t}\hat{a}^{\dagger}\mathrm{e}^{-\mathrm{i}\omega_0 \hat{a}^{\dagger}\hat{a}t} = \hat{a}^{\dagger}\mathrm{e}^{\mathrm{i}\omega_0 t}, \tag{2.149b}$$

$$\begin{aligned}\tilde{\Gamma}_1(t) = \tilde{\Gamma}^{\dagger}(t) &= \exp\left(\mathrm{i}\sum_n \omega_n \hat{r}_n^{\dagger}\hat{r}_n t\right)\left(\sum_j \kappa_j^{*}\hat{r}_j^{\dagger}\right)\exp\left(-\mathrm{i}\sum_m \omega_m \hat{r}_m^{\dagger}\hat{r}_m t\right)\\ &= \sum_j \kappa_j^{*}\hat{r}_j^{\dagger}\mathrm{e}^{\mathrm{i}\omega_j t},\end{aligned} \tag{2.149c}$$

$$\begin{aligned}\tilde{\Gamma}_2(t) = \tilde{\Gamma}(t) &= \exp\left(\mathrm{i}\sum_n \omega_n \hat{r}_n^{\dagger}\hat{r}_n t\right)\left(\sum_j \kappa_j \hat{r}_j\right)\exp\left(-\mathrm{i}\sum_m \omega_m \hat{r}_m^{\dagger}\hat{r}_m t\right)\\ &= \sum_j \kappa_j \hat{r}_j \mathrm{e}^{-\mathrm{i}\omega_j t}.\end{aligned} \tag{2.149d}$$

As a prerequisite for the Born-Markov approximation, $\mathrm{tr}_{\mathrm{R}}(\tilde{V}_{\text{S-R}}(t)\hat{R}_0) = 0$ holds, and thus it follows $\langle\tilde{\Gamma}_1(t)\rangle_R = \langle\tilde{\Gamma}_2(t)\rangle_R = 0$ and $\langle\tilde{\Gamma}^{\dagger}(t)\tilde{\Gamma}^{\dagger}(t')\rangle_R =$

$\langle\tilde{\Gamma}(t)\tilde{\Gamma}(t')\rangle_R = 0.$ Taking it into account, we modify the quantum master equation as

$$\begin{aligned}
\frac{\partial\tilde{\rho}^{(\mathrm{S})}(t)}{\partial t} &= -\sum_{i,j=1}^{2}\int_0^t dt'\Big\{\Big[\tilde{s}_i(t)\tilde{s}_j(t')\tilde{\rho}^{(\mathrm{S})}(t') - \tilde{s}_j(t')\tilde{\rho}^{(\mathrm{S})}(t')\tilde{s}_i(t)\Big]\langle\tilde{\Gamma}_i(t)\tilde{\Gamma}_j(t')\rangle_{\mathrm{R}} \\
&\quad + \Big[\tilde{\rho}^{(\mathrm{S})}(t')\tilde{s}_j(t')\tilde{s}_i(t) - \tilde{s}_i(t)\tilde{\rho}^{(\mathrm{S})}(t')\tilde{s}_j(t')\Big]\langle\tilde{\Gamma}_j(t')\tilde{\Gamma}_i(t)\rangle_{\mathrm{R}}\Big\} \\
&= -\int_0^t dt'\Big\{[\hat{a}\hat{a}^\dagger\tilde{\rho}^{(\mathrm{S})}(t') - \hat{a}^\dagger\tilde{\rho}^{(\mathrm{S})}(t')\hat{a}]\,\mathrm{e}^{-\mathrm{i}\omega_0(t-t')}\langle\tilde{\Gamma}^\dagger(t)\tilde{\Gamma}(t')\rangle_{\mathrm{R}} \\
&\quad + [\tilde{\rho}^{(\mathrm{S})}(t')\hat{a}\hat{a}^\dagger - \hat{a}^\dagger\tilde{\rho}^{(\mathrm{S})}(t')\hat{a}]\mathrm{e}^{\mathrm{i}\omega_0(t-t')}\langle\tilde{\Gamma}^\dagger(t')\tilde{\Gamma}(t)\rangle_{\mathrm{R}} \\
&\quad + [\hat{a}^\dagger\hat{a}\tilde{\rho}^{(\mathrm{S})}(t') - \hat{a}\tilde{\rho}^{(\mathrm{S})}(t')\hat{a}^\dagger]\mathrm{e}^{\mathrm{i}\omega_0(t-t')}\langle\tilde{\Gamma}(t)\tilde{\Gamma}^\dagger(t')\rangle_{\mathrm{R}} \\
&\quad + [\tilde{\rho}^{(\mathrm{S})}(t')\hat{a}^\dagger\hat{a} - \hat{a}\tilde{\rho}^{(\mathrm{S})}(t')\hat{a}^\dagger]\mathrm{e}^{-\mathrm{i}\omega_0(t-t')}\langle\tilde{\Gamma}(t')\tilde{\Gamma}^\dagger(t)\rangle_{\mathrm{R}}\Big\},
\end{aligned} \tag{2.150}$$

where it is noted that nonzero contributions to the correlation functions relating to the system R are given by

$$\begin{aligned}
\langle\tilde{\Gamma}^\dagger(t)\tilde{\Gamma}(t')\rangle_{\mathrm{R}} &= \sum_{j,k}\kappa_j^*\kappa_k\mathrm{e}^{\mathrm{i}\omega_j t}\,\mathrm{e}^{-\mathrm{i}\omega_k t'}\mathrm{tr}_{\mathrm{R}}(\hat{R}_0\hat{r}_j^\dagger\hat{r}_k) \\
&= \sum_j|\kappa_j|^2\mathrm{e}^{\mathrm{i}\omega_j(t-t')}\overline{n}(\omega_j,T),
\end{aligned} \tag{2.151a}$$

$$\langle\tilde{\Gamma}^\dagger(t')\tilde{\Gamma}(t)\rangle_{\mathrm{R}} = \sum_j|\kappa_j|^2\mathrm{e}^{\mathrm{i}\omega_j(t'-t)}\overline{n}(\omega_j,T), \tag{2.151b}$$

$$\begin{aligned}
\langle\tilde{\Gamma}(t)\tilde{\Gamma}^\dagger(t')\rangle_{\mathrm{R}} &= \sum_{j,k}\kappa_j\kappa_k^*\mathrm{e}^{-\mathrm{i}\omega_j t}\,\mathrm{e}^{\mathrm{i}\omega_k t'}\mathrm{tr}_{\mathrm{R}}\left(\hat{R}_0\hat{r}_j\hat{r}_k^\dagger\right) \\
&= \sum_j|\kappa_j|^2\mathrm{e}^{-\mathrm{i}\omega_j(t-t')}[\overline{n}(\omega_j,T)+1],
\end{aligned} \tag{2.151c}$$

$$\langle\tilde{\Gamma}(t')\tilde{\Gamma}^\dagger(t)\rangle_{\mathrm{R}} = \sum_j|\kappa_j|^2\mathrm{e}^{-\mathrm{i}\omega_j(t'-t)}[\overline{n}(\omega_j,T)+1], \tag{2.151d}$$

with $\overline{n}(\omega_j,T) = \mathrm{tr}_{\mathrm{R}}(\hat{R}_0\hat{r}_j^\dagger\hat{r}_j)$. In order to replace the summation over $j$ by the integration, we define the density of states $\mathrm{g}(\omega)$ so that the number of the harmonic oscillators with angular frequency in the interval $\omega$ to $\omega + \mathrm{d}\omega$ is given by $g(\omega)\mathrm{d}\omega$. In addition, replacing the integral variable $t'$ by $\tau = t - t'$, we obtain

$$\langle \tilde{\Gamma}^{\dagger}(t)\tilde{\Gamma}(t-\tau)\rangle_{\mathrm{R}} = \int_0^{\infty} d\omega\, \mathrm{e}^{\mathrm{i}\omega\tau} g(\omega)\, |\kappa(\omega)|^2\, \bar{n}(\omega,T), \tag{2.152a}$$

$$\langle \tilde{\Gamma}^{\dagger}(t-\tau)\tilde{\Gamma}(t)\rangle_{\mathrm{R}} = \int_0^{\infty} d\omega\, \mathrm{e}^{-\mathrm{i}\omega\tau} g(\omega)\, |\kappa(\omega)|^2\, \bar{n}(\omega,T), \tag{2.152b}$$

$$\langle \tilde{\Gamma}(t)\tilde{\Gamma}^{\dagger}(t-\tau)\rangle_{\mathrm{R}} = \int_0^{\infty} d\omega\, \mathrm{e}^{-\mathrm{i}\omega\tau} g(\omega)\, |\kappa(\omega)|^2\, [\bar{n}(\omega,T)+1], \tag{2.152c}$$

$$\langle \tilde{\Gamma}(t-\tau)\tilde{\Gamma}^{\dagger}(t)\rangle_{\mathrm{R}} = \int_0^{\infty} d\omega\, \mathrm{e}^{\mathrm{i}\omega\tau} g(\omega)\, |\kappa(\omega)|^2\, [\bar{n}(\omega,T)+1]. \tag{2.152d}$$

With the help of these relations, the quantum master equation can be rewritten as

$$\begin{aligned}
\frac{\partial\tilde{\rho}^{(\mathrm{S})}(t)}{\partial t} = &-\int_0^t d\tau\, \{[\hat{a}\hat{a}^{\dagger}\tilde{\rho}^{(\mathrm{S})}(t-\tau) - \hat{a}^{\dagger}\tilde{\rho}^{(\mathrm{S})}(t-\tau)\hat{a}]\, \mathrm{e}^{-\mathrm{i}\omega_0\tau}\langle \tilde{\Gamma}^{\dagger}(t)\tilde{\Gamma}(t-\tau)\rangle_{\mathrm{R}} \\
&+ [\tilde{\rho}^{(\mathrm{S})}(t-\tau)\hat{a}\hat{a}^{\dagger} - \hat{a}^{\dagger}\tilde{\rho}^{(\mathrm{S})}(t-\tau)\hat{a}]\mathrm{e}^{\mathrm{i}\omega_0\tau}\langle \tilde{\Gamma}^{\dagger}(t-\tau)\tilde{\Gamma}(t)\rangle_{\mathrm{R}} \\
&+ [\hat{a}^{\dagger}\hat{a}\tilde{\rho}^{(\mathrm{S})}(t-\tau) - \hat{a}\tilde{\rho}^{(\mathrm{S})}(t-\tau)\hat{a}^{\dagger}]\mathrm{e}^{\mathrm{i}\omega_0\tau}\langle \tilde{\Gamma}(t)\tilde{\Gamma}^{\dagger}(t-\tau)\rangle_{\mathrm{R}} \\
&+ [\tilde{\rho}^{(\mathrm{S})}(t-\tau)\hat{a}^{\dagger}\hat{a} - \hat{a}\tilde{\rho}^{(\mathrm{S})}(t-\tau)\hat{a}^{\dagger}]\mathrm{e}^{-\mathrm{i}\omega_0\tau}\langle \tilde{\Gamma}(t-\tau)\tilde{\Gamma}^{\dagger}(t)\rangle_{\mathrm{R}}\} \\
= &-\int_0^t d\tau \int_0^{\infty} d\omega\, \{[\hat{a}\hat{a}^{\dagger}\tilde{\rho}^{(\mathrm{S})}(t-\tau) - \hat{a}^{\dagger}\tilde{\rho}^{(\mathrm{S})}(t-\tau)\hat{a}]\, \mathrm{e}^{\mathrm{i}(\omega-\omega_0)\tau} g(\omega)\, |\kappa(\omega)|^2\, \bar{n}(\omega,T) \\
&+ [\tilde{\rho}^{(\mathrm{S})}(t-\tau)\hat{a}\hat{a}^{\dagger} - \hat{a}^{\dagger}\tilde{\rho}^{(\mathrm{S})}(t-\tau)\hat{a}]\mathrm{e}^{-\mathrm{i}(\omega-\omega_0)\tau} g(\omega)\, |\kappa(\omega)|^2\, \bar{n}(\omega,T) \\
&+ [\hat{a}^{\dagger}\hat{a}\tilde{\rho}^{(\mathrm{S})}(t-\tau) - \hat{a}\tilde{\rho}^{(\mathrm{S})}(t-\tau)\hat{a}^{\dagger}]\mathrm{e}^{-\mathrm{i}(\omega-\omega_0)\tau} g(\omega)\, |\kappa(\omega)|^2\, [\bar{n}(\omega,T)+1] \\
&+ [\tilde{\rho}^{(\mathrm{S})}(t-\tau)\hat{a}^{\dagger}\hat{a} - \hat{a}\tilde{\rho}^{(\mathrm{S})}(t-\tau)\hat{a}^{\dagger}]\mathrm{e}^{\mathrm{i}(\omega-\omega_0)\tau} g(\omega)\, |\kappa(\omega)|^2\, [\bar{n}(\omega,T)+1]\},
\end{aligned} \tag{2.153}$$

where the $\tau$ integration is dominated by times, that is, the reservoir correlation time $t_R$ that is much shorter than $t_s$, the time scale for the evolution of $\tilde{\rho}^{(\mathrm{S})}(t)$, and thus $\tilde{\rho}^{(\mathrm{S})}(t-\tau)$ is replaced by $\tilde{\rho}^{(\mathrm{S})}(t)$ (Markov approximation). Moreover, becausee $t$ is of the order of $t_s$, we can extend the $\tau$ integration to infinity, and performing the integral

$$\lim_{t\to\infty}\int_0^t d\tau\, \mathrm{e}^{-\mathrm{i}(\omega-\omega_0)\tau} = \pi\delta(\omega-\omega_0) + \mathrm{i}\frac{P}{\omega_0-\omega}, \tag{2.154}$$

where $P$ designates the Cauchy principal value. Finally, we obtain the following equation

$$\begin{aligned}
\frac{\partial\tilde{\rho}^{(S)}(t)}{\partial t} &= -[\hat{a}\hat{a}^{\dagger}\tilde{\rho}^{(S)}(t) - \hat{a}^{\dagger}\tilde{\rho}^{(S)}(t)\hat{a}]\{\pi g(\omega_0)\,|\kappa(\omega_0)|^2\,\bar{n}(\omega_0,T) - \mathrm{i}\Delta'\} \\
&\quad - [\tilde{\rho}^{(S)}(t)\hat{a}\hat{a}^{\dagger} - \hat{a}^{\dagger}\tilde{\rho}^{(S)}(t)\hat{a}]\{\pi g(\omega_0)\,|\kappa(\omega_0)|^2\,\bar{n}(\omega_0,T) + \mathrm{i}\Delta'\} \\
&\quad - [\hat{a}^{\dagger}\hat{a}\tilde{\rho}^{(S)}(t) - \hat{a}\tilde{\rho}^{(S)}(t)\hat{a}^{\dagger}]\{\pi g(\omega_0)\,|\kappa(\omega_0)|^2\,[\bar{n}(\omega_0,T)+1] + \mathrm{i}(\Delta+\Delta')\} \\
&\quad - [\tilde{\rho}^{(S)}(t)\hat{a}^{\dagger}\hat{a} - \hat{a}\tilde{\rho}^{(S)}(t)\hat{a}^{\dagger}]\{\pi g(\omega_0)\,|\kappa(\omega_0)|^2\,[\bar{n}(\omega_0,T)+1] - \mathrm{i}(\Delta+\Delta')\} \\
&= -\mathrm{i}\Delta[\hat{a}^{\dagger}\hat{a}, \tilde{\rho}^{(S)}(t)] + \frac{\gamma}{2}(2\hat{a}\tilde{\rho}^{(S)}(t)\hat{a}^{\dagger} - \hat{a}^{\dagger}\hat{a}\tilde{\rho}^{(S)}(t) - \tilde{\rho}^{(S)}(t)\hat{a}^{\dagger}\hat{a}) \\
&\quad + \gamma\bar{n}(\omega_0,T)(\hat{a}\tilde{\rho}^{(S)}(t)\hat{a}^{\dagger} + \hat{a}^{\dagger}\tilde{\rho}^{(S)}(t)\hat{a} - \hat{a}^{\dagger}\hat{a}\tilde{\rho}^{(S)}(t) - \tilde{\rho}^{(S)}(t)\hat{a}\hat{a}^{\dagger}).
\end{aligned} \tag{2.155}$$

Here we used the boson commutation relation $[\hat{a}, \hat{a}^{\dagger}] = 1$ and set $\Delta$, $\Delta'$, and $\gamma$ as

$$\begin{aligned}
\Delta &\equiv P\int_0^{\infty} d\omega \frac{g(\omega)\,|\kappa(\omega)|^2}{\omega_0 - \omega}, \\
\Delta' &\equiv P\int_0^{\infty} d\omega \frac{g(\omega)\,|\kappa(\omega)|^2}{\omega_0 - \omega}\bar{n}(\omega,T), \\
\gamma &\equiv 2\pi g(\omega_0)\,|\kappa(\omega_0)|^2 .
\end{aligned} \tag{2.156}$$

For transformation of the representation from $\tilde{\rho}^{(S)}(t)$ (interaction representation) to $\hat{\rho}^{(S)}(t)$ (Schrödinger representation),

$$\hat{\rho}^{(S)}(t) = \exp\left(-\frac{\mathrm{i}}{\hbar}\hat{H}_S t\right)\tilde{\rho}^{(S)}(t)\exp\left(\frac{\mathrm{i}}{\hbar}\hat{H}_S t\right) \tag{2.157}$$

the time derivative is used as follows:

$$\begin{aligned}
\frac{\partial\hat{\rho}^{(S)}(t)}{\partial t} &= \frac{1}{\mathrm{i}\hbar}\left\{\hat{H}_S \exp\left(-\frac{\mathrm{i}}{\hbar}\hat{H}_S t\right)\tilde{\rho}^{(S)}(t)\exp\left(\frac{\mathrm{i}}{\hbar}\hat{H}_S t\right)\right. \\
&\quad \left. - \exp\left(-\frac{\mathrm{i}}{\hbar}\hat{H}_S t\right)\tilde{\rho}^{(S)}(t)\exp\left(\frac{\mathrm{i}}{\hbar}\hat{H}_S t\right)\hat{H}_S\right\} \\
&\quad + \exp\left(-\frac{\mathrm{i}}{\hbar}\hat{H}_S t\right)\frac{\partial\tilde{\rho}^{(S)}(t)}{\partial t}\exp\left(\frac{\mathrm{i}}{\hbar}\hat{H}_S t\right) \\
&= \frac{1}{\mathrm{i}\hbar}\left[\hat{H}_S, \hat{\rho}^{(S)}(t)\right] + \exp\left(-\frac{\mathrm{i}}{\hbar}\hat{H}_S t\right)\frac{\partial\tilde{\rho}^{(S)}(t)}{\partial t}\exp\left(\frac{\mathrm{i}}{\hbar}\hat{H}_S t\right).
\end{aligned} \tag{2.158}$$

The first term on the right-hand side is explicitly calculated as

$$\frac{1}{\mathrm{i}\hbar}\left[\hat{H}_{\mathrm{S}},\hat{\rho}^{(\mathrm{S})}(t)\right]=-\mathrm{i}\omega_0[\hat{a}^{\dagger}\hat{a},\hat{\rho}^{(\mathrm{S})}(t)], \tag{2.159}$$

while the substitution of Eq. (155) modifies the second term as

$$\begin{aligned}&-\mathrm{i}\Delta[\hat{a}^{\dagger}\hat{a},\hat{\rho}^{(\mathrm{S})}(t)]+\frac{\gamma}{2}(2\hat{a}\hat{\rho}^{(\mathrm{S})}(t)\hat{a}^{\dagger}-\hat{a}^{\dagger}\hat{a}\hat{\rho}^{(\mathrm{S})}(t)-\hat{\rho}^{(\mathrm{S})}(t)\hat{a}^{\dagger}\hat{a})\\&\qquad+\gamma\bar{n}(\omega_0,T)(\hat{a}\hat{\rho}^{(\mathrm{S})}(t)\hat{a}^{\dagger}+\hat{a}^{\dagger}\hat{\rho}^{(\mathrm{S})}(t)\hat{a}-\hat{a}^{\dagger}\hat{a}\hat{\rho}^{(\mathrm{S})}(t)-\hat{\rho}^{(\mathrm{S})}(t)\hat{a}\hat{a}^{\dagger}),\end{aligned} \tag{2.160}$$

where explicit transformation of each operator from the interaction to Schrödinger representation is employed as

$$\begin{aligned}&\exp\left(-\mathrm{i}\omega_0\hat{a}^{\dagger}\hat{a}t\right)\hat{a}\tilde{\rho}^{(\mathrm{S})}(t)\hat{a}^{\dagger}\exp\left(\mathrm{i}\omega_0\hat{a}^{\dagger}\hat{a}t\right)\\&=\exp\left(-\mathrm{i}\omega_0\hat{a}^{\dagger}\hat{a}t\right)\hat{a}\left[\exp\left(\mathrm{i}\omega_0\hat{a}^{\dagger}\hat{a}t\right)\hat{\rho}^{(\mathrm{S})}(t)\exp\left(-\mathrm{i}\omega_0\hat{a}^{\dagger}\hat{a}t\right)\right]\hat{a}^{\dagger}\exp\left(\mathrm{i}\omega_0\hat{a}^{\dagger}\hat{a}t\right)\\&=\hat{a}\hat{\rho}^{(\mathrm{S})}(t)\hat{a}^{\dagger},\\&\exp\left(-\mathrm{i}\omega_0\hat{a}^{\dagger}\hat{a}t\right)\hat{a}^{\dagger}\hat{a}\tilde{\rho}^{(\mathrm{S})}(t)\exp\left(\mathrm{i}\omega_0\hat{a}^{\dagger}\hat{a}t\right)=\hat{a}^{\dagger}\hat{a}\hat{\rho}^{(\mathrm{S})}(t),\\&\exp\left(-\mathrm{i}\omega_0\hat{a}^{\dagger}\hat{a}t\right)\tilde{\rho}^{(\mathrm{S})}(t)\hat{a}^{\dagger}\hat{a}\exp\left(\mathrm{i}\omega_0\hat{a}^{\dagger}\hat{a}t\right)=\hat{\rho}^{(\mathrm{S})}(t)\hat{a}^{\dagger}\hat{a},\\&\exp\left(-\mathrm{i}\omega_0\hat{a}^{\dagger}\hat{a}t\right)\hat{a}^{\dagger}\tilde{\rho}^{(\mathrm{S})}(t)\hat{a}\exp\left(\mathrm{i}\omega_0\hat{a}^{\dagger}\hat{a}t\right)=\hat{a}^{\dagger}\hat{\rho}^{(\mathrm{S})}(t)\hat{a},\\&\exp\left(-\mathrm{i}\omega_0\hat{a}^{\dagger}\hat{a}t\right)\tilde{\rho}^{(\mathrm{S})}(t)\hat{a}\hat{a}^{\dagger}\exp\left(\mathrm{i}\omega_0\hat{a}^{\dagger}\hat{a}t\right)=\hat{\rho}^{(\mathrm{S})}(t)\hat{a}\hat{a}^{\dagger}.\end{aligned} \tag{2.161}$$

Finally, the quantum master equation for a damped oscillator is derived in the Schrödinger representation as

$$\begin{aligned}\frac{\partial\hat{\rho}^{(\mathrm{S})}(t)}{\partial t}&=-\mathrm{i}(\omega_0+\Delta)[\hat{a}^{\dagger}\hat{a},\hat{\rho}^{(\mathrm{S})}(t)]+\frac{\gamma}{2}(2\hat{a}\hat{\rho}^{(\mathrm{S})}(t)\hat{a}^{\dagger}-\hat{a}^{\dagger}\hat{a}\hat{\rho}^{(\mathrm{S})}(t)-\hat{\rho}^{(\mathrm{S})}(t)\hat{a}^{\dagger}\hat{a})\\&\quad+\gamma\bar{n}(\omega_0,T)(\hat{a}\hat{\rho}^{(\mathrm{S})}(t)\hat{a}^{\dagger}+\hat{a}^{\dagger}\hat{\rho}^{(\mathrm{S})}(t)\hat{a}-\hat{a}^{\dagger}\hat{a}\hat{\rho}^{(\mathrm{S})}(t)-\hat{\rho}^{(\mathrm{S})}(t)\hat{a}\hat{a}^{\dagger})\\&=-\mathrm{i}(\omega_0+\Delta)[\hat{a}^{\dagger}\hat{a},\hat{\rho}^{(\mathrm{S})}(t)]+\frac{\gamma}{2}([\hat{a},\hat{\rho}^{(\mathrm{S})}(t)\hat{a}^{\dagger}]+[\hat{a}\hat{\rho}^{(\mathrm{S})}(t),\hat{a}^{\dagger}])\\&\quad+\gamma\bar{n}(\omega_0,T)([\hat{a}\hat{\rho}^{(\mathrm{S})}(t),\hat{a}^{\dagger}]+[\hat{a}^{\dagger},\hat{\rho}^{(\mathrm{S})}(t)\hat{a}]),\end{aligned} \tag{2.162}$$

or in the Lindblad form as

$$\begin{aligned}\frac{\partial\hat{\rho}^{(\mathrm{S})}(t)}{\partial t}&=-\mathrm{i}(\omega_0+\Delta)[\hat{a}^{\dagger}\hat{a},\hat{\rho}^{(\mathrm{S})}(t)]\\&\quad+\frac{\gamma}{2}(\bar{n}(\omega_0,T)+1)(2\hat{a}\hat{\rho}^{(\mathrm{S})}(t)\hat{a}^{\dagger}-\hat{a}^{\dagger}\hat{a}\hat{\rho}^{(\mathrm{S})}(t)-\hat{\rho}^{(\mathrm{S})}(t)\hat{a}^{\dagger}\hat{a})\\&\quad+\frac{\gamma}{2}\bar{n}(\omega_0,T)(2\hat{a}^{\dagger}\hat{\rho}^{(\mathrm{S})}(t)\hat{a}-\hat{a}\hat{a}^{\dagger}\hat{\rho}^{(\mathrm{S})}(t)-\hat{\rho}^{(\mathrm{S})}(t)\hat{a}\hat{a}^{\dagger}).\end{aligned} \tag{2.163}$$

The energy shift caused by the reservoir system R is denoted by $\omega_0 + \Delta$, while the terms proportional to $\gamma$ represent the relaxation process.

### 2.2.6 Exciton Population Dynamics and Nanophotonic Logic Operation

On the basis of the above formulation, we will investigate the dynamics of exciton population in a two-QD system and a three-QD system, each of which is coupled to the phonon reservoir. This kind of study enables us to understand nanophotonic functional devices [56].

#### *Dynamics of a Two-QD System*

In Figure 2.12, we schematically illustrate a two-QD system interacting with a phonon reservoir system, where all the energy-transfer paths are depicted except for the coupling to far-field light because of different time scales. The Hamiltonian for the system is modeled as

$$\hat{H} = \hat{H}_0 + \hat{H}_{\text{int}} + \hat{H}_{\text{SR}} \tag{2.164}$$

and

$$\hat{H}_0 = \hbar\Omega_2 \hat{A}^{\dagger}\hat{A} + \hbar\Omega_1 \hat{B}_1^{\dagger}\hat{B}_1 + \hbar\Omega_2 \hat{B}_2^{\dagger}\hat{B}_2 + \hbar\sum_n \omega_n \hat{b}_n^{\dagger}\hat{b}_n, \tag{2.165a}$$

$$\hat{H}_{\text{int}} = \hbar U\left(\hat{A}^{\dagger}\hat{B}_2 + \hat{B}_2^{\dagger}\hat{A}\right), \tag{2.165b}$$

$$\hat{H}_{\text{SR}} = \hbar\sum_n \left(g_n \hat{b}_n^{\dagger}\hat{B}_1^{\dagger}\hat{B}_2 + g_n^{*}\hat{b}_n \hat{B}_2^{\dagger}\hat{B}_1\right). \tag{2.165c}$$

When we assume that initial and final states are constructed only in terms of one-exciton states, the creation and annihilation operators of an exciton with

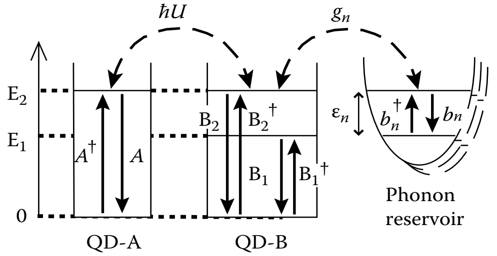

**FIGURE 2.12**
Schematic illustration of two-QD system. QD-A and QD-B are resonantly coupled via an optical near-field interaction, and the sublevels in QD-B are coupled with a phonon reservoir.

energy of $E_2 = \hbar\,\Omega_2$ or $E_1 = \hbar\,\Omega_1$ can be written as follows:

$$\begin{aligned}&\hat{A}^{\dagger} = (\,|e\rangle\langle g|\,)_{A},\ \hat{A} = \left(|g\rangle\langle e|\right)_{A},\ \hat{B}_1^{\dagger} = (\,|e\rangle\langle g\,|\,)_{B_1},\\ &\hat{B}_1 = (\,|g\rangle\langle e|\,)_{B_1},\ \hat{B}_2^{\dagger} = (|\,e\rangle\langle g\,|\,)_{B_2},\ \hat{B}_2 = (\,|g\rangle\langle e)_{B_2},\end{aligned} \tag{2.166}$$

where $|e\rangle_i$ and $|g\rangle_i$ represent the exciton and crystal ground states, respectively, relating to QD-A or QD-B specified by the suffix. It easily follows that the commutation relations hold as

$$\begin{aligned}&\left[\hat{B}_i,\hat{B}_j^{\dagger}\right] = \delta_{ij}(\,|g\rangle\langle g|_{B_i} - |e\rangle\langle e|_{B_i}),\\ &[\hat{B}_i,\hat{B}_j] = 0 = \left[\hat{B}_i^{\dagger},\hat{B}_j^{\dagger}\right]\ \ (i,j=1,2).\end{aligned} \tag{2.167}$$

This means that the operators are neither bosonic nor fermionic. Bosonic operators $(\hat{b}_n^{\dagger},\hat{b}_n)$ are for the phonons with energy eigenvalues $\hbar\omega_n$. In the following discussion, for simplicity, the rotating wave approximation is used in the interaction Hamiltonian $\hat{H}_{\text{int}}$ as

$$(\hat{A}+\hat{A}^{\dagger})\left(\hat{B}_2+\hat{B}_2^{\dagger}\right) \approx \hat{A}^{\dagger}\hat{B}_2 + \hat{A}\hat{B}_2^{\dagger}. \tag{2.168}$$

Phonon reservoir is assumed to be a collection of multiple harmonic oscillators labeled $n$. Optical near-field couplings are denoted by $\hbar U$, whereas exciton-phonon couplings are designated by $\hbar g_n$. Let us consider the one-exciton dynamics in the system, using three bases, as illustrated in Figure 2.13. The quantum master equation for the density matrix, within the Born-Markov approximation, is given in the Schrödinger representation as

$$\frac{d\rho_{11}(t)}{dt} = iU(r)[\rho_{12}(t)-\rho_{21}(t)], \tag{2.169a}$$

$$\frac{d\rho_{12}(t)}{dt} - \frac{d\rho_{21}(t)}{dt} = 2iU(r)\,[\rho_{11}(t)-\rho_{22}(t)] - (n+1)\gamma\,[\rho_{12}(t)-\rho_{21}(t)], \tag{2.169b}$$

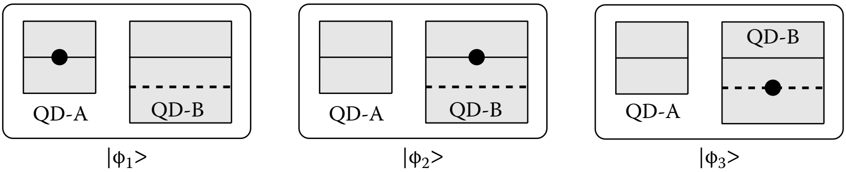

**FIGURE 2.13**
Three bases for the one-exciton dynamics in a two-QD system. The filled circles marked on the levels represent the exciton occupation of each level.

$$\frac{d\rho_{22}(t)}{dt} = -iU(r)[\rho_{12}(t) - \rho_{21}(t)] - 2(n+1)\gamma\,\rho_{22}(t) + 2n\gamma\,\rho_{33}(t), \tag{2.169c}$$

$$\frac{d\rho_{33}(t)}{dt} = 2(n+1)\gamma\,\rho_{22}(t) - 2n\gamma\,\rho_{33}(t), \tag{2.169d}$$

where the abbreviation $\rho_{mn}(t) \equiv \langle\phi_m|\,\hat{\rho}(t)\,|\phi_n\rangle$ is employed. When the temperature, $T$, equals to zero ($n = 0$), these coupled equations can be analytically solved. The diagonal parts representing the population probability for each energy level in QD-A and QD-B, as well as the off diagonal parts representing quantum coherence, are written as

$$\rho_{11}(t) = \frac{1}{Z^2}\mathrm{e}^{-\gamma t}\left[\frac{\gamma}{2}\sinh(Zt) + Z\cosh(Zt)\right]^2, \tag{2.170a}$$

$$\rho_{22}(t) = \frac{U^2}{Z^2}\mathrm{e}^{-\gamma t}\sinh^2(Zt), \tag{2.170b}$$

$$\rho_{33}(t) = 1 - [\rho_{11}(t) + \rho_{22}(t)], \tag{2.170c}$$

$$\rho_{12}(t) = -\rho_{21}(t) = \mathrm{i}\frac{U}{Z^2}\mathrm{e}^{-\gamma t}\sinh(Zt)\left[\frac{\gamma}{2}\sinh(Zt) + Z\cosh(Zt)\right], \tag{2.170d}$$

where $Z \equiv \sqrt{(\gamma/2)^2 - U^2}$, and the initial conditions $\rho_{11}(0) = 1$ and $\rho_{mn}(0) = 0$ for the other matrix elements are used. When we define the state filling time $\tau_S$ as $\rho_{33}(\tau_S) = 1 - \mathrm{e}^{-1}$ which corresponds to the time for the excitation energy transfer from QD-A to the lower energy level in QD-B. It follows from Eqs. (170a)–(170d) that the temporal evolution of the population is quite different at $U > \gamma/2$ and $U < \gamma/2$. Although Eqs. (170a)–(170d) seem to be undefined at $U = \gamma/2$ $(Z = 0)$, taking a limit value, there is a definite solution regardless of whether $Z \to +0$, or $-0$ is taken. In Figure 2.14, the state-filling time $\tau_s$ is plotted as a function of the ratio of $\gamma/2$ to $U$. For $U > \gamma/2$, the population shows a damped oscillation with envelope function $\mathrm{e}^{-\gamma t}$; thus, $\tau_S$ is determined by the relaxation constant $\gamma$ as $\tau_S \sim \gamma^{-1}$. By contrast, for $U < \gamma/2$, $\rho_{22}(t)$ decays monotonically. At first glance, as $\gamma/2$ increases, we expect $\tau_s$ to decrease monotonically, because the population flows into the lower energy level more quickly; nevertheless, $\tau_s$ increases again, as shown in Figure 2.14. This occurs because the upper energy level in QD-B becomes effectively broad with increasing $\gamma$, which results in a decrease in the resonant energy transfer between the QDs. When the ratio $\gamma/2U$ is sufficiently large, $\tau_s$ increases linearly, as seen in Figure 2.14. Therefore the state-filling time is not only determined by the coupling strength between two QDs via the optical near field,

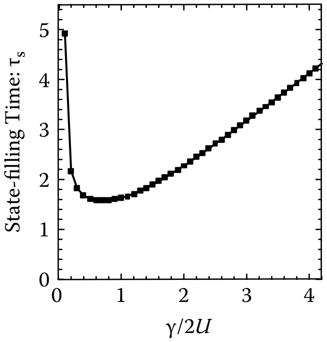

**FIGURE 2.14**
The state-filling time $\tau_s$ plotted as a function of the exciton-phonon coupling strength $\gamma/2$ to the interdot optical near-field coupling strength *U*.

but also by the coupling strength to the phonon reservoir system. It follows from the figure that the fastest energy transfer is obtained when $\gamma/2 \sim U$ is satisfied.

The term $2\gamma n \rho_{33}(t)$ on the right-hand side of Eq. (169c) indicates that the finite temperature effect caused by the finite number of phonons $(n \neq 0)$ induces back transfer of the excitation energy from the reservoir to the two-QD system. Within the Born-Markov approximation adopted, this term incoherently increases the population $\rho_{22}(t)$. As the population $\rho_{33}(t)$ increases, the back transfer becomes large, and gives the residual populations $\rho_{11}(t)$ and $\rho_{22}(t)$ in the upper levels in both QDs.

So far, the theoretical modeling of the population dynamics in a two-QD system has an ideally perfect resonance condition, which may be too tight to fabricate such a system with definite size ratios. In order to release the resonance condition, we estimate allowable tolerance, or size deviation of QDs from designed values. When the deviation from the resonant energy $\hbar\Delta\Omega$ in QD-B is introduced, the factor on the right-hand side in Eq. (170a) is modified, and the ratio of that in off-resonance to on-resonance is approximately proportional to $\frac{\gamma^2}{\gamma^2+\Delta\Omega^2}$ $(\gamma/2 \gg U)$. Therefore, we can achieve efficiency more than 50 % even if the deviation $\Omega < \gamma$ is introduced. When the dot size and relaxation constant are set as 7.1 nm (= $5\sqrt{2}$ *nm*) and $\hbar\gamma = 3$ meV, respectively, approximately 10 %-deviation of the dot size can be allowed. As the size of QDs is larger, the tolerable deviation is more relaxed. It is feasible to make such QDs by the recent advancement of nanofabrication techniques. In fact, experimental results show the consistent population dynamics as discussed in references 39 and 40.

### Dynamics of a Three-QD System

Let us consider the dynamics of the excitation energy transfer driven by an optical near field in a three-QD system illustrated in Figure 2.15. In this

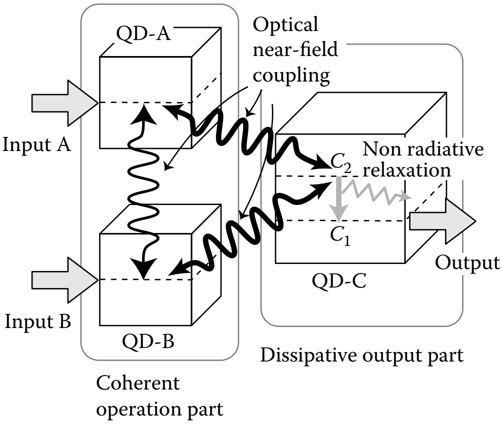

**FIGURE 2.15**
Three-QD system with spatially symmetric configuration. It consists of two identical two-level dots (QD-A and QD-B) and a three-level dot (QD-C). From the configuration, the coupling between QD-A and QD-B is stronger than that between QD-A and QD-C (QD-B and QD-C), and thus the system is divided into two parts: a coherent operation part with optical nutation and a dissipative output part with nonradiative relaxation.

system two identical QDs (QD-A and QD-B) are resonantly coupled with each other via an optical near field, which form a coherent operation part, while the third QD with larger size than the other two corresponds to a dissipative output part. Following the reduced density operator (matrix) formalism, we examine the temporal evolution of one-exciton states or that of two-exciton states created via optical near fields. First of all, it is necessary to choose an appropriate basis constructing matrix elements. The one-exciton and two-exciton states, for the purpose, are adopted so that the number of density matrix elements is minimized in the quantum master equation [57]. As a one-exciton state, that is, the state that one exciton exists in either one of three QDs, QD-A, QD-B, and QD-C, the following four states are adopted:

$$\begin{cases} |\mathrm{S}_1\rangle = \dfrac{1}{\sqrt{2}}\left(|A^*,B,C_1,C_2\rangle + |A,B^*,C_1,C_2\rangle\right), \\ |\mathrm{A}_1\rangle = \dfrac{1}{\sqrt{2}}\left(|A^*,B,C_1,C_2\rangle - |A,B^*,C_1,C_2\rangle\right), \\ |\mathrm{P}_1'\rangle = |A,B,C_1,C_2^*\rangle, \qquad |\mathrm{P}_1\rangle = |A,B,C_1^*,C_2\rangle, \end{cases} \tag{2.171}$$

where the symmetric and antisymmetric states relating to the one-exciton are abbreviated to S and A with suffix 1 on the left-hand side, respectively. The suffix A, B, and $C_i$ ($i = 1,2$) denote that no excitons exist in QD-A, QD-B, and QD-C, whereas A$^*$, B$^*$, and $C_i^*$ ($i = 1{,}2$) represent one exciton exists in QD-A, QD-B, and QD-C, respectively. For example, the state vector $|A^*, B, C_1, C_2\rangle$ shows that one exciton exists in QD-A while no excitons exist in other QDs, and $|A, B^*, C_1, C_2\rangle$ represents that there is one exciton in QD-B only. Because the exchange of A and B keeps the state vector $|S_1\rangle$ unchanged, $|S_1\rangle$ is symmetric in this sense. Similarly, the two-exciton states are classified by whether the lower level in QD-C, $C_1$ is occupied or not. For the states without $C_1$ occupation, we adopt

$$\begin{cases} |\mathrm{S}_2'\rangle = \dfrac{1}{\sqrt{2}}\left(|A^*, B, C_1, C_2^*\rangle + |A, B^*, C_1, C_2^*\rangle\right), \\ |\mathrm{A}_2'\rangle = \dfrac{1}{\sqrt{2}}\left(|A^*, B, C_1, C_2^*\rangle - |A, B^*, C_1, C_2^*\rangle\right) \\ |\mathrm{P}_2'\rangle = |A^*, B^*, C_1, C_2\rangle, \end{cases} \tag{2.172}$$

and for the states with $C_1$ occupation

$$\begin{cases} |\mathrm{S}_2\rangle = \dfrac{1}{\sqrt{2}}\left(|A^*, B, C_1^*, C_2\rangle + |A, B^*, C_1^*, C_2\rangle\right), \\ |\mathrm{A}_2\rangle = \dfrac{1}{\sqrt{2}}\left(|A^*, B, C_1^*, C_2\rangle - |A, B^*, C_1^*, C_2\rangle\right) \\ |\mathrm{P}_2\rangle = |A, B, C_1^*, C_2^*\rangle. \end{cases} \tag{2.173}$$

Then we obtain the reduced density matrix elements in terms of these ten states, which satisfy the quantum master equation as

$$\begin{aligned} \frac{\partial}{\partial t}\hat{\rho}(t) = -\frac{\mathrm{i}}{\hbar}[\hat{H}_s, \hat{\rho}(t)] + \frac{\Gamma}{2}\Big\{&2\hat{C}_1^\dagger\hat{C}_2\hat{\rho}(t)\hat{C}_2^\dagger\hat{C}_1 \\ &-\hat{C}_2^\dagger\hat{C}_1\hat{C}_1^\dagger\hat{C}_2\hat{\rho}(t) - \hat{\rho}(t)\hat{C}_2^\dagger\hat{C}_1\hat{C}_1^\dagger\hat{C}_2\Big\}. \end{aligned} \tag{2.174}$$

Here we consider the Hamiltonian $\hat{H}_S$ describing excitons in QDs coupled via optical near fields as

$$\begin{aligned} &\hat{H}_\mathrm{S} = \hat{H}_0 + \hat{H}_\mathrm{int}, \quad \hat{H}_0 = \hbar\Omega(\hat{A}^\dagger\hat{A} + \hat{B}^\dagger\hat{B}) + \hbar\sum_{i=1}^{2}\Omega_{C_i}\hat{C}_i^\dagger\hat{C}_i, \\ &\hat{H}_\mathrm{int} = \hbar U(\hat{A}^\dagger\hat{B} + \hat{B}^\dagger\hat{A}) + \hbar U'\left(\hat{B}^\dagger\hat{C}_2 + \hat{C}_2^\dagger\hat{B} + \hat{C}_2^\dagger\hat{A} + \hat{A}^\dagger\hat{C}_2\right), \end{aligned} \tag{2.175}$$

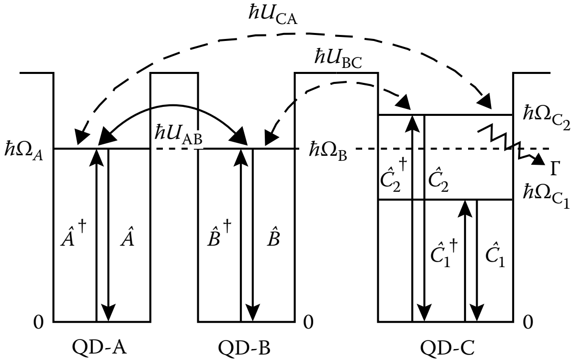

**FIGURE 2.16**
Schematic energy diagram in a three-QD system for exciton creation and annihilation operators and excitation transfer. The optical near-field couplings for the QD pairs are denoted by $U_{\mathrm{AB}}$ for QD-A and QD-B, $U_{\mathrm{BC}}$ for QD-B and QD-C, and $U_{\mathrm{CA}}$ for QD-C and QD-A. The nonradiative relaxation coupling caused by the exciton-phonon coupling is designated by Γ.

where the creation (annihilation) operator of an exciton in QD-A is denoted by $\hat{A}^\dagger$ $(\hat{A})$ and its energy eigenvalue by $\hbar\Omega_{\mathrm{A}} = \hbar\Omega$. The creation (annihilation) operator of an exciton in QD-B is likewise denoted by $\hat{B}^\dagger$ $(\hat{B})$ and its energy eigenvalue by $\hbar\Omega_{\mathrm{B}} = \hbar\Omega$, while the creation (annihilation) operator of an exciton in QD-C is expressed by $\hat{C}_i^\dagger$ $(\hat{C}_i)$ and their energy eigenvalues by $\hbar\Omega_{C_i}$. The coupling strengths of excitons, via optical near fields, between QD-A and QD-B, QD-B and QD-C, and QD-C and QD-A are designated by $U_{\mathrm{AB}} = U$, and $U_{\mathrm{BC}} = U_{\mathrm{CA}} = U'$, respectively, as illustrated in Figure 2.16. Inserting Eq. (175) into Eq. (174) and using the one-exciton states, we obtain the quantum master equation in the matrix form.

$$\frac{\partial}{\partial t}\rho_{S_1,S_1}(t) = \mathrm{i}\sqrt{2}U'\{\rho_{S_1,P_1'}(t) - \rho_{P_1',S_1}(t)\}, \tag{2.176a}$$

$$\frac{\partial}{\partial t}\rho_{S_1,P_1'}(t) = \left\{\mathrm{i}\left(\Delta\Omega - U\right) - \frac{\Gamma}{2}\right\}\rho_{S_1,P_1'}(t) + \mathrm{i}\sqrt{2}U'\left\{\rho_{S_1,S_1}(t) - \rho_{P_1',P_1'}(t)\right\}, \tag{2.176b}$$

$$\frac{\partial}{\partial t}\rho_{P_1',S_1}(t) = -\left\{\mathrm{i}(\Delta\Omega - U) + \frac{\Gamma}{2}\right\}\rho_{P_1',S_1}(t) - \mathrm{i}\sqrt{2}U'\left\{\rho_{S_1,S_1}(t) - \rho_{P_1',P_1'}(t)\right\}, \tag{2.176c}$$

$$\frac{\partial}{\partial t}\rho_{P_1',P_1'}(t) = -\Gamma\rho_{P_1',P_1'}(t) - \mathrm{i}\sqrt{2}U'\{\rho_{S_1,P_1'}(t) - \rho_{P_1',S_1}(t)\}, \tag{2.176d}$$

$$\frac{\partial}{\partial t}\rho_{P_1,P_1}(t) = \Gamma\rho_{P_1',P_1'}(t), \tag{2.176e}$$

where the matrix elements $\langle\alpha|\,\hat{\rho}(t)\,|\beta\rangle$ are abbreviated to $\rho_{\alpha,\beta}(t)$, and the energy difference $\hbar(\Omega_{C_2}-\Omega)$ is denoted by $\hbar\Delta\Omega$. The density matrix using the two-exciton states can similarly obtained as follows:

$$\frac{\partial}{\partial t}\rho_{S_2',S_2'}(t)=\mathrm{i}\sqrt{2}U'\{\rho_{S_2',P_2'}(t)-\rho_{P_2',S_2'}(t)\}-\Gamma\rho_{S_2',S_2'}(t), \tag{2.177a}$$

$$\frac{\partial}{\partial t}\rho_{S_2',P_2'}(t)=-\left\{\mathrm{i}(\Delta\Omega+U)+\frac{\Gamma}{2}\right\}\rho_{S_2',P_2'}(t)+\mathrm{i}\sqrt{2}U'\left\{\rho_{S_2',S_2'}(t)-\rho_{P_2',P_2'}(t)\right\}, \tag{2.177b}$$

$$\frac{\partial}{\partial t}\rho_{P_2',S_2'}(t)=\left\{\mathrm{i}(\Delta\Omega+U)-\frac{\Gamma}{2}\right\}\rho_{P_2',S_2'}(t)-\mathrm{i}\sqrt{2}U'\left\{\rho_{S_2',S_2'}(t)-\rho_{P_2',P_2'}(t)\right\}, \tag{2.177c}$$

$$\frac{\partial}{\partial t}\rho_{P_2',P_2'}(t)=-\mathrm{i}\sqrt{2}U'\left\{\rho_{S_2',P_2'}(t)-\rho_{P_2',S_2'}(t)\right\}. \tag{2.177d}$$

It should be noted that the matrix elements relating to both the symmetric states $|\mathrm{S}_1\rangle, |\mathrm{S}_2'\rangle$ and the antisymmetric states $|\mathrm{A}_1\rangle, |\mathrm{A}_2'\rangle$ never appear simultaneously in these equations when QDs are spatially allocated in a symmetric way as considered here. In addition, opposite contributions, that is, $\hbar(\Delta\Omega-U)$ and $\hbar(\Delta\Omega+U)$, are involved in these equations corresponding to the one-exciton and two-exciton states, respectively. This kind of difference in resonance conditions indicates that two-input logic operations are possible, as discussed in later chapter.

The differential equations for typical initial conditions can be solved analytically with the help of Laplace transformation. When an exciton is initially generated only in QD-A, that is, $\rho_{S_1,S_1}(0)=\rho_{A_1,A_1}(0)=\rho_{S_1,A_1}(0)=\rho_{A_1,S_1}(0)=1/2$, the probability that the exciton is transferred to the $C_1$ level in QD-C is given by

$$\begin{aligned}\rho_{P_1,P_1}(t)&=\Gamma\int_0^t\rho_{P_1',P_1'}(t')dt'\\&=\frac{1}{2}+\frac{4U'^2}{\omega_+^2-\omega_-^2}\{\cos\phi_+\,\cos(\omega_+t+\phi_+)-\cos\phi_-\,\cos(\omega_-t+\phi_-)\}\mathrm{e}^{-\left(\frac{\Gamma}{2}t\right)}\end{aligned} \tag{2.178}$$

with

$$\omega_\pm=\frac{1}{\sqrt{2}}\left[(\Delta\Omega-U)^2+W_+W_-\pm\sqrt{\{(\Delta\Omega-U)^2+W_+^2\}\{(\Delta\Omega-U)^2+W_-^2\}}\right]^{\frac{1}{2}},$$

$$\phi_\pm=\tan^{-1}\left(\frac{2\omega_\pm}{\Gamma}\right),\quad W_\pm=2\sqrt{2}U'\pm\frac{\Gamma}{2}. \tag{2.179}$$

Analytic solutions for two-exciton states can be similarly obtained. Under the initial condition $\rho_{P_2',P_2'}(0)=1$, that is, when both QD-A and QD-B are occupied by one excitons, the probability of an exciton transferred to the lower energy level in QD-C is

$$\begin{aligned}\rho_{S_2,S_2}(t)+\rho_{P_2,P_2}(t)&=\Gamma\int_0^t \rho_{S_2',S_2'}(t')dt'\\&=2\left[\frac{1}{2}+\frac{4U'^2}{\omega_+'^2-\omega_-'^2}\left\{\cos\phi_+'\cos\left(\omega_+'t+\phi_+'\right)-\cos\phi_-'\cos\left(\omega_-'t+\phi_-'\right)\right\}e^{-\left(\frac{\Gamma}{2}t\right)}\right]\end{aligned} \tag{2.180}$$

with

$$\begin{aligned}\omega_\pm'&=\frac{1}{\sqrt{2}}\left[(\Delta\Omega+U)^2+W_+W_-\pm\sqrt{\left\{(\Delta\Omega+U)^2+W_+^2\right\}\left\{(\Delta\Omega+U)^2+W_-^2\right\}}\right]^{\frac{1}{2}},\\\phi_\pm'&=\tan^{-1}\left(\frac{2\omega_\pm'}{\Gamma}\right).\end{aligned} \tag{2.181}$$

Here note that in Eqs. (178) and (180) the second terms with the denominators $\omega_+^2-\omega_-^2$ and $\omega_+'^2-\omega_-'^2$, respectively, contribute to the increase of the population in the output energy levels. It follows that efficiency of energy transfer is dominant for the one-exciton state when $\Delta\Omega=U$ is satisfied, while that is dominant for the two-exciton state in the case of $\Delta\Omega=-U$. These are analytical description of resonant energy transfer depending on the number of input excitons and a basic idea for logic operations. Based on the dynamics of excitons, or temporal evolution of density matrix for excitation energy transfer, functionality of a variety of nanophotonic devices will be discussed later, as well as AND-logic and XOR-logic operations that will be explained later.

### *Nanophotonic Logic Gates: AND- and XOR-Operations*

When the upper energy level in QD-C is negatively shifted to $\hbar(\Omega-U)$, an AND-logic gate operation can be realized. Let us explain it, by using Figure 2.17, which illustrates the energy diagram in the system with negative detuning in QD-C. The resonant energy transfer occurs only for the two-exciton state via the symmetric state in QD-A and QD-B, while the energy transfer for the one-exciton state does not occur because the upper energy level in QD-C is resonant to the antisymmetric state that is dipole forbidden for the symmetrically arranged QD system. This selective energy transfer assures an AND-logic operation.

The temporal evolution of the exciton population on the lower energy level in QD-C is plotted in Figure 2.18 to numerically examine the earlier

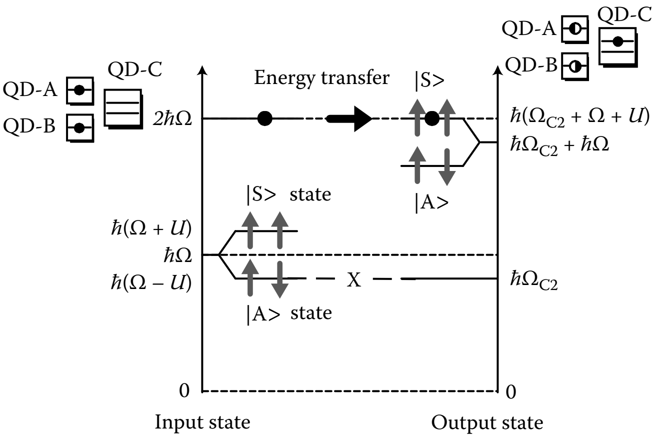

**FIGURE 2.17**
Energy diagram in a three-QD system with negative detuning in QD-C, $\hbar\Delta U = -\hbar U$. Here the filled circles represent that the occupation probability is unity, while the half filled circles show that the occupation probability is 1/2. It follows from the diagram that two excitons existing in the input state can be only transferred to the output state.

qualitative discussion (cf. Eqs. (178) to (181)). Here the strengths of the optical near-field coupling, $\hbar U = 89\ \mu\text{eV}$ and $\hbar U' = 14\ \mu\text{eV}$ are used for CuCl quantum cubes embedded in NaCl matrix. By contrast, the coupling to far-field light is neglected because the population dynamics caused by the optical

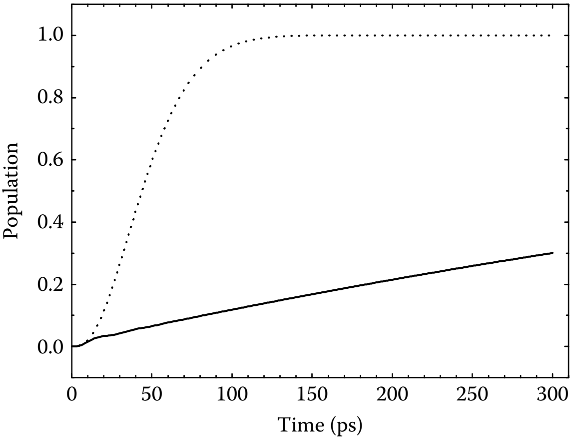

**FIGURE 2.18**
Temporal evolution of exciton population on the lower energy level (output level) in QD-C. The solid curve shows the result for one-exciton state, while the dotted curve represents the result for two-exciton state. The coupling strength between QD-A and QD-B is $\hbar U = 89\ \mu\text{eV}$, while that between QD-A and QD-C (QD-B and QD-C) is $\hbar U' = 14\ \mu\text{eV}$. The energy shift of the upper level in QD-C is assumed to be $\hbar U$ below $\hbar\Omega$, corresponding to Figure 2.17.

near-field coupling is much faster than that of the far-field coupling, by typically two orders of magnitude. The energy shift of the upper level in QD-C is assumed to be 89 $\mu$eV below $\hbar\Omega$, and the nonradiative relaxation time to be 10 ps. It follows from the figure that the exciton population is occupied nearly in 100 ps for the two-exciton state, which is determined by the coupling strength $\hbar U'$ between QD-A and QD-C (QD-B and QD-C). The output population is observed only for the two-exciton state as expected, because the coupling between the input and output states occur via the symmetric state. On the other hand, the population of the one-exciton state increases very slowly, owing to the weak coupling between the symmetric state in the input side and the output state. The state-filling time is much longer than the spontaneous emission lifetime caused by the e-h recombination, and thus the exciton population for the one-exciton state does not affect the output signal. In this manner, these behaviors for the one- and two-exciton states surely correspond to the AND-logic gate whose size is much smaller than the diffraction limit of light.

When the upper energy level in QD-C is positively shifted to $\hbar(\Omega + U)$, opposite to the AND-logic gate, an XOR-logic gate operation can be realized. It follows from the energy diagram shown in Figure 2.19 that the symmetric and antisymmetric states for one- and two-exciton states satisfy the conditions for an XOR-logic operation. Namely, the resonant energy transfer from the input to output systems occurs for the one-exciton state in either QD-A or QD-B via the symmetric state, while it does not occur for the two-exciton state since the input system is resonant to the antisymmetric state in the output system that is dipole forbidden for the symmetrically arranged QD system.

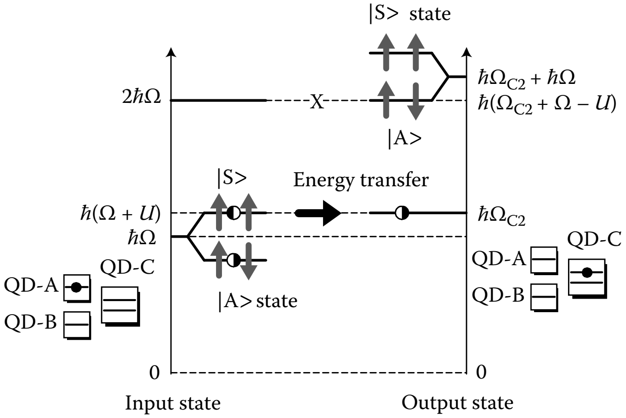

**FIGURE 2.19**
Energy diagram in a three-QD system with positive detuning in QD-C, $\hbar\Delta U = \hbar U$. The filled circles represent that the occupation probability is unity, while the half filled circles show that the occupation probability is 1/2. It follows from the diagram that one exciton existing in the input state can be only transferred to the output state.

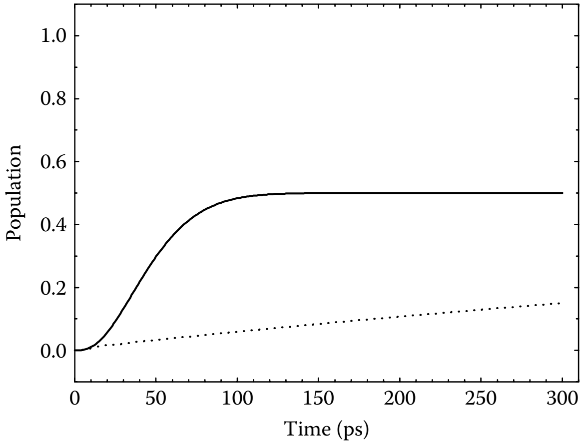

**FIGURE 2.20**
Temporal evolution of exciton population on the lower energy level (output level) in QD-C. The solid curve shows the result for one-exciton state, while the dotted curve represents the result for two-exciton state. The coupling strength between QD-A and QD-B is $\hbar U = 89\ \mu$eV, while that between QD-A and QD-C (QD-B and QD-C) is $\hbar U' = 14\ \mu$eV. The energy shift of the upper level in QD-C is assumed to be $\hbar U$ above $\hbar\Omega$, corresponding to Figure 2.19.

Figure 2.20 shows the temporal evolution for the one- and two-exciton states calculated from Eqs. (178)–(181). The parameters used are the same as those in Figure 2.18. In Figure 2.20, the output population appears for the one-exciton state, and the state-filling time is determined by the coupling strength $U'$ between QD-A and QD-C (QD-B and QD-C). The situation is the same as the AND-logic operation. Here the readers may ask why the exciton population reaches a half of the maximum for the one-exciton state in the XOR-logic gate operation. This is because a one-side QD is locally excited as an initial condition, in which both the symmetric and antisymmetric states are simultaneously excited with the same occupation probability as described in Eqs. (171). On the other hand, the output population for the two-exciton state shows slower increase, though it is as twice fast as that for the AND-logic gate operation. The reason also originates from the initial state; the symmetric state in the input system is occupied the half of the maximum at the initial time because of the local excitation, whereas the full of the initial population for the two-exciton state can couple to QD-C in the case of positive energy shift. It should be noted that the XOR-logic operation in this case can be performed stochastically, that is, repetition of operations are meaningful.

Now let us summarize these operations realized in three QD system in Table 2.1. The system behaves as an AND-logic gate when the energy difference is set to $\Delta\Omega = -U$, whereas it does as an XOR-logic gate when $\Delta\Omega = U$ is satisfied. These operations are classical, not quantum mechanical, and so quantum coherence time is not a critical parameter. Instead, the

**TABLE 2.1**

Relationship between the input and output populations for the energy difference, and the corresponding logic gate operations.

| Input | | Output: C | |
|---|---|---|---|
| A | B | AND-gate ($\Delta\Omega = -U$) | XOR-gate ($\Delta\Omega = U$) |
| 0 | 0 | 0 | 0 |
| 1 | 0 | 0 | 0.5 |
| 0 | 1 | 0 | 0.5 |
| 1 | 1 | 1 | 0 |

operations are limited by energy transfer time from the coherent operation part to the dissipative part, which is estimated about 50 ps for the CuCl quantum-cube system, which is enough shorter than the radiative lifetime (~1 ns) of excitons in each QD.

## 2.3 Principles of Nanofabrication Using Optical Near Fields

It is the first theoretical step for understanding of nanofabrication with optical near fields to consider how steep gradient electric fields of optical near fields affect nanometric particles, or nanomaterials. We briefly show that the steep gradient fields lead a molecule to a nonadiabatic transition, from a quantum-theoretical consideration. We then outline the nanofabrication technique using the optical near field [58,59], and discuss the unique feature found in the results of photodissociation experiments using a simple (exciton-phonon polariton (EPP)) model [60,61]. Finally the mechanism of photon localization in space with phonon's degrees of freedom, and phonon's role to the elementary process of photochemical reactions with optical near fields are discussed in detail [62,63].

### 2.3.1 Field Gradient and Force

A variety of theories have been developed to derive a force exerted on a neutral atom placed in a gradient electric field of light [64–66], one of which uses the energy shift of the atom depending on the spatial variance of the field. The energy levels of the atom become position-dependent, and their gradient $\vec{\nabla}$ gives the force exerted on the atom, according to the theory. Because the optical near field is expressed by the Yukawa function and has a steep spatial gradient, we expect the stronger force exerted on an atom, a molecule, nanoparticles and so on, than that by a propagating far field. We apply the theory, as an example, to a neutral molecule.

Let us assume an effective Hamiltonian $\hat{H}_{\text{eff}}$, which describes an interacting system of the electric field of light and molecules, and is given in terms of eigenstate vectors $|\psi_\alpha(\vec{r})\rangle$ with eigenvalues $E_\alpha(\vec{r})$ by

$$\hat{H}_{\text{eff}} = \sum_\alpha E_\alpha(\vec{r})\,|\psi_\alpha(\vec{r})\rangle\langle\psi_\alpha(\vec{r})|\,, \tag{2.182}$$

where $\vec{r}$ denotes the molecular position in space, and the suffix $\alpha$ identifies the electronic and vibrational states of the molecules. The gradient force exerted on the molecules is written

$$\vec{F} = -\langle\vec{\nabla}\hat{H}_{\text{eff}}\rangle = -\mathrm{Tr}(\hat{\rho}\vec{\nabla}\hat{H}_{\text{eff}}), \tag{2.183}$$

in terms of the density operator $\hat{\rho}$. Substituting Eq. (182) into Eq. (183), we have

$$\begin{aligned}\vec{F} &= -\sum_\alpha[\vec{\nabla}E_\alpha \mathrm{Tr}(\hat{\rho}\,|\psi_\alpha\rangle\langle\psi_\alpha|)] - \sum_\alpha E_\alpha \mathrm{Tr}\,[\hat{\rho}\{(\vec{\nabla}\,|\psi_\alpha\rangle)\langle\psi_\alpha| + |\psi_\alpha\rangle(\vec{\nabla}\langle\psi_\alpha|)\}]\\ &= -\sum_\alpha[(\vec{\nabla}E_\alpha)\,\langle\psi_\alpha|\,\hat{\rho}\,|\psi_\alpha\rangle] - \sum_\alpha E_\alpha[\langle\psi_\alpha|\,\hat{\rho}(\vec{\nabla}\,|\psi_\alpha\rangle) + (\vec{\nabla}\langle\psi_\alpha\,|)\hat{\rho}\,|\psi_\alpha\rangle],\end{aligned} \tag{2.184}$$

where the vector $\vec{r}$ is, for simplicity, omitted from the expression, and the definition of the trace

$$\mathrm{Tr}(\cdots) = \sum_\beta \langle\psi_\beta|\,(\cdots)\,|\psi_\beta\rangle \tag{2.185}$$

and the orthonormal conditions of the eigenstates $\langle\psi_\alpha\,|\,\psi_\beta\rangle = \delta_{\alpha\beta}$ are used. The first term on the right-hand side shows the average force originating in the spatial gradient of energy for each level multiplied by the occupation probability. In order to examine the meaning of the second term, we evaluate the work done by an infinitesimal displacement of the molecule from $\vec{r}$ to $\vec{r} + d\vec{r}$ as

$$-\vec{F}\cdot \mathrm{d}\vec{r} = \sum_\alpha \langle\psi_\alpha|\,\hat{\rho}\,|\psi_\alpha\rangle\cdot \mathrm{d}E_\alpha + \sum_\alpha E_\alpha[\langle\psi_\alpha|\,\hat{\rho}\,|\mathrm{d}\psi_\alpha\rangle + \langle \mathrm{d}\psi_\alpha|\,\hat{\rho}\,|\psi_\alpha\rangle], \tag{2.186}$$

where the following notations, $\mathrm{d}E_\alpha = \mathrm{d}\vec{r}\cdot\vec{\nabla}E_\alpha$ and $|\mathrm{d}\psi_\alpha\rangle = \mathrm{d}\vec{r}\cdot\vec{\nabla}\,|\psi_\alpha\rangle$ are used.

Expanding the state vector $|\psi_\alpha(\vec{r}+\mathrm{d}\vec{r})\rangle$ as

$$|\psi_\alpha(\vec{r}+\mathrm{d}\vec{r})\rangle = |\psi_\alpha(\vec{r})\rangle + \mathrm{d}\vec{r}\cdot\vec{\nabla}\,|\psi_\alpha(\vec{r})\rangle = |\psi_\alpha(\vec{r})\rangle + |\mathrm{d}\psi_\alpha(\vec{r})\rangle, \tag{2.187}$$

we have

$$\begin{aligned}&\langle\psi_\alpha(\vec{r}+\mathrm{d}\vec{r})|\,\hat{\rho}\,|\psi_\alpha(\vec{r}+\mathrm{d}\vec{r})\rangle - \langle\psi_\alpha(\vec{r})|\,\hat{\rho}\,|\psi_\alpha(\vec{r})\rangle\\ &= \langle\psi_\alpha(\vec{r})|\,\hat{\rho}\,|\mathrm{d}\psi_\alpha(\vec{r})\rangle + \langle\mathrm{d}\psi_\alpha(\vec{r})|\,\hat{\rho}\,|\psi_\alpha(\vec{r})\rangle,\end{aligned} \tag{2.188}$$

and thus can rewrite the second term in Eq. (184) as follows:

$$\sum_\alpha E_\alpha[\langle\psi_\alpha(\vec{r}+\mathrm{d}\vec{r})|\,\hat{\rho}\,|\psi_\alpha(\vec{r}+\mathrm{d}\vec{r})\rangle - \langle\psi_\alpha(\vec{r})|\,\hat{\rho}\,|\psi_\alpha(\vec{r})\rangle]. \tag{2.189}$$

This equation indicates that the occupation probability of the energy level specified by $\alpha$ varies according to the spatial change of the eigenstate $|\psi_\alpha(\vec{r})\rangle$, and results in the nonadiabatic transition, not the conventional adiabatic one. Therefore it is expected that this kind of nonadiabatic transition becomes more apparent since the optical near field is localized in a nanometer region.

### 2.3.2 Near-Field Nanofabrication and Phonon's Role

As discussed in Section 2.1, optical near-field probes, whose tips are sharpened to a few nanometers, can generate a light field localized around the apex of the same order. The spatial localization is, of course, independent of the wavelength of incident light, and the size of the localization is much smaller than the wavelength. In fabricating nanophotonic devices [8,47], [67–69] with such probes, for example, it is critical to control the size and position of the nanostructures, which requires efficient control and manipulation of the localization of light fields. If one could control and manipulate the localization of light field at will, one would necessarily obtain more efficient and functional probes with higher precision, which will be applicable to predict quantum phenomena. It is true not only in a probe system, but also in an optical near-field problem, in general. In these respects it is very important to clarify the mechanism of spatial localization of optical near fields on a nanometer scale.

Experiments on photodissociation of diethylzinc (DEZn) and zinc-bis (acethlacetonate) or Zn(acac)$_2$ molecules and deposition of Zn atoms using an optical near field have been conducted for nanostructure fabrication, as will be discussed later. The experimental results show that the molecules illuminated by the optical near field are dissociated even if the energy of incident light is lower than the dissociation energy, which is impossible when a far field with the same energy and intensity is used. A simple analysis indicates that data cannot be explained by conventional theories based

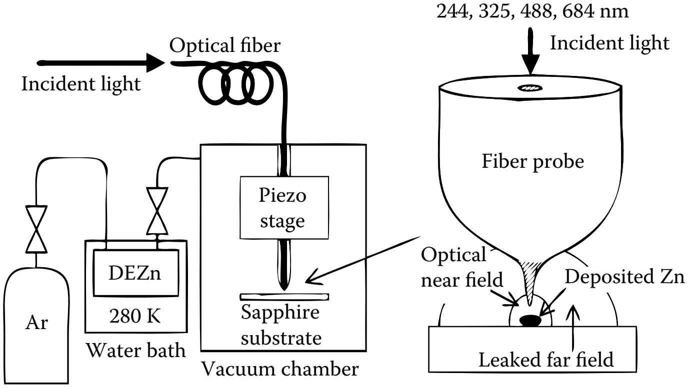

**FIGURE 2.21**
Experimental setup for optical near-field chemical vapor deposition (NFO CVD). The DEZn bottle and CVD chamber were kept at 7 and 25 degrees C, respectively, to prevent the condensation of DEZn on the sapphire substrate. During deposition, the partial pressure of DEZn was 100 mTorr and the total pressure in the chamber was 8 Torr.

on the Franck-Condon principle* or the adiabatic approximation for nuclear motions in a molecule, and suggests that phonons in an optically excited probe system might assist the molecular dissociation process in a nonadiabatic way [60,61,71]. In this situation, it is necessary to study the photon-phonon interaction as well as the photon-electronic excitation interaction in a nanometer space, and to clarify the phonon's role in the nanometric optical near-field probe system, or more generally in light-matter interacting system on a nanometer scale. Then a quantum theoretical approach is appropriate to describe an interacting system of photon and matter (electronic excitation and phonon) fields. It will allow us not only to understand an elementary process of photochemical reactions with optical near fields, but also to explore phonon's role in nanostructures interacting with localized photon fields.

In this subsection we review the nanofabrication technique using the optical near field, and discuss the unique feature in the results of photodissociation experiments, using a simple model (exciton-phonon polariton (EPP) model).

### *Photodissociation of Molecules—Experimental*

As schematically illustrated in Figure 2.21, optical near-field chemical vapor deposition (NFO-CVD) is used to fabricate a nanometer-scale structure

---

* It takes into account in an intuitively clear way the fact that the electronic motions are rapid in comparison to the nuclear motions: during an electronic transition, the position and velocity of the nuclear coordinates will thus not change noticeably, and thus electronic transitions maintain the internuclear distance. By the electronic selection rules, transitions between vibrational levels in a ground state of a molecule are prohibited.

while controlling position and size [58,72]. Incident laser light is introduced into an optical near-field probe, that is, a glass fiber that is chemically etched to have a nanometric sized apex without metal coating usually employed. The propagating far field is generated by light leaking through the circumference of the fiber, while the optical near field is mainly generated at the apex. This allows us to investigate the deposition by an optical near field and far field simultaneously. The separation between the fiber probe and the sapphire (0001) substrate is kept within a few nanometers by shear-force feedback control. By appropriately selecting reactant molecules to be dissociated, NFO-CVD is applicable to various materials such as metals, semiconductors, and insulators. In the following, however, we concentrate on diethylzinc (DEZn) and zinc-bis (acetylacetonate) ($Zn(acac)_2$) as reactant molecules, at 70–100 mTorr at room temperature. In order to investigate the mechanism of the photochemical process, deposition rates depending on photon energy and intensity have been measured with several laser sources: for DEZn molecules,

- the second harmonic of an $Ar^+$ laser ($\hbar\omega = 5.08$ eV, corresponding wavelength $\lambda = 244$ nm), whose energy is close to the electronic excitation energy (5 eV) of a DEZn molecule.
- an He-Cd laser ($\hbar\omega = 3.81$ eV, corresponding wavelength $\lambda = 325$ whose energy is close to $E_{abs} \sim 4.13$ eV[73,74], corresponding to the energy of the absorption band edge.
- an $Ar^+$ laser ($\hbar\omega = 2.54$ eV, corresponding wavelength $\lambda = 488$ whose energy is larger than the dissociation energy of the molecule (2.26 eV), but much smaller than the electronic excitation energy and $E_{abs}$.
- a diode laser ($\hbar\omega = 1.81$ eV, corresponding wavelength $\lambda = 684$ whose energy is smaller than both the dissociation and electronic excitation energies, as well as $E_{abs}$.

and for $Zn(acac)_2$ molecules

- an $Ar^+$ laser $\hbar\omega = 2.71$ eV, corresponding wavelength $\lambda = 457$ nm), whose energy is much smaller than the electronic excitation energy and $E_{abs} \sim 5.17$ eV.

Shear-force topographical images are shown in Figure 2.22 after NFO-CVD at photon energies listed earlier. In conventional CVD using a propagating light, photon energy must be higher than $E_{abs}$ because dissociative molecules should be excited from the ground state to an excited electronic state, according to the adiabatic approximation [70,75]. In contrast, even if photon energy less than $E_{abs}$ is employed in NFO-CVD, the deposition of Zn dots are observed on the substrate just below the apex of the probe used. Much more interested, photons with less energy than the dissociation energy can resolve both DEZn and $Zn(acac)_2$ molecules into composite atoms and

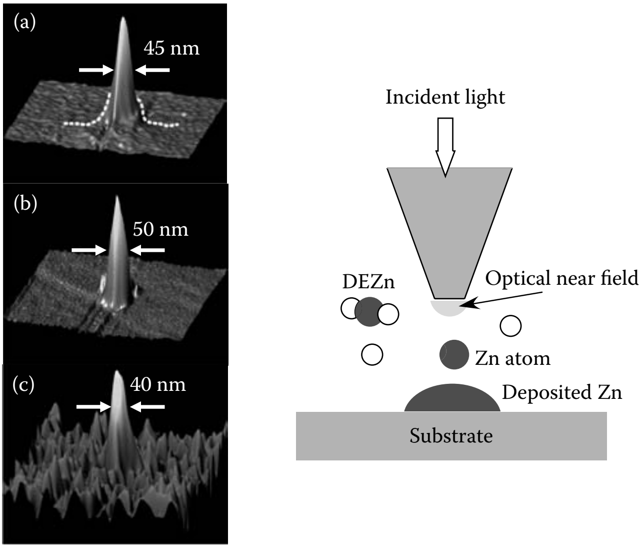

**FIGURE 2.22**
Schematic drawing of NFO-CVD and experimental results. Incident photon energies used are (a) 3.81 eV, (b) 2.54 eV, and (c) 1.81 eV.

deposit them as nanometric dots [60,71]. One possibility inferred from the results is a multiple photon absorption process, which is negligibly small because the optical power density used in the experiment was less than 10 kW/cm$^2$ that is too low for the process. The other possibility is a multiple step transition via an excited molecular vibrational level that is forbidden by the Frank-Condon principle, but allowed in a nonadiabatic process. In order to clarify the unique feature of NFO-CVD, we will give a simple model to discuss the process later.

### EPP Model

We consider a quasiparticle (exciton-phonon polariton) model as a simple model of an optically excited probe system, in order to investigate the physical mechanisms of the chemical vapor deposition using an optical near field (NFO-CVD) [61]. We assume that exciton-phonon polaritons, the quanta of which are transferred from the optical near-field probe tip to both gas and adsorbed molecules, are created at the apex of the optical near-field probe. Here it should be noted that the quasi-particle transfer is valid only if the molecules are very close to the probe tip because the optical near field is highly localized near the probe tip, which has been discussed in Section 2.1 and will be discussed later. The optical near field generated on the nanometric probe tip, which is a highly mixed state with material excitation rather than the propagating light field [6,7], is described in terms of the following model Hamiltonian:

$$\begin{aligned}\hat{H} &= \sum_{\vec{p}} \hbar \left\{ \omega_{\vec{p}} \hat{a}_{\vec{p}}^{\dagger} \hat{a}_{\vec{p}} + \omega_{\vec{p}}^{\mathrm{ex}} \hat{b}_{\vec{p}}^{\dagger} \hat{b}_{\vec{p}} + \frac{i\Omega_{\mathrm{c}}}{2} \left( \hat{a}_{\vec{p}}^{\dagger} \hat{b}_{\vec{p}} - \hat{b}_{\vec{p}}^{\dagger} \hat{a}_{\vec{p}} \right) \right\} \\ &\quad + \sum_{\vec{p}} \hbar \Omega_{\vec{p}} \hat{c}_{\vec{p}}^{\dagger} \hat{c}_{\vec{p}} + \sum_{\vec{p},\vec{q}} \left[ i\hbar M(\vec{p}-\vec{q}) \hat{b}_{\vec{p}}^{\dagger} \hat{b}_{\vec{q}} \left\{ \hat{c}_{\vec{p}-\vec{q}} + \hat{c}_{\vec{q}-\vec{p}}^{\dagger} \right\} + \mathrm{h.c.} \right] \\ &= \sum_{\vec{p}} \hbar \omega_{\vec{p}}^{\mathrm{pol}} \hat{B}_{\vec{p}}^{\dagger} \hat{B}_{\vec{p}} + \sum_{\vec{p}} \hbar \Omega_{\vec{p}} \hat{c}_{\vec{p}}^{\dagger} \hat{c}_{\vec{p}} \\ &\quad + \sum_{\vec{p},\vec{q}} \left[ i\hbar M'(\vec{p}-\vec{q}) \hat{B}_{\vec{p}}^{\dagger} \hat{B}_{\vec{q}} \left\{ \hat{c}_{\vec{p}-\vec{q}} + \hat{c}_{\vec{q}-\vec{p}}^{\dagger} \right\} + \mathrm{h.c.} \right], \end{aligned} \tag{2.190}$$

where the creation (annihilation) operators for a photon, an exciton (a quasiparticle for an electronic polarization field), a renormalized phonon (whose physical meanings will be discussed later), and an exciton polariton are respectively denoted by $\hat{a}_{\vec{p}}^{\dagger}\,(\hat{a}_{\vec{p}})$, $\hat{b}_{\vec{p}}^{\dagger}\,(\hat{b}_{\vec{p}})$, $\hat{c}_{\vec{p}}^{\dagger}\,(\hat{c}_{\vec{p}})$, and $\hat{B}_{\vec{p}}^{\dagger}\,(\hat{B}_{\vec{p}})$, and their frequencies are $\omega_{\vec{p}}$, $\omega_{\vec{p}}^{\mathrm{ex}}$, $\Omega_{\vec{p}}$, and $\omega_{\vec{p}}^{\mathrm{pol}}$, respectively. The subscripts $\vec{p}$ and $\vec{q}$ indicate the momenta of the relevant particle in the momentum representation such as a photon, an exciton, a renormalized phonon, an exciton polariton, or an exciton-phonon polariton. Each coupling between a photon and an exciton, a phonon and an exciton, and an exciton polariton and a phonon is designated as $\Omega_{\mathrm{c}}$, $M(\vec{p}-\vec{q})$, and $M'(\vec{p}-\vec{q})$ respectively. The first line of this description expresses the Hamiltonian for a photon-exciton interacting system and is transformed into the exciton-polariton representation as shown in the third line [25], whereas the second line represents the Hamiltonian for a phonon-exciton interacting system. Note that electronic excitations near the probe tip, driven by photons incident into the fiber probe, cause mode-mode couplings or anharmonic couplings of phonons, and that they are taken into account as a renormalized phonon; therefore, multiple phonons as coherently squeezed phonons in the original representation can interact with an exciton or an exciton polariton simultaneously. In the model, quasiparticles (exciton-phonon polaritons) in bulk material (glass fiber) are approximately used, and thus their states are specified by the momentum. Strictly speaking, momentum is not a good quantum number to specify the quasiparticle states at the apex of the probe, from the symmetry consideration, and they should be a superposition of such momentum-specified states with different weights. Instead of this kind of treatment, we simply assume that the quasiparticles specified by the momentum are transferred to a vapor or adsorbed molecule that is located near the probe tip, utilizing highly spatial localization of the optical near field to be discussed in detail later.

Now we assume that exciton polaritons near the probe tip are expressed in the mean field approximation as

$$\left\langle \hat{B}_{\vec{k}_0}^{\dagger} \right\rangle = \langle \hat{B}_{\vec{k}_0} \rangle = \sqrt{\frac{I_0(\omega_0)V}{\hbar\omega_0 d}}. \tag{2.191}$$

Here $I_0(\omega_0)$ is the photon intensity inside the probe tip with frequency $\omega_0$ and momentum $\hbar\vec{k}_0$, and $V$ represents the volume to be considered while the probe tip size is denoted by *d*. Using the unitary transformation as

$$\begin{pmatrix}\hat{B}_{\vec{p}}\\ \hat{c}_{\vec{p}-\vec{k}_0}\end{pmatrix}=\begin{pmatrix} iv'_{\vec{p}} & u'_{\vec{p}}\\ u'_{\vec{p}} & iv'_{\vec{p}}\end{pmatrix}\begin{pmatrix}\hat{\xi}_{(-)\vec{p}}\\ \hat{\xi}_{(+)\vec{p}}\end{pmatrix}, \tag{2.192}$$

we can diagonalize the Hamiltonian in the exciton-phonon polariton representation [76] as

$$\begin{aligned}\hat{H}&=\sum_{\vec{p}}\hbar\omega_{\vec{p}}^{\mathrm{pol}}\hat{B}_{\vec{p}}^{\dagger}\hat{B}_{\vec{p}}+\sum_{\vec{p}}\hbar\Omega_{\vec{p}}\hat{c}_{\vec{p}}^{\dagger}\hat{c}_{\vec{p}}\\ &\quad+\sum_{\vec{p}}\left[i\hbar\sqrt{\frac{I_0(\omega_0)V}{\hbar\omega_0 d}}M'(\vec{p}-\vec{k}_0)\left\{\hat{B}_{\vec{p}}^{\dagger}\hat{c}_{\vec{p}-\vec{k}_0}+\hat{B}_{\vec{p}}\hat{c}_{\vec{p}-\vec{k}_0}^{\dagger}\right\}+\mathrm{h.c.}\right]\\ &=\sum_{\vec{p}}\sum_{j=(\pm)}\hbar\omega(\vec{p})\hat{\xi}_{j\vec{p}}^{\dagger}\hat{\xi}_{j\vec{p}}\end{aligned} \tag{2.193}$$

where the creation (annihilation) operator for an exciton-phonon polariton and the frequency are denoted by $\hat{\xi}_{j\vec{p}}^{\dagger}(\hat{\xi}_{j\vec{p}})$ and $\omega(\vec{p})$, respectively. The suffix (–) or (+) indicates the lower or the upper branch of the exciton-phonon polariton. The transformation coefficients $u'_{\vec{p}}$ and $v'_{\vec{p}}$ are given by

$$u'^2_{\vec{p}}=\frac{1}{2}\left(1+\frac{\Delta}{\sqrt{\Delta^2+(2Q)^2}}\right),\; v'^2_{\vec{p}}=\frac{1}{2}\left(1-\frac{\Delta}{\sqrt{\Delta^2+(2Q)^2}}\right), \tag{2.194}$$

where the detuning between an exciton polariton and a phonon is denoted by $\Delta\equiv\omega_{\vec{p}}^{\mathrm{pol}}-\Omega_{\vec{p}-\vec{k}_0}$, and the effective coupling constant is expressed as $Q\equiv\sqrt{I_0(\omega_0)/\hbar\omega_0 d}\,M'(\vec{p}-\vec{k}_0)$ Therefore, in this model, a molecule located near the probe tip does absorb not simple photons but exciton-phonon polaritons whose energies are transferred to the molecule, which excite molecular vibrations as well as electronic transitions. In the following sections, we will discuss how phonons work in the optically excited probe system in detail.

### 2.3.3 Lattice Vibration in Pseudo One-Dimensional System

Before discussing the optically excited probe system, lattice vibrations in a pseudo one-dimensional system are briefly described, and its quantization is outlined. We also examine the effects of impurities or defects in such a system to show that the localized vibration modes exist as eigenmodes, and those energies are higher than those of delocalized ones.

Owing to the progress in nanofabrication, the apexes of optical near-field probes are sharpened on the order of a few nanometers. In this region, the

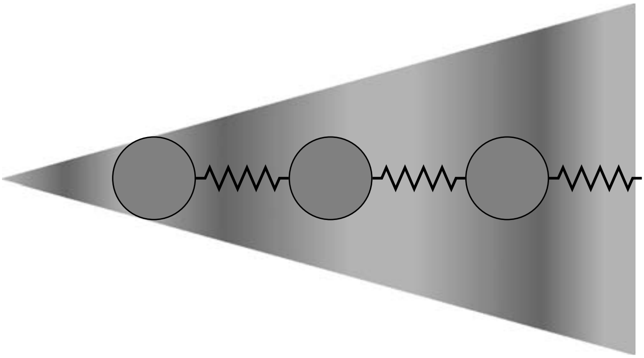

**FIGURE 2.23**
A pseudo one-dimensional system for a near-field optical probe tip.

guiding modes of light field are cut off and visible light cannot propagate in a conventional way. Therefore it is necessary to clarify the interactions among light, induced electronic, and vibrational fields in the nanometer space such as the optically excited probe tip, and the mechanism of localization (delocalization) of light field as a result of self-consistency of those interacting fields. As the first step, we examine the lattice vibrations themselves in this section. Let us assume a pseudo one-dimensional system for the probe tip, as schematically illustrated in Figure 2.23. The system consists of a finite number ($N$) of atoms or molecules, which will be representatively called molecules. Each molecule is located at a discrete site and is connected with the nearest-neighbor molecules by springs. The size of each molecule and the spacing between the molecules depend on how the system is coarse-grained. In any case, the total site number $N$ is finite, and the wave number is not a good quantum number because the system breaks the translational invariance [77]. That is why we begin with the Hamiltonian of the system to analyze vibrational (phonon) modes, instead of the conventional method using the dynamical matrix [78]. By denoting a displacement from an equilibrium point of a molecule by $\vec{x}_i$ and its conjugate momentum by $\vec{p}_i$, the model Hamiltonian* is given by

$$H = \sum_{i=1}^{N} \frac{\vec{p}_i^{\,2}}{2m_i} + \sum_{i=1}^{N-1} \frac{k}{2} (\vec{x}_{i+1} - \vec{x}_i)^2 + \frac{k}{2} \left( \vec{x}_1^{\,2} + \vec{x}_N^{\,2} \right), \tag{2.195}$$

where $m_i$ is the mass of a molecule at site $i$, and $k$ represents the spring constant. Both edges ($i = 1$ and $i = N$) are assumed to be fixed, and longitudinal

---

* In this subsection, the Hamiltonian is not quantum mechanical, but classical, and thus not an operator that is indicated by the hat notation "^."

motions in one-dimension are considered in the following. The equations of motion are determined by the Hamilton equation as

$$\frac{d}{dt}\vec{x}_i = \frac{\partial H}{\partial \vec{p}_i}, \quad \frac{d}{dt}\vec{p}_i = -\frac{\partial H}{\partial \vec{x}_i}. \tag{2.196}$$

If one uses a matrix form defined by

$$M = \begin{pmatrix} m_1 & 0 & \cdots & 0 \\ 0 & m_2 & \vdots & \vdots \\ \vdots & \vdots & \ddots & \vdots \\ 0 & \cdots & \cdots & m_N \end{pmatrix}, \quad \Gamma = \begin{pmatrix} 2 & -1 & \cdots & 0 \\ -1 & 2 & \cdots & \vdots \\ \vdots & \vdots & \ddots & -1 \\ 0 & \cdots & -1 & 2 \end{pmatrix}, \tag{2.197}$$

one can obtain the following compact equations of motion:

$$M\frac{d^2}{dt^2}\vec{x} = -k\Gamma\vec{x}, \tag{2.198}$$

with transpose of the column vector $\vec{x}$ as $\vec{x}^{\mathrm{T}} \equiv (\vec{x}_1, \vec{x}_2, \cdots, \vec{x}_N)$. Multiplying the both hand sides of (198) by $\sqrt{M}^{-1}$ with $(\sqrt{M})_{ij} = \delta_{ij}\sqrt{m_i}$ we have

$$\frac{d^2}{dt^2}\vec{x}' = -k\mathrm{A}\vec{x}', \tag{2.199}$$

where the notation $\vec{x}' = \sqrt{M}\vec{x}$ and $\mathrm{A} = \sqrt{M}^{-1}\Gamma\sqrt{M}^{-1}$ are used. Since it is symmetric, the matrix A can be diagonalized by an orthonormal matrix P as follows:

$$\Lambda = \mathrm{P}^{-1}\mathrm{AP}, \quad \text{or} \quad (\Lambda)_{pq} = \delta_{pq}\frac{\Omega_p^2}{k}. \tag{2.200}$$

Substitution of Eq. (200) into Eq. (199) leads us to equations of motion for a set of harmonic oscillators as

$$\frac{d^2}{dt^2}\vec{y} = -k\Lambda\vec{y}, \quad \text{or} \quad \frac{d^2}{dt^2}\vec{y}_p = -\Omega_p^2\vec{y}_p, \tag{2.201}$$

where $\vec{y}$ is set as $\vec{y} = \mathrm{P}^{-1}\vec{x}'$. There are $N$ normal coordinates to describe the harmonic oscillators, each of which is specified by the mode number $p$. The original spatial coordinates $\vec{x}$ are transformed to the normal coordinates $\vec{y}$ as

$$\vec{x} = \sqrt{M}^{-1}\mathrm{P}\vec{y}, \quad \text{or} \quad \vec{x}_i = \frac{1}{\sqrt{m_i}}\sum_{p=1}^{N}\mathrm{P}_{ip}\vec{y}_p. \tag{2.202}$$

### Quantization of Vibration

In order to quantize the vibration field described by Eq. (261), we first rewrite the Hamiltonian Eq. (195) in terms of normal coordinates $\vec{y}_p$ and conjugate momenta $\vec{\pi}_p$, which should be replaced by the corresponding operators $\hat{\vec{y}}_p$ and $\hat{\vec{\pi}}_p$ to have

$$\hat{H}(\hat{\vec{y}},\hat{\vec{\pi}}) = \sum_{p=1}^{N} \frac{\hat{\vec{\pi}}_p^2}{2} + \sum_{p=1}^{N} \frac{1}{2}\Omega_p^2 \hat{\vec{y}}_p^2. \tag{2.203}$$

Then the commutation relation between $\hat{\vec{y}}_p$ and $\hat{\vec{\pi}}_q$ as

$$\left[\hat{\vec{y}}_p, \hat{\vec{\pi}}_q\right] \equiv \hat{\vec{y}}_p \hat{\vec{\pi}}_q - \hat{\vec{\pi}}_q \hat{\vec{y}}_p = i\hbar\delta_{pq}, \tag{2.204}$$

is imposed for quantization. When we define operators $\hat{b}_p$ and $\hat{b}_p^\dagger$ as

$$\hat{b}_p = \frac{1}{\sqrt{2\hbar\Omega_p}}\left(\hat{\vec{\pi}}_p - i\Omega_p \hat{\vec{y}}_p\right), \tag{2.205a}$$

$$\hat{b}_p^\dagger = \frac{1}{\sqrt{2\hbar\Omega_p}}\left(\hat{\vec{\pi}}_p + i\Omega_p \hat{\vec{y}}_p\right), \tag{2.205b}$$

they satisfy the boson commutation relation

$$\left[\hat{b}_p, \hat{b}_q^\dagger\right] \equiv \hat{b}_p \hat{b}_q^\dagger - \hat{b}_q^\dagger \hat{b}_p = \delta_{pq}. \tag{2.206}$$

The Hamiltonian describing the lattice vibration of the system, (203), can then be rewritten as

$$\hat{H}_{\text{phonon}} = \sum_{p=1}^{N} \hbar\Omega_p \left(\hat{b}_p^\dagger \hat{b}_p + \frac{1}{2}\right), \tag{2.207}$$

and it follows that $\hat{b}_p(\hat{b}_p^\dagger)$ is the annihilation (creation) operator of a phonon with energy of $\hbar\Omega_p$ specified by the mode number *p*.

### Vibration Modes: Localized vs Delocalized

In this subsection, we examine the effects of impurities or defects in the system. When all the molecules are identical, that is, $m_i = m$, the Hamiltonian Eq. (195), or the matrix A can be diagonalized in terms of the orthonormal matrix P whose elements are given by

$$\mathrm{P}_{ip} = \sqrt{\frac{2}{N+1}} \sin\left(\frac{ip}{N+1}\pi\right), \quad (1 \le i, p \le N), \tag{2.208}$$

and the eigenfrequencies squared are obtained as follows:

$$\Omega_p^2 = 4\frac{k}{m}\sin^2\left[\frac{p}{2(N+1)}\pi\right]. \tag{2.209}$$

In this case, all the vibration modes are delocalized, that is, they are spread over the whole system. By contrast, if there are some doped impurities or defects with different mass, the vibration modes highly depend on geometrical configuration and mass ratio of the impurities to the others. In particular, localized vibration modes manifest themselves when the mass of the impurities is lighter than that of the others, where vibrations with higher frequencies are localized around the impurity sites [79–82].

Figures 2.24(a) and (b) illustrate that the localized vibration modes exist as eigenmodes in the one-dimensional system caused by the doped molecules with different mass in the chain, and eigenenergies of localized modes are higher than those of delocalized ones. In Figure 2.24(a), phonon energies are plotted as a function of the mode number when the total number of sites is 30. The rectangles represent the eigenenergies of phonons in the case of no impurities, and the circles show those in the case of six impurities, where the doped molecules are located at site 5, 9, 18, 25, 26, 27. It follows from the figure that phonon energies of the localized modes are higher than those of the delocalized modes. The mass ratio of the doped molecules to the others is 1/2, and the parameter $\hbar\sqrt{k/m} = 22.4$ meV is used. Figure 2.24(b) shows the vibration amplitude as a function of the site number. The solid and dashed curves represent two localized modes with the highest and the next highest energies of phonons, respectively, while the dotted curve illustrates the delocalized mode with the lowest energy. In the localized modes, the vibration amplitudes are localized around the impurity sites.

In the next section, we will discuss the interactions between photons and inhomogeneous phonon fields on the nanometer scale, since we have found inhomogeneous phonon fields in the one-dimensional system with impurities.

### 2.3.4 Optically Excited Probe System and Phonons

In this section, we consider a simple model for a pseudo one-dimensional optical near-field probe system to discuss the mechanism of photon localization in space as well as phonon's role. In order to focus on the photon-phonon interaction, the interacting part between photon and electronic excitation is first expressed in terms of a polariton, and is called a photon in the model. Then the model Hamiltonian, which describes the photon and phonon interacting system, is presented. Using the Davydov transformation [77,83,84], we rewrite the Hamiltonian in terms of quasiparticles. On the basis of the Hamiltonian, we present numerical results on spatial distribution of photons, and discuss the mechanism of photon localization caused by phonons.

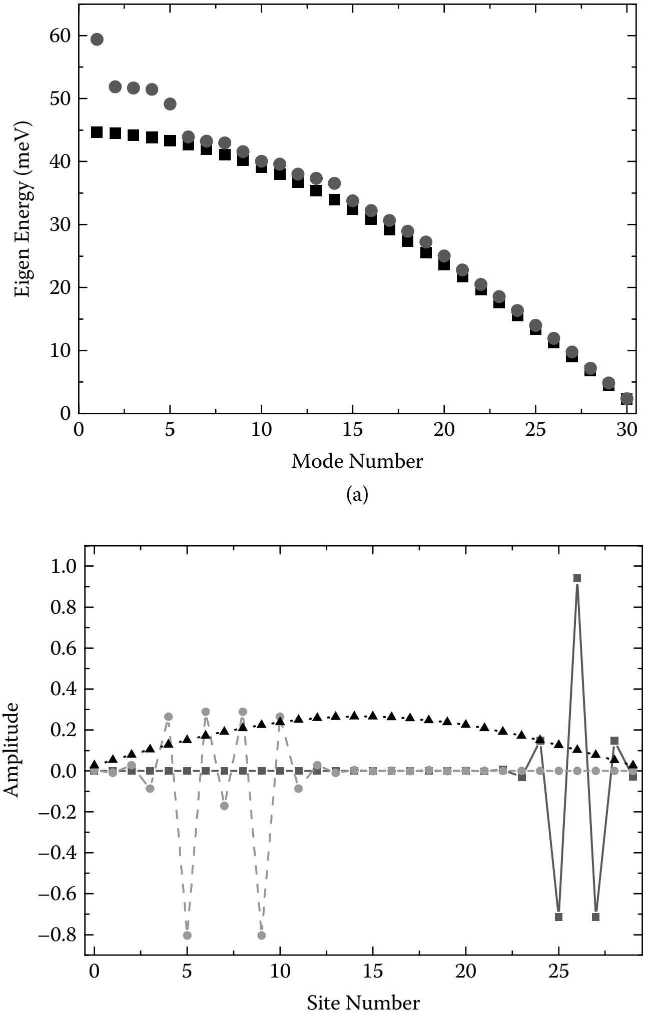

(a)

(b)

**FIGURE 2.24**
(a) Eigen energies of all vibration modes with/without impurities (depicted with the filled circles/rectangles), in the case of $N = 30$, and (b) the first and second localized vibration modes and the lowest delocalized vibration mode (represented by the solid, dashed, and dotted curves). Impurities are doped at site 5, 9, 18, 25, 26 and 27. The mass ratio of the host molecules to the impurities is set as 1 to 0.5, and $\hbar\sqrt{k/m} = 22.4$ meV is used for both (a) and (b).

## *Model Hamiltonian*

We consider an optical near-field probe schematically shown in Figure 2.23, as a system where light interacts with both phonons and electrons in the probe on a nanometer scale. Here the interaction of a photon and an electronic excitation is assumed to be expressed in terms of a polariton basis [6,7] as discussed earlier, and is hereafter called a photon so that a special attention is paid on the photon-phonon interaction. The system is simply modeled as a one-dimensional atomic or molecular chain coupled with photon and phonon fields. The chain consists of a finite *N* molecules (representatively called) each of which is located at a discrete point (called a molecular site) whose separation represents a characteristic scale of the near-field system. Photons are expressed in the site representation and can hop to the nearest neighbor sites [11] because of the short-range interaction nature of the optical near fields (see Eq. (1) in Section 2.1).

The Hamiltonian for this model is given by

$$\begin{aligned}\hat{H} &= \sum_{i=1}^{N} \hbar\omega \hat{a}_i^\dagger \hat{a}_i \\ &+ \left\{ \sum_{i=1}^{N} \frac{\hat{p}_i^2}{2m_i} + \sum_{i=1}^{N-1} \frac{k}{2}(\hat{x}_{i+1} - \hat{x}_i)^2 + \sum_{i=1,N} \frac{k}{2}\hat{x}_i^2 \right\} \\ &+ \sum_{i=1}^{N} \hbar\chi \hat{a}_i^\dagger \hat{a}_i \hat{x}_i + \sum_{i=1}^{N-1} \hbar J\left(\hat{a}_i^\dagger \hat{a}_{i+1} + \hat{a}_{i+1}^\dagger \hat{a}_i\right),\end{aligned} \tag{2.210}$$

where $\hat{a}_i^\dagger$ and $\hat{a}_i$ correspondingly denote the creation and annihilation operators of a photon with energy of $\hbar\omega$ at site *i* in the chain, $\hat{x}_i$ and $\hat{p}_i$ represent the displacement and conjugate momentum operators of the vibration, respectively. The mass of a molecule at site *i* is designated by $m_i$, and each molecule is assumed to be connected by springs with spring constant *k*. The third and the fourth terms in Eq. (210) stand for the photon-vibration interaction with coupling constant $\chi$ and the photon hopping with hopping constant *J*, respectively.

After the vibration field is quantized in terms of phonon operators of mode *p* and frequency $\Omega_p$, $\hat{b}_p^\dagger$ and $\hat{b}_p$, the Hamiltonian Eq. (210) can be rewritten as

$$\begin{aligned}\hat{H} &= \sum_{i=1}^{N} \hbar\omega \hat{a}_i^\dagger \hat{a}_i + \sum_{p=1}^{N} \hbar\Omega_p \hat{b}_p^\dagger \hat{b}_p \\ &+ \sum_{i=1}^{N}\sum_{p=1}^{N} \hbar\chi_{ip} \hat{a}_i^\dagger \hat{a}_i \left(\hat{b}_p^\dagger + \hat{b}_p\right) \\ &+ \sum_{i=1}^{N-1} \hbar J\left(\hat{a}_i^\dagger \hat{a}_{i+1} + \hat{a}_{i+1}^\dagger \hat{a}_i\right),\end{aligned} \tag{2.211}$$

with the coupling constant $\chi_{ip}$ of a photon at site *i* and a phonon of mode *p*. This site-dependent coupling constant $\chi_{ip}$ is related to the original coupling constant $\chi$ as

$$\chi_{ip} = \chi \mathrm{P}_{ip} \sqrt{\frac{\hbar}{2m_i\Omega_p}}, \tag{2.212}$$

and the creation and annihilation operators of a photon and a phonon satisfy the boson commutation relation as follows:

$$\begin{gathered}\left[\hat{a}_i,\hat{a}_j^\dagger\right]=\delta_{ij},\quad \left[\hat{b}_p,\hat{b}_q^\dagger\right]=\delta_{pq},\\ [\hat{a}_i,\hat{a}_j]=\left[\hat{a}_i^\dagger,\hat{a}_j^\dagger\right]=[\hat{b}_p,\hat{b}_q]=\left[\hat{b}_p^\dagger,\hat{b}_q^\dagger\right]=0,\\ [\hat{a}_i,\hat{b}_p]=\left[\hat{a}_i,\hat{b}_p^\dagger\right]=\left[\hat{a}_i^\dagger,\hat{b}_p\right]=\left[\hat{a}_i^\dagger,\hat{b}_q^\dagger\right]=0.\end{gathered} \tag{2.213}$$

The Hamiltonian Eq. (211), which describes the model system, is not easily handled because of the third order of the operators in the interaction term. To avoid the difficulty, this direct photon-phonon interaction term in Eq. (211) will be eliminated by the Davydov transformation in the following subsection.

### *Davydov Transformation*

Before going into the explicit expression, we discuss a unitary transformation $\hat{U}$ generated by an anti-Hermitian operator $\hat{S}$ defined as

$$\hat{U}\equiv\exp(\hat{S}),\quad \text{with}\quad \hat{S}^\dagger=-\hat{S}, \tag{2.214a}$$

and

$$\hat{U}^\dagger=\hat{U}^{-1}. \tag{2.214b}$$

Suppose a Hamiltonian $\hat{H}$ that consists of a diagonalized part $\hat{H}_0$ and a nondiagonal interaction part $\hat{V}$ as

$$\hat{H}=\hat{H}_0+\hat{V}. \tag{2.215}$$

Transforming the Hamiltonian in Eq. (215) as

$$\tilde{H}\equiv\hat{U}\hat{H}\hat{U}^\dagger=\hat{U}\hat{H}\hat{U}^{-1}, \tag{2.216}$$

we have

$$\begin{aligned}\tilde{H}&=\hat{H}+[\hat{S},\hat{H}]+\frac{1}{2}[\hat{S},[\hat{S},\hat{H}]]+\cdots\\ &=\hat{H}_0+\hat{V}+[\hat{S},\hat{H}_0]+[\hat{S},\hat{V}_0]+\frac{1}{2}[\hat{S},[\hat{S},\hat{H}_0]]+\cdots.\end{aligned} \tag{2.217}$$

If the interaction $\hat{V}$ can be perturbative, and if the operator $\hat{S}$ is chosen so that the second and the third terms in Eq. (217) are canceled out as

$$\hat{V}=-[\hat{S},\hat{H}_0], \tag{2.218}$$

the Hamiltonian Eq. (217) is rewritten as

$$\tilde{H} = \hat{H}_0 - \frac{1}{2}[\hat{S},[\hat{S},\hat{H}_0]] + \cdots, \tag{2.219}$$

and can be diagonalized within the first order of $\hat{V}$.

Now we apply this discussion to the model Hamiltonian Eq. (211),

$$\hat{H}_0 = \sum_{i=1}^{N} \hbar\omega \hat{a}_i^\dagger \hat{a}_i + \sum_{p=1}^{N} \hbar\Omega_p \hat{b}_p^\dagger \hat{b}_p, \tag{2.220a}$$

$$\hat{V} = \sum_{i=1}^{N}\sum_{p=1}^{N} \hbar\chi_{ip} \hat{a}_i^\dagger \hat{a}_i \left(\hat{b}_p^\dagger + \hat{b}_p\right), \tag{2.220b}$$

tentatively neglecting the hopping term. Assuming the anti-Hermitian operator $\hat{S}$ as

$$\hat{S} = \sum_i \sum_p f_{ip} \hat{a}_i^\dagger \hat{a}_i \left(\hat{b}_p^\dagger - \hat{b}_p\right), \tag{2.221}$$

we can determine $f_{ip}$ from Eq. (218) as follows:

$$f_{ip} = \frac{\chi_{ip}}{\Omega_p}. \tag{2.222}$$

This operator form of $\hat{S}$ leads us to not the perturbative but the exact transformation of the photon and phonon operators as

$$\hat{\alpha}_i^\dagger \equiv \hat{U}^\dagger \hat{a}_i^\dagger \hat{U} = \hat{a}_i^\dagger \exp\left\{-\sum_{p=1}^{N} \frac{\chi_{ip}}{\Omega_p}\left(\hat{b}_p^\dagger - \hat{b}_p\right)\right\}, \tag{2.223a}$$

$$\hat{\alpha}_i \equiv \hat{U}^\dagger \hat{a}_i \hat{U} = \hat{a}_i \exp\left\{\sum_{p=1}^{N} \frac{\chi_{ip}}{\Omega_p}\left(\hat{b}_p^\dagger - \hat{b}_p\right)\right\}, \tag{2.223b}$$

$$\hat{\beta}_p^\dagger \equiv \hat{U}^\dagger \hat{b}_p^\dagger \hat{U} = \hat{b}_p^\dagger + \sum_{i=1}^{N} \frac{\chi_{ip}}{\Omega_p} \hat{a}_i^\dagger \hat{a}_i, \tag{2.223c}$$

$$\hat{\beta}_p \equiv \hat{U} \hat{b}_p \hat{U}^\dagger = \hat{b}_p + \sum_{i=1}^{N} \frac{\chi_{ip}}{\Omega_p} \hat{a}_i^\dagger \hat{a}_i. \tag{2.223d}$$

These transformed operators can be regarded as the creation and annihilation operators of quasiparticles—dressed photons and phonons—that satisfy the same boson commutation relations as those of photons and phonons before the transformation:

$$\left[\hat{\alpha}_i, \hat{\alpha}_j^\dagger\right] = \hat{U}^\dagger[\hat{a}_i, \hat{a}_j]\,\hat{U} = \delta_{ij}, \tag{2.224a}$$

$$\left[\hat{\beta}_p, \hat{\beta}_q^\dagger\right] = \hat{U}^\dagger\left[\hat{b}_p, \hat{b}_q^\dagger\right]\hat{U} = \delta_{pq}. \tag{2.224b}$$

Using the quasiparticle operators, we can rewrite the Hamiltonian Eq. (211) as

$$\begin{aligned}\hat{H} = &\sum_{i=1}^{N} \hbar\omega\hat{\alpha}_i^\dagger\hat{\alpha}_i + \sum_{p=1}^{N} \hbar\Omega_p\hat{\beta}_p^\dagger\hat{\beta}_p - \sum_{i=1}^{N}\sum_{j=1}^{N}\sum_{p=1}^{N} \frac{\hbar\chi_{ip}\chi_{jp}}{\Omega_p}\hat{\alpha}_i^\dagger\hat{\alpha}_i\hat{\alpha}_j^\dagger\hat{\alpha}_j \\ &+ \sum_{i=1}^{N-1} \hbar\left(\hat{J}_i\hat{\alpha}_i^\dagger\hat{\alpha}_{i+1} + \hat{J}_i^\dagger\hat{\alpha}_{i+1}^\dagger\hat{\alpha}_i\right),\end{aligned} \tag{2.225}$$

with

$$\hat{J}_i = J\exp\left\{\sum_{p=1}^{N} \frac{(\chi_{ip} - \chi_{i+1p})}{\Omega_p}\left(\hat{\beta}_p^\dagger - \hat{\beta}_p\right)\right\}, \tag{2.226}$$

where it is noted that the direct photon-phonon coupling term has been eliminated while the quadratic form $\hat{N}_i\hat{N}_j$ with the number operator of $\hat{N}_i = \hat{\alpha}_i^\dagger\hat{\alpha}_i$ has emerged as well as the site-dependent hopping operator Eq. (226). The number states of quasiparticles are thus eigenstates of each terms of the Hamiltonian Eq. (225), except the last term that represents the higher order effect of photon-phonon coupling through the dressed photon hopping. Therefore it is a more appropriate form to discuss the phonon's effect on photon's behavior as localization.

### Quasiparticle and Coherent State

In the previous section, we have transformed the original Hamiltonian by the Davydov transformation. In order to grasp the physical meanings of the quasiparticles introduced earlier, the creation operator $\hat{\alpha}_i^\dagger$ is applied to the vacuum state $|0\rangle$. Then it follows from Eq. (223a)

$$\begin{aligned}\hat{\alpha}_i^\dagger\,|0\rangle &= \hat{a}_i^\dagger\exp\left\{-\sum_{p=1}^{N}\frac{\chi_{ip}}{\Omega_p}\left(\hat{b}_p^\dagger - \hat{b}_p\right)\right\}|0\rangle \\ &= \hat{a}_i^\dagger\exp\left\{-\sum_{p=1}^{N}\frac{1}{2}\left(\frac{\chi_{ip}}{\Omega_p}\right)^2\right\}\exp\left\{-\frac{\chi_{ip}}{\Omega_p}\hat{b}_p^\dagger\right\}|0\rangle,\end{aligned} \tag{2.227}$$

where a photon at site $i$ is associated with phonons in coherent state, that is, a photon is dressed by an infinite number of phonons. This corresponds to the fact that an optical near field is generated from a result of interactions between the photon and matter fields.

When $\hat{\beta}_p^\dagger$ is applied to the vacuum state $|0\rangle$, we have

$$\hat{\beta}_p^\dagger |0\rangle = \hat{b}_p^\dagger |0\rangle, \tag{2.228}$$

and it is expressed by only the bare phonon operator (before the transformation) in the same $p$ mode. Therefore we mainly focus on the quasiparticle expressed by $\hat{\alpha}_i^\dagger$, $\hat{\alpha}_i$ in the following section. Note that it is valid only if the bare photon number (the expectation value of $\hat{a}_i^\dagger \hat{a}_i$ is not so large that the fluctuation is more important than the bare photon number. In other words, the model we are considering is suitable for discussing the quantum nature of a few photons in an optically excited probe system.

The coherent state of phonons is not an eigenstate of the Hamiltonian, and thus the number of phonons as well as energy is fluctuating. This fluctuation allows incident photons into the probe system to excite phonon fields. When all the phonon fields are in the vacuum at time $t = 0$, the excitation probability $P(t)$ that a photon incident on site $i$ in the model system excites the phonon mode $p$ at time $t$ is given by

$$P(t) = 1 - \exp\left\{2\left(\frac{\chi_{ip}}{\Omega_p}\right)^2 [\cos(\Omega_p t) - 1]\right\}, \tag{2.229}$$

where the photon-hopping term is neglected for simplicity. The excitation probability oscillates at frequency of $2\pi/\Omega_p$, and has the maximum value at $t = \pi/\Omega_p$. The frequencies of the localized phonon modes are higher than those of the delocalized ones, and the localized modes at the earlier time are excited by the incident photons.

Figure 2.25 shows the temporal evolution of the excitation probability $P_{p_0}(t)$ calculated from

$$\begin{aligned} P_{p_0}(t) &= \left[1 - \exp\left\{2\left(\frac{\chi_{ip_0}}{\Omega_{p_0}}\right)^2 [\cos(\Omega_{p_0} t) - 1]\right\}\right] \\ &\quad \times \exp\left\{\sum_{p \neq p_0} 2\left(\frac{\chi_{ip}}{\Omega_p}\right)^2 [\cos(\Omega_p t) - 1]\right\}, \end{aligned} \tag{2.230}$$

where a specific phonon mode $p_0$ is excited while other modes are in the vacuum state. In Figure 2.25, the solid curve represents the probability that a localized phonon mode is excited as the $p_0$ mode, while the dashed curve illustrates how the lowest phonon mode is excited as the $p_0$ mode. It follows

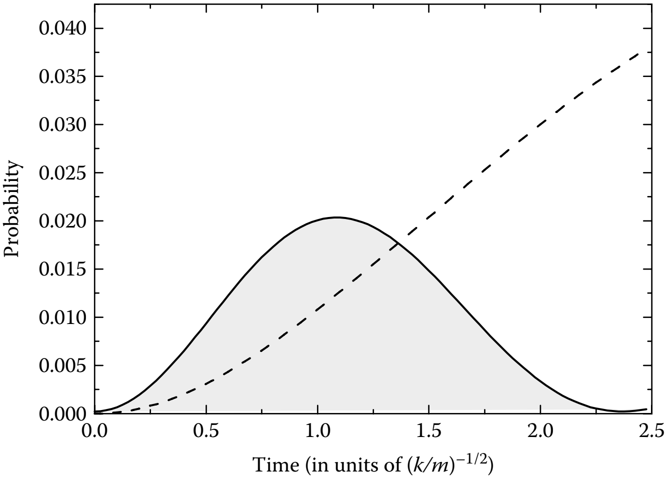

**FIGURE 2.25**
Temporal evolution of the excitation probability of a localized (delocalized) phonon mode that is represented by the solid (dashed) curve. The system is initially excited by a photon at the impurity site 26. The coupling constant $\chi = 10.0\ \text{fs}^{-1}\text{nm}^{-1}$ and the parameter $\hbar\sqrt{k/m} = 22.4$ meV are used, while other parameters are the same as those in Figure 2.24.

from the figure that the localized phonon mode is dominantly excited at the earlier time.

### 2.3.5 Localization Mechanism of Dressed Photons

In this section, we discuss how phonons contribute to the spatial distribution of photons in the pseudo one-dimensional system under consideration. When there are no interactions between photons and phonons, the frequency and hopping constant are equal at all sites, and thus the spatial distribution of photons are symmetric. It means that no photon localization occurs at any specific site. However, if there are any photon-phonon interactions, spatial inhomogeneity or localization of phonons affects the spatial distribution of photons. On the basis of the Hamiltonian Eq. (225), we analyze the contribution from the diagonal and off-diagonal parts in order to investigate the localization mechanism of photons.

#### *Contribution from the Diagonal Part*

Let us rewrite the third term of the Hamiltonian Eq. (225) with the mean field approximation as

$$-\sum_{i=1}^{N}\sum_{j=1}^{N}\sum_{p=1}^{N}\frac{\hbar\chi_{ip}\chi_{jp}}{\Omega_p}\hat{\alpha}_i^\dagger\hat{\alpha}_i\left\langle\hat{\alpha}_j^\dagger\hat{\alpha}_j\right\rangle \equiv -\sum_{i=1}^{N}\hbar\omega_i\hat{\alpha}_i^\dagger\hat{\alpha}_i, \tag{2.231}$$

with

$$\omega_i = \sum_{j=1}^{N}\sum_{p=1}^{N}\frac{\chi_{ip}\chi_{jp}}{\Omega_p}\left\langle \hat{\alpha}_j^\dagger \hat{\alpha}_j \right\rangle = \sum_{j=1}^{N}\sum_{p=1}^{N}\frac{\hbar\chi^2 \mathrm{P}_{ip}\mathrm{P}_{jp}}{2N\Omega_p^2 (m_i m_j)^{1/2}}, \tag{2.232}$$

where Eq. (212) is used to obtain the expression in the last line of Eq. (232). In addition, we neglect the site dependence of the hopping operator $\hat{J}_i$ to approximate $J$, for the moment. Then the Hamiltonian regarding the quasi-particles ($\hat{\alpha}$ and $\hat{\alpha}^\dagger$) can be expressed as

$$\hat{H} = \sum_{i=1}^{N}\hbar(\omega - \omega_i)\,\hat{\alpha}_i^\dagger\hat{\alpha}_i + \sum_{i=1}^{N-1}\hbar J\left(\hat{\alpha}_i^\dagger\hat{\alpha}_{i+1} + \hat{\alpha}_{i+1}^\dagger\hat{\alpha}_i\right), \tag{2.233}$$

or in the matrix form as

$$\hat{H} = \hbar\hat{\vec{\alpha}}^\dagger \begin{pmatrix} \omega-\omega_1 & J & \cdots & 0 \\ J & \omega-\omega_2 & \ddots & \vdots \\ \vdots & \ddots & \ddots & J \\ 0 & \cdots & J & \omega-\omega_N \end{pmatrix} \hat{\vec{\alpha}}, \tag{2.234a}$$

with

$$\hat{\vec{\alpha}}^\dagger \equiv \left(\hat{\alpha}_1^\dagger, \hat{\alpha}_2^\dagger, \cdots, \hat{\alpha}_N^\dagger\right), \tag{2.234b}$$

where the effect from the phonon fields is involved in the diagonal elements $\omega_i$. Denoting an orthonormal matrix to diagonalize the Hamiltonian Eq. (234a) as Q and the $r$-th eigenvalue as $E_r$, we have

$$\hat{H} = \sum_{r=1}^{N}\hbar E_r \hat{A}_r^\dagger \hat{A}_r, \tag{2.235a}$$

with

$$\hat{A}_r = \sum_{i=1}^{N}(\mathrm{Q}^{-1})_{ri}\hat{\alpha}_i = \sum_{i=1}^{N}\mathrm{Q}_{ir}\hat{\alpha}_i, \tag{2.235b}$$

and

$$\left[\hat{A}_r, \hat{A}_s^\dagger\right] \equiv \hat{A}_r\hat{A}_s^\dagger - \hat{A}_s^\dagger\hat{A}_r = \delta_{rs}. \tag{2.235c}$$

Using these relations Eqs. (235a)–(235c), we can write down the time evolution of the photon number operator at site $i$ as follows;

$$\begin{aligned}\hat{N}_i(t) &= \exp\left(i\frac{\hat{H}}{\hbar}t\right)\hat{N}_i \exp\left(-i\frac{\hat{H}}{\hbar}t\right) \\ &= \sum_{r=1}^{N}\sum_{s=1}^{N} \mathrm{Q}_{ir}\mathrm{Q}_{is}\hat{A}_r^{\dagger}\hat{A}_s \exp\{i(E_r - E_s)t\}.\end{aligned} \tag{2.236}$$

The expectation value of the photon number operator $\hat{N}_i(t)$ is then given by

$$\langle N_i(t)\rangle_j = \langle \psi_j | \hat{N}_i(t) | \psi_j \rangle = \sum_{r=1}^{N}\sum_{s=1}^{N} \mathrm{Q}_{ir}\mathrm{Q}_{jr}\mathrm{Q}_{is}\mathrm{Q}_{js} \cos\{(E_r - E_s)t\}, \tag{2.237}$$

in terms of one photon state at site $j$ defined by

$$|\psi_j\rangle = \hat{\alpha}_j^{\dagger}\,|0\rangle = \sum_{r=1}^{N} \mathrm{Q}_{jr}\hat{A}_r^{\dagger}\,|0\rangle. \tag{2.238}$$

Since the photon number operator $\hat{N}_i$ commutes with the Hamiltonian Eq. (233), the total photon number is conserved, which means that a polariton called as a photon in this chapter conserves the total particle number within the lifetime. Moreover, $\langle N_i(t)\rangle_j$ can be regarded as the observation probability of a photon at an arbitrary site $i$ and time $t$, initially populated at site $j$. This function is analytically expressed in terms of the Bessel function as

$$\langle N_i(t)\rangle_j = \left\{ J_{j-i}(2Jt) - (-1)^i J_{j+i}(2Jt) \right\}^2, \tag{2.239}$$

when there are no photon-phonon interactions $(\omega_i = 0)$ and the total site number $N$ becomes infinite. Here the argument $J$ is the photon hopping constant, and Eq. (239) shows that a photon initially populated at site $j$ delocalizes to a whole system.

Focusing on the localized phonon modes, we take the summation in Eq. (232) over the localized modes only, which means that an earlier stage is considered after the incident photon excites the phonon modes, or that the duration of the localized phonon modes dominant over the delocalized modes is focused (see Figure 2.25). This kind of analysis provides us with an interesting insight to the photon-phonon coupling constant and the photon hopping

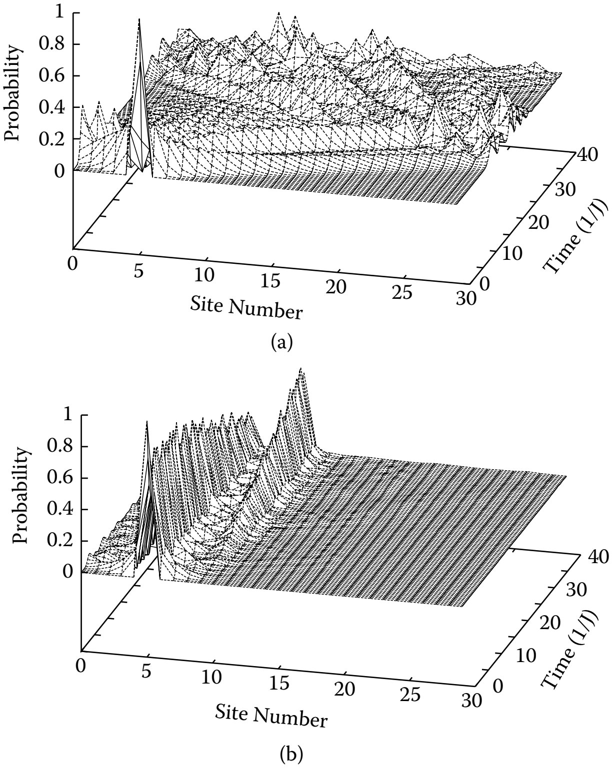

**FIGURE 2.26**
(a) The probability that a photon is found at each site as a function of time in the case of $\chi = 0$ and $\hbar J = 1$ eV. Other parameters are the same as those in Figure 2.24. (b) The probability that a photon is found at each site as a function of time, in the case of $J \sim (\hbar/k)(\chi/N)$[22] Other parameters used are the same as those in Figure 2.24.

constant, which is necessary for the understanding of the mechanism of photon's localization.

The temporal evolution of the observation probability of a photon at each site is shown in Figure 2.26. Without the photon-phonon coupling ($\chi = 0$), a photon spreads over the whole system as a result of the photon hopping, as shown in Figure 2.26(a). Here the photon energy $\hbar\omega = 1.81$ eV and the hopping constant $\hbar J = 0.5$ eV are used in the calculation. The impurities are assumed to be doped at site 3, 7, 11, 15, and 19 while the total site number $N$ is 20 and the mass ratio of the host molecules to the impurities is 5. Figure 2.26(b) shows a result with $\chi = 1.4 \times 10^3$ fs$^{-1}$ nm$^{-1}$ whereas other parameters used are the same as those in Figure 2.26(a). It follows from the figure that a photon moves from one impurity to other impurity sites instead of delocalizing to a whole system. As the photon-phonon coupling constant becomes much larger than $\chi = 1.4 \times 10^3$ fs$^{-1}$ nm$^{-1}$, a photon cannot move from the initial impurity site to others and stay there.

The effect caused by the photon-phonon coupling $\chi$ is expressed by the diagonal component in the Hamiltonian, whereas the off-diagonal component involves the photon hopping effect caused by the hopping constant $J$. These results indicate that photon's spatial distribution depends on the competition between the diagonal and off-diagonal components in the Hamiltonian, that is, $\chi$ and $J$, and that a photon can move among impurity sites and localize at those sites when both components are comparable under the condition

$$\chi \sim N\sqrt{\frac{kJ}{\hbar}}, \tag{2.240}$$

where the localization width seems very narrow.

### Contribution from the off-Diagonal Part

In the previous section, we have approximated $J$ as a constant independent of the sites, in order to examine the photon's spatial distribution as well as the mechanism of the photon localization. Now let us treat the photon hopping operator $\hat{J}_i$ more rigorously, and investigate the site dependence of the off-diagonal contribution, which includes the inhomogeneity of the phonon fields. Noticing that a quasiparticle transformed from a photon operator by the Davydov transformation is associated with phonons in the coherent state (see Eq. (227)), we take expectation values of $\hat{J}_i$ in terms of the coherent state of phonons $|\gamma\rangle$ as

$$J_i \equiv \langle\gamma|\,\hat{J}_i\,|\gamma\rangle. \tag{2.241}$$

Here the coherent state $|\gamma\rangle$ is an eigenstate of the annihilation operator $\hat{b}_p$ with eigenvalue $\gamma_p$ and satisfies the following equations

$$\hat{b}_p\,|\gamma\rangle = \gamma_p\,|\gamma\rangle \tag{2.242a}$$

and

$$\exp\left(-\sum_p c_p\hat{b}_p\right)|\gamma\rangle = \exp\left(-\sum_p c_p\gamma_p\right)|\gamma\rangle, \tag{2.242b}$$

where $c_p$ is a real number. Since the difference between the creation and annihilation operators of a phonon is invariant under the Davydov transformation, the following relation holds:

$$\hat{\beta}_p^\dagger - \hat{\beta}_p = \hat{b}_p^\dagger - \hat{b}_p. \tag{2.243}$$

Using Eqs. (242a), (242b), and (243), we can rewrite the site-dependent hopping constant $J_i$ in Eq. (241) as

$$\begin{aligned}
J_i &= J\langle\gamma|\exp\left\{\sum_{p=1}^{N} C_{ip}\left(\hat{b}_p^\dagger - \hat{b}_p\right)\right\}|\gamma\rangle \\
&= J\exp\left(-\frac{1}{2}\sum_{p=1}^{N} C_{ip}^2\right)\langle\gamma|\exp\left(\sum_{p'=1}^{N} C_{ip'}\hat{b}_{p'}^\dagger\right)\exp\left(-\sum_{p''=1}^{N} C_{ip''}\hat{b}_{p''}\right)|\gamma\rangle \\
&= J\exp\left(-\frac{1}{2}\sum_{p=1}^{N} C_{ip}^2\right)\langle\gamma|\exp\left(\sum_{p'=1}^{N} C_{ip'}\gamma_{p'}\right)\exp\left(-\sum_{p''=1}^{N} C_{ip''}\gamma_{p''}\right)|\gamma\rangle \\
&= J\exp\left(-\frac{1}{2}\sum_{p=1}^{N} C_{ip}^2\right),
\end{aligned} \tag{2.244}$$

where $C_{ip}$ is denoted by

$$C_{ip} \equiv \frac{\chi_{ip} - \chi_{i+1p}}{\Omega_p}. \tag{2.245}$$

Figure 2.27 shows the site dependence of $J_i$ in the case of $N = 21$. Impurities are doped at site 4, 6, 13, and 19. The mass ratio of the host molecules to the impurities is 5, while $\hbar J = 0.5$ eV and $\chi = 14.0$ fs$^{-1}$ nm$^{-1}$ are used. It follows from the figure that the hopping constants are highly modified around the impurity sites and the edge sites. The result implies that photons are strongly affected by localized phonons and hop to the impurity sites to localize. Here we have not considered the temperature dependence of $J_i$, which is important for phenomena dominated by incoherent phonons [85]. This is because coherent phonons weakly depend on the temperature of the system. However, there remains room to discuss more fundamental issue, that is, whether the probe system is in a thermal equilibrium state or not.

In Figure 2.28, we present a typical result that photons localize around the impurity sites in the system as the photon-phonon coupling constants $\chi$ vary from zero to 40.0 fs$^{-1}$ nm$^{-1}$ or 54.0 fs$^{-1}$ nm$^{-1}$ with $\hbar J = 0.5$ eV kept. As depicted with the filled squares in the figure, photons delocalize and spread over the system without the photon-phonon couplings. When the photon-phonon couplings are comparable to the hopping constants, $\chi = 40.0$ fs$^{-1}$ nm$^{-1}$, photons can localize around the impurity site with a finite width, two sites at HWHM, as shown with the filled circles. This finite width of photon localization comes from the site-dependent hopping constants. As the photon-phonon couplings are larger than $\chi = 40.0$ fs$^{-1}$ nm$^{-1}$, photons can localize at the edge sites with a finite width, as well as the impurity sites.

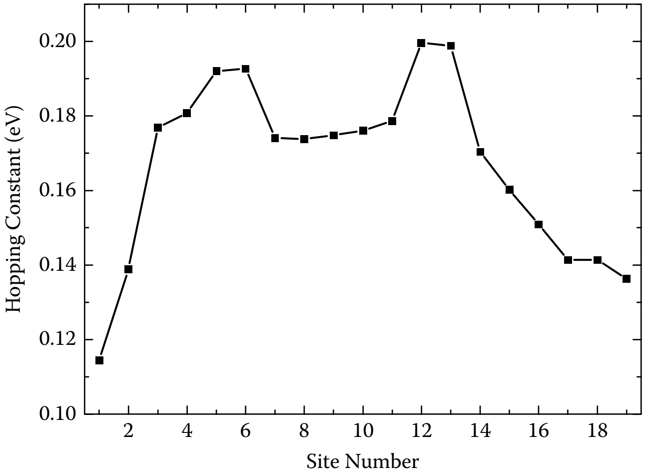

**FIGURE 2.27**
The site dependence of the hopping constants $J_i$ in the case of $N = 20$. Impurities are doped at site 4, 6, 13, 19. The mass ratio of the host molecules to the impurities is 1 to 0.2, whereas $\hbar J = 0.5$ eV and $\chi = 40.0\ \mathrm{fs^{-1}nm^{-1}}$ are used.

In Figure 2.28, the photon localization at the edge site is shown with the filled triangles, which originates from the finite size effect of the molecular chain [77,86]. This kind of localization of photons dressed by the coherent state of phonons leads us to a simple understanding of phonon-assisted photodissociation using an optical near field; molecules in the electronic ground

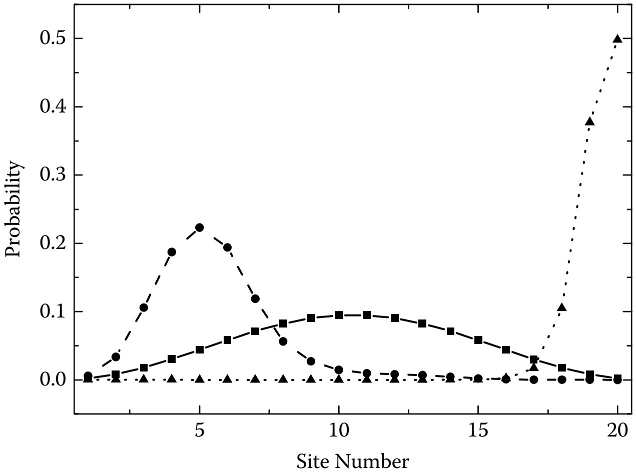

**FIGURE 2.28**
Probability of photons observed at each site. The filled squares, circles, and triangles represent the results for $\chi = 0$, 40.0, and 54.0 $\mathrm{fs^{-1}nm^{-1}}$, respectively. Other parameters used are the same as those in Figure 2.27.

state approach to the probe tip within the localization range of the dressed photons, and can be vibrationally excited by the dressed-photon transfer to the molecules, via multiphonon component of the dressed photons, which might be followed by the electronic excitation. Thus it leads to the dissociation of the molecules even if the incident photon energy less than the dissociation energy is used.

As a natural extension of the localized photon model, we have discussed the inclusion of phonon's effects into the model. The study was initially motivated by the experiments of photodissociation of molecules by optical near fields, whose results show unique feature different from the conventional one with far fields. After clarifying delocalized or localized vibration modes in a pseudo one-dimensional system, we have focused on the interaction between dressed photons and phonons by using the Davydov transformation. We have theoretically shown that photons are dressed by the coherent state of phonons, and found that the competition between the photon-phonon coupling constant and the photon hopping constant governs the photon localization or delocalization in space. The obtained results lead us to a simple understanding of an optical near field itself as an interacting system of photon, electronic excitation (induced polarization), and phonon fields in a nanometer space, which are surrounded by macroscopic environments, as well as phonon-assisted photodissociation using an optical near field.

## References

1. Sakurai, J. J., *Advanced Quantum Mechanics* Addison-Wesley, Reading, 1967.
2. Newton, T. D. and Wigner, E. P., Localized States for Elementary Systems *Rev. Mod. Phys.* 21, 400, 1949.
3. Sipe, J. E., Photon wave functions *Phys. Rev. A* 52, 1875–1883, 1995.
4. Scully, M. O. and Zubairy, M. S., *Quantum Optics* Cambridge Univ. Press, Cambridge, 1997.
5. Kobayashi, K. and Ohtsu, M., Quantum theoretical approach to a near-field optical system, *J. Microsc.* 194, 249–254, 1999.
6. Kobayashi, K., Sangu, S., Ito, H., and Ohtsu, M., Near-field optical potential for a neutral atom. *Phys. Rev. A* 63 (1), 013806, 2001.
7. Kobayashi, K., Sangu, S., and Ohtsu, M., Quantum Theoretical Approach to Optical Near-Fields and Some Related Application, in *Progress in Nano-Electro-Optics I,* Ohtsu, M. Springer, Berlin Heidelber, 2003, pp. 119—157.
8. Sangu, S., Kobayashi, K., Shojiguchi, A., and Ohtsu, M., Logic and functional operations using a near-field optically coupled QD system, *Phys. Rev. B* 69, 115334, 2004.
9. John, S. and Quang, T., Photon-hopping conduction and collectively induced transparency in a photonic band gap. *Phys. Rev. A* 52 (5), 4083, 1995.
10. Suzuura, H., Tsujikawa, T., and Tokihiro, T., Quantum theory for exciton polaritons in a real-space representation, *Phys. Rev. B* 53 (3), 1294–1301 1996.

11. Shojiguchi, A., Kobayashi, K., Sangu, S., Kitahara, K., and Ohtsu, M., Superradiance and Dipole Ordering of an N Two-Level System Interacting with Optical Near Fields, *J. Phys. Soc. Jpn.* 72 (11), 2984–3001, 2003.
12. Dirac, P. A. M., *Principles of Quantum Mechanics,* 4th Rev. ed., Oxford University Press, Oxford, 1958.
13. Sakurai, J. J., *Modern Quantum Mechanics,* Rev. ed., Addison-Wesley, Reading, 1994.
14. Fulde, P., *Electron Correlations in Molecules and Solids,* 2nd ed., Springer, Berlin Heidelberg New York, 1993.
15. Grabert, H., *Projection Operator Techniques in Nonequilibrium Statistical Mechanics.* Springer, Berlin Heidelberg New York, 1982.
16. Haake, F., *Statistical Treatment of Open Systems by Generalized Master Equations.* Springer, Berlin Heidelberg New York, 1973.
17. Rau, J. and Müller, B., From reversible quantum microdynamics to irreversible quantum transport, *Phys. Rep.* 272 (1), 1–59, 1996.
18. Weiss, U., *Quantum Dissipative Systems,* 2nd ed. World Scientific Publishing, Singapore, 1999.
19. Willis, C. R. and Picard, R. H., Time-dependent projection-operator approach to master equations for coupled systems, *Phys. Rev. A* 9 (3), 1343, 1974.
20. Hyuga, H. and Ohtsubo, H., Breakdown of the Siegert theorem and the many-body charge density operators, *Nucl. Phys. A* 294 (3), 348–356, 1978.
21. Fetter, A. L. and Walecka, J. D., *Quantum Theory of Many-Particle Systems* McGraw-Hill, New York, 1971.
22. Anderson, P. W., *Concepts in Solids.* World Scientific, Singapore, 1997.
23. Cho, K., "ABC"-Free Theory of Polariton: From Semi-Infinite Medium to Quantum. *J. Phys. Soc. Jpn.* 55 (11), 4113, 1986.
24. Haken, H., *Quantum Field Theory of Solids.* North-Holland, Amsterdam, 1983.
25. Hopfield, J. J., Theory of the Contribution of Excitons to the Complex Dielectric Constant of Crystals, *Phys. Rev.* 112 (5), 1555, 1958.
26. Kittel, C., *Quantum Theory of Solids.* John Wiley & Sons, New York, 1972.
27. Pines, D., *Elementary Excitations in Solids.* Perseus Books, Reading, 1999.
28. Cohen-Tannoudji, C., *Atoms in Electromagnetic Fields.* World Scientific, Singapore, 1994.
29. Cohen-Tannoudji, C., J. Dupont-Roc, and Grynberg, G., *Photons and Atoms.* John Wiley & Sons, New York, 1989.
30. Cohen-Tannoudji, C., J. Dupont-Roc, and Grynberg, G., *Atom-Photon Interactions.* John Wiley & Sons, New York, 1992.
31. Craig, D. P. and Thirunamachandran, T., *Molecular Quantum Electrodynamics* Dover, New York, 1998.
32. Kaku, M., *Quantum Field Theory.* Oxford University Press, Oxford, 1993.
33. Weinberg, S., *The Quantum Theory of Fields I, II, and III,* Cambridge University Press, Cambridge, 1995.
34. Bányai, L. and Koch, S. W., *Semiconductor QDs.* World Scientific Publishing, Singapore, 1993.
35. Gaponenko, S. V., *Optical Properties of Semiconductor Nanocrystals.* Cambridge University Press, Cambridge, 1998.
36. Haug, H. and Koch, S. W., *Quantum Theory of the Optical and Electronic Properties of Semiconductors* 3rd ed. World Scientific Publishing, Singapore, 2001.
37. Masumoto, Y. and Takagahara, T., *Semiconductor QDs*, Springer, Berlin Heidelberg, 2002.

38. Woggon, U., *Optical Properties of Semiconductor QDs,* Springer, Berlin Heidelberg, 1997.
39. Kobayashi, K., Sangu, S., Kawazoe, T., and Ohtsu, M., Exciton dynamics and logic operations in a near-field optically coupled QD system, *J. Lumin.* 112, 117–121 2005.
40. Kobayashi, K., Sangu, S., Kawazoe, T., and Ohtsu, M., Erratum to: "Exciton dynamics and logic operations in a near-field optically coupled QD system": [J. Lumin. 112 (2005) 117], *J. Lumin.* 114, 315–316, 2005.
41. Crooker, S. A., Hollingsworth, J. A., Tretiak, S., and Klimov, V. I., Spectrally Resolved Dynamics of Energy Transfer in QD Assemblies: Towards Engineered Energy Flows in Artificial Materials, *Phys. Rev. Lett.* 89 (18), 186802, 2002.
42. Kagan, C. R., Murray, C. B., Nirmal, M., and Bawendi, M. G., Electronic Energy Transfer in CdSe QD Solids, *Phys. Rev. Lett.* 76 (9), 1517, 1996.
43. Kawazoe, T., Kobayashi, K., Lim, J., Narita, Y., and Ohtsu, M., Direct Observation of Optically Forbidden Energy Transfer between CuCl Quantum Cubes via Near-Field Optical Spectroscopy, *Phys. Rev. Lett.* 88 (6), 067404, 2002.
44. Jordan, P., Fromme, P., Witt, H. T., Klukas, O., Saenger, W., and Krausz, N., Three-dimensional structure of cyanobacterial photosystem I at 2.5[thinspangst] resolution, *Nature* 411 (6840), 909–917, 2001.
45. McDermott, G., Prince, S. M., Freer, A. A., Hawthornthwaite-Lawless, A. M., Papiz, M. Z., Cogdell, R. J., and Isaacs, N. W., Crystal structure of an integral membrane light-harvesting complex from photosynthetic bacteria, *Nature* 374 (6522), 517–521, 1995.
46. Mukai, K., Abe, S., and Sumi, H., Theory of Rapid Excitation-Energy Transfer from B800 to Optically-Forbidden Exciton States of B850 in the Antenna System LH2 of Photosynthetic Purple Bacteria, *J. Phys. Chem. B* 103 (29), 6096–6102, 1999.
47. Kobayashi, K., Sangu, S., Shojiguchi, A., Kawazoe, T., Kitahara, K., and Ohtsu, M., Excitation dynamics in a three-QD system driven by optical near-field interaction: towards a nanometric photonic device. *J. Microsc.* 210 (3), 247–251, 2003.
48. M.Ohtsu, Kobayashi, K., Kawazoe, T., Sangu, S., and Yatsui, T., Nanophotonics: design, fabrication, and operation of nanometric devices using optical near fields, *IEEE J. Sel. Top. Quant. Electron.* 8 (4), 839–862, 2002.
49. Sangu, S., Kobayashi, K., Shojiguchi, A., Kawazoe, T., and Ohtsu, M., Excitation energy transfer and population dynamics in a QD system induced by optical near-field interaction, *J. Appl. Phys.* 93 (5), 2937–2945, 2003.
50. Heinrich, A. J., Lutz, C. P., Gupta, J. A., and Eigler, D. M., Molecule Cascades, *Science* 298, 1381–1387, 2002.
51. Lent, C. S., MOLECULAR ELECTRONICS: Bypassing the Transistor Paradigm *Science.* 288, 1597–1599 2000.
52. Blum, K., *Density Matrix Theory and Applications,* 2nd ed. Plenum, New York, 1996.
53. Breuer, H.-P. and Petruccione, F., *The Theory of Open Quantum Systems.* Oxford University Press, New York, 2002.
54. Carmichael, H. J., *Statistical Methods in Quantum Optics 1: Master Equations and Fokker-Planck Equations.* Springer, Berlin Heidelberg, 1999.
55. Haken, H., *Light I.* North-Holland, Amsterdam, 1986.
56. Sangu, S., Kobayashi, K., Shojiguchi, A., Kawazoe, T., and Ohtsu, M., Theory and Principles of Operation of Nanophotonic Functional Devices, in *Progress in Nano-Electro-Optics V,* Ohtsu, M. Springer, Berlin Heidelberg, 2006, pp. 1–62.

57. Coffey, B. and Friedberg, R., Effect of short-range Coulomb interaction on cooperative spontaneous emission, *Phys. Rev. A* 17 (3), 1033–1048 1978.
58. Yamamoto, Y., Kourogi, M., Ohtsu, M., Polonski, V., and Lee, G. H., Fabrication of nanometric zinc pattern with photodissociated gas-phase diethylzinc by optical near field, *Applied Physics Letters* 76 (16), 2173–2175, 2000.
59. Yatsui, T., Kawazoe, T., Ueda, M., Yamamoto, Y., Kourogi, M., and Ohtsu, M., Fabrication of nanometric single zinc and zinc oxide dots by the selective photodissociation of adsorption-phase diethylzinc using a nonresonant optical near field, *Appl. Phys. Lett.* 81 (19), 3651–3653, 2002.
60. Kawazoe, T., Kobayashi, K., Takubo, S., and Ohtsu, M., Nonadiabatic photodissociation process using an optical near field, *J. Chem. Phys.* 122 (2), 024715, 2005.
61. Kobayashi, K., Kawazoe, T., and Ohtsu, M., Importance of multiple-phonon interactions in molecular dissociation and nanofabrication using optical near fields, *IEEE Trans. Nanotechnol.* 4 (5), 517–522, 2005.
62. Tanaka, Y. and Kobayashi, K., Spatial localization of an optical near field in one-dimensional nanomaterial system, *Physica E,* 40(2), 297–300, 2007.
63. Tanaka, Y. and Kobayashi, K., Optical near field dressed by localized and coherent phonons, *J. Microsc.,* 229(2), 228–232, 2008.
64. Bonderup, E. and M$\phi$lmer, K., Calculations on cooling of fast, multilevel atoms by intense laser fields, *J. Opt. Soc. Am. B* 6 (11), 2125–2129, 1989.
65. Cohen-Tannoudji, C., Atomic motion in laser light, in *Fundamental systems in quantum optics,* Dalibard, J., Raimond, J.-M., and Zinn-Justin, J. North-Holland, Amsterdam, 1992.
66. Dalibard, J. and Cohen-Tannoudji, C., Dressed-atom approach to atomic motion in laser light: the dipole force revisited, *J. Opt. Soc. Am. B* 2 (11), 1707–1720 1985.
67. Kawazoe, T., Kobayashi, K., Sangu, S., and Ohtsu, M., Demonstration of a nanophotonic switching operation by optical near-field energy transfer, *Appl. Phys. Lett.* 82 (18), 2957–2959, 2003.
68. Kawazoe, T., Kobayashi, K., and Ohtsu, M., Optical nanofountain: A biomimetic device that concentrates optical energy in a nanometric region, *Appl. Phys. Lett.* 86 (10), 103102, 2005.
69. Yatsui, T., Sangu, S., Kawazoe, T., Ohtsu, M., An, S. J., Yoo, J., and Yi, G.-C., Nanophotonic switch using ZnO nanorod double-quantum-well structures, *Appl.Phys. Lett.* 90 (22), 223110, 2007.
70. Haken, H. and Wolf, H. C., *Molecular Physics and Elements of Quantum Chemistry.* Springer, Berlin Heidelberg, 1995.
71. Kawazoe, T., Kobayashi, K., and Ohtsu, M., Near-field optical chemical vapor deposition using Zn(acac)2 with a non-adiabatic photochemical process, *Appl. Phys. B.* 84 (1), 247–251, 2006.
72. Kawazoe, T., Yamamoto, Y., and Ohtsu, M., Fabrication of a nanometric Zn dot by nonresonant near-field optical chemical-vapor deposition, *Appl. Phys. Lett.* 79 (8), 1184–1186, 2001.
73. Jackson, R. L., Metal-alkyl bond dissociation energies for (CH3)2Zn, (C2H5)Zn, (CH3)2Cd, and (CH3)2Hg, *Chem. Phys. Lett.* 163 (4–5), 315–322, 1989.
74. Jackson, R. L., Vibrational energy of the monoalkyl zinc product formed in the photodissociation of dimethyl zinc, diethyl zinc, and dipropyl zinc, *J. Chem. Phys.* 96 (8), 5938–5951, 1992.

75. Schinke, R., *Photodissociation Dynamics.* Cambridge University Press, Cambridge, 1995.
76. Ivanov, A. L., Haug, H., and Keldysh, L. V., Optics of excitonic molecules in semiconductors and semiconductor microstructures, *Phys. Rep.* 296 (5–6), 237–336, 1998.
77. Falvo, C. and Pouthier, V., Vibron-polaron critical localization in a finite size molecular nanowire, *J. Chem. Phys.* 122 (1), 014701, 2005.
78. Striefler, M. E. and Barsch, G. R., Lattice dynamics of alpha -quartz, *Phys. Rev. B* 12 (10), 4553, 1975.
79. Payton, D. N. and Visscher, W. M., Dynamics of Disordered Harmonic Lattices. I. Normal-Mode Frequency Spectra for Randomly Disordered Isotopic Binary Lattices, *Phys. Rev.* 154 (3), 802, 1967.
80. Sievers, A. J., Maradudin, A. A., and Jaswai, S. S., Infrared Lattice Absorption by Gap Modes and Resonance Modes in KI, *Phys. Rev.* 138 (1A), A272, 1965.
81. Mizuno, S., Eigenfrequency and decay factor of the localized phonon in a superlattice with a defect layer, *Phys. Rev. B* 65 (19), 193302, 2002.
82. Yamamoto, T. and Watanabe, K., Nonequilibrium Green's Function Approach to Phonon Transport in Defective Carbon Nanotubes, *Phys. Rev. Lett.* 96 (25), 255503, 2006.
83. Davydov, A. S. and Pestryakov, G. M., On the canonical transformation in the theory of exciton-phonon interaction, *phys. stat. sol. (b)* 49 (2), 505–512, 1972.
84. Jacak, L., Machnikowski, P., Krasnyj, J., and Zoller, P., Coherent and incoherent phonon processes in aritificial atoms, *Eur. Phys. J. D* 22, 319–331, 2003.
85. Mizoguchi, K., Furuichi, T., Kojima, O., Nakayama, M., Saito, S., Syouji, A., and Sakai, K., Intense terahertz radiation from longitudinal optical phonons in GaAs/AlAs multiple quantum wells, *Appl. Phys. Lett.* 87 (9), 093102, 2005.
86. Pouthier, V. and Girardet, C., Critical localization of confined phonons in finite size admonolayers, *J. Chem. Phys.* 112 (11), 5100–5104, 2000.

# 3

# *Nanophotonic Devices*

This chapter reviews the principles of a qualitative innovation in device operation—nanophotonic devices—which operate by near-field optical energy transfer and subsequent energy dissipation. As examples, the operations of an AND gate, NOT gate, and optical nanofountain are demonstrated.

## 3.1 Excitation Energy Transfer

Unlike a single QD, a system consisting of coupled QDs possesses unique properties, such as the Kondo effect [1,2] and Coulomb blockade [3, 4], and violates Kohn's theorem [5]. The QD system is involved in a variety of interactions, for example, carrier tunneling [1–3,6], Coulomb coupling [4], and the spin interaction [5]. Moreover, it is important to investigate the interactions among QDs, not only for elucidating various physical phenomena, but also for developing novel functional devices [1–6]. Recently, studies on the carrier distribution in a single QD have been performed using near-field optical spectroscopy [7], which indicated that the optical near field couples strongly with the excitation in a QD and can act as an intermediate in the interaction between QDs. In addition, it is stronger than a propagating optical field. This optical near-field interaction [7] is of particular interest because it governs the coupling strength among QDs.

Mukai et al. reported ultrafast "optically forbidden" energy transfer from the outer ring of loosely packed bacteriochlorophyll molecules called B800 to the inner ring of closely packed bacteriochlorophyll molecules known as B850 in the light-harvesting antenna complex of photosynthetic purple bacteria [8]. Theoretically, they showed that this transfer is possible when the point transition dipole approximation is violated as a result of the size effect of B800 and B850. This transfer is a result of the optical near-field interaction between B800 and B850. Similarly, energy can be transferred from one dot to another via the optical near-field interaction in the QD system, even if it is a dipole (optically)-forbidden transfer. The energy transfer from smaller to larger QDs has been studied in a spectrally, spatially, and time-resolved experiment. Kagan et al. observed the energy transfer among CdSe QDs coupled via a dipole–dipole interdot interaction [9]. Crooker et al. also studied the dynamics of the exciton energy transfer in close-packed assemblies of monodisperse and mixed-size CdSe nanocrystal QDs and reported the energy-dependent transfer rate of excitons from smaller to larger dots [10]. These examples are based on the optical near-field interaction. The physical model for the unidirectional resonant energy transfer between QDs via the optical near-field interaction has been explained, and the optically forbidden energy transfer among randomly dispersed CuCl QDs has been demonstrated experimentally using optical near-field spectroscopy [11]. The theoretical analysis and temporal evolution of the energy transfer via the optical near-field interaction were discussed in Chapter 2. This section reviews experimental works involving the direct observation of energy transfer from the exciton state in a CuCl QD to the optically forbidden exciton state in another CuCl QD using optical near-field spectroscopy.

Cubic CuCl QDs embedded in a NaCl matrix have the potential to be an optical near-field coupling system that exhibits this optically forbidden energy transfer. This is made possible because for this system, other forms of energy transfer, such as carrier tunneling and Coulomb coupling, can be neglected as the carrier wave function is localized in the QDs; this occurs because the potential depth exceeds 4 eV and the Coulomb interaction is weak because of the small exciton Bohr radius of 0.68 nm in CuCl [11]. The energy transfer via a propagating light is also negligible, since the optically forbidden transition in nearly perfect cubic CuCl QDs is used here; that is, the transition to the confined exciton energy levels has an even principal quantum number [12]. Sakakura et al. have already described the transition to the optically forbidden levels in a hole-burning experiment using cubic CuCl QDs [13]. Although they attributed the transition to an imperfect cubic shape, the experimental and simulation results did not show such imperfection. Thus, the transition was attributable to the energy transfer between the CuCl QDs via the optical near-field interaction, which is similar to the optically forbidden energy transfer between B800 and B850 in the earlier-mentioned photosynthetic system.

So far, this type of energy transfer has not been observed directly because such a nanometric system is usually extremely complex. However, CuCl QDs in a NaCl matrix is a very simple system. The translational motion of the exciton center of mass is quantized because of the small exciton Bohr radius for CuCl QDs, and CuCl QDs become cubic in a NaCl matrix [13–15]. The potential barrier of CuCl QDs in a NaCl crystal can be regarded as infinitely high, and the energy eigenvalues for the quantized $Z_3$ exciton energy level ($n_x$, $n_y$, $n_z$) in a CuCl QD with side length $L$ are given by

$$E_{n_x,n_y,n_z} = E_B + \frac{\hbar^2\pi^2}{2M(L-a_B)^2}\left(n_x^2+n_y^2+n_z^2\right), \tag{3.1}$$

where $E_B$ is the bulk $Z_3$ exciton energy; $M$ is the translational mass of an exciton; $a_B$ is its Bohr radius; $n_x$, $n_y$, and $n_z$ are quantum numbers ($n_x, n_y, n_z =$ 1, 2, 3,…); and $d = (L - a_B)$ corresponds to the effective side length found

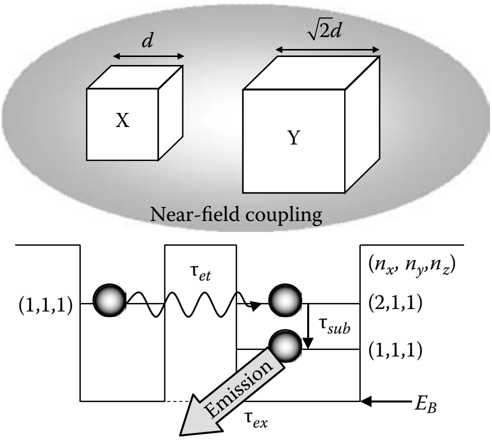

**FIGURE 3.1**
Upper: Schematic drawings of closely located cubic CuCl QDs X and Y with effective side lengths ($L$—$a_B$) of $d$ and $\sqrt{2}\,d$, respectively, where $L$ and $a_B$ are the side lengths of the cubic QDs and the exciton Bohr radius, respectively. Lower: Their exciton energy levels. $n_x$, $n_y$, and $n_z$ represent quantum numbers of an exciton. $E_B$ is the exciton energy level in a bulk crystal.

after considering the dead layer correction [13]. The exciton energy levels with even quantum numbers are dipole-forbidden states, which are optically forbidden [12]. However, the optical near-field interaction is finite for such coupling to the forbidden energy state [16].

Figure 3.1 shows schematic drawings of different-sized cubic CuCl QDs (X and Y) and the confined-exciton $Z_3$ energy levels. Here, $d$ and $\sqrt{2}d$ are the effective side lengths of cubic QDs X and Y, respectively. According to Eq. (3.1), the quantized exciton energy levels of (1,1,1) in QD X and (2,1,1) in QD Y resonate with each other. Under this resonant condition, the coupling energy of the optical near-field interaction is given by the following Yukawa function [16,17], which was discussed in Chapter 2:

$$V(r) = \alpha \frac{\exp(-\mu \cdot r)}{r}. \tag{3.2}$$

Here, $r$ is the separation between the two QDs, $\alpha$ is the coupling coefficient, and the effective mass of the Yukawa function $\mu$ is given by

$$\mu = \frac{\sqrt{2E_{n_x,n_y,n_z}(E_{NaCl} + E_{n_x,n_y,n_z})}}{\hbar c}, \tag{3.3}$$

where $E_{NaCl}$ is the exciton energy of the NaCl matrix. The value of $\alpha$ depends on the experimental conditions, which were estimated in Chapter 2. Assuming that the two CuCl QDs in the NaCl matrix have side lengths 5 and 7 nm (a size ratio of $1:\sqrt{2}$) and the interdot distance is 6.1 nm, then the coupling energy $V(r)$ is 5.05 $\mu$eV. This corresponds to an energy transfer time of 130 ps because of the optical near-field coupling, which is much shorter than the exciton lifetime of a few nanoseconds. In addition, the intersublevel transition $\tau_{sub}$, from higher exciton energy levels to the lowest [18], as shown in Figure 3.1, is generally less than a few picoseconds and is much shorter than the transfer time. Therefore, most of the energy of the excitation in a cubic CuCl QD with a side length of $d$ is transferred to the lowest exciton energy level in a neighboring QD with a side length of $\sqrt{2}d$ and recombines radiatively in the lowest level of (1, l, 1) in QD Y.

The CuCl QDs embedded in NaCl matrix used experimentally were fabricated using the Bridgman method and successive annealing, and the average size of the QDs was found to be 4.3 nm. The sample was cleaved just before the near-field optical spectroscopy experiment to keep the sample surface clean. The cleaved surface of a 100-$\mu$m-thick sample was sufficiently flat for the experiment; that is, its roughness was less than 50 nm, at least within a few microns squared. A 325-nm He–Cd laser was used as the light source. A double-tapered fiber probe was fabricated using chemical etching and a 150-nm gold coating was applied [19]. A 50-nm aperture was fabricated using the pounding method [20].

The curve in Figure 3.2(a) shows the far-field luminescence spectrum of a sample that was recorded with a probe-sample separation of 3 $\mu$m in collection-mode operation [17] of a cryogenic near-field optical microscope at 15 K. It represents the collective luminescence intensity from several cubic CuCl QDs, and is inhomogeneously broadened owing to the size distribution of the QDs. Figure 3.2(b) shows the differential spectrum, which is the

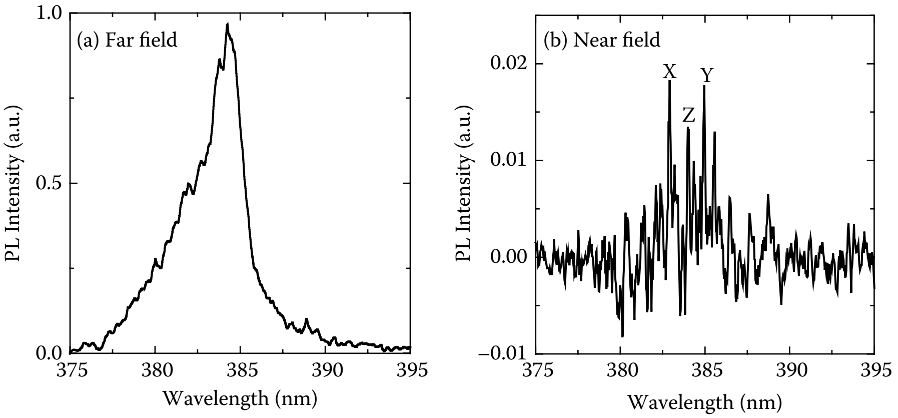

**FIGURE 3.2**
PL spectra. (a) Far-field PL spectrum of a sample recorded with a probe-sample separation of 3 μm for collection-mode operation at 15 K. (b) The differential PL spectrum, which is the intensity difference between the luminescence measured with probe-sample separations of 3 $\mu$m and less than 10 nm. X, Y, and Z correspond to the wavelengths of the lowest exciton state in cubic QDs with side lengths of 4.6, 6.3, and 5.3 nm, respectively.

intensity difference between the luminescence measured with probe-sample separations of 3 $\mu$m and less than 10 nm. This curve consists of several fine structures that appear as the contribution of the QDs near the apex of the probe because of the drastic increase in the measured luminescence intensity for a probe-sample separation of less than 10 nm. The average density of the QDs is $10^{17}$ cm$^{-3}$. Therefore, the average separation between the QDs is less than 30 nm as estimated from the concentration of CuCl. Consequently, the spectral peaks in Figure 3.2(b), obtained from near-field measurements using the 50-nm aperture fiber probe, originate from several QDs of different sizes. Among these, peaks X and Y correspond to the confined $Z_3$-exciton energy levels of quantum number (1,1,1) for the cubic QDs with side lengths ($L$) of 4.6 and 6.3 nm, respectively. Their effective side lengths $d$ are 3.9 and 5.6 nm, which is a size ratio close to $1:\sqrt{2}$, so the (1,1,1) and (2,1,1) quantized exciton levels resonate with each other and this is responsible for the energy transfer between the QDs. Figures 3.3(a) and (b) show the spatial distributions of the luminescence intensity, that is, near-field optical microscope images, for peaks X and Y in Figure 3.2(b), respectively. The spatial resolution, which depends on the aperture diameter of the near-field probe, was smaller than 50 nm. These images clearly show anticorrelation features in their intensity distributions, as manifested by the dark and bright regions surrounded by dashed white curves.

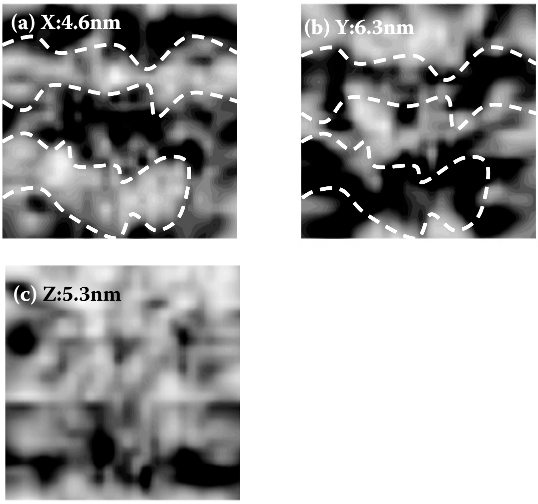

**FIGURE 3.3**
Spatial distributions of the near-field luminescence intensity for the peaks marked X, Y, and Z in Figure 3.2(b).

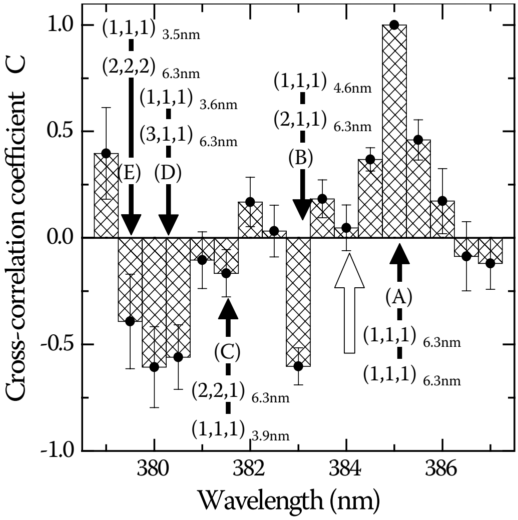

**FIGURE 3.4**

Values of the cross-correlation coefficient *C* between the spatial distribution of the intensity of the luminescence emitted from the $(n_x, n_y, n_z)$ level exciton in a QD with a 6.3 nm side length and that from the (1,1,1) level in a QD with a different side length *L*. They have been normalized to that of the auto-correlation coefficient of the luminescence intensity from the (1,1,1) level in a 6.3-nm QD, which is identified by an arrow A. The other four arrows (B–E) represent the cross-correlation coefficient *C* between higher levels in a 6.3-nm QD and other sized QDs. They are between (B) the (2,1,1) level in a 6.3-nm QD and the (1,1,1) level in a 4.6-nm QD, (C) the (2,2,1) level in a 6.3-nm QD and the (1,1,1) level in a 3.9-nm QD, (D) the (3,1,1) level in a 6.3-nm QD and the (1,1,1) level in a 3.6-nm QD, and (E) the (2,2,2) level in a 6.3-nm QD and the (1,1,1) level in a 3.5-nm QD. For reference, the white arrow represents the value of *C* between the (2,1,1) level in a 6.3-nm QD and the nonresonant (1,1,1) level in a 5.3-nm QD.

To confirm the anticorrelation feature more quantitatively, Figure 3.4 shows the values of the cross-correlation coefficient *C* between the spatial distribution of the intensity of the luminescence emitted from the $(n_x, n_y, n_z)$ level of an exciton in a cubic QD with a 6.3 nm side length and that from the (1,1,1) level in a QD with a different side length *L*. They have been normalized to that of the auto-correlation coefficient of the luminescence intensity from the (1,1,1) level in a 6.3-nm QD, which is identified by an arrow A in Figure 3.4. To calculate the values of *C*, a spatial Fourier transform was performed on the series of luminescence intensities in the chain of pixels inside the region surrounded by the dashed white curves in Figure 3.3. The large negative value of *C* identified by an arrow B clearly shows the anticorrelation feature between Figures 3.3(a) and (b), that is, between the (2,1,1) level in a 6.3-nm QD and the (1,1,1) level in a 4.6-nm QD.

This anticorrelation feature can be clarified by noting that these spatial distributions in luminescence intensity represent not only the spatial distributions of the QDs, but also some kind of resonant interaction between the

QDs. This interaction induces energy transfer from QDs X ($L$ = 4.6 nm) to QDs Y ($L$ = 6.3 nm) because most of the 4.6-nm QDs located close to 6.3-nm QDs cannot emit light, but instead transfer the energy to the 6.3-nm QDs. As a result, in the region containing embedded 6.3-nm QDs, the luminescence intensity in Figure 3.3(a) from 4.6-nm QDs is low, while the corresponding position in Figure 3.3(b) is high. As noted earlier, it is reasonable to attribute the origin of the interaction to the near-field energy transfer. Anticorrelation features appear for every pair of QDs with different sizes to satisfy the resonant conditions of the confinement exciton energy levels. This is the first spatially resolved observation of energy transfer between QDs via an optical near field.

Conversely, no anticorrelation features were found in the spatial distributions of the luminescence intensities from other QDs whose sizes did not satisfy the resonant condition given by Eq. (3.1). This was confirmed by comparing Figure 3.3(a) to Figure 3.3(c). Here, Figure 3.3(c) shows the spatial distribution of the luminescence intensity of peak Z in Figure 3.2(b), which corresponds to cubic QDs with a side length of 5.3 nm. The white arrow in Figure 3.4 indicates the relationship between Figures 3.3(b) and (c). The negligibly small value of $C$ identified by this arrow confirms the absence of the anticorrelation feature between the exciton energy levels in a 6.3-nm QD and the (1,1,1) level in a 5.3-nm QD as a result of their nonresonant state.

Furthermore, arrows C–E clearly represent large negative values of $C$, which indicates the existence of the anticorrelation feature between higher levels in 6.3-nm QD and other sized QDs. They are; (arrow C) the (2,2,1) level in a 6.3-nm QD and the (1,1,1) level in a 3.9-nm QD, (arrow D) the (3,1,1) level in a 6.3-nm QD and the (1,1,1) level in a 3.6-nm QD, and (arrow E) the (2,2,2) level in a 6.3-nm QD and the (1,1,1) level in a 3.5-nm QD. These anticorrelation features can also be explained by the resonant optical near-field energy transfer. The features represented in this figure support the interpretation of the experimental results. The large cross-correlation coefficient $C$ identified by arrows D and E in Figure 3.4 are evidence of multiple energy transfers. Since the (1,1,1) levels in 3.5- and 3.6-nm QDs resonate or nearly resonate with the (2,1,1) level in a 4.6-nm QD, another route of energy transfer exists in addition to direct transfer from the 3.5- and 3.6-nm QDs to 6.3-nm QDs, that is, the transfer via the 4.6-nm QDs. Such multiple energy transfers increase the value of $C$ identified by arrows D and E in Figure 3.4.

The anticorrelation features appear for every pair of QDs if the resonant conditions of the confinement exciton energy levels are satisfied. Figure 3.5 shows two-dimensional plots of the cross-correlation coefficient $C$ between two QDs. The white broken lines indicate the QD pairs with resonant energy levels of (2,1,1)–(1,1,1), (2,2,1)–(1,1,1), (3,1,1)–(1,1,1), and (2,2,2)–(1,1,1). The large negative value along the broken lines results from the optical near-field energy transfer between QDs. This evidence of the near-field energy transfer between QDs can give rise to a variety of applications, as shown in the following sections.

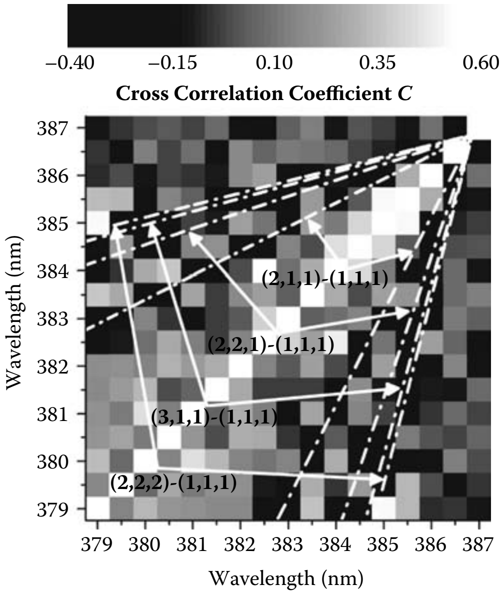

**FIGURE 3.5**
Two-dimensional plots of the cross-correlation coefficient $C$ between two cubic QDs. The white lines show QDs pairs with resonant energy levels of (2,1,1)–(1,1,1), (2,2,1)–(1,1,1), (3,1,1)–(1,1,1), and (2,2,2)–(1,1,1).

## 3.2 Device Operation

Optical fiber transmission systems require increased integration of photonic devices for higher data transmission rates. It is estimated that the size of photonic matrix switching devices should be reduced to a subwavelength scale because in the near future it will be necessary to integrate more than 10,000 × 10,000 input and output channels on a substrate [7]. Because conventional photonic devices, for example, diode lasers and optical waveguides, have to confine light waves within their cavities and core layers, respectively, their minimum sizes are limited by the diffraction of light [21]. Therefore, they cannot meet the size requirement, which is beyond this diffraction limit. An optical near field is free from the diffraction of light and enables the operation and integration of nanometric optical devices. That is, by using a localized optical near field as the carrier, which is transmitted from one nanometric element to another, the above requirements can be met. Based on this idea, nanometer-sized photonic devices have been proposed, which are called *"nanophotonic devices"* [7]. A nanometric all-optical AND gate (i.e., a nanophotonic switch) is one of the most important devices for realizing nanophotonic integrated circuits, and the operation of a nanophotonic AND gate has been already demonstrated using a coupled QD system.

A logic gate, for example, an AND gate and a NOT gate, is a block in a digital system. Logic gates have some inputs and some outputs, and every terminal is under one of two binary conditions, low (0) or high (1), given by different optical intensities for the optical device. The logic state of the input terminal is controlled by the optical input signal, and the logic state of the output terminal changes depending on the logic state of the input terminals. An intensity of approximately zero and a much higher intensity are preferable in the low and high logic states, respectively, such that the ratio of high to low intensity exceeds 30 db. For nanophotonic devices, the high state (1), which is called "true," is defined simply as the higher intensity state and the low state (0), which is called "false," is defined as the lower intensity state.

Section 3.2.1 presents the operation of nanophotonic AND gates using three CuCl QDs [22, 23], whereas Section 3.4.2 presents the use of a ZnO nanorod for room-temperature operation [24]. A nanophotonic NOT gate using CuCl QDs is outlined in Section 3.2.2. The optically forbidden energy transfer between neighboring nanostructures via the optical near-field interaction, which was reviewed in Section 3.1, is a key phenomenon for these operations.

### 3.2.1 Nanophotonic and Gate

Operation of a nanophotonic AND gate using cubic CuCl QDs embedded in a NaCl matrix has been demonstrated [22,23]. When closely spaced QDs with quantized energy levels resonate with each other, near-field energy is transferred between them, even if the transfer is optically forbidden, as noted in Chapter 2 and Section 3.1. Figure 3.6(a) shows the circuit symbol and logic combinations for an AND gate. The output is "true" when both inputs are "true"; otherwise, the output is "false." Figures 3.6(b) and (c) explain the "false" and "true" states of the proposed nanophotonic AND gate. Three cubic QDs, $QD_{inputA}$, $QD_{inputB}$, and $QD_{output}$, are used as the two inputs and output ports of the AND gate, respectively. Assuming an effective size ratio of $1:\sqrt{2}:2$, the quantized energy levels (1,1,1) in $QD_{inputA}$, (2,1,1) in $QD_{output}$, and (2,2,2) in $QD_{inputB}$ resonate with each other. Furthermore, energy levels (1,1,1) in $QD_{output}$ and (2,1,1) in $QD_{inputB}$ also resonate. In the "false" state operation (Figure 3.6(b)), for example, input A is "true" and input B is "false," almost all of the exciton energy in $QD_{inputA}$ is transferred to the (1,1,1) level in the neighboring $QD_{output}$, and then to the (1,1,1) level in $QD_{inputB}$. Therefore, the input energy escapes to $QD_{inputB}$, and consequently no optical output signals are generated from $QD_{output}$. This means that the output is "false." In the "true" state (Figure 3.6(b)) when inputs A and B are both "true," the escape route to $QD_{inputB}$ is blocked by the excitation of $QD_{inputB}$ because of state filling in $QD_{inputB}$ on applying the input B signal. Therefore, the input energy is transferred to $QD_{output}$ and an optical output signal is generated. This means that the output is "true." These operating principles are realized with the condition $\tau_{ex} > \tau_{et} > \tau_{sub}$, where $\tau_{ex}$, $\tau_{et}$, and $\tau_{sub}$ are the exciton lifetime, energy transfer time between QDs, and inter sublevel transition time, respectively. Since $\tau_{ex}$, $\tau_{et}$, and $\tau_{sub}$ are a few nanoseconds, 100 ps, and a few picoseconds, respectively,

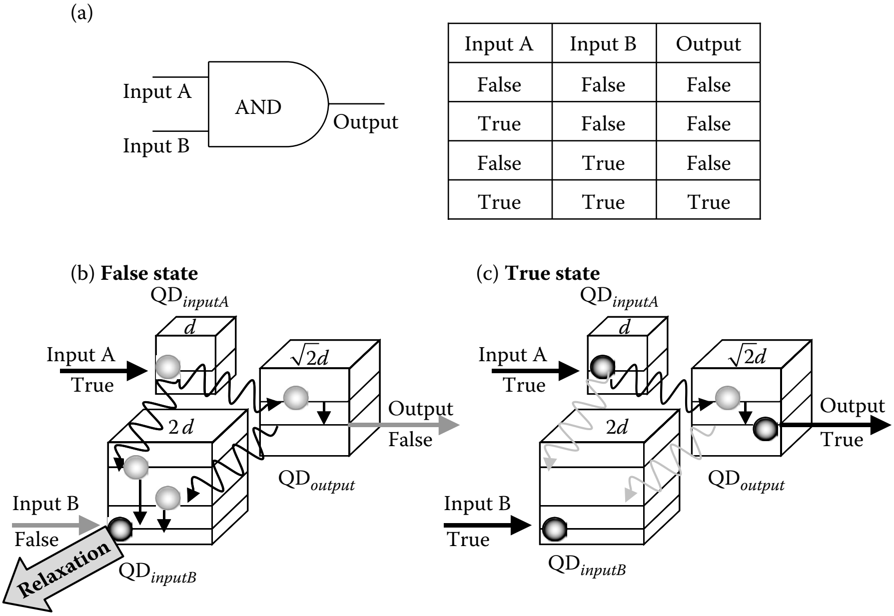

| Input A | Input B | Output |
|---|---|---|
| False | False | False |
| True | False | False |
| False | True | False |
| True | True | True |

**FIGURE 3.6**
Principle of AND-gate operation. (a) The circuit symbol and logic combinations for an AND gate. (b) and (c) The "false" and "true" states of the nanophotonic AND gate.

for the CuCl QDs used in a NaCl matrix, the condition of operation described in Section 3.1 is satisfied.

In an experiment using CuCl QDs embedded in a NaCl matrix, a double-tapered UV fiber probe was fabricated using chemical etching and coated with 150-nm-thick aluminum (Al) film. An aperture less than 50 nm in diameter was formed by the pounding method [20]. To confirm the AND-gate operation, the fiber probe was used to search for a trio of QDs that had an effective size ratio of $1:\sqrt{2}:2$. Since the homogeneous line width of a CuCl QD increases with the sample temperature [25,26], the allowance in the resonatable size ratio is 10% at 15 K. The separation of the QDs must be less than 30 nm for operation of the proposed AND gate because the energy transfer time increases with the separation; moreover, it must be shorter than the exciton lifetime. It is estimated that at least one trio of QDs that satisfies these conditions exists in a $2 \times 2$ $\mu$m scan area. To demonstrate AND-gate operation, a QD trio had to be found in the sample, as shown in Figure 3.6.

Near-field photoluminescence (PL) pump-probe spectroscopy was used to find the QD trio by fixing the fiber probe under three excitation conditions: (1) with the pump laser only ($\lambda = 385$ nm), (2) with the probe laser only ($\lambda = 325$ nm), and (3) with both the pump and probe lasers. The wavelength of the pump laser was tuned to the (1,1,1) exciton energy level in a 6.3-nm CuCl QD. To clarify the PL difference with and without the pump, the

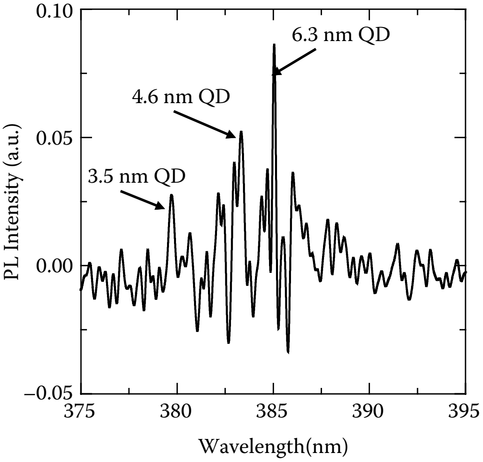

**FIGURE 3.7**
Near-field differential PL spectra measured at the position of a QD trio acting as a nanophotonic AND gate.

differential PL intensity ($PL_{diff}$) was defined as $PL_{diff} = PL_{pump\&probe} – PL_{pump} – PL_{probe}$, where $PL_{pump}$, $PL_{probe}$, and $PL_{pump\&probe}$ are the PL intensities measured under conditions (1), (2), and (3), respectively. Figure 3.7 shows the $PL_{diff}$ spectrum obtained at the position where the QD trio exists. In this figure, two satellite peaks appear at the positions of the (1,1,1) levels in the 4.6-nm and 3.5-nm QDs. The appearance of the satellite peaks means that the AND-gate system proposed in Figure 3.6 was present in the area under the probe. In other words, a trio of cubic QDs with sizes of 3.5, 4.6, and 6.3 nm existed. Because their effective respective sizes $L - a_B$ were 2.8, 3.9, and 5.6 nm ($a_B$: an exciton Bohr radius of 0.68 nm in CuCl), the size ratio was close to $1:\sqrt{2}:2$ and they could be used as $QD_{inputA}$, $QD_{output}$, and $QD_{inputB}$, respectively. The pumping to the 6.3-nm QD blocks the energy transfer from the 3.5-nm and 4.6-nm QDs to the 6.3-nm QD because of state filling of the 6.3-nm QD, and the 3.5-nm and 4.6-nm QDs emit light that results in the satellite peaks in Figure 3.7. Therefore, a QD-trio for a nanophotonic AND gate was found. The PL peak from the 4.6-nm QD corresponds to the output signal in Figure 3.6(c). The $PL_{diff}$ intensity from the 4.6-nm QD was 0.05–0.02 times the PL intensity from the 6.3-nm QD, which was obtained with the probe laser only. This value is quite reasonable considering the pumping pulse energy density of 10 $\mu W/cm^2$ because the probability density of excitons in a 6.3-nm QD is 0.1–0.05 [25], which is close to the $PL_{diff}$ intensity from the 4.6-nm QD. This result indicates that the internal quantum efficiency of the AND-gate system is close to unity.

In the experiment examining the AND-gate operation, the second harmonics of Ti:sapphire lasers (wavelengths 379.5 and 385 nm), which were tuned to the (1,1,1) exciton energy levels of $QD_{inputA}$ and $QD_{inputB}$, respectively,

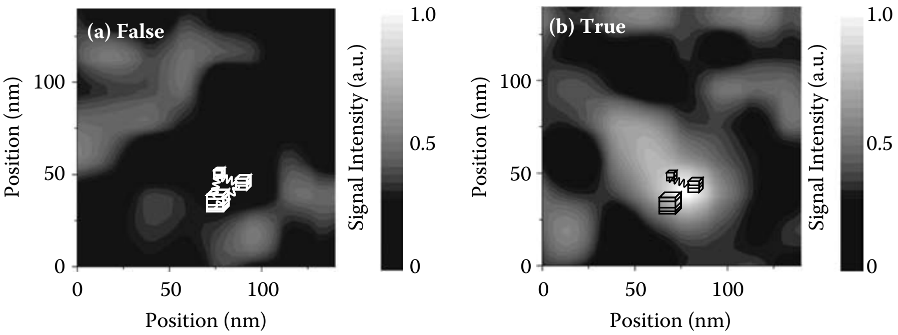

**FIGURE 3.8**
Spatial distribution of the output signal from the nanophotonic AND gate in the "false" (a) and "true" (b) states measured using near-field microscopy.

were used as the signal light sources for inputs A and B. The output signal was collected by the fiber probe, and its intensity was measured using a cooled microchannel plate after passing through three interference filters of 1 nm bandwidth tuned to the (1,1,1) exciton energy level in $QD_{output}$ at 383 nm. Figures 3.8(a) and (b) show the spatial distribution of the output signal intensity in the "false" state (i.e., with one input signal only) and in the "true" state (i.e., with both input A and input B signals) using near-field spectroscopy at 15 K. The insets in this figure are schematic drawings of the existing QD trio used for the AND gate, which was confirmed by the near-field PL spectra. Here, separation of the QDs by less than 20 nm was estimated theoretically from time-resolved PL measurements, as explained in the next paragraph (see the illustrations in Figure 3.8). In the "false" state, no output signal was observed because the energy of the input signal was transferred to $QD_{inputB}$ and swept out as PL at 385 nm. To quench the output signal in the "false" state, which was generated by accumulating excitons in $QD_{inputB}$, the input signal density to $QD_{inputA}$ was regulated to less than 0.1 excitons in $QD_{inputB}$. In the "true" state, a clear output signal was obtained. The output signal was proportional to the intensity of the input B signal, which had a density of 0.01 to 0.1 excitons in $QD_{inputB}$.

Next, the dynamic properties of the nanophotonic AND gate were evaluated using the time-correlation single-photon counting method. As a pulse-input B signal source, the 385 nm second harmonic of a mode-locked Ti:sapphire laser was used. The repetition rate of the laser was 80 MHz. To avoid cross talk originating from spectral broadening of the pulse duration between input signals A and B, the pulse duration of the mode-locked laser was set to 10 ps. The time resolution of the experiment was 15 ps. Figure 3.9 shows the temporal evolution of the input B pulse signal (lower part) applied to $QD_{inputB}$ and the output signal (upper part) from $QD_{output}$. The output signal increases synchronously with the input B pulse within less than 100 ps, which agrees with the theoretically expected result based on the Yukawa model [16]. As this

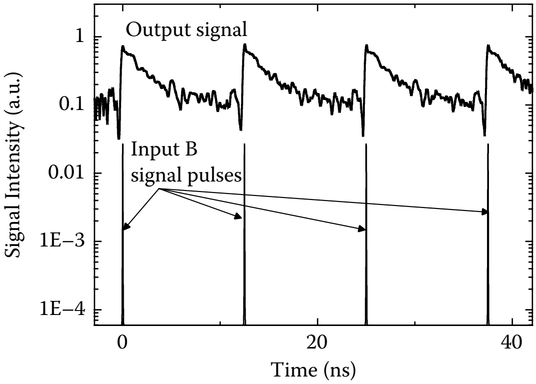

**FIGURE 3.9**
Temporal evolution of the input B pulse signal (upper part) and output signal (lower part) from the nanophotonic AND gate located in the dashed circle in Figure 3.8(b). The duration and repetition rate of the control pulse were 10 ps and 80 MHz, respectively.

signal rise time is determined by the energy transfer time between the QDs, the separation between the QDs can be estimated from the rise time as being less than 20 nm; the rise time can be shortened to a few picoseconds by decreasing the separation of the QDs. Since the decay time of the output signal is limited by the exciton lifetime, this nanophotonic AND gate can be operated at a few hundred megahertz, and the operating frequency can be increased to several gigahertz by exciton quenching using plasmon coupling [27]. The output signal ratio between "true" and "false" was about 10, which is sufficient for use as an all-optical AND gate, and can be increased using a saturable absorber and electric field enhancement of the surface plasmon [28].

The advantages of this nanophotonic device are its small size and high-density integration capability based on the locality of the optical near field. The figure of merit (FOM) of an optical AND gate should be more important than the switching speed. Here, the FOM is defined as $F = C/Vt_{sw}P_{sw}$, where $C$, $V$, $t_{sw}$, and $P_{sw}$ are the "true"–"false" (ON–OFF) ratio, volume of the device, switching time, and switching energy, respectively. Table 3.1 compares the nanophotonic AND gate and conventional photonic gates. The FOM of the AND gate is 10–100 times higher than that of conventional photonic gates because its volume and switching energy are $10^{-5}$ times and $10^{-3}$ times those of conventional photonic gates, respectively. The materials and fabrication methods for realizing practical nanophotonic devices will be reviewed in Section 3.4 and Chapter 4.

### 3.2.2 Nanophotonic NOT Gate

A nanophotonic NOT gate is a key device for realizing a functionally complete set of logic gates for nanophotonic systems, and its operation is demonstrated in this section using CuCl QDs [29]. Figure 3.10 shows a schematic

**TABLE 3.1**

Figure of merits of an optical AND-gate (*$n$ is a real number much larger than unity)

| Classification | Size: $V$ | Switching Time: $t_{sw}$ | Switching Energy: $P_{sw}$ | True-False Ratio: $C$ | FOM: $F$ |
|---|---|---|---|---|---|
| Nanophotonic | $(\lambda/10)^3$ | <100 ps | 1 photon | 10 | >1 |
| Sublevel transition | $(n\lambda)^{3*}$ | 100 fs | $10^3$ photons | $10^3$ | $10^{-1}$ |
| Mach-Zhender | $(n\lambda)^3$ | 10 ps | $10^{-18}$ J | $10^2$ | $10^{-2}$ |
| $\chi^{(3)}$: Nonresonant | $(n\ \lambda)^3$ | 10 fs | $10^6$ photons | $10^3$ | $10^{-3}$ |
| $\chi^{(3)}$: Resonant | $(n\lambda)^3$ | 1 ns | $10^3$ photons | $10^4$ | $10^{-4}$ |
| Optical MEMS | $(n\lambda)^3$ | 1$\mu$s | $10^{-18}$ J | $10^4$ | $10^{-5}$ |

explanation of the nanophotonic NOT gate. $QD_{IN}$ and $QD_{OUT}$ correspond to the input and output terminals of the NOT gate, respectively. Assuming a pair of QDs with a size ratio of $1+\alpha:\sqrt{2}$ ($\alpha << 1$), the quantized energy levels with the set of quantum numbers (2,1,1) in $QD_{IN}$ and (1,1,1) in $QD_{OUT}$

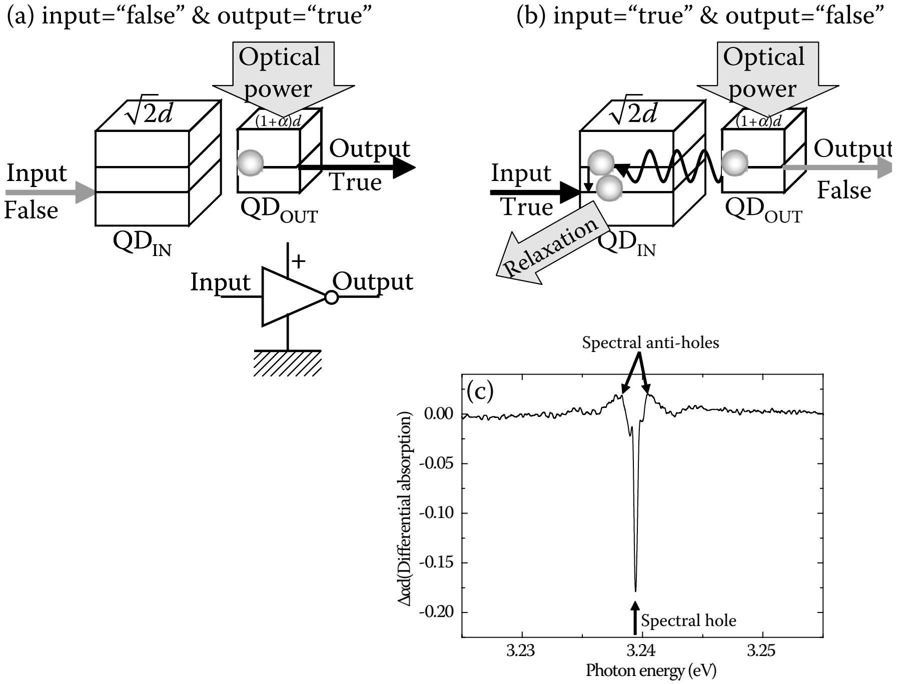

**FIGURE 3.10**

A nanophotonic NOT gate. (a) and (b) Schematic explanation of the "true" and "false" states using cubic QDs. (c) The experimental result of hole burning for CuCl QDs embedded in a NaCl matrix at 5 K.

are slightly nonresonant with each other. The energy from the optical power supply generates an exciton in $QD_{OUT}$. Without the input signal (i.e., the input is "false"), the exciton in $QD_{OUT}$ disappears and emits a photon, which is observed as an output signal, as shown in Figure 3.10(a). That is, input = "false" and output = "true." Conversely, by applying the input signal (i.e., the input is "true"), the energy level (2,1,1) in $QD_{IN}$ becomes resonant to (1,1,1) in $QD_{OUT}$ because of broadening of its line width. This broadening was confirmed experimentally for CuCl QDs. Figure 3.10(c) shows the spectral hole in the absorption spectrum of CuCl QDs observed in a far-field hole-burning experiment at 5 K; antiholes appear on both sides of the spectral hole. This experimental result shows that the excitation broadens the homogeneous line width of QDs, which might arise from shortening of the phase relaxation time of the excitons in QDs because of carrier–carrier scattering. Consequently, the exciton energy in $QD_{OUT}$ is transferred to $QD_{IN}$ via an optical near-field interaction [11], which suppresses output signal generation (Figure 3.10(b), that is, input = "true" and output = "false"). As a result, the temporal behavior of the output signal is the inverse of that of the input signal. By selecting a suitable threshold to distinguish "true" and "false," these behaviors are used for a NOT gate.

CuCl QDs embedded in a NaCl matrix were used to verify operation of the NOT gate, as CuCl QDs offer discrete energy levels similar to the exciton described in Figure 3.10 [13]. The mean size of the QDs was 4.1 nm and the mean distance between the QDs was 25 nm. In the experiment, the second harmonics of a continuous-wave (CW) Ti:sapphire laser ($\hbar\omega = 3.2704$ eV) and a mode-locked Ti:sapphire laser ($\hbar\omega = 3.2195$ eV) were used as the optical power supply and input signal pulse, respectively. The respective power densities were 1 and 2 W/cm$^2$ at the sample surface. Under the excitation condition, fewer than 0.1 excitons occurred in a QD. These lasers excited the sample from its back and the output signal was observed using a near-field spectrometer in collection mode. The sample temperature was controlled at 15 K. To find the QD pair acting as a nanophotonic NOT gate, the QD positions were mapped by measuring the luminescence distribution on the sample, which was obtained using a near-field spectrometer using He–Cd laser excitation ($\hbar\omega = 3.81$ eV). The signal was observed after several QD pairs were selected as candidates for nanophotonic NOT-gate operation. Finally, a nanophotonic NOT gate was found, with the probability of about one device per 1 $\mu$m$^2$ of scanning area. Figure 3.11(a) shows the spatial distribution of the optical near-field output-signal intensity when an input signal is "false" (i.e., with the optical power supply only). Figure 3.11(b) shows the distribution when the input signal is "true." The insets in this figure are schematic drawings of an existing QD pair that function as a NOT gate, which was confirmed from the PL spectra. The sizes of the two QDs estimated from the wavelengths of their luminescence were 5.0 and 6.3 nm, which satisfy the NOT-gate operation condition, as shown in Figure 3.10. Note that the photon energy of the optical power supply ($\hbar\omega = 3.2704$ eV) is maintained nonresonant to the (1,1,1) exciton level in the 5.0-nm QD ($\hbar\omega = 3.2304$ eV) to decrease

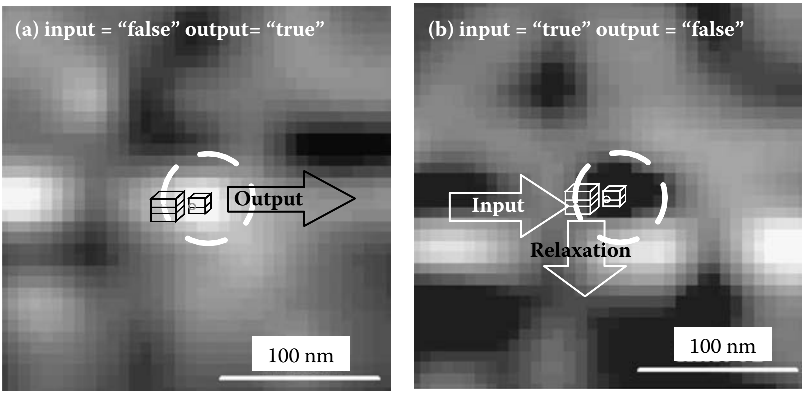

**FIGURE 3.11**
The spatial distribution of the output signal from a nanophotonic NOT gate measured using near-field microscopy at Input = "false" (a) and Input = "true" (b).

the artifact originating from the laser by using narrowband optical filters and observing a clear output signal. Sufficiently low optical power was supplied to the 5.0-nm QD from neighboring QDs [11,30]. The NOT-gated signal appears at the center of the dashed circle in Figure 3.11, from which the size of the device was estimated to be 20 nm. Comparison of Figs. 3.11(a) and (b) clearly demonstrates the operation of a NOT gate.

The dynamic behavior of the NOT gate was observed using the time-correlation single-photon counting method. Figure 3.12 shows the temporal evolution of the output signal. The horizontal dashed line indicates the output signal level without the input signal pulses (i.e., the input is "false"). Without

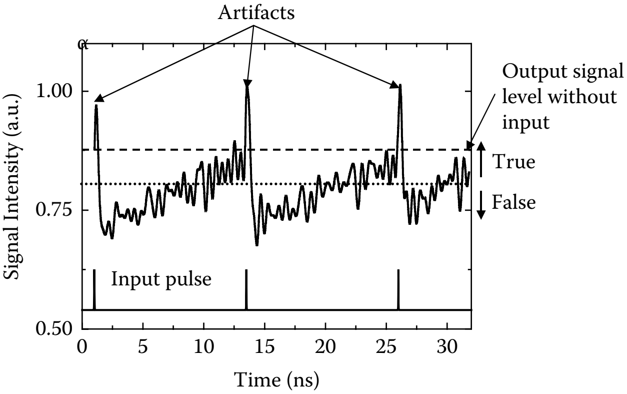

**FIGURE 3.12**
The temporal evolution of the output (upper) and input pulse (lower) signals from the nanophotonic NOT gate circled in Figure 3.11.

the input pulses, the signal level is constant, since a CW-laser was used as the optical power supply. This signal level is defined as "true." With the input pulses, the output signal increases within a time period shorter than the time resolution of 20 ps because of the artifact of the input pulses, and it decreases to a level lower than the initial level. Here, the signal level lower than the dotted line is defined as "false." Then, the output signal level becomes "false" 50 ps after the "true" input pulse. The fall time of the output signal to the minimum level is about 100 ps, which corresponds to the energy transfer time between QDs. The "false" output signal level recovers to the "true" level within 10 ns. The recovery time is longer than the exciton lifetime in 6.3-nm CuCl QDs ($\tau_{ex}$ ~ 1 ns) because the energy transfer from the optical power supply affects the recovery. That is, the recovery time depends on the competition between exciton annihilation via recombination and exciton creation via energy transfer.

The advantages of this nanophotonic NOT gate are its small size and low power consumption, as explained in Section 3.2.1.

## 3.3 Interconnection with Photonic Devices

An interconnection device needs to be developed to collect the incident propagating light and drive the nanophotonic device for efficient operation of the system [7,31,32]. Conventional far-field optical devices, such as convex lenses and concave mirrors, cannot be used for this interconnection because of their diffraction-limited operation. This section demonstrates a novel optical device, the *optical nanofountain,* which concentrates optical energy in a nanometric region using optical near-field energy transfer among QDs. This nanometric optical device enables not only highly efficient interconnection to nanophotonic devices, but also a variety of nanometric optical operations and measurements, such as a nanometric optical tweezers and highly sensitive nanometric-resolution microscopes.

As noted [10,11], the principle of the energy transfer among QDs is equivalent to that of the light-harvesting photosynthetic system, which concentrates and harvests optical energy into nanometric photosynthetic systems in a sophisticated manner. Figure 3.13 shows a schematic explanation of the photosynthetic purple bacteria *Rhodopseudomonas acidophila* [33,34], which has two light-harvesting antennae: LH1 and LH2. LH1 contains a 32-bacteriochlorophyll (BChl) ring and LH2 contains a B800 ring with nine BChls and a B850 ring with 18 BChls. They harvest photons and efficiently transfer the excitation energy from B800 to LH1, where the excitonic energy of B800 is higher than that of LH1. This unidirectional energy transfer is a result of the nanometric dipole–dipole interaction, that is, an optical near-field interaction [16], among BChl rings with low energy dissipation [8]. The optical nanofountain, i.e., the optical energy concentrator, operates in the same manner as the light-harvesting system in photosynthetic bacteria.

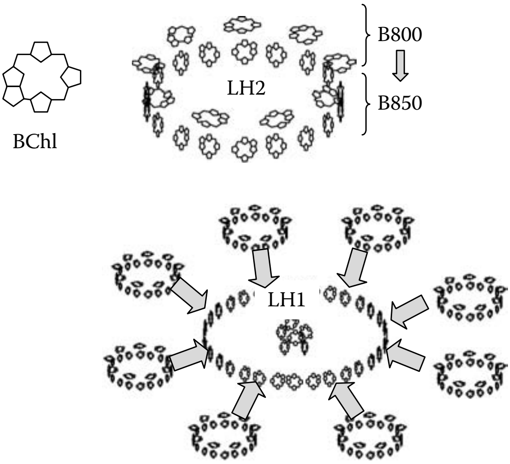

**FIGURE 3.13**
Schematic explanation of the photosynthetic purple bacteria *Rhodopseudomonas acidophila.*

The optical nanofountain is operated using the energy transfer between QDs via an optical near-field interaction, as shown in Figure 3.14(a) [16–18]. When closely spaced QDs with quantized energy levels resonate with each other, near-field energy is transferred between them. Assuming that an effective size ratio between closely located cubic QD-A and QD-B is $1:\sqrt{2}$, the quantized energy levels (1,1,1) in QD-A and (2,1,1) in QD-B resonate with each other, so that almost all of the excitation energy in QD-A is transferred to the (1,1,1) level in QD-B via near-field energy transfer and subsequent intersublevel relaxation [18]. This unidirectional energy transfer from smaller to larger QDs concentrates the optical energy in a nanometric region in a biomimetic manner. When different sized QDs with resonant energy sublevels are distributed as shown in Figure 3.14(b), energy transfer occurs via the optical near field, as illustrated by the arrows. Light incident to the QD array is ultimately concentrated in the largest QD. The area of optical energy concentration corresponds to the size of the QD.

The name optical nanofountain was proposed because light spurts from the largest QD after it is concentrated by stepwise energy transfer from smaller neighboring QDs, so that this device looks like a fountain in a basin, as shown schematically in Figure 3.14(c). From the experimental tests of nanophotonic AND-gate operation in Section 3.2.1, the concentration efficiency of this device should be close to unity because no other possible relaxation paths exist in the system. The operation of an optical nanofountain was demonstrated using CuCl cubic QDs embedded in a NaCl matrix. The average QD size was 4.2 nm and the average separation was less than 20 nm. Although the QDs have an inhomogeneous size distribution and are arranged in the matrix randomly, the operation can be confirmed if an appropriate QD group is found using a nanometric-resolution near-field spectrometer. For the operation, the optimum sample temperature $T$ was 40 K. At $T < 40$ K, the resonant condition becomes tight

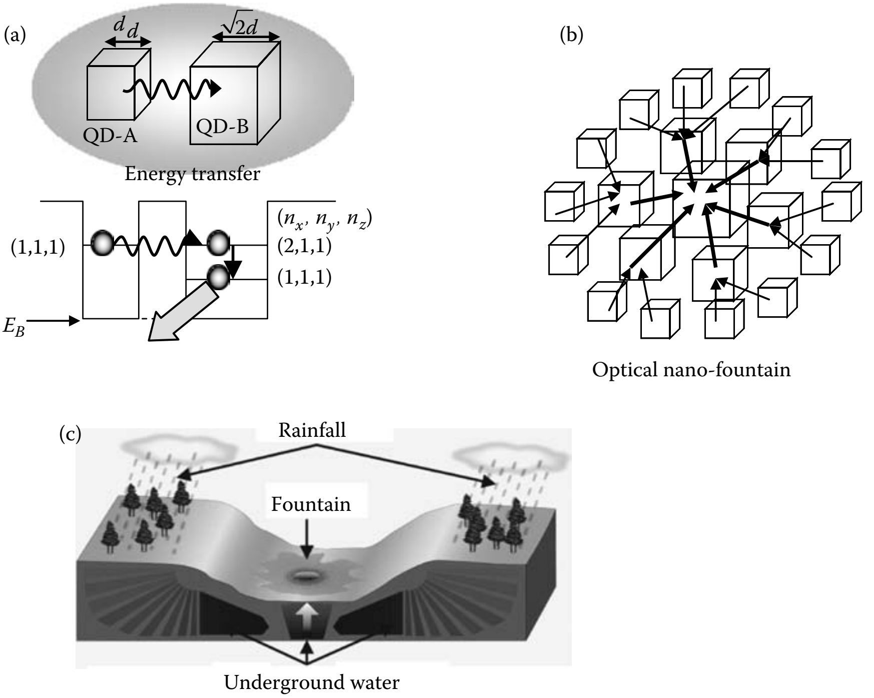

**FIGURE 3.14**
Optical nanofountain. (a) Schematic explanation of the energy transfer between QDs via an optical near-field interaction. $E_{nx}$, $E_{ny}$, $E_{nz}$ ($n_x$, $n_y$, $n_z$) = (1,1,1) or (2,1,1) is the quantum number representing the excitonic energy level in a QD. (b) Schematic explanation of the optical nanofountain and unidirectional energy transfer. (c) Schematic drawing of a nanofountain in a basin.

because of narrowing of the homogeneous line width of the quantized energy sublevels, while at T > 40 K, the unidirectional energy transfer is obstructed by the thermal activation of excitons in the QDs. A 325-nm He–Cd laser was used as the excitation light source. A double-tapered UV fiber probe with an aperture 20 nm in diameter was fabricated using chemical etching and coated with a 150-nm-thick Al film to ensure sufficiently high detection sensitivity [19].

Figure 3.15(a) shows a typical near-field PL spectrum of the sample in collection-mode operation [17]. It is broadened inhomogeneously because of the quantum size effect and size distribution of the QDs. The PL of the exciton molecules has never been observed since the excitation density is less than 1 W/cm². The spectral curve includes several fine peaks, which are the PL spectra that come from different sized QDs. Because of the size-selective QD position from the spatial distribution of the PL peak intensity, the two-dimensional scanning measurement of the PL intensity collected by the photon energy allows us to search for QDs acting as optical nanofountains. At 40 K, approximately one optical nanofountain was found in a 5 × 5 $\mu$m region on the sample surface experimentally.

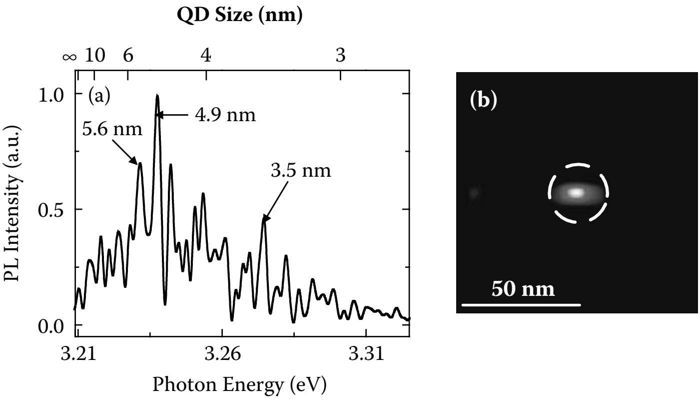

**FIGURE 3.15**
Experimental results for an optical nanofountain. (a) Near-field PL spectrum of CuCl QDs at 40 K. The relationship between the photon energy of PL and the size of the QDs is shown above and below the horizontal axes. (b) Spatial distribution of the PL intensity in an optical nanofountain. The bright spot surrounded by a dashed circle is the focal spot.

Figure 3.15(b) shows the typical spatial distribution of the PL from QDs operating as an optical nanofountain. Here, the collected PL photon energy, $E_p$, was 3.215 eV $\leq E_p \leq$ 3.350 eV, which corresponds to the PL from QDs of size 2.5 nm $\leq L \leq$ 10 nm. The bright spot inside the dashed circle corresponds to a spurt from an optical nanofountain, that is, the focal spot of the nanometric optical condensing device. The diameter of the focal spot was less than 20 nm, which was limited by the spatial resolution of the near-field spectrometer. From the Rayleigh criterion (i.e., resolution = $0.61 \cdot \lambda/\mathrm{NA}$) [35], its numerical aperture (NA) was estimated to be 12 for $\lambda$ = 385 nm. To demonstrate the detailed operating mechanism of the optical nanofountain, we show the size-selective PL intensity distribution; that is, the photon energy is shown in Figures 3.16(a)–(d). The dashed circles and areas scanned by the probe are equivalent to those in Figure 3.15(b). The PL intensity distribution is shown using a gray scale, with normalized scales of (a) 0–0.6, (b) 0–0.2, (c) 0–0.1, and (d) 0–1. The cubes represent QDs whose positions were estimated from the PL intensity distribution. In Figure 3.16(a), a single QD of 6 nm $\leq L \leq$ 10 nm is observed at the center. In Figures 3.16(b) and (c), the observed QDs are 4 nm $\leq L \leq$ 6 nm and 2.5 nm $\leq L \leq$ 4 nm, respectively, and they are located around the dashed circles. Figure 3.16(d) shows the total luminescence intensity distribution obtained as the integral of Figures 3.16(a)–(c). The bright spot in this figure agrees with the position of the largest QD in Figure 3.16(a) and the smaller QDs are distributed around it. This means that the optical energy is concentrated to the largest QD. The PL intensity at the bright spot is more than five times greater than that from a single isolated QD with $L$ = 10 nm, while the PL intensities of the smaller surrounding QDs are lower than those of the isolated QDs. This indicates that optical energy is transferred

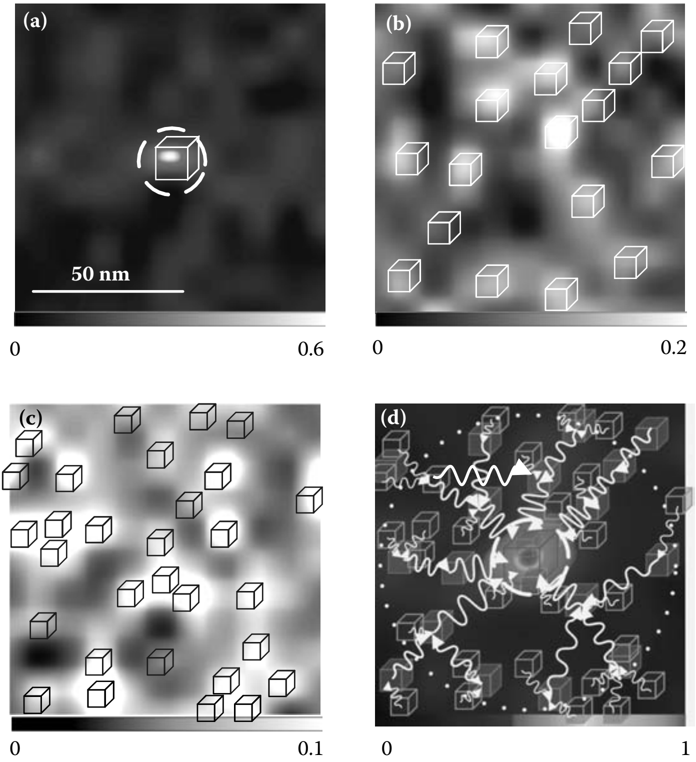

**FIGURE 3.16**
Spatial distribution of the PL intensity of CuCl QDs of (a) 6 nm ≤ $L$ ≤ 10 nm (3.215 eV ≤ $E_p$ ≤ 3.227 eV), (b) 4 nm ≤ $L$ ≤ 6 nm (3.227 eV ≤ $E_p$ ≤ 3.254 eV), (c) 2.5 nm ≤ $L$ ≤ 4 nm (3.271 eV ≤ $E_p$ ≤ 3.350 eV), and (d) the total for 2.5 nm ≤ $L$ ≤ 10 nm (3.215 eV ≤ $E_p$ ≤ 3.350 eV) for the same area as in Figure 3.15(b). The cubes represent the positions estimated from the PL intensity distribution.

from smaller to larger QDs and is concentrated in the largest QD, as shown by the arrows in Figure 3.16(d). This device can also be used as a frequency selector based on the resonant frequency of the QDs, which can be applied, for example, to frequency domain measurements, multiple optical memories, multiple optical signal processing, and frequency division multiplexing. The application of the optical nanofountain will be discussed in Chapter 5.

## 3.4 Room-Temperature Operation

Practical nanophotonic devices for room-temperature operation are under development using III-V compound semiconductor QDs and ZnO nanorods. They are reviewed in this section.

### 3.4.1 Using III-V Compound Semiconductor QDs

Of the III-V semiconductors, InAlAs is one of the best materials for such practical devices because its bandgap energy can be controlled widely from 0.3 to 2.2 eV and it is easy to prepare samples with a high density of QDs. As the first step, $In_{0.5}Al_{0.5}As$ QDs were prepared using molecular beam epitaxy (MBE) in S-K mode growth [36] to make the bandgap energy exceed 1.6 eV, at which standard photodetectors have high sensitivity. Figures 3.17(a) and (b) show sample structures and an atomic force microscope (AFM) image after the growth of QD layers. To operate the nanophotonic device, double QD layers were grown; the mean QD size was 5 nm in height and 25 nm in diameter. Using this fabrication method, the QDs could be aligned vertically and the sheet density of QDs was $10^{11}$ $cm^{-2}$. Therefore, both the vertical and horizontal distances between QDs were about 30 nm, and vertical and horizontal coupling of QDs was expected via the optical near-field interactions.

To investigate the suitability of the fabricated sample as a nanophotonic device, the far- and near-field PL spectra were measured. In Figure 3.17(c), the

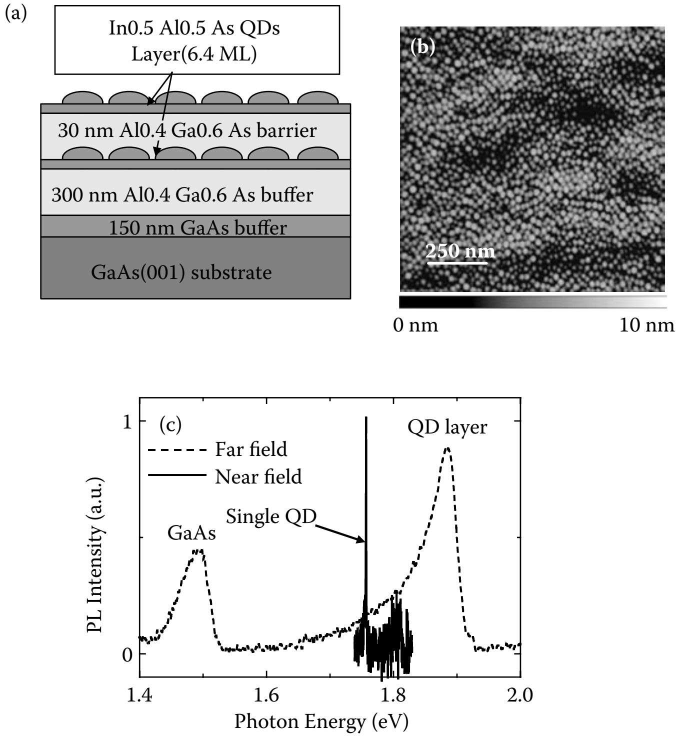

**FIGURE 3.17**
InAlAs QDs and PL spectra. (a) The structures of InAlAs QDs. (b) An AFM image after the growth of QD layers. (c) Far-field (dashed curve) and near-field (solid curve) PL spectra of InAlAs QDs.

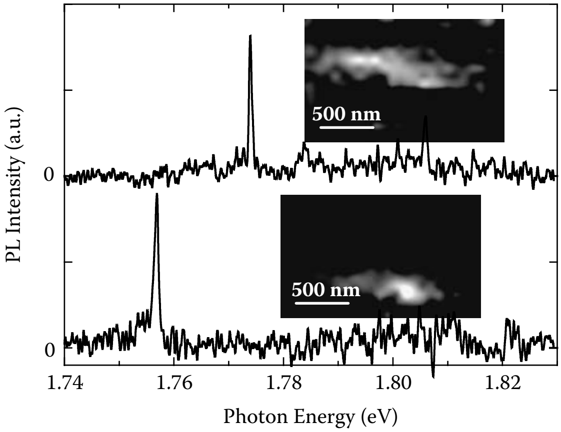

**FIGURE 3.18**
Near-field PL spectra of different InAlAs QDs at different positions. The insets show the PL intensity distributions on the sample surface.

dashed curve shows the far-field PL spectrum at 12 K. The PL around 1.8 eV comes from the $In_{0.5}Al_{0.5}As$ QDs that were broadened owing to their size inhomogeneity. The solid curve shows the typical near-field PL spectrum at 11 K. For near-field spectroscopy, a He–Ne laser ($\hbar\omega = 1.958$ eV) was used to obtain the PL peak from a single QD at 1.7569 eV in illumination-collection mode operation. The spectral line width was less than 500 $\mu$eV. It was free from size inhomogeneity and limited by the spectral resolution of the spectrometer. This narrowness of the PL spectra indicates that the sample was of high quality.

Figure 3.18 shows near-field PL spectra at different positions on the sample surface. The insets show the intensity distributions of the respective PL peaks $QD_1$ and $QD_2$. As their photon energies and intensity distributions differed, PL peaks $QD_1$ and $QD_2$ came from different QDs, confirming the existence of several QDs within an area of 1 $\mu m^2$. The observed density of QDs was much lower than the density of the QDs measured using AFM because the energy transfer to the nonradiative relaxation path in the surface QD layer and nonradiative energy dissipation caused the low QD density measured using near-field spectroscopy. The PL efficiency of QDs without a cap layer is very low because of nonradiative recombination [37]. When horizontal and vertical energy transfer to the top QD layer takes place without a cap layer, most of the QDs dissipate the excitation energy nonradiatively. This supports the postulate that the sample acted as the desired nanophotonic device because the energy transfer is necessary for the operation of the nanophotonic device. In addition, in this sample, the intralayer energy transfer is negligible in the experiment because most of the excitation energy was transferred to the QDs with the fastest relaxation time and lowest energy level, and the observed QDs had no transfer destinations (or negligible small), since a single QD was observed with high-intensity PL.

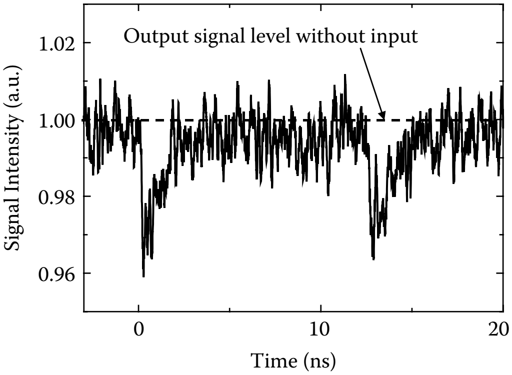

**FIGURE 3.19**
Temporal evolution of the output signals from the InAlAs QDs acting as a nanophotonic NOT gate.

Figure 3.19 shows the temporal evolution of the signal obtained from the InAlAs QDs. In the measurement, the probe position was fixed at the bright region on the sample surface, that is, the bright spot shown in Figure 3.18, and this region was excited using a CW He–Ne laser ($\hbar\omega$ = 1.958 eV) and mode-locked Ti:sapphire laser ($\hbar\omega$= 1.722 eV). The photon energy of the luminescence collected using a spectral filter was 1.745–1.796 eV. The output signal decreased synchronously with the excitation pulse of the mode-lock laser and recovered to the signal level without pumping. Specifically, the observed QDs acted as a NOT gate. The mechanism of this NOT-gate operation observed in the double-layer InAlAs QDs is explained as follows: With the CW laser only, part of the scanning region is bright because most of the excitation energy is dissipated via nonradiative relaxation following the energy transfer between QDs. Some of the excitation energy can reach the radiative QDs. With the CW and mode-locked lasers, the energy transfer paths to the radiative QDs disappear because other relaxation paths to the nonradiative QDs are generated because of spectral broadening by the mode-locked laser pulses.

### 3.4.2 Using a ZnO Nanorod with Quantum Wells

This section reviews AND-gate operation using ZnO nanorods [38]. ZnO is a promising material for realizing the room-temperature operation of nanophotonic devices since its exciton binding energy, $E_{ex}$, exceeds the thermal energy (26 meV) at room temperature. $E_{ex}$ is reported to increase to 110 meV in ZnO/ZnMgO multiple quantum well (QW) structures [39], which is much larger than the value for other materials such as GaN/AlGaN multiple QWs (68 meV) [40], CdSe/ZnSe quantum structures (15 meV) [41], and InAs QDs on GaAs substrate (12 meV) [42]. Furthermore, ZnO/ZnMgO

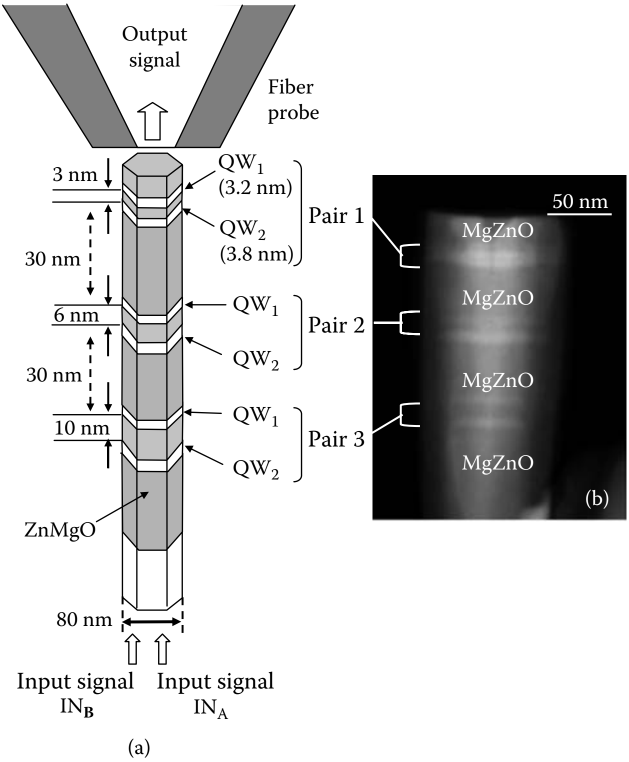

**FIGURE 3.20**
Structure of ZnO/ZnMgO double QWs grown on a ZnO nanorod. (a) Schematic explanation. (b) Z-contrast transmission electron microscopic image.

nanorod heterostructures have been fabricated and the quantum confinement effect has been observed from single QW structures [43].

To confirm the promising performance of the nanophotonic AND gate, three pairs of ZnO/$Zn_{0.8}Mg_{0.2}O$ QWs were fabricated in a ZnO nanorod with a mean diameter of 80 nm using catalyst-free metal–organic vapor phase epitaxy [44]. As shown in Figure 3.20(a), the two QWs were 3.2 ($QW_1$) and 3.8 nm ($QW_2$) thick ($L_w$), and their separations in the three pairs were 3, 6, and 10 nm. Figure 3.20(b) is a transmission electron microscopic image. The routes of energy transfer and subsequent relaxation are shown in Figure 3.21(a). The ground state of the exciton in $QW_1$ ($E_{A1}$, wavelength ($\lambda$) = 361 nm) and first excited state in $QW_2$ ($E_{B2}$) resonate with each other [43]. On applying a single input signal ($IN_A = 1$ and $IN_B = 0$), all the exciton energy in $QW_1$ is transferred to the excited state in the neighboring $QW_2$. Furthermore, since $E_{B2}$ is the dipole-forbidden energy level because of its odd wave function, the energy transferred to $E_{B2}$ relaxes rapidly to the ground state in $QW_2$ ($E_{B1}$, $\lambda = 362$ nm). Consequently, no output signals are generated from $QW_1$. When applying two input signals ($IN_A = 1$ and $IN_B = 1$), the routes of energy

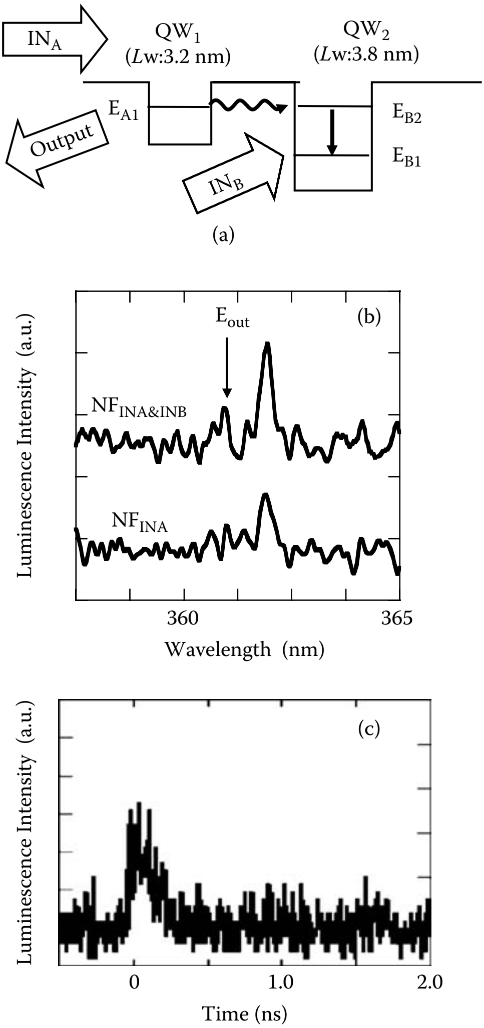

**FIGURE 3.21**
AND-gate operation with ZnO/ZnMgO double QWs. (a) Schematic of the energy transfer and dissipation. (b) $NF_{INA}$ and $NF_{INA\&INB}$ show PL spectra obtained by applying a single input signal $IN_A$ and two ($IN_A$ and $IN_B$) input signals, respectively. (c) Time-resolved PL signal.

transfer to $QW_2$ are blocked by the excitation of $QW_2$. As a result, an output signal is generated from $QW_1$.

Figure 3.21(b) shows the luminescence spectra monitored from the top of the nanorod using the fiber probe (aperture diameter: 30 nm) of a near-field optical spectrometer. A microchannel plate and band-pass filter (1 nm bandwidth, central $\lambda = 361$ nm) were used for the measurement. Curve $NF_{INA}$ was obtained with a single input signal $IN_A$ by illuminating the bottom of the nanorod with CW He–Cd laser light ($\lambda = 325$ nm). No emission was observed from the exciton ground state of $QW_1$ ($E_{A1}$) or the excited state of $QW_2$ ($E_{B2}$) at $\lambda = 361$ nm, indicating that the excited energy in $QW_1$ was transferred to the dipole-forbidden excited state of $QW_2$. On applying the two input signals ($IN_A$ and $IN_B$) simultaneously, the route for the energy transfer from the ground state of $QW_1$ to the excited state of $QW_2$ was blocked because of state filling in the ground state of $QW_2$. As a result, an output signal was generated, which is represented by the spectral peak $E_{out}$ at 361 nm on the curve $NF_{INA\&INB}$. The dynamic behavior of the AND-gate operation was evaluated using the time-correlation single-photon counting method by measuring the time-resolved luminescence signals, as shown in Figure 3.21(c). The rise time is 100 ps, which is determined by the near-field optical coupling strength between the two QWs. Note that the rise times of the three pairs of QWs are not resolved in the curve in this figure because the output signals from these pairs were detected simultaneously using a fiber probe located on the top of the nanorod. However, this value of the rise time is correct because previous papers [38, 45] have estimated values of 36 and 125 ps for QW separations of 3 and 10 nm, respectively. The decay time constant is 483 ps, which is common to the three pairs as it depends on the exciton lifetime in the ground energy level of $QD_2$ ($EB_1$) and is independent of the separation between the two QWs.

Because the spectral width reaches the thermal energy (26 meV) at room temperature, a higher Mg concentration in the barrier layers and narrower $L_w$ are required for room-temperature operation to avoid overlap of the spectral peaks of the ground and first excited states. This can be achieved by using two QWs with $L_w = 1.5$ nm ($QW_1$) and 2 nm ($QW_2$) with a Mg concentration of 50%, where the energy difference between the ground and first excited states in $QW_2$ is 50 meV [46].

## References

1. Goldhaber-Gordon, D., Shtrikman, H., Mahalu, D., Abusch-Magder, D., Meirav, U., and Kastner, M. A., 1998. Kondo effect in a single-electron transistor. *Nature* 391: 156–159.
2. Simmel, F., Blick, R. H., Kotthaus, J. P., Wegscheider, W., and Bichler, M., 1999. Anomalous Kondo effect in a QD at nonzero bias. *Phys. Rev. Lett.* 83: 804–807.
3. Molenkamp, L. W., Flensberg, K., and Kemerink, M., 1995. Scaling of the Coulomb energy due to quantum fluctuations in the charge on a QD. *Phys. Rev. Lett.* 75: 4282–4285.
4. Taut, M., 2000. Solution of the Schrödinger equation for QD lattices with Coulomb interaction between dots. *Phys. Rev. B* 62: 8126–8136.
5. Burkard, G., Seelig, G., and Loss, D., 2000. Spin interactions and switching in vertically tunnel-coupled QDs. *Phys. Rev. B* 62: 2581–2592.
6. Waugh, F., R., Berry, M. J., Mar, D. J., Westervelt, R. M., Campman, K. L., and Gossard, A. C., 1995. Single-electron charging in double and triple QDs with tunable coupling. *Phys. Rev. Lett.* 75: 705–708.

7. Ohtsu, M., Kobayashi, K., Kawazoe, T., Sangu, S., and Yatsui, T., 2002. Nanophotonics: Design, Fabrication, and Operation of Nanometric Devices using Optical Near Fields. *IEEE J. Sel. Top. Quant. Electron.* 8: 839–862.
8. Mukai, K., Abe, S., and Sumi, H., 1999. Theory of rapid excitation-energy transfer from B800 to optically-forbidden exciton state of B850 in the antenna system LH2 of photosynthetic purple bacteria. *J. Phys. Chem. B* 103: 6096–6102.
9. Kagan, C. R., Murray, C. B., Nirmal, M., and Bawendi, M. G., 1996. Electronic Energy Transfer in CdSe QD Solids. *Phys. Rev. Lett.* 76: 1517–1520.
10. Crooker, S. A., Hollingsworth, J. A., Tretiak, S., and Klimov, V. I., 2002. Spectrally Resolved Dynamics of Energy Transfer in QD Assemblies: Towards Engineered Energy Flows in Artificial Materials. *Phys. Rev. Lett.* 89: 186802 1–4.
11. Kawazoe, T., Kobayashi, K., Lim, J., Narita, Y., and Ohtsu M., 2002. Direct Observation of Optically-Forbidden Energy Transfer between CuCl Quantum Cubes via Optical Near-Field. *Phys. Rev. Lett.*, 88: 067404 1–4.
12. Tang, Z. K., Yanase, A., Yasui, T., Segawa, Y., and Cho, K., 1993. Optical selection rule and oscillator strength of confined exciton system in CuCl thin films. *Phys. Rev. Lett.* 71: 1431–1434.
13. Sakakura, N., and Masumoto, Y., 1997. Persistent spectral-hole-burning spectroscopy of CuCl quantum cubes. *Phys. Rev. B* 56: 4051–4055.
14. Ekimov, A. I., Eflos, AI. L., and Onushchenko, A. A., 1985. Quantum size effect in semiconductor microcrystals. *Solid State Commun.* 56: 921–924.
15. Itoh, T., Yano, S., Katagiri, N., Iwabuchi, Y., Gourdon, C., and Ekimov, A. I., 1994. Interface effect on the properties of confined excitons in CuCl microcrystals. *J. Lumin.* 60&61: 396–399.
16. Kobayashi, K., Sangu, S., Ito H., and Ohtsu, M., 2001. Near-field optical potential for a neutral atom. *Phys. Rev. A* 63: 013806 1–9.
17. Ohtsu, M., 1998. *Near-Field Nano/Atom Optics and Technology.* Berlin: Springer.
18. Suzuki, T., Mitsuyu, T., Nishi, K., Ohyama, H., Tomimasu, T., Noda, S., Asano, T., and Sasaki A., 1996. Observation of ultrafast all-optical modulation based on intersubband transition in n-doped quantum wells by using free electron laser. *Appl. Phys. Lett.* 69: 4136–4138.
19. Saiki, T., Mononobe, S., Ohtsu, M., Saito, N., and Kusano J., 1996. Tailoring a high-transmission fiber Probe for photon scanning tunneling microscope. *Appl. Phys. Lett.* 68: 2612–2614.
20. Saiki, T., and Matsuda, K., 1999. Near-field optical fiber probe optimized for illumination-collection hybrid mode operation. *Appl. Phys. Lett.* 74: 2773–1775.
21. Yariv, A., 1971. *Introduction to Optical Electronics,* New York: Holt, Rinehart and Winston.
22. Kawazoe, T., Kobayashi, K., Sangu, S., and Ohtsu, M., 2003. Demonstration of a nanophotonic switching operation by optical near-field energy transfer. *Appl. Phys. Lett.* 82: 2957–2959.
23. Kawazoe, T., Kobayashi, K., Sangu, S., Ohtsu, M., 2003. Demonstrating nanophotonic switching using near-field pump-probe photoluminescence spectroscopy of CuCl quantum cubes. *J. Microscopy* 209: 261–266.
24. Yatsui, T., Sangu, S., Kawazoe, T., Ohtsu, M., An, S.-J., Yoo, J., and Yi, G.-C., 2007. Nanophotonic switch using ZnO nanorod double-quantum-well structures. *Appl. Phys. Lett.* 90: 223110 1–3.

25 *Landolt-Bornstein, Physics of II-VI and I-VII Compounds, Semimagnetic Semiconductors 17b,* 1982. Berlin: Springer-Verlag.

26. Masumoto, Y., Kawazoe, T., and Matsuura, N., 1998. Exciton-confined-phonon interaction in QDs. *J. Lumin.* 76&77: 189–192.
27. Neogi, A., Lee, C. W., Everitt, H. O., Kuroda, T., Tackeuchi, A., and Yablonovitch, E., 2002. Enhancement of spontaneous recombination rate in a quantum well by resonant surface plasmon coupling. *Phys. Rev. B* 66: 153305 1–4.
28. Raether, H., *Surface Plasmons, Vol. III of Springer Tracts in Modern Physics,* 1988. Springer.
29. Kawazoe, T., Kobayashi, K., Akahane, K., Naruse, M., Yamamoto, N., and Ohtsu, M., 2006. Demonstration of nanophotonic NOT gate using near-field optically coupled QDs. *Applied Physics B* 84: 243–246.
30. Kawazoe, T., Kobayashi, K., and Ohtsu, M., 2005. Optical nanofountain: A biomimetic device that concentrates optical energy in a nanometric region. *Appl. Phys. Lett.* 86: 103102 1–3.
31. Nomura, W., Ohtsu, M., and Yatsui, T., 2005. Nanodot coupler with a surface plasmon polariton condenser for optical far/near-field conversion. *Appl. Phys. Lett.* 86: 181108 1–3.
32. Nomura, W., Yatsui, T., and Ohtsu, M., 2006. Efficient optical near-field energy transfer along an Au nanodot coupler with size-dependent resonance. *Appl. Phys. B* 84: 257–259.
33. McDermott, G., Prince, S. M., Freer, A. A., Hawthornthwaite-Lawless, A. M., Papiz, M. Z., Cogdell, R. J., and Isaacs N. W., 1995. Crystal structure of an integral membrane light-harvesting complex from photosynthetic bacteria. *Nature* 374: 517–521.
34. Jordan, P., Fromme, P., Witt, H., T., Klukas, O., Saenger, and W., Krauss, N., 2001. Three-dimensional structure of cyanobacterial photosystem I at 2.5 Å resolution. *Nature* 411: 909–917.
35. Born, M., and Wolf, E., 1983. *Principles of Optics, Sixth Edition,* Pergamon Press.
36. Goldstein, L., Glas, F., Marzin, J. Y., Charasse, M. N., and Roux, G. Le, 1985. Growth by molecular beam epitaxy and characterization of InAs/GaAs strained-layer superlattices. *Appl. Phys. Lett.* 47: 1099–1101.
37. Saito, H., Nishi K., and Sugou, S., 1998. Influence of GaAs capping on the optical properties of InGaAs/GaAs surface QDs with 1.5 $\mu$m emission. *Appl. Phys. Lett.* 73: 2742–2744.
38. Yatsui, T., Sangu, S., Kawazoe, T., Ohtsu, M. An, S.-J., Yoo, J., and Yi, G.-C. 2007. Nanophotonic switch using ZnO nanorod double-quantum-well structures. *Appl. Phys. Lett.* **90**: 223110 1–3.
39. Sun, H. D., Makino, T., Segawa, Y., Kawasaki, M., Ohtomo, A., Tamura, K., and Koinuma, H. 2002. Enhancement of exciton binding energies in ZnO/ZnMgO multiquantum wells. *J. Appl. Phys.* **91**: 1993–1997.
40. Senger R. T., and Bajaj, K. K. 2003. Binding energies of excitons in polar quantum well heterostructures. *Phys. Rev. B* **68**: 205314 1–9.
41. Gindele, F., Woggon, U., Langbein, W., Hvam, J. M., Leonardi, K., Hommel, D., and Selke, H. 1999. Excitons, biexcitons, and phonons in ultrathin CdSe/ZnSe quantum structures. *Phys. Rev. B* **60**: 8773–8782.
42. Wang, P. D., Merz, J. L., Ledentsov, N. N., Kop'ev, P. S., Ustinov, V. M., and Sotomayor Torres, C. M. 1996. Enhanced exciton binding energy in InAs monolayers grown on (311)A GaAs substrates. *Solid State Comm.* **100**: 763–767.
43. Park, W. I., An, S. J., Yang, J.L., Yi, G.-C., Hong, S., Joo, T., and Kim, M. Y. 2004. Photoluminescent properties of ZnO/$Zn_{0.8}Mg_{0.2}O$ nanorod single-quantum-well wtructures. *J. Phys. Chem. B* **108**: 15457–15460.

44. Park, W. I., Yi, G.-C., Kim, M. Y., and Pennycook, S. J. 2003. Quantum confinement observed in ZnO/ZnMgO nanorod heterostructures. *Adv. Mater.* **15**: 526–529.
45. Sangu, S., Kobayashi, K., Shojiguchi, A., Kawazoe, T., and Ohtsu, M. 2003. Excitation energy transfer and population dynamics in a QD system induced by optical near-field interaction. *J. Appl. Phys.* **93**: 2937–2945.
46. Park, W. I., Yi, G.-C., and Jang, H. M. 2001. Metalorganic vapor-phase epitaxial growth and photoluminescent properties of $Zn_{1-x}Mg_xO$ ($0 \le x \le 0.49$) thin films. *Appl. Phys. Lett.* **79**: 2022–2024.

# 4

# *Nanophotonic Fabrication*

This chapter reviews the principle of nanophotonic fabrication based on the localized photon model. The performance of several fabrication methods is presented: photochemical vapor deposition, lithography, and size- and position-controlled growth.

## 4.1 Adiabatic Nanofabrication

As an introduction to nanophotonic fabrication, adiabatic nanofabrication is reviewed; that is, the use of an optical near field can realize nanoscale fabrication and quantitative innovations are demonstrated. Near-field optical chemical vapor deposition (NFO-CVD; Figure 4.1) has been developed, and enables the fabrication of nanometer-scale structures while controlling their size and position precisely [1–6]. That is, the position can be controlled accurately by regulating the position of the fiber probe used to generate the optical near field. To guarantee the generation of an optical near field with sufficiently high efficiency, a sharpened UV fiber probe was used, which was fabricated using a pulling/etching technique [7]. Under the uncoated condition, the diameter of the sharpened probe tip remained sufficiently small, which enabled high-resolution position control and *in situ* shear-force topographic imaging of the deposited nanometer-scale structures. Because the deposition time was sufficiently short, the deposition of metal on the fiber probe and the resultant decrease in the throughput of optical near-field generation were negligible. The separation between the fiber probe and sapphire (0001) substrate was kept within a few nanometers by shear-force feedback control. Immediately after the nanodots were deposited, their sizes and shapes were measured via *in situ* vacuum shear-force microscopy [8], using the same probe as used for deposition. Because of the photochemical reaction between the reactant molecules and the optical near field generated at the tip of an optical fiber probe, NFO-CVD is applicable to various materials, including metals, semiconductors, and insulators.

Conventional optical CVD method uses a light source that resonates the absorption band of metal–organic (MO) vapor and has a photon energy that

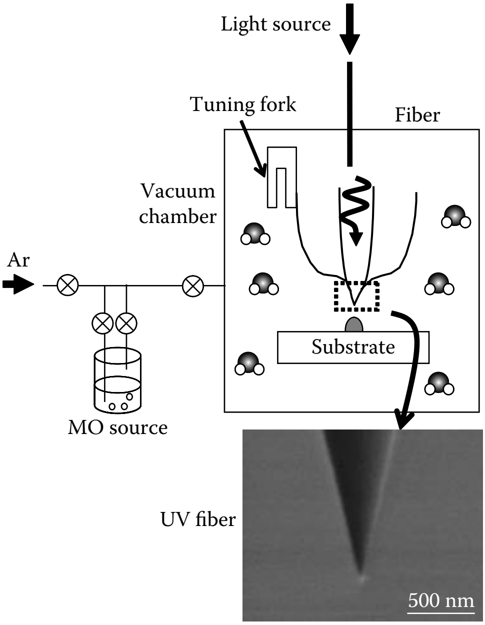

**FIGURE 4.1**
Schematic explanation of NFO-CVD.

exceeds the dissociation energy [9]. Therefore, it utilizes a two-step process: gas-phase photodissociation and subsequent adsorption. In this process, resonant photons excite molecules from the ground state to the excited electronic state and the excited molecules relax to the dissociation channel, and then the dissociated metallic atoms adsorb to the substrate [10]. However, it was found that the dissociated MO molecules migrate on the substrate before adsorption, which limits the minimum lateral size of the deposited dots (Figure 4. 2(a)). A promising method for avoiding this migration is dissociation and deposition in the adsorption phase (Figure 4.2(b)) [11].

An example of NFO-CVD is the deposition of a Zn dot. Because the absorption band edge energy of gas-phase diethylzinc (DEZn) is 4.6 eV ($\lambda$ = 270 nm) [9], a He–Cd laser (3.81 eV, $\lambda$ = 325 nm) was used as the light source for the deposition of Zn; it is nonresonant to gas-phase DEZn. However, a red-shift occurs in the absorption spectrum of DEZn with respect to that in the gas-phase; that is, it resonates the adsorption phase DEZn. The red-shift is attributable to perturbations of the free molecule potential surface in the adsorbed phase [9, 12]. Using a sharpened UV fiber probe, DEZn was dissociated selectively and 20-nm Zn dots were fabricated successfully with 65 nm separation on a sapphire (0001) substrate (see Figure 4.3(a)) [6]. Furthermore, because the nonresonant propagating light that leaked from the probe did not dissociate the gas-phase DEZn, atomic-level sapphire

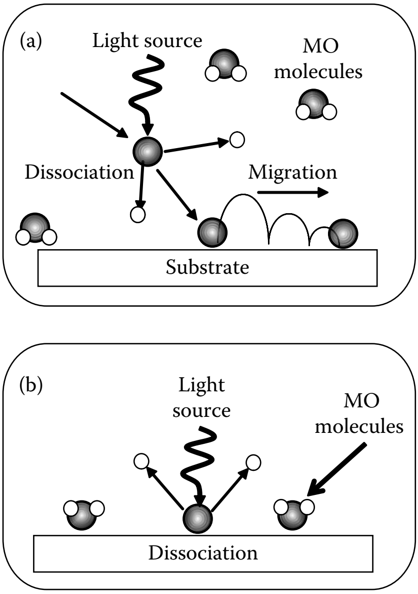

**FIGURE 4.2**
Photodissociation of MO molecules: (a) gas phase and (b) adsorption phase.

steps around the deposited dots were clearly observed after deposition. By changing the reactant molecules during deposition, nanometric Zn and Al dots were deposited successively on the same sapphire substrate with high precision (see Figure 4.3(b)) [4].

To realize sub-10-nm scale controllability in size, the precise growth mechanism of Zn dots with NFO-CVD was investigated [6]. The deposition rate was found to be maximal when the dot grew to a size equivalent to the probe apex diameter. This dependence is accounted for by the theoretically calculated dipole–dipole coupling with a Förster field. The theoretical support and experimental results indicate the potential advantages of this technique for better regulating the size and position of deposited nanometer-scale dots.

Figures 4.4(a) and (b) show scanning electron micrographic (SEM) images of the fiber probe used in this study. The estimated apex diameter, $2a_p$, was 9 nm based on the fitted dashed circle (see Figure 4.4(b)). Figure 4.5(a) shows a shear-force image of four Zn dots deposited with irradiation times of 60 (dot 1), 30 (dot 2), 10 (dot 3), and 5 s (dot 4) with a laser output power $P$ of 5 $\mu$W. The Zn dots were deposited as 300 and 260 nm separation along the $x$- and $y$-axes, respectively, under servo-control of the position of the fiber probe. As shown in the cross-sectional profiles in Figure 4.5(b), Zn dots as small as 30 nm in diameter were fabricated. Their separations are 306 and 299 nm along the $x$-axis and 260 and 254 nm along the $y$-axis, confirming the high

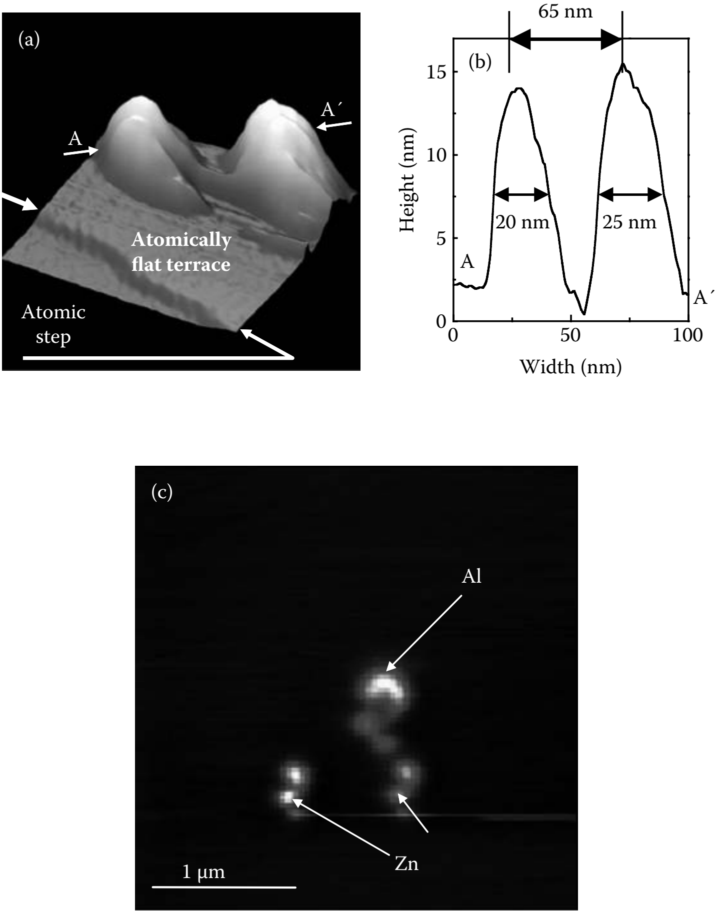

**FIGURE 4.3**
Shear-force image of closely spaced dots: (a) Zn dots. (b) The cross sectional profile along the line indicated by arrows A and A′ in (a). (c) Zn and Al dots.

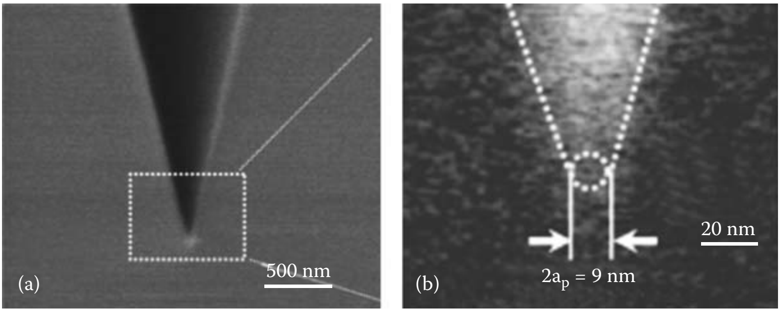

**FIGURE 4.4**
SEM images of an ultraviolet fiber probe. The magnified image of (a) is shown in (b). $2a_p$: apex diameter.

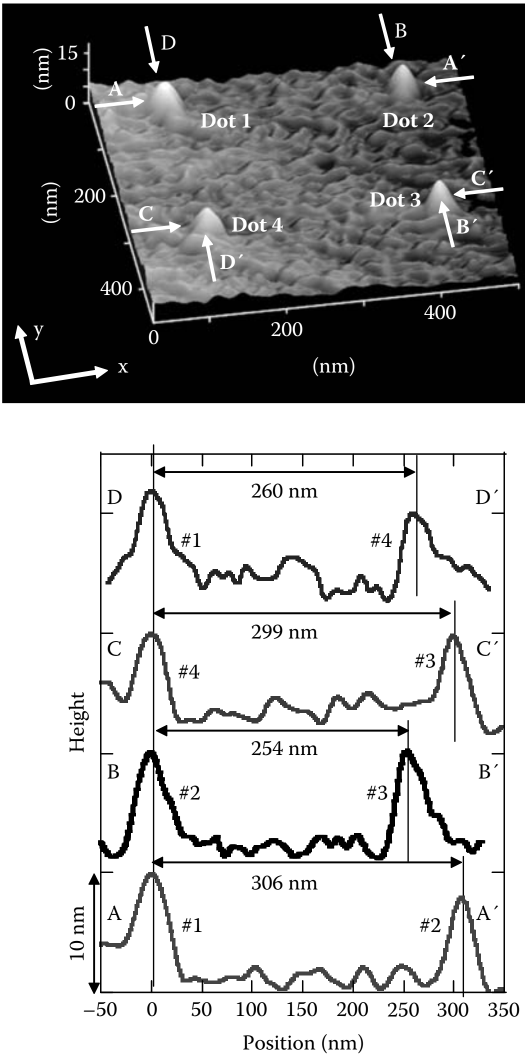

**FIGURE 4.5**
Deposited Zn dots. (a) A shear-force image. The laser irradiation times of dots 1–4 were 60, 30, 10, and 5 s, respectively. (b) The cross-sectional profiles along the lines indicated by *arrows* A–A,′ B–B,′ C–C,′ and D–D,′ respectively.

positional accuracy (<10 nm). The main source of the residual inaccuracy is the hysteresis of the piezoelectric transducer (PZT) used for scanning the fiber probe, which can be decreased by carefully selecting the transducer.

Figure 4.6(a) plots the normalized deposition rate $R$ of Zn dots as a function of the dot size $S$. Because the measured dot size $S'$ was a convolution of the probe apex diameter $2a_p$ and the real size $S$, which was estimated as $S = S' - 2a_p$. Note that $R$ is maximal at $S = 2a_p$. This indicates that the

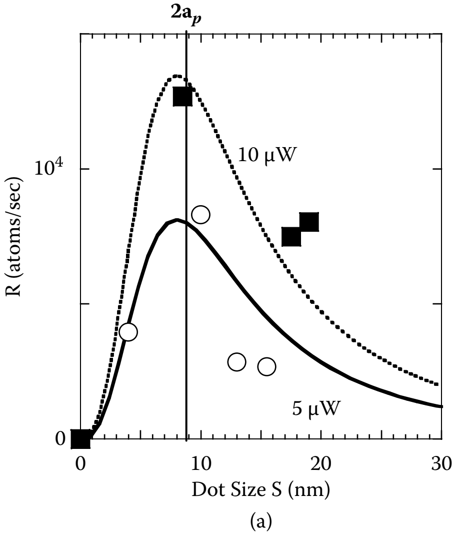

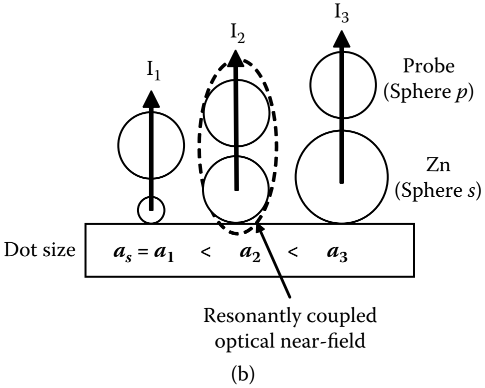

**FIGURE 4.6**
The time-dependent deposition rate $R$. (a) Experimental results. Solid squares and open circles indicate the normalized deposition rate with a laser power $P$ of 10 and 5 $\mu$W, respectively. Dashed and solid curves indicate the calculated values of $I_2/I_1$. (b) Schematic of the growth of a Zn dot.

magnitude of the near-field optical interaction between the deposited Zn dot and the probe apex is enhanced resonantly with respect to $S$, resulting in the resonant increase in $R$. In other words, the near-field optical interaction exhibits size-dependent resonance characteristics.

To determine the origin of this size-dependent resonance, the magnitude of the near-field optical interaction was calculated between closely spaced nanoparticles (Figure 4.6(b)). Spheres *'p'* and *'s'* represent the probe apex and Zn dot, respectively. Because the separation between two particles is much narrower than the wavelength, the Förster field (proportional to $R^{-3}$, where $R$ is the distance from the dipole) is dominant in the oscillating dipole electric field. In this quasi-static model, the intensity $I_s$ of the light scattered from the two closely spaced spheres, '*p*' and '*s*,' is given by [13]:

$$I_S = I_1 + I_2 = (\alpha_p + \alpha_S)^2 \,|\, E \,|^2 + 4\Delta\alpha(\alpha_p + \alpha_S)^2 \,|\, E \,|^2, \tag{4.1}$$

where $\alpha_i = 4\pi\varepsilon_0(\varepsilon_i - \varepsilon_0)/(\varepsilon_i + 2\varepsilon_0)a_i^3$ is the polarizability of sphere $i$ (= $p$, $s$) with radius $a_i$. $\Delta\alpha$ is the polarizability due to the dipole-dipole interaction. $I_1$ represents the light intensity scattered from the spheres and $I_2$ represents the light because of the dipole–dipole interaction induced by the Förster field. Therefore, the light intensity under study, normalized to $I_1$, is given by

$$I_2/I_1 = \frac{G_P A_P{}^3}{(A_P + 1)^3(G_P A_P{}^3 + 1)}, \tag{4.2}$$

where $A_p = a_p/a_s$ and $G_p = (\varepsilon_p - 1)(\varepsilon_s + 2)/(\varepsilon_p + 2)(\varepsilon_s - 1)$. For deposition by the fiber probe, the dielectric constants of Zn and fiber probe are $\varepsilon_s = (0.6 + i4)^2$ [14] and $\varepsilon_p = 1.52$, respectively. The diameter $2a_p$ of sphere $p$ was 9 nm (see Figure 4.4(b)). The dashed curve in Figure 4.6(a) show the calculated value of $I_2/I_1$ as a function of the Zn dot size $S$ (= $2a_s$), which agrees well with the experimental results. This agreement indicates that the increase in $R$ originates from the dipole–dipole coupling with the Förster field at a dot size equivalent to the probe apex diameter.

The experimental results and suggested mechanisms demonstrate the potential advantages of this technique for improving regulation of the size and position of deposited nanometer-scale dots.

## 4.2 Nonadiabatic Nanofabrications

This section presents the nonadiabatic processes involved in optical CVD and photolithography. These methods have realized qualitative innovation in nanofabrications by utilizing the spatially localized nature of optical near fields.

### 4.2.1 Nonadiabatic Near-Field Optical CVD

Conventional optical CVD utilizes a two-step process: photodissociation and adsorption. For photodissociation, a propagating light must resonate the reacting molecular gases to excite molecules from the ground state to an excited electronic state. The Franck–Condon principle holds that this resonance is essential for excitation. The excited molecules then relax to the dissociation channel, and the dissociated atoms adsorb to the substrate surface. However, a nonadiabatic photodissociation process is observed in NFO-CVD under the nonresonant condition of the electronic transition, which violates the Franck–Condon principle. This section discusses the nonadiabatic

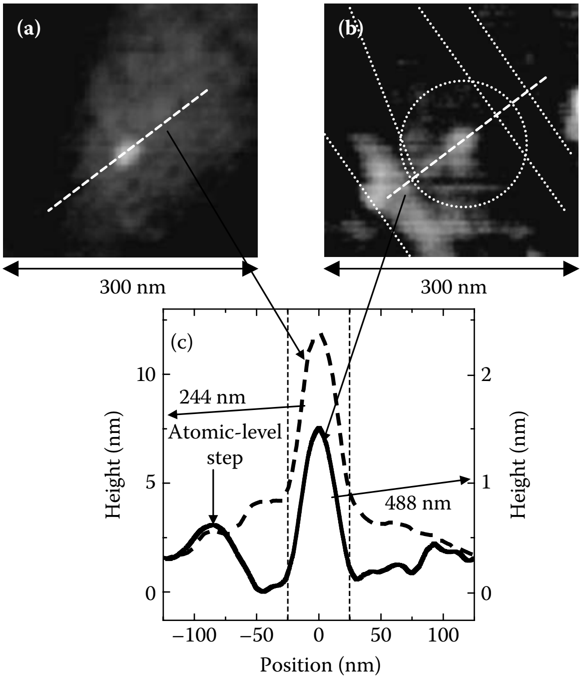

**FIGURE 4.7**
Shear-force topographical images after NFO-CVD at a photon energy of 5.08 eV ($\lambda$ = 244 nm) (a) and 2.54 eV ($\lambda$ = 488 nm) (b). The image sizes are 300 × 300 nm. Four dotted lines in (b) represent the atomic-level steps of the substrate surface. (c) Cross-sectional profiles of the deposited Zn patterns. Dashed and solid curves represent profiles along dashed lines (a) and (b), respectively.

NFO-CVD of nanometric Zn dots and presents experimental results based on the exciton–phonon–polariton (EPP) model.

Figure 4.7 shows shear-force topographical images after NFO-CVD for photon energies of 5.08 eV ($\lambda$ = 244 nm) (a) and 2.54 eV ($\lambda$ = 488 nm) (b), and the cross-sectional profiles (c) of Zn dots deposited on a sapphire substrate in atomic-level steps [15]. In the experiment, DEZn was used as the CVD gas source. The experimental setup for NFO-CVD is same as that used in Section 4.1. For Figure 4.7(a) ($\hbar\omega = 5.08$ eV), the laser power was 1.6 $\mu$W and the irradiation time was 60 s. Before carrying out NFO-CVD, 0.4-nm-high atomic-level step structures were clearly observed on the sapphire substrate. After NFO-CVD, they disappeared and a deposited Zn dot less than 50 nm in diameter was seen at the center of the image. This occurred because the optical near field deposited the Zn dot directly under the apex of the fiber probe. Furthermore, because high-intensity propagating light leaks from a bare fiber probe, that is, one without a metallic coating, and is absorbed by the DEZn, a Zn layer was deposited on top of the atomic-step structures. For Figure 4.7(b), the laser power was 150 $\mu$W and the irradiation time was 75 s. The photon energy ($\hbar\omega = 2.54$ eV) was higher than the dissociation energy of DEZn, but it was still lower than the absorption edge of DEZn [16]. Therefore, it was not absorbed by DEZn. A Zn dot less than 50 nm in diameter appears at the center of the dotted circle in this figure. While using conventional CVD with propagating light, a Zn film cannot be grown using a light source with a photon energy lower than the absorption edge ( $\hbar\omega < 4.13$ eV: $\lambda > 300$ nm) [17]. Deposited Zn dots were observed on the substrate just below the apex of the fiber probe using NFO-CVD. The atomic-level steps in this figure are still observed, despite the leakage of the propagating light from the bare fiber probe. In Figure 4.7(c), the dashed curve represents the cross-sectional profile of the Zn dot deposited at $\lambda = 244$ nm taken along the dashed line in Figure 4.7(a). The solid curve is a cross-sectional profile of the Zn dot deposited using a $\lambda = 488$ nm light source, taken along the dashed line in Figure 4.7(b). These curves confirm that Zn dots with a full-width at half-maximum (FWHM) of 30 nm were deposited in the region where the optical near field is dominant. The dashed curve has 4-nm-high tails on both sides of the dot, which represent the deposition caused by the leaked propagating light. This deposition process is based on the conventional adiabatic photochemical process described in Section 4.1. In contrast, the solid curve has no tails; therefore, it is clear that the leaked 488-nm propagating light did not deposit a Zn layer. Note that a Zn dot 30 nm in diameter without tails was deposited under nonabsorbed conditions ($\lambda = 488$ nm).

Figure 4.8 shows shear-force topographical images of the sapphire substrate after NFO-CVD using an optical near field with photon energies of 3.81 eV ($\lambda = 325$ nm) (a), 2.54 eV ($\lambda = 488$ nm) (b), and 1.81 eV ($\lambda = 684$ nm) (c). The respective laser power and irradiation time were (a) 2.3 $\mu$W and 60 s, (b) 360 $\mu$W and 180 s, and (c) 1 mW and 180 s. The high quality of the deposited Zn was confirmed by X-ray photoelectron spectroscopy. Furthermore, photoluminescence was observed from ZnO dots, which were fabricated by oxidizing the Zn dots deposited by NFO-CVD [8]. In Figure 4.8(a), the photon energy ($\hbar\omega$) exceeds the dissociation energy ($E_\mathrm{d}$) of DEZn, and is close to the absorption band edge ($E_{abs}$) of DEZn, that is, $\hbar\omega > E_d$ and $\hbar\omega \cong E_{abs}$ [16]. The diameter (FWHM) and height of the topographical image were 45 and 26 nm, respectively. The small tail (shown by the dotted curve) represents a Zn layer less than 2 nm thick, and was deposited by the propagating light leaking from the bare fiber probe. This deposition is possible because the DEZn absorbs some of the propagating light at $\hbar\omega = 3.18$ eV. The very high peak suggests that the optical near field enhances the photodissociation rate at this photon energy because its intensity increases rapidly at the apex of the fiber probe. In Figure 4.8(b), the photon energy still exceeds the dissociation energy of DEZn, but is lower than the absorption band edge of DEZn, that is, $E_{abs} > \hbar\omega > E_d$ [16]. The diameter and height of the image were 50 nm and 24 nm, respectively. This image has no tail because Zn was not deposited by the high-intensity propagating light leaking from the bare fiber probe. This confirmed that the photodissociation of DEZn and Zn deposition occurred only with an optical near field of $\hbar\omega = 2.54$ eV. Figure 4.8(c) represents the cases $\hbar\omega < E_d$ and $\hbar\omega < E_{abs}$. Zn dots were deposited successfully at these

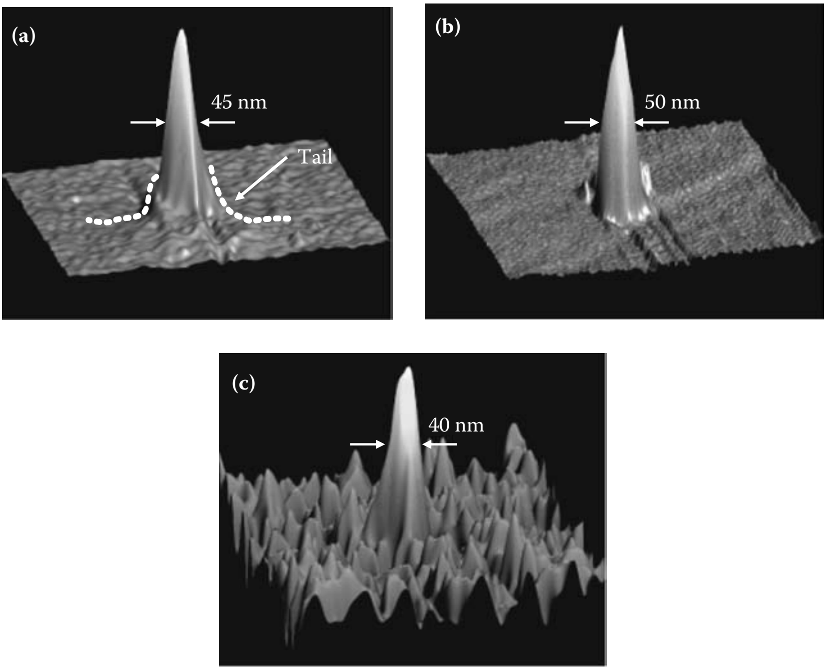

**FIGURE 4.8**
Shear-force topographical images after NFO-CVD at wavelengths of $\lambda = 325$ (a), 488 (b), and 684 (c) nm. The image sizes are $450 \times 450$ nm. The laser output power and irradiation time for deposition were 2.3 $\mu$W and 60 s (a), 360 μW and 180 s (b), and 1 mW and 180 s (c), respectively.

low photon energies. The topographical image showed dots with a diameter of 40 nm and a height of 2.5 nm. The experimental results in Figure 4.8 demonstrate dissociation based on a nonadiabatic photochemical process that violates the Franck–Condon principle.

To discuss this novel dissociation process quantitatively, Figure 4.9 shows the relationship between the photon-flux ($I$) and the deposition rate of Zn ($R$). For $\hbar\omega = 3.81$ eV (●), $R$ is proportional to $I$. For $\hbar\omega = 2.54$ eV (■) and 1.81 eV (▲), higher-order dependencies appear and $R$ is fitted by the third-order function $R = a_{\hbar\omega} I + b_{\hbar\omega} I^2 + c_{\hbar\omega} I^3$. The respective values of $a_{\hbar\omega}$, $b_{\hbar\omega}$, and $c_{\hbar\omega}$ are $a_{3.81} = 5.0 \times 10^{-6}$, $b_{3.81} = 0$, and $c_{3.81} = 0$ for $\hbar\omega = 3.81$ eV, $a_{2.54} = 4.1 \times 10^{-12}$, $b_{2.54} = 2.1 \times 10^{-27}$, and $c_{2.54} = 1.5 \times 10^{-42}$ for $\hbar\omega = 2.54$ eV, and $a_{1.81} = 0$, $b_{1.81} = 4.2 \times 10^{-29}$, and $c_{1.81} = 3.0 \times 10^{-44}$ for $\hbar\omega = 1.81\ eV$. The results of fitting are shown with the solid, dashed, and dotted curves in Figure 4.9. Because no conventional photochemical processes, for example, the Raman process and two-photon absorption, can explain these experimental results, the discussion later in this chapter uses a unique theoretical model based on the discussion in Chapter 2.

Figure 4.10 shows the potential curves of an electron in a DEZn molecular orbital drawn as a function of the internuclear distance of the C–Zn

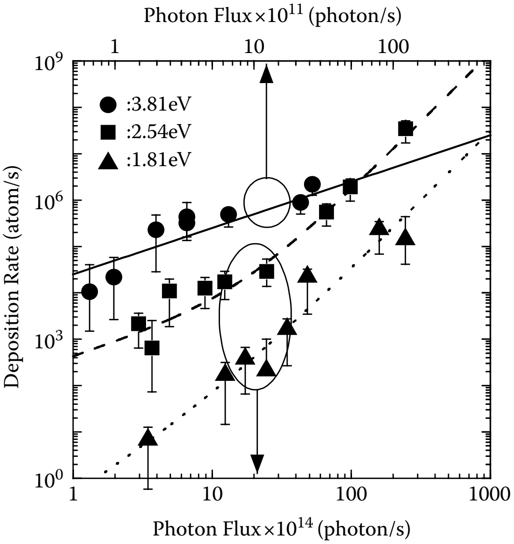

**FIGURE 4.9**
The relationship between the photon-flux and the rate of Zn deposition. The dotted, solid, and dashed curves represent the calculated values fitted to the experimental results.

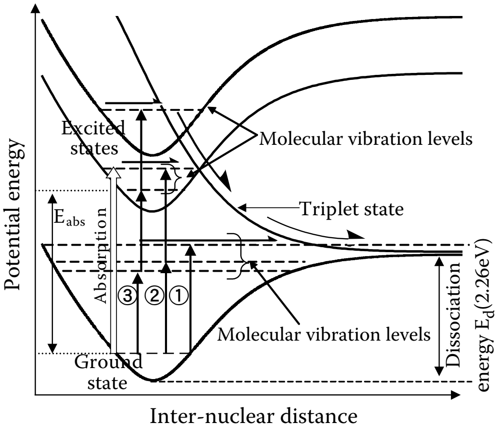

**FIGURE 4.10**
Potential curves of an electron in DEZn molecular orbitals. The relevant energy levels of the molecular vibration modes are indicated by the horizontal broken lines.

bond, which is involved in photodissociation [16]. The relevant energy levels of the molecular vibration mode are indicated by the horizontal broken lines in each potential curve. When a propagating light is used, photo-absorption (indicated by the white arrow) triggers the dissociation of DEZn [19]. With an optical near field nonresonant to the electronic state, there are three possible origins of photodissociation [20]: (1) the multiple photon absorption process; (2) a multiple step transition process via the intermediate energy level induced by the fiber probe; and (3) multiple step transition via an excited state of the molecular vibration mode. Case (1) is negligible because the optical power density was less than 10 kW/cm$^2$. Case (2) is also negligible because the DEZn was dissociated by ultraviolet–near-infrared light, although DEZn does not have relevant energy levels over such a broad wavelength region. As a result, the experimental results strongly support case (3). That is, the photodissociation is caused by a transition to an excited state via a molecular vibration mode, which involves three multiple-step excitation processes, as shown in Figure 4.10. Because the system is strongly coupled with the vibration state, it must be considered a nonadiabatic system.

For this consideration, an exciton–phonon polariton (EPP) model was presented in Chapter 2. The EPP model holds that the optical near fields excite the molecular vibration mode because of the steep spatial gradient. Because the optical near-field energy distribution is spatially inhomogeneous in a molecule because of its gradient, the electrons respond inhomogeneously. As a result, the molecular vibration modes are excited because the molecular orbital changes and the molecule is polarized as a result of the inhomogeneous response of the electrons, as shown in Figure 4.11(a). The EPP model describes this excitation process quantitatively. The EPP is a quasiparticle, which is an exciton polariton carrying the phonon (lattice vibration) generated by the steep spatial gradient of the optical field energy distribution, as shown in Figure 4.11(b). In contrast, because the propagating light energy distribution is homogeneous in a molecule, only the electrons in the molecule respond to the electric field of the propagating light. Therefore, the propagating light cannot excite the molecular vibration.

$Zn(acac)_2$ has never been used for conventional optical CVD because of its low optical activity. With NFO-CVD, however, the optical near field can activate the molecule nonadiabatically and the dissociated Zn atom is adsorbed under the fiber probe. Figure 4.12(a) shows a shear-force topographical image of Zn deposited on a sapphire substrate. The laser power and irradiation time were 1 mW and 15 s, respectively. The Zn dot was 70 nm in diameter and 24 nm high [21,22]. The chemical stability of $Zn(acac)_2$ keeps the substrate surface clean and helps to fabricate an isolated nanostructure. Figure 4.12(b) shows the shear-force topographical image of a deposited Zn dot that is among the smallest ever fabricated using NFO-CVD (5 nm in diameter and 0.3 nm high). The deposition conditions consisted of $Zn(acac)_2$ at a pressure of 70 mTorr in the CVD chamber and a laser wavelength, power, and irradiation time of 457 nm, 65 $\mu$W, and 30 s, respectively.

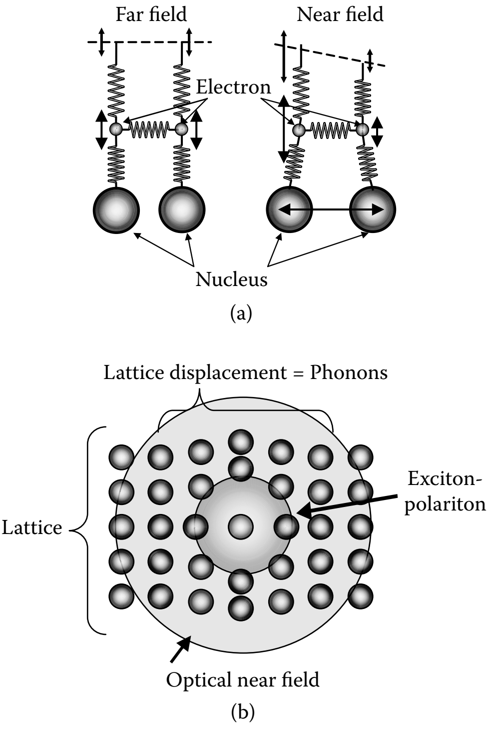

**FIGURE 4.11**
Schematic explanations of the excitation of molecular vibration mode using an optical near field (a) and exciton–phonon polariton (b).

### 4.2.2 Nonadiabatic Near-Field Photolithography

Section 4.2.1 reviewed a unique nonadiabatic photochemical reaction, which was explained using the EPP model [20–23]. According to this model, the nonadiabatic photochemical reaction can be considered a universal phenomenon and is applicable to several photochemical processes. This section reviews the application of the nonadiabatic photochemical reaction to photolithography, which can be called *nonadiabatic photolithography* [22, 23]. For the mass production of photonic and electronic devices, nonadiabatic photolithography can be used because conventional photolithographic components can be applied to this system.

The wave properties of propagating light cause problems for high-resolution photolithography because of diffraction and the dependence on the coherency and polarization of the light source. To fabricate high-density corrugations, the optical coherent length is too long compared to the separation between adjacent corrugation elements, even when a Hg lamp is used. In addition, the absorption by the photoresist is insufficient to suppress interference of scattered light. Furthermore, because the intensity of the propagating light transmitted through a photomask strongly depends on its polarization, the photomask must be designed

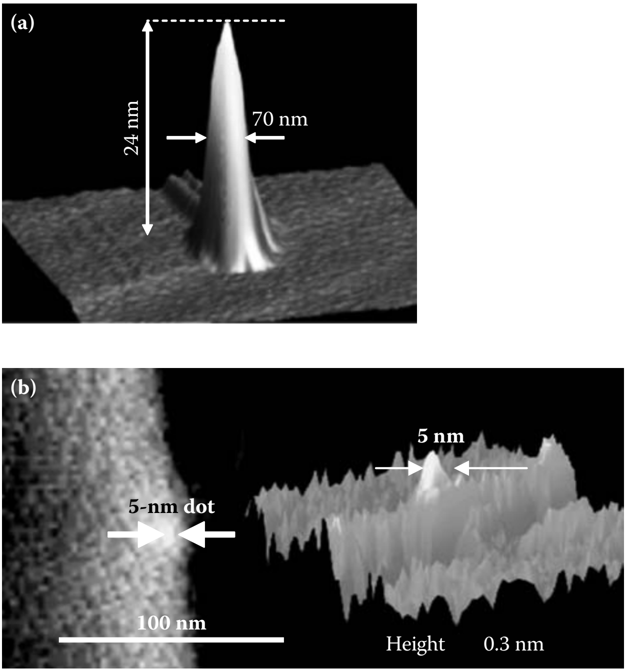

**FIGURE 4.12**
Shear-force topographical images after NFO-CVD using Zn(acac)$_2$ with a 457-nm-wavelength light source. (a) A deposited Zn dot. The image sizes are 750 × 750 nm. (b) A deposited Zn with a diameter of 5 nm and height of 0.3 nm. The image sizes are 150 × 150 nm.

while considering these dependences. In contrast, the outstanding advantage of nonadiabatic photolithography is that it is free from these problems.

Figure 4.13(a) shows a schematic configuration of the photomask and the Si substrate on which the photoresist (OFPR-800: Tokyo-Ohka Kogyo) was spin-coated. They were used in contact mode. Figures 4.13(b) and (c) show atomic force microscopy (AFM) images of the photoresist surface after development. Figure 4.13(b) shows the result obtained using conventional photolithography. The g-line (436 nm) from a Hg lamp was used as the light source. The fabricated pattern of corrugation was an exact replica of the photomask. Conversely, with nonadiabatic photolithography using a 672-nm wavelength light source, the grooves on the photoresist appeared along the edges of the Cr mask pattern, as shown in Figure 4.13(c). The corrugated pattern was 30 nm deep. The line width was 150 nm, which was narrower than the wavelength of the light source. On the photomask, a steep spatial gradient of optical energy distribution is expected because of optical near fields, whereas direct irradiation with 672-nm light cannot expose the photoresist. This demonstrated that the photoresist was patterned using a nonadiabatic process.

Figure 4.14 shows AFM images of another photoresist surface (TDMR-AR87 for the 365-nm wavelength i-line from a Hg lamp: Tokyo-Ohka Kogyo)

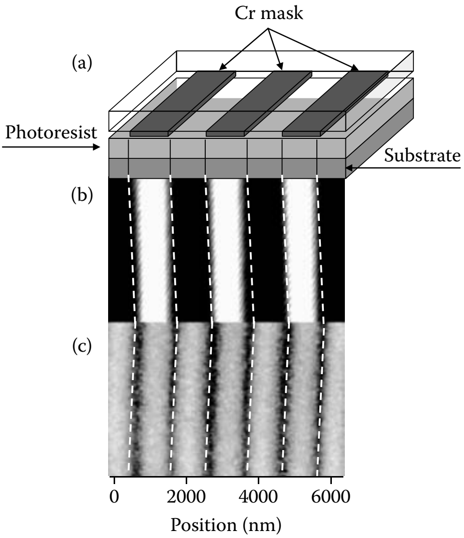

**FIGURE 4.13**
Experimental results of nonadiabatic photolithography. (a) A schematic of the photomask and Si substrate on which the photoresist (OFPR-800) was spin-coated. (b) Atomic force microscopy images of photoresist OFPR-800 exposed to the g-line of a Hg lamp. (c) AFM images of photoresist OFPR-800 developed after a 4-h exposure with a 672-nm laser.

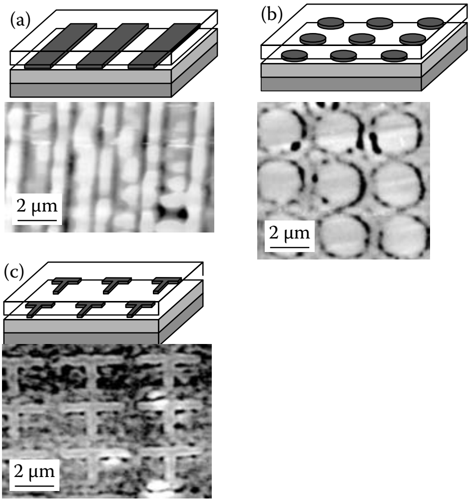

**FIGURE 4.14**
Experimental results of nonadiabatic photolithography. (a) AFM images of photoresist TDMR-AR87 exposed to the linearly polarized g-line of a Hg lamp for 3 s. (b) AFM images of photoresist TDMR-AR87 exposed to the linearly polarized g-line of a Hg lamp for 10s using a circle-shaped array photomask; (c) AFM images of photoresist OTDMR-AR87 developed after a 40-s exposure to the g-line of a Hg lamp using a T-shaped array photomask.

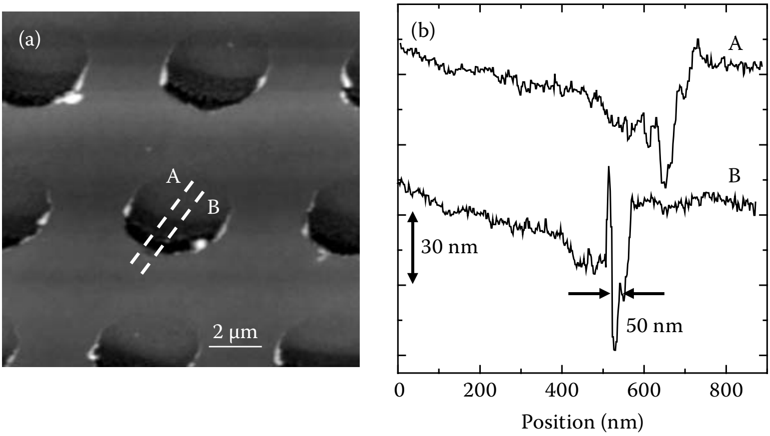

**FIGURE 4.15**
Surface of an electron beam resist exposed for 5 min using a Q-switched laser (355 nm) and a circle-shaped (1 um diameter) array photomask. (a) AFM image. (b) Cross-sectional profiles along dashed lines A and B in (a).

after development. Figure 4.14(a) shows the corrugated pattern fabricated using linearly polarized g-line light. Two-dimensional arrays of circles and T-shapes have also been fabricated successfully on this photoresist (see Figures 4.14(b) and (c)). This would be impossible using adiabatic photolithography because of its polarization-dependent nature and interference effects.

An optically inactive electron beam (EB) resist film (ZEP-520: ZEON) can also be patterned nonadiabatically. Figure 4.15 shows an AFM image of the developed EB resist surfaces. The light source was the third harmonic of a Q-switched Nd:YAG laser and the exposure time was 5 min. A two-dimensional array of 1-$\mu$m-diameter disks was fabricated successfully, even on the EB resist, which would be impossible using propagating light. The developed pattern had a depth of 70 nm, which is sufficient for the subsequent etching of the substrate. Because the EB resist film has an extremely smooth surface, the homogeneity in the contact with the photomask was improved. This suggests that a smooth organic or inorganic thin film can be used as a photoresist irrespective of its optical inactivity.

## 4.3 Self-Assembling Method Via Optical Near-Field Interactions

This section demonstrates the size- and position-controlled deposition of nanometric materials based on the size-dependent resonance between the optical near field and materials. This method of deposition enables highly precision nanofabrication without using an optical fiber probe and photomask.

### 4.3.1 Regulating the Size and Position of Nanoparticles Using Size-Dependent Resonance

To improve the size controllability, the dependence of plasmon resonance on the photon energy of optical near fields can be used and the growth of nanoparticles can be controlled during the deposition process. Using this dependence, this section demonstrates the deposition of a nanometer-scale Zn dot using NFO-CVD [5].

First, nanoparticles were deposited on the cleaved facets of UV fibers (core diameter = 10 $\mu$m) using conventional optical CVD (see Figure 4.16(a)). Gas-phase DEZn at a partial pressure of 5 mTorr was used as the source gas. The total pressure, including that of the Ar buffer gas, was 3 Torr. As the light source for the photodissociation of DEZn, a 500-$\mu$W He–Cd laser (photon energy $E_{p1} = 3.81$ eV [$\lambda = 325$ nm]) was coupled to the other end of the fiber. The irradiation time was 20 s. This irradiation covered the facet of the fiber core with a layer of Zn nanodots (see Figure 4.16(b)). Figure 4.17(a) shows a SEM image of the deposited Zn nanodots and their size distribution. The peak radius and FWHM of this curve are 55 and 25 nm, respectively.

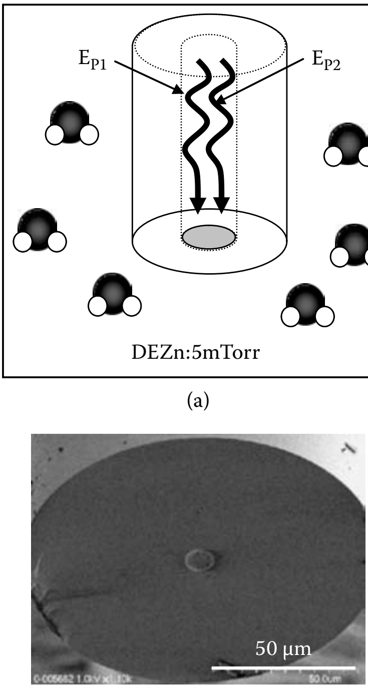

(a)

(b)

**FIGURE 4.16**
Conventional optical CVD on the cleaved facet of an optical fiber. (a) Schematic explanation. (b) SEM image of the end of the fiber.

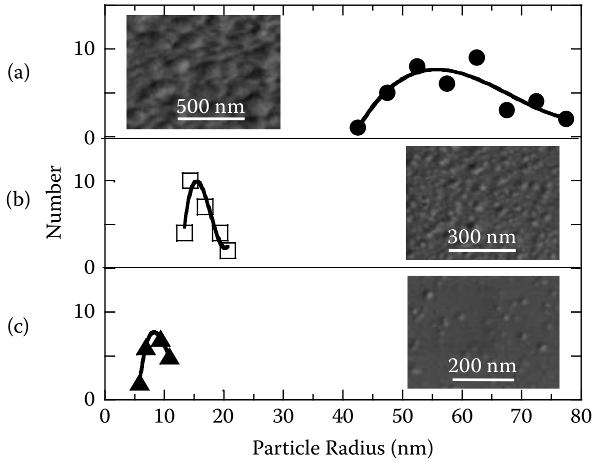

**FIGURE 4.17**
The radius distributions of Zn nanoparticles deposited using optical CVD with (a) $E_p = 3.81$ eV, (b) $E_p = 3.81$ and 2.54 eV, and (c) $E_p = 3.81$ and 1.96 eV. Inset: SEM images of Zn nanoparticles.

To control the size distribution, 20 $\mu$W Ar$^+$ ($E_{p2} = 2.54$ eV [$\lambda = 488$ nm]) or He–Ne ($E_{p2} = 1.96$ eV [$\lambda = 633$ nm]) laser light was introduced into the fiber, in addition to the He–Cd laser. Their photon energies are lower than the absorption band edge energy of DEZn; that is, they are nonresonant light sources for the dissociation of DEZn. The irradiation time was 20 s. The inset of Figures. 4.17(b) and (c) show SEM images of Zn nanodots deposited with irradiation at $E_p = 3.81$ and 2.54 eV and at $E_p = 3.81$ and 1.96 eV, respectively. Figures 4.17(b) and (c) show the respective size distributions. The peak radii are 15 and 9 nm, respectively, which are smaller than those of the dots in Figure 4.17(a), and depend on the photon energy of the additional light. Furthermore, the FWHM (5 and 6 nm, respectively) was definitely narrower than that in Figure 4.17(a). These results suggest that the additional light controls the size of the dots and reduces the size fluctuation; that is, size regulation is realized.

Possible mechanisms for the size regulation of the dots using additional light are now discussed. A metal nanoparticle has strong optical absorption because of plasmon resonance [24, 25], which strongly depends on particle size. This can induce the desorption of the deposited metal nanoparticles [26,27]. As the deposition of metal nanoparticles proceeds in the presence of light, the growth of the particles is affected by a trade-off between deposition and desorption, which determines their size, and depends on the photon energy. It has been reported that surface plasmon resonance in a metal nanoparticle is red-shifted with increasing particle size [26, 27]. However, the experimental results do not agree with these reports (compare Figures 4.17(a)–(c)). To find the origin of this discrepancy, a series of calculations was performed and resonant sizes were evaluated. Mie's theory of scattering by a

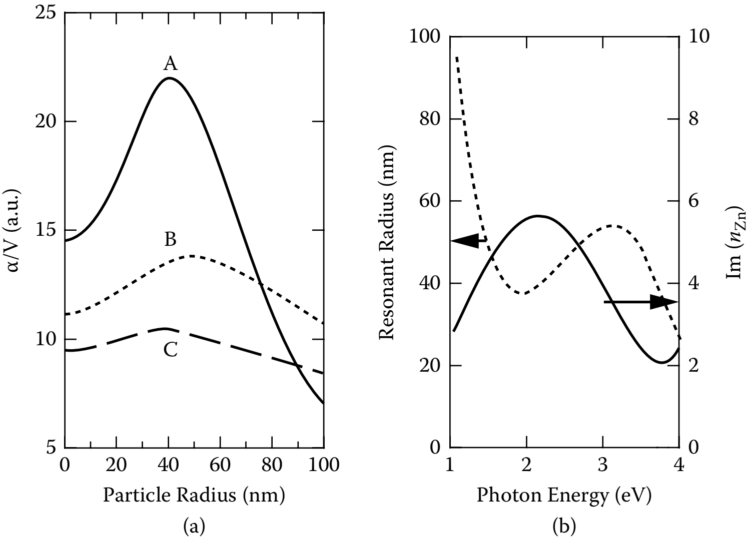

**FIGURE 4.18**
Calculated results. (a) Curves A–C show the polarizability $\alpha$ normalized to the volume $V$ for a Zn sphere surrounded by air for $E_p$ = 3.81, 2.51, and 1.96 eV, respectively. (b) The resonant radius of a Zn sphere (dashed curve). The imaginary part of the refractive index of Zn, $n_{Zn}$, used for the calculation (solid curve) (refer to [14]).

Zn sphere was used while considering the first mode only [28]. The curves in Figure 4.18(a) represent the calculated polarizability $\alpha$ with respect to three photon energies. The vertical axis is the value of $\alpha$ normalized to the volume, $V$, of a Zn sphere in air, which depends on its radius and is maximal at the resonant radius. The dashed curve in Figure 4.18(b) represents the resonant radius as a function of the photon energy, which is not a monotonous function and is minimal at $E_p$ = 2.0 eV ($\lambda$ = 620 nm). Because the imaginary part of the refractive index of Zn is also minimal at $E_p$ = 2.0 eV ($\lambda$ = 620 nm) (see the solid curve in Figure 4.18(b)), the minimum of the solid curve is because of the strong absorption in Zn.

Although Figure 4.18(a) shows that the resonant radius (47.5 nm) for $E_p$ = 2.54 eV exceeds that (40 nm) for $E_p$ = 3.81 eV, the calculated resonant radius for $E_p$ = 3.81 eV is in good agreement with the experimentally confirmed particle size (see curve A in Figure 4.17(a)). Because the He–Cd laser light ($E_p$ = 3.81 eV) is resonant for the dissociation of DEZn and is responsible for the deposition, irradiation with a He–Cd laser during deposition causes the particles to grow, and this growth halts when the particles reach the resonant radius because the rate of desorption increases because of resonant plasmon excitation. This is further supported by the fact that the resonant radius (37.5 nm) for $E_p$ = 1.96 eV is smaller than that for $E_p$ = 3.81 eV (see Figure 4.18(a)) and illumination with the additional light causes the particles to shrink (see Figure 4.17(c)).

Another possible mechanism involves the acceleration of dissociation by the additional light. The photodissociation of DEZn produces transient monoethylzinc and Zn results from the dissociation of the monoethylzinc. Although the absorption band of monoethylzinc was not determined, the photon-energy dependence of the size observed using the additional light might have been because of the acceleration of the dissociation rate; that is, the additional light, which was nonresonant for DEZn, resonated the monoethylzinc [10], because the first metal–alkyl bond dissociation had a larger dissociation energy than the subsequent metal–alkyl bond dissociation [29, 30].

Based on the dependence described earlier, NFO-CVD was used to control the position of the deposited particle (see Figure 4.19). Figures 4.19(a)–(c) show topographical images of Zn deposited by NFO-CVD with illumination from a 1-$\mu$W He–Cd laser ($E_p$ = 3.81 eV) alone, or together with a 1-$\mu$W Ar$^+$ laser ($E_p$ = 2.54 eV) or a 1-$\mu$W He–Ne laser ($E_p$ = 1.96 eV), respectively. The irradiation times were 60 s. During deposition, the partial pressure of DEZn and the total pressure including the Ar buffer gas were maintained at

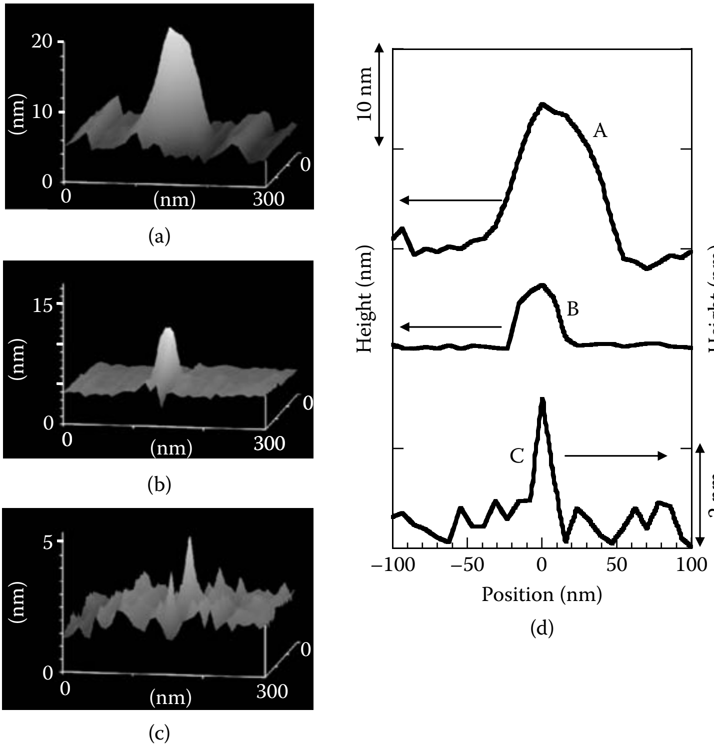

**FIGURE 4.19**
Bird's-eye view of shear-force topographical images of Zn deposited by NFO-CVD with (a) $E_p$ = 3.81 eV, (b) $E_p$ = 3.81 and 2.54 eV, and (c) $E_p$ = 3.81 and 1.96 eV, respectively. (d) Curves A–C show the respective cross-sectional profiles through the Zn dots deposited in (a)–(c).

100 mTorr and 3 Torr, respectively. In Figure 4.19(d), curves A–C are the respective cross-sectional profiles through the Zn dots in Figures 4.19(a)–(c). The respective FWHM was 60, 30, and 15 nm; that is, lower photon energy gave rise to smaller particles, which is consistent with the experimental results shown in Figure 4.17.

These results suggest that the additional light controls the size of the dots and reduces the size fluctuation. Furthermore, the position can be controlled accurately by regulating the position of the fiber probe used to generate the optical near field. The experimental results and suggested mechanisms described earlier show the potential advantages of this technique for controlling the size and position of the deposited nanodots. Furthermore, because our deposition method is based on a photodissociation reaction, it could be widely used for the nanofabrication of other materials, such as GaN [31] and GaAs.

### 4.3.2 Size-, Position-, and Separation-Controlled Alignment of Nanoparticles

To realize the mass production of nanometric structures, near-field desorption can be applied to other deposition techniques without using a fiber probe. An example is a self-assembling method that fabricates nanodot chains by controlling the desorption with an optical near field [32]. This approach is illustrated schematically in Figure 4.20(a). A chain of metallic nanoparticles was fabricated using radio frequency (RF) sputtering under illumination on a glass substrate. To realize self-assembly, a simple groove of 100 nm wide and 30 nm deep was fabricated on the glass substrate. During deposition of the metal, linearly polarized light illuminating the groove directly above ($E_{90}$) was used to excite a strong optical near field at the edge of the groove (see Figure 4.20(b)), which induced the desorption of the deposited metallic nanoparticles [5]. A metallic dot has strong optical absorption because of plasmon resonance [24, 25], which strongly depends on the particle size. This can induce desorption of the deposited metallic nanodot when it reaches the resonant diameter [26, 27]. As the deposition of metallic dots proceeds, the growth is governed by a trade-off between deposition and desorption, which determines dot size, depending on the photon energy of the incident light. Consequently, the metallic nanoparticles should align along the groove (Figure 4.20(b) and (c)).

Illumination with 2.33-eV light (50 mW) during the deposition of aluminum (Al) resulted in the formation of 99.6-nm-diameter Al nanodot chains with 27.9 nm separation that were as long as 100 $\mu$m in a highly size- and position-controlled manner (Figures 4.21(a) and (b)). The deviation of both nanodot size and the separation, determined from SEM images, was as little as 5 nm. To identify the position of the chain, we compared topographic atomic force microscopic (AFM) images of the surface of the glass substrate at the same position before and after Al deposition. Curves A and B in Figure 4.21(c) show the respective cross-sectional profiles across the groove. Comparison of these profiles showed that the nanodot chain formed around edge $G_2$.

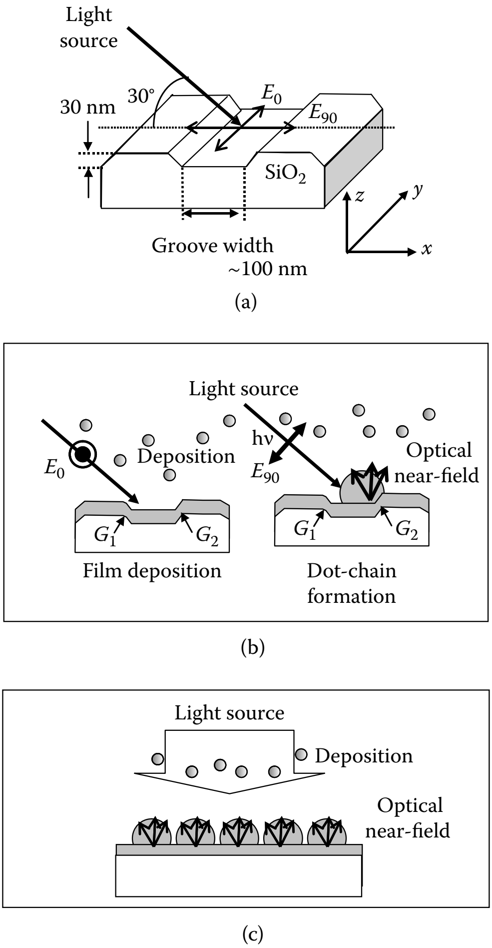

**FIGURE 4.20**
Size- and position-controlled formation of an ultra-long nanodot chain. (a) The groove is parallel to the *y*-axis. The slanted light had a spot diameter of 1 mm. $E_{90}$ and $E_0$ are perpendicular and parallel to the *y*-axis, respectively. (b), (c) Cross sections in the *x*–*z*- and *y*–*z*-planes, respectively.

Furthermore, illumination with parallel polarization $E_0$ along the groove resulted in film growth along the groove structure and no dot structure was obtained. Because the near-field intensity with $E_{90}$ (polarization perpendicular to the groove) was strongly enhanced at the metallic edge of the groove in comparison with $E_0$ owing to edge enhancement of the electrical field (see Figure 4.20(b)), a strong near-field intensity resulted in nanodot chain formation. Dot formation at the one-sided edge originated from the asymmetric electric-field intensity distribution, owing to the slanted illumination.

Chains of Al dots were also observed with RF sputtering of Al under illumination from 2.62-eV light (100 mW) with $E_{90}$ using the same grooved (100 nm wide and 30 nm deep) glass substrate, which resulted in the formation

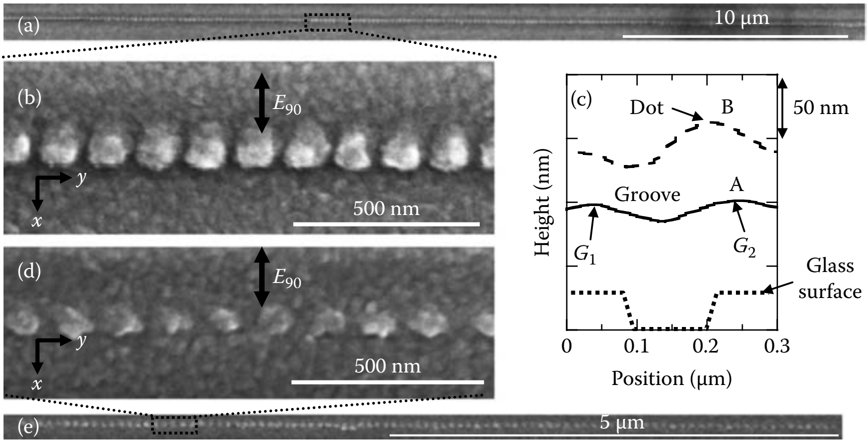

**FIGURE 4.21**
Experimental results. (a) SEM image of deposited Al with perpendicular polarization $E_{90}$ ($\hbar\omega = 2.33$ eV). (b) Magnified image of (a). (c) Curves A and B show the respective cross-sectional profiles of AFM images across the groove before and after Al deposition, at the same position. (d) and (e) SEM image of deposited Al with perpendicular polarization $E_{90}$ ($\hbar\omega = 2.62$ eV).

of 84.2-nm nanodots with 48.6 nm separation (Figures 4.21(d) and (e)). Although the deviation of both nanodot size and the separation were as large as 10 nm, the dot size was reduced in proportion to the increase in the photon energy (99.6 nm × (2.33/2.62) = 88.6 nm). This indicates that the obtained size is determined by the photon energy and that the size-controlled dot-chain formation originates from photo-desorption of the deposited metallic nanoparticles [5]. The period under 2.62-eV light illumination (132.8 nm) was longer than that (127.5 nm) using the 2.33-eV light. However, the ratios of the center–center distance (*d*) and radius (*a*) of the nanodots ($d/a = 2.56$ and 3.15 obtained under 2.33-eV and 2.62-eV light illumination, respectively) are similar to the optimum value. This is in the range of 2.4 to 3.0 for the efficient transmission of the optical energy along a chain of spherical metal dots calculated using Mie's theory [33]. This is determined by the trade-off between the increase in the transmission loss in the metal and the reduction in the coupling loss between adjacent metallic nanoparticles as the separation increases. To explain the optimum separation of the nanoparticles depending on the photon energy, theoretical analysis that includes the effect of the metallic film underneath the nanodot chain is required. However, these results imply that the center–center distance is set at the optimum distance for efficient energy transfer of the optical near field, given that such a strong optical near field can induce desorption of the deposited metallic nanoparticles and result in position-controlled dot-chain formation.

We anticipate that the fabricated structure will have high efficiency for optical near-field energy transfer, making it suitable as a nanodot coupler.

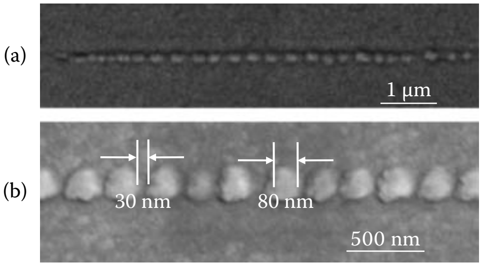

**FIGURE 4.22**
SEM images of an Au dot-chain with 1.96-eV light illumination (a) and a Pt dot-chain with 2.33-eV light illumination (b).

Such efficient energy transfer has been reported along a nanodot chain with a metallic film underneath the nanodot chain [34]. Furthermore, because our deposition method is based on a photo-desorption reaction, illumination using a simple lithographically patterned substrate could realize the fabrication of size- and position-controlled nanoscale structures with other metals, *e.g.*, Au (see Figure 4.22(a)) and Pt (see Figure 4.22(b)) or semiconductors. The use of the self-assembling method with a simple lithographically patterned substrate will dramatically increase the throughput of the production of nanoscale structures required by future systems.

## References

1. Polonski, V.V., Yamamoto, Y., Kourogi, M., Fukuda, H., and Ohtsu, M. 1999. Nanometric patterning of zinc by optical near-field photochemical vapour deposition. *J. Microsc.* **194**: 545–551.
2. Yamamoto, Y., Kourogi, M., Ohtsu, M., Polonski, V.V., and Lee, G.H. 2000. Fabrication of nanometric zinc pattern with photodissociated gas-phase diethylzinc by optical near field. *Appl. Phys. Lett.* **76**: 2173–2175.
3. Yatsui, T., Kawazoe, T., Ueda, M., Yamamoto, Y., Kourogi, M., and Ohtsu, M. 2002. Fabrication of nanometric single zinc and zinc oxide dots by the selective photodissociation of adsorption-phase diethylzinc using a nonresonant optical field. *Appl. Phys. Lett.* **81**: 3651–3653.
4. Yamamoto, Y., Kourogi, M., Ohtsu, M., Lee, G. H., and Kawazoe, T. 2002. Lateral integration of Zn and Al dots with nanometer-scale precision by near field optical chemical vapor deposition using a sharpened optical fiber probe. *IEICE Trans. Electron.* **E85-C**: 2081–2085.
5. Yatsui, T., Takubo, S., Lim, J., Nomura, W., Kourogi, M., and Ohtsu, M. 2003. Regulating the size and position of deposited Zn nanoparticles by optical near-field desorption using size-dependent resonance. *Appl. Phys. Lett.* **83**:1716–1718.

6. Lim, J., Yatsui, T., and Ohtsu, M. 2005. Observation of size-dependent resonance of near-field coupling between a deposited Zn dot and the probe apex during near-field optical chemical vapor deposition. *IEICE Trans. Electron.* **E 88-C:** 1832–1835.
7. Mononobe. S. 1999. Probe fabrication. In *Near-field nano/atom optics and technology,* ed. M. Ohtsu. 31–69. Tokyo: Springer-Verlag.
8. Polonski, V.V., Yamamoto, Y., White, J.D., Kourogi, M., and Ohtsu, M. 1999. Vacuum shear force microscopy application to high resolution work. *Jpn. J. Appl. Phys.* 38: L826– L829.
9. Krchnavek, R.R., Gilgen, H.H., Chen, J.C., Shaw, P.S., Licata, T.J., and Osgood, Jr., R.M., 1987. Photodeposition rates of metal from metal alkyls. *J. Vac. Sci. Technol. B* **5:** 20–26.
10. Jackson, R.L. 1989. Metal-alkyl bond dissociation energies for $(CH_3)_2Zn$, $(C_2H_5)Zn$, $(CH_3)_2Cd$, and $(CH_3)_2Hg$. *Chem. Phys. Lett.* **163:** 315–322.
11. Ehrlich, D.J., Osgood, Jr., R.M., Deutsch, T.E. 1982. Photodeposition of metal films with ultraviolet laser light. *J. Vac. Sci. Technol.* **21:** 23–32.
12. Chen, C.J., and Osgood, Jr., R. M., 1983. Direct Observation of the Local-Field-Enhanced Surface Photochemical Reactions. *Phys. Rev. Lett.* **50:** 1705–1708.
13. Ohtsu, M., and Kobayashi, K. 2003. *Optical Near Fields,* Berlin: Springer-Verlag.
14. Yarovaya, R.G., Shklyarevskiĭ I.N., and El-Shazly, A.F.A., 1974. Temperature dependence of the optical properties and the energy spectrum of zinc. *Sov. Phys. JETP* **38:** 331–334.
15. Yoshimoto, M., Maeda, T., Ohnishi, T., Koinuma, H., Ishiyama, O., Shinohara, M., Kubo, M., Miura, R., and Miyamoto, A., 1995. Atomic-scale formation of ultrasmooth surfaces on sapphire substrates for high-quality thin film fabrication. *Appl. Phys. Lett.* 67: 2615–2617.
16. Calvert, J. G., and Patts, Jr., J. N., 1996. *Photochemistry,* New York: Wiley.
17. Shimizu, M., Kamei, H., Tanizawa, M., Shiosaki, T., and Kawabata, A., 1988. Low temperature growth of ZnO film by photo-MOCVD. *J. Cryst. Growth* 89: 365–370.
18. Yatsui, T., Shimizu, T., Yamamoto, Y., Kourogi, M., Lee, G. H., and Ohtsu, M., 2001. Near-field ultraviolet photoluminescence spectroscopy for evaluating the crystallinity of polycrystalline zinc oxide. *Appl. Phys. Lett.* **79**: 2369–2371.
19. Kawazoe, T., Kobayashi, K., Takubo, S., and Ohtsu, M., 2005. Nonadiabatic photodissociation process using an optical near field. 2005. *J. Chem. Phys.* **122**: 024715 1–5.
20. Kawazoe, T., Yamamoto, Y., and Ohtsu, M., 2001. Fabrication of a nanometric Zn dot by nonresonant near-field optical chemical vapor deposition. *Appl. Phys. Lett.* **79**: 1184–1186.
21. Kawazoe, T., Kobayashi, K., and Ohtsu, M., 2006. Near-field optical chemical vapor deposition using $Zn(acac)_2$ with a non-adiabatic photochemical process. *Appl. Phys. B* **84**: 247–251.
22. Kawazoe, T., and Ohtsu, M., 2004. Adiabatic and nonadiabatic nanofabrication by localized optical near fields. *Proceedings of SPIE* **5339**: 619–630.
23. Yonemitsu, H., Kawazoe, T., Kobayashi, K., and Ohtsu, M., 2007. Nonadiabatic photochemical reaction and application to photolithography. *J. Luminescence* **122–123**: 230–233.

24. Boyd, G.T., Rasing, Th., Leite, J.R.R., and Shen, Y.R. 1984. Local-field enhancement on rough surfaces of metals, semimetals, and semiconductors with the use of optical second-harmonic generation. *Phys. Rev. B* **30**: 519–526.
25. Wokaun, A., Gordon, J.P., and Liao, P.F. 1982. Radiation damping in surface-enhanced raman scattering. *Phys. Rev. Lett.* **48**: 957–960.
26. MacDonald, K.F., Fedotov, V.A., Pochon, S., Ross, K.J., Stevens, G.C., Zheludev, N.I., Brocklesby, W.S., and Emel'yanov, V.I. 2002. Optical control of gallium nanoparticle growth. *Appl. Phys. Lett.* **80**: 1643–1645.
27. Bosbach, J., Martin, D., Stietz, F., Wenzel, T., and Träger, F., 1999. Laser-based method for fabricating monodisperse metallic nanoparticles. *Appl. Phys. Lett.* **74**: 2605–2607.
28. Kuwata, H., Tamaru, H., Esumi, K., and Miyano, K. 2003. Resonant light scattering from metal nanoparticles: Practical analysis beyond Rayleigh approximation. *Appl. Phys. Lett.* **83**: 4625–4627.
29. Sato, A., Tanaka, Y., Tsunekawa, M., Kobayashi, M., and Sato, H. 1993. Laser photodissociation of Trimethylgallium in the gas phase and on a quartz substrate as studied by multiphoton ionization-time of flight mass spectroscopy. *J. Phys. Chem.* **97**: 8458–8463.
30. Young, P.J., Gosavi, R.K., Connor, J., Strausz, O.P., and Gunning, H.E. 1973. Ultraviolet absorption spectra of $CdCH_3$, $ZnCH_3$, and $TeCH_3$. *J. Chem. Phys.* **58**: 5280–5283.
31. Yamazaki, S., Yatsui, T., Ohtsu, M., Kim, T. W., and Fujioka, H. 2004. Room-temperature synthesis of ultraviolet-emitting nanocrystalline GaN films using photochemical vapor deposition. *Appl. Phys. Lett.* **85**: 3059–3061.
32. Yatsui, T., Nomura, W., and Ohtsu, M. 2005. Self-assembly of size- and position-controlled ultralong nanodot chains using near-field optical desorption. *Nano Lett.* **5**: 2548–2551.
33. Quinten, M., Leitner, A., Krenn, J.R., and Aussenegg, F.R. 1998. Electromagnetic energy transport via linear chains of silver nanoparticles. *Opt. Lett.* **23**: 1331–1333.
34. Nomura, W., Yatsui, T., and Ohtsu, M. 2005. Nanodot coupler with a surface plasmon polariton condenser for optical far/near-field conversion. *Appl. Phys. Lett.* **86**: 181108 1–3.

# 5

# Fundamentals of Nanophotonic Systems

## 5.1 Introduction

To accommodate the continuously growing amount of digital data handled in information and communications systems [1], optics is expected play a wider role in enhancing overall system performance by performing certain functional behavior [2] in addition to merely serving as the communication medium. The application of inherent optical features, such as parallelism, to computing systems has also been investigated [3, 4]. However, many technological difficulties remain to be overcome in adopting optical technologies in critical information and communication systems: one problem is the poor integrability of optical hardware because of spatial density restrictions imposed by the diffraction limit of light, resulting in relatively bulky hardware configurations.

Nanophotonics, by contrast, which is based on local interactions between nanometer-scale matter, such as QDs, via optical near-fields, offers ultra-high-density integration because it is not constrained by the diffraction limit [5, 6, 7, 8, 9]. Fundamental nanophotonic processes, such as optical excitation transfer via optical near-fields between QDs [5] or metal nanoparticles [9], have been studied in detail. This higher integration density, however, is only one of the recognized benefits of optical near-fields over conventional optics and electronics. From an architectural perspective, nanophotonics drastically changes the fundamental design rules of functional optical systems at the physical layer, and suitable architectures may be built to exploit this.

This chapter approaches nanophotonics from a system perspective, considering the unique physical principles of optical near-field interactions. In particular, this chapter deals with two representative physical features in nanophotonics: one is optical excitation transfer via optical near-field interactions, and the other is the hierarchical property in optical near-field interactions.

First, in Section 5.2, optical excitation transfer between QDs via optical near-field interactions is briefly reviewed, as well as its implications in computational theory (Section 5.2.1). Then, a so-called memory-based architecture will be introduced in which functionality or computations are associated with table lookup operations (Section 5.2.2). As its fundamentally required functionalities, two basic features are then discussed: One is a mechanism for global summation, or collection, of information; the other is interconnects. Their enabling architectures will be shown by appropriate use of resonant energy levels between QDs and inter-dot interactions via optical near-fields. Also, the optical excitation transfer process is analyzed by noting the environmental factors prevalent on the nanometer scale for signal transfer; this will impact the security of practical devices and systems, specifically, tamper resistance against attacks (Section 5.2.3).

Second, in Section 5.3, the hierarchical nature in optical near-field interactions and its application to systems are discussed (Section 5.3.1). A dipole-dipole interaction model will be shown, together with its application to hierarchical memory architectures (Section 5.3.2). Furthermore, it is shown that an unscalable hierarchy is achievable in optical near-field interactions where a coarse graining process is not related to a mean-field approximation of the fine-grained lower-layer signals. Its foundations are described based on an angular spectrum representation of optical near-fields (Section 5.3.3). Also, such hierarchical properties can be exploited by combining them with energy dissipation processes occurring on the nanometer-scale, which is also one of the key physical aspects of the optical excitation transfer discussed in Section 5.2. As one such example, a traceable memory architecture that can record memory access events will be presented (Section 5.3.4).

The overall structure of this chapter is outlined in Figure 5.1. Through such architectural and physical insights, nanophotonic information and communications systems will be demonstrated that can overcome the

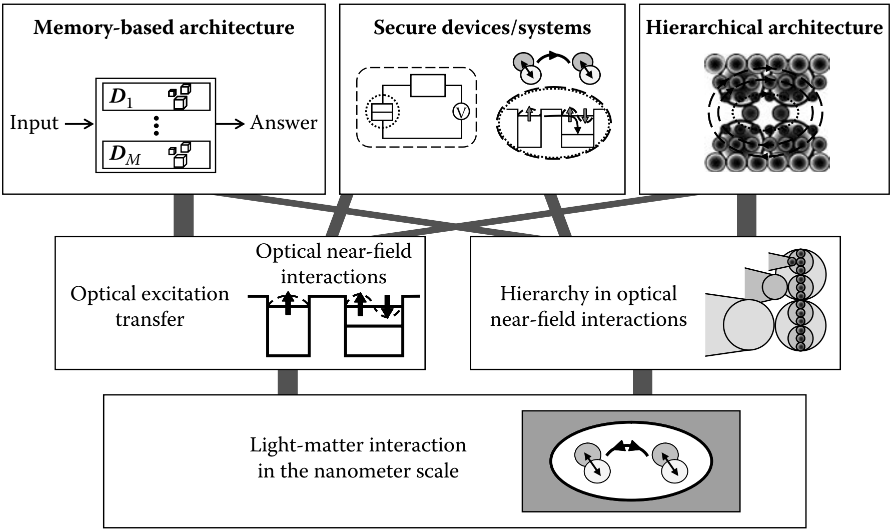

**FIGURE 5.1**
Overview of this chapter: from light-matter interactions on the nanometer scale to functionalities and system architectures.

integration-density limit imposed by the diffraction of light with ultra-low-power operation, as well as providing unique functionalities which are only achievable using optical near-field interactions.

## 5.2 Optical Excitation Transfer and System Fundamentals

### 5.2.1 Optical Excitation Transfer Via Optical Near-Field Interactions and Its Functional Features

In this section, optical excitation transfer processes involving optical near-field interactions are reviewed from a system perspective. Their theoretical details and their experimental demonstrations have been discussed in Chapters 2, 3, and 4. Here, their fundamental principles are first briefly reviewed and their functional features are introduced for the later discussion.

The interaction Hamiltonian between an electron and an electric field is given by

$$\hat{H}_{\mathrm{int}} = -\int \hat{\psi}^{\dagger}(\vec{r})\vec{\mu}\hat{\psi}(\vec{r}) \bullet \hat{\vec{D}}(\vec{r})d\vec{r}, \tag{5.1}$$

where $\vec{\mu}$ is a dipole moment, $\hat{\psi}^{\dagger}(\vec{r})$and $\hat{\psi}(\vec{r})$ are respectively creation and annihilation operators of an electron at $\vec{r}$, and $\hat{\vec{D}}(\vec{r})$ is the operator of electric flux density. In usual light-matter interactions, the operator $\hat{\vec{D}}(\vec{r})$ is a constant because the electric field of propagating light is considered to be constant on the nanometer scale. Therefore, as is well known, one can derive optical selection rules by calculating a transfer matrix of an electrical dipole. As a consequence, in the case of cubic QDs for instance, transitions to states described by quantum numbers containing an even number are prohibited. In the case of optical near-field interactions, by contrast, because of the steep electric field of optical near-fields in the vicinity of nanoscale matter, an optical transition that violates conventional optical selection rules is allowed. Detailed theory can be found in Chapter 2.

Optical excitations in nanostructures, such as QDs, can be transferred to neighboring ones by using near-field interactions [5, 9, 10]. For instance, assume two cubic QDs whose side lengths $L$ are $a$ and $\sqrt{2}a$, which are called $\mathrm{QD_A}$ and $\mathrm{QD_B}$, respectively (see Figure 5.2(a)). Suppose that the energy eigenvalues for the quantized exciton energy level specified by quantum numbers $(n_x, n_y, n_z)$ in a QD with side length $L$ are given by

$$E_{(n_x,n_y,n_z)} = E_B + \frac{\hbar^2\pi^2}{2ML^2}\left(n_x^2 + n_y^2 + n_z^2\right), \tag{5.2}$$

where $E_B$ is the energy of the bulk exciton, and $M$ is the effective mass of the exciton. According to eq. (5.2), there exists a resonance between the level of

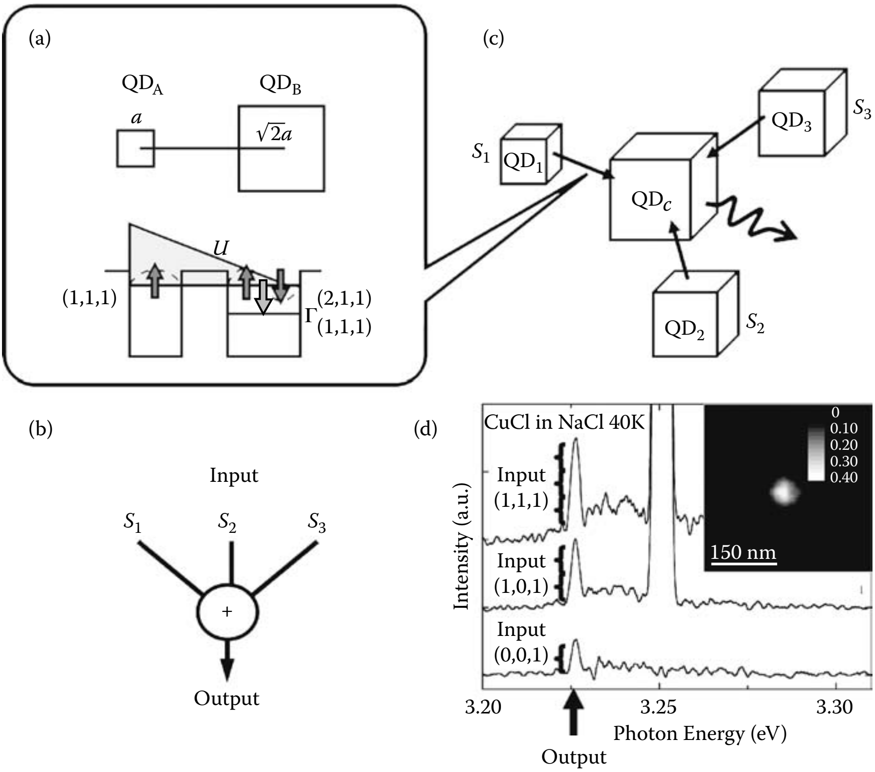

**FIGURE 5.2**
(a) Optical excitation transfer between QDs via optical near-field interactions. (b) Global summation: a basic function for memory-based architectures. (c) QD arrangement for summation via an optical near-fields. (d) Intensity for three different input combinations and spatial intensity distribution of the output photon energy.

quantum number (1,1,1) for QD$_A$ and that of quantum number (2,1,1) for QD$_B$. There is an optical near-field interaction, which is denoted by $U$, because of the steep electric field in the vicinity of QD$_A$. Therefore, excitons in QD$_A$ can move to the (2,1,1)-level in QD$_B$. Note that such a transfer is prohibited for propagating light because the (2,1,1)-level in QD$_B$ contains an even number [11]. In QD$_B$, the exciton sees a sublevel energy relaxation, denoted by Γ, which is faster than the near-field interaction, and so the exciton goes to the (1,1,1)-level of QD$_B$. It should be emphasized that the sublevel relaxation determines the unidirectional exciton transfer from QD$_A$ to QD$_B$.

Now, several unique functional aspects should be noted in these excitation transfer processes. First, as already mentioned, the transition from the (1,1,1)-level in QD$_A$ to the (2,1,1)-level in QD$_B$ is usually a dipole-forbidden transfer. In contrast, the optical near-field allows such processes. Second, in the resonant energy levels of those QDs, optical excitation can go back and forth between QD$_A$ and QD$_B$, which is called optical nutation. The direction of excitations is determined by the energy dissipation processes. Therefore, based on these mechanisms, the flow of optical excitations can be controlled in QD systems via optical near-field interactions.

From an architectural standpoint, such a flow of excitations directly leads to digital processing systems and computational architectures. First of all, two different physical states appear by controlling the dissipation processes in the larger dot; this is the principle of the nanophotonic switch discussed in Chapters 2 and 3. Also, such a flow control itself allows an architecture known as a binary decision diagram, where an arbitrary combinatorial logic operation is determined by the destination of a signal flowing from a root [12].

Such optical excitation transfer processes also lead to unique system architectures. In this regard, Section 5.2.2 discusses memory-based architectures and their nanophotonic implementations, including the issue of interconnects. Also, Section 5.2.3 demonstrates that optical excitation transfer provides higher tamper resistance against attacks than conventional electrically wired devices by exploiting environmental factors for signal transfer. Based on those architectural and physical insights, unique functional capabilities of nanophotonics, breaking through the diffraction limit of light, will be clearly grasped.

## 5.2.2 Parallel Architecture Using Optical Excitation Transfer

### *5.2.2.1 Memory-Based Architecture*

This section discusses a memory-based architecture, as an architecture utilizing optical excitation transfer. In this architecture, computations are regarded as a table lookup or database search problem. The inherent parallelism of a memory-based architecture is well matched with the physics of optical excitation transfer, and provides performance benefits in high-density, low-power operations.

Here, a packet forwarding application is first introduced as a concrete example of memory-based architectures. In this application, the output port for an incoming packet is determined based on a routing table in a router. A content addressable memory (CAM) [13] or its equivalent is typically used for such functions. In a CAM, an input signal (content) serves as a query to a lookup table, and the output is the address of data matching the input.

All-optical means for implementing such functions have been proposed, for instance, by using planar lightwave circuits [14]. However, because separate optical hardware for each table entry is needed if based on today's known methods, if the number of entries in the routing table is on the order of 10,000 or more, the overall physical size of the system becomes impractically large. By contrast, by using diffraction-limit-free nanophotonic principles, huge lookup tables can be configured compactly.

Then, it is important to note that the table lookup problem is equivalent to an inner product operation. Assume an $N$-bit input signal $\boldsymbol{S} = (s_1, \cdots, s_N)$ and reference data $\boldsymbol{D} = (d_1, \cdots, d_N)$. Here, the inner product $\boldsymbol{S} \bullet \boldsymbol{D} = \sum_{i=1}^{N} s_i \bullet d_i$ will provide a maximum value when the input perfectly matches the reference data, assuming an appropriate modulation format [15, 16]. Then, the function of a CAM is to derive $j$ that maximizes $\boldsymbol{S} \bullet \boldsymbol{D}_j$. A nanophotonic implementation of such a function can be implemented in a highly dense form, as shown in Section 5.2.2.2. In addition, a large array of such inner product operations will allow a massively parallel processing system to be constructed.

Consequently, multiple inner products are equivalent to a matrix-vector multiplication, which is capable of implementing a wide range of parallel computations [4]. As a simple example, digital-to-analog conversion will be demonstrated by tuning the near-field interaction strength, as discussed at the end of Section 5.2.2.2.

Furthermore, arbitrary combinational logic can be reformulated as a table lookup operation; more specifically, any computation is equivalent to performing a lookup in a table in which all possible input/answer combinations are pre-recorded. For example, consider a two-input, two-bit ADD operation, $\boldsymbol{A} + \boldsymbol{B}$. In the ADD operation, the third-bit of the output (the carry bit) should be logical 1 when the second bits (that is, the $2^1$ bit positions) of both inputs are 1, regardless of their first bits, that is, when $(\boldsymbol{A}, \boldsymbol{B}) = (1^*, 1^*)$ where * denotes either 0 or 1 (i.e., a don't care bit). Therefore, following the data representation format such as Logic 1 = 10, Logic 0 = 01, and don't care = 11, the table lookup entry $\boldsymbol{D}$ should be (10111011), so that any input combination satisfying $(\boldsymbol{A}, \boldsymbol{B}) = (1^*, 1^*)$ will provide a maximum inner product $\boldsymbol{S} \bullet \boldsymbol{D}$.

#### 5.2.2.2 Global Summation Using Near-Field Interactions

As discussed in Section 5.2.2.1, the inner product operations are the key functionality of this architecture. The multiplication of two bits, namely $x_i = s_i \bullet d_i$, has already been demonstrated by a combination of three QDs [17,18]. Therefore, one of the key operations remaining is the summation, or data gathering scheme, denoted by $\sum x_i$, where all data bits should be taken into account, as schematically shown in Figure 5.2(b).

In known optical methods, wave propagation in free-space or in waveguides, using focusing lenses or fiber couplers, for example, well matches such a data gathering scheme because the physical nature of propagating light is inherently suitable for collection or distribution of information such as global summation. However, the level of integration of these methods is restricted because of the diffraction limit of light. In nanophotonics, by contrast, the near-field interaction is inherently physically local, although functionally global behavior is required.

The global data gathering mechanism, or summation, is realized based on the unidirectional energy flow via an optical near-field, as schematically shown in Figure 5.2(c), where surrounding excitations are transferred towards a QD $\mathrm{QD_C}$ located at the center [19, 20]. This is based on the excitation transfer processes presented in Section 5.2.1 and in Figure 5.2(a), where an optical excitation is transferred from a smaller dot ($\mathrm{QD_A}$) to a larger one

($QD_B$) through a resonant energy sublevel and a sublevel relaxation process occurring at a larger dot. In the system shown in Figure 5.2(c), similar energy transfers may take place among the resonant energy levels in the dots surrounding $QD_C$ so that excitation transfer can occur. One may worry that if the lower energy level of a larger dot is occupied, another signal cannot be transferred to that level because of the Pauli exclusion principle. Here, thanks again to the nature of the optical near-field interaction, the excitation population goes back and forth in the resonant energy level between a smaller dot and a larger dot, a phenomenon which is known as optical nutation [17, 18, 21]. Finally, both excitons can be transferred to $QD_B$. The lowest energy level in each QD is coupled to a free photon bath to sweep out the excitation radiatively. The output signal is proportional to the (1,1,1)-level population in $QD_B$.

A proof-of-principle experiment was performed to verify the nanoscale summation using CuCl QDs in a NaCl matrix, which has also been employed for demonstrating nanophotonic switches [17] and optical nano-fountains [20]. A QD arrangement where small QDs ($QD_1$ to $QD_3$) surrounded a large QD at the center ($QD_C$) was chosen. Here, at most three light beams with different wavelengths, 325 nm, 376 nm, and 381.3 nm, are irradiated, which respectively excite the QDs $QD_1$ to $QD_3$ having sizes of 1 nm, 3.1 nm, and 4.1 nm. The excited excitons are transferred to $QD_C$, and their radiation is observed by a near-field fiber probe tip. Notice the output signal intensity at a photon energy level of 3.225 eV in Figure 5.2(d), which corresponds to a wavelength of 384 nm, or a $QD_C$ size of 5.9 nm. The intensity varies approximately as 1:2:3 depending on the number of excited QDs in the vicinity, as observed in Figure 5.2(d). The spatial intensity distribution was measured by scanning the fiber probe, as shown in the inset of Figure 5.2(d), where the energy is converged at the center. Hence, this architecture works as a summation mechanism, counting the number of input channels, based on exciton energy transfer via optical near-field interactions.

Such a QD-based data-gathering mechanism is also extremely energy efficient compared to other optical methods such as focusing lenses or optical couplers. For example, the transmittance between two materials with refractive indexes $n_1$ and $n_2$ is given by $4n_1n_2/(n_1+n_2)^2$; this gives a 4% loss if $n_1$ and $n_2$ are 1 and 1.5, respectively. The transmittance of an N-channel guided wave coupler is 1/N from the input to the output if the coupling loss at each coupler is 3 dB. In nanophotonic summation, the loss is attributed to the dissipation between energy sublevels, which is significantly smaller. Incidentally, it is energy- and space-efficient compared to electrical CAM VLSI chips [8, 22, 23].

In the summation mechanism shown earlier, the coupling strengths between the input QDs and the output QD are uniform. However, these coupling strengths can be independently configured, for instance, by modifying the relative distances. Theoretically, this corresponds to configuring the near-field coupling strengths between QDs. For instance, consider three input QDs, $QD_1$ to $QD_3$, coupled to $QD_C$ approximately in a ratio of 1:2:4. This arrangement can be described by a digital-to-analog conversion formula given by

$$d = 2^0 s_1 + 2^1 s_2 + 2^2 s_3, \tag{5.3}$$

where $d$ is the output, and $s_1$, $s_2$, and $s_3$ represent the presence/absence of excitations in $QD_1$ to $QD_3$, respectively. Each of the inputs $s_i$ is optically applied to the system, whose frequency is resonant with the (1,1,1)-level in $QD_i$. Experimental demonstrations are shown in Ref. [8]; the output intensity is approximately linearly correlated to the input bit set combination, showing the validity of the digital-to-analog conversion mechanism. Compared to known optical approaches, such as those based on space-domain filtering and focusing lenses [3, 4], or optical waveguides and intensity filters [24], the nanophotonic approach achieves a significantly higher spatial density.

It should also be noted that, in terms of interconnections, the input data should be commonly applied to all lookup table entries, which allows another possible interconnection mechanism. Because the internal functionality is based on energy transfer via optical near-field interactions and it is forbidden for far-field light, global input data irradiation, that is, broadcast interconnects, via far-field light may be possible; this is discussed in Section 5.2.3.2.

### 5.2.3 Interconnections for Nanophotonics

#### *5.2.3.1 Interconnections for Nanophotonics*

Nanophotonics allows the realization of nanometer-scale device integration, but stringent interconnection requirements are imposed in coupling external signals to nanophotonic devices. Interconnection within nanophotonic devices is another important asset from a systems perspective. To fulfill such requirements, far- and near-field conversion and other interconnection technologies have been developed [25,26,27,28]. In this subsection, rather than showing technological details of such interconnections, their fundamental differences compared with conventional lightwave-based optical interconnections are reviewed.

As shown in Section 5.2.1, the unidirectional signal flow is produced by the energy dissipation process at the destination. With conventional propagating light, by contrast, unidirectional flow is determined by the fact that there is no reflection at the destination. One practical consequence of this is the importance of fabricating antireflection coatings on devices receiving optical inputs in order to avoid interference in the system. In addition, incoming input light reflected by a mirror will be completely returned to the original input port. This is because there exists no chemical potential in usual light because a photon has no mass; this is one of the fundamental differences between conventional propagating light and nanophotonics.

#### 5.2.3.2 Broadcast Interconnects

In this subsection, another interconnection scheme is shown based on both far- and near-field interactions for data broadcasting purposes, as schematically shown in Figure 5.3 [29]. As discussed at the end of Section 5.2.2.2, data broadcasting is a fundamental operation found in memory-based architectures in which multiple functional blocks require the same input data, as schematically shown in Figure 5.3(a). Examples of such architectures include matrix-vector product [3,4] and switching operations, such as those used in a broadcast-and-select architecture [30]. For example, consider a matrix-vector multiplication given by $\boldsymbol{v} = A\boldsymbol{s}$, where $\boldsymbol{v} = (v_1, \cdots, v_m)$ and $\boldsymbol{s} = (s_1, \cdots, s_n)$, and $A$ is an $m \times n$ matrix. To compute every $v_j$ from the input data $\boldsymbol{s}$, broadcast interconnects are required if every $v_j$ is calculated at distinct processing hardware. Optics is in fact well-suited to such broadcast operations in the form of simple imaging optics [3, 4] or in optical waveguide couplers thanks to the nature of wave propagation. However, the integration density of this approach is physically limited by the diffraction limit, which leads to bulky system configurations.

The overall physical operation principle of broadcasting is as follows. In nanophotonics, unidirectional energy transfer is possible between

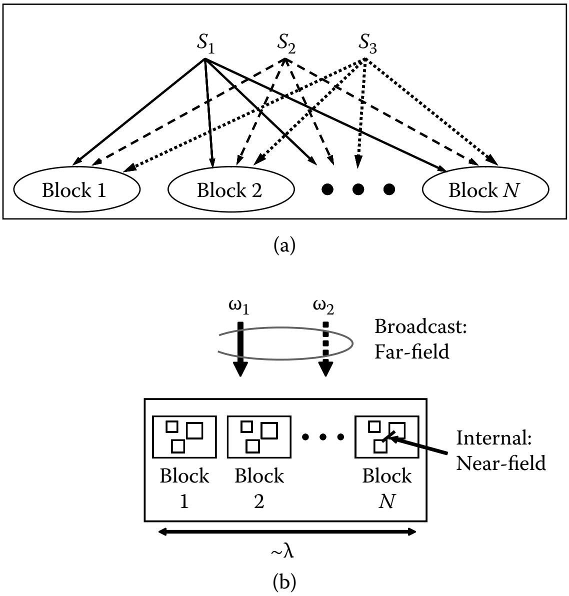

**FIGURE 5.3**
(a) Broadcast interconnects for parallel processing. (b) Their nanophotonic implementation using near-field interaction between QDs for internal functions and far-field excitation for identical data input (broadcast) to nanophotonic devices within a diffraction-limit-sized area.

neighboring QDs via local optical near-field interactions and sublevel relaxation, as discussed in Section 5.2.1.

Suppose that arrays of nanophotonic circuit blocks, such as the nanophotonic switches described later, are distributed within an area whose size is comparable to the wavelength, as shown in Figure 5.3(b). For broadcasting, multiple input QDs simultaneously accept identical input data carried by diffraction-limited far-field light by tuning their optical frequency so that the light is coupled to dipole-allowed energy sublevels, as illustrated in Figure 5.3(b); this is described in more detail later.

In a frequency multiplexing sense, this interconnection method is similar to multi-wavelength chip-scale interconnects [31]. Known methods, however, require a physical space comparable to the number of diffraction-limited input channels because of wavelength demultiplexing, whereas in the proposed scheme, the device arrays are integrated on the subwavelength scale, and multiple frequencies are multiplexed in the far-field light supplied to the device.

The far- and near-field coupling mentioned earlier is explained here based on a model assuming cubic QDs, which was introduced in Section 5.2.1. According to eq. (5.2), there exists a resonance between the quantized exciton energy sublevel of quantum number (1,1,1) for the QD with effective side length $a$ and that of quantum number (2,1,1) for the QD with effective side length $\sqrt{2}a$. (For simplicity, the QDs with effective side lengths $a$ and $\sqrt{2}a$ are referred as "QD $a$" and "QD$\sqrt{2}a$," respectively.) Energy transfer between QD $a$ and QD$\sqrt{2}a$ occurs via optical near fields, which is forbidden for far-field light [17, 18, 21].

It should be noted that the input energy level for the QDs, that is, the (1,1,1)-level, can also couple to the far-field excitation. This fact can be utilized for data broadcasting. One of the design restrictions is that energy sublevels for input channels do not overlap with those for output channels. Also, if there are QDs internally used for near-field coupling, dipole-allowed energy sublevels for those QDs cannot be used for input channels because the inputs are provided by far-field light, which may lead to misbehavior of internal near-field interactions if resonant levels exist. Therefore, frequency partitioning among the input, internal, and output channels is important. The frequencies used for broadcasting, denoted by $\Omega_i = \{\omega_{i,1}, \omega_{i,2}, \cdots, \omega_{i,A}\}$, should be distinct values and should not overlap with the output channel frequencies $\Omega_o = \{\omega_{o,1}, \omega_{o,2}, \cdots, \omega_{o,B}\}$. $A$ and $B$ indicate the number of frequencies used for input and output channels, respectively. Also, there will be frequencies needed for internal device operations, which are not used for either input or output (discussed later in the sum of product examples), denoted by $\Omega_n = \{\omega_{n,1}, \omega_{n,2}, \cdots, \omega_{n,C}\}$, where $C$ is the number of those frequencies. Therefore, the design criteria for global data broadcasting is to exclusively assign input, output, and internal frequencies, $\Omega_i$, $\Omega_o$, and $\Omega_n$, respectively.

Figure 5.4 illustrates two examples of frequency partitioning, where the horizontal axis shows QD size and the vertical axis shows energy sublevels. The 3-digit sets in the diagram are the quantum numbers of the QDs. In an

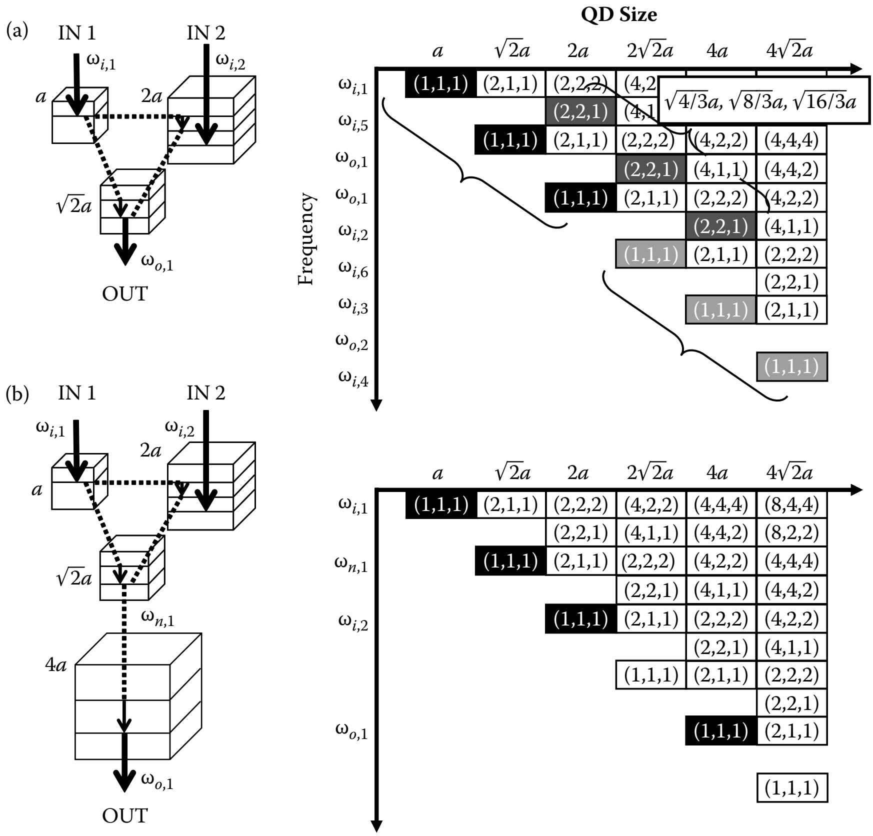

**FIGURE 5.4**
Frequency partitioning among external and internal channels, and examples in (a) multiple implementations of 3-dot nanophotonic switches, and (b) 4-dot configuration for sum of products.

example shown in Figure 5.4(a), a nanophotonic switch (2-input AND gate) composed of three QDs with a size ratio of $1:\sqrt{2}:2$ is used. The details of the switching principle are shown in Ref. [17]. The two input channels are assigned to QD *a* and QD 2*a*, and the output appears from $QD\sqrt{2}a$. Here, multiple input dots QD *a* and QD 2*a* can accept identical input data via far-field light for broadcasting purposes. Adding more optical switches for different channels means adding different size dots, for instance, by multiplying the scale of the QDs by a constant while maintaining the ratio $1:\sqrt{2}:2$, such as a QD trio of $2\sqrt{2}a$, $4a$, and $4\sqrt{2}a$, so that the corresponding far-field resonant frequencies do not overlap with the other channels. More dense integration is also possible by appropriately configuring the size of the QDs. As an example, consider a QD whose size is $\sqrt{4/3}a$. The (1,1,1)-level in this QD $\sqrt{4/3}a$ can couple to the far-field excitation. It should be noted that this particular energy level is equal to the (2,2,1)-level in QD 2*a*, which is an already-used input QD; however, the far-field excitation in this particular energy level cannot couple to QD 2*a* because the (2,2,1)-level in QD 2*a* is a dipole-forbidden energy sublevel. Therefore, a QD trio composed of QDs of size $\sqrt{4/3}a$, $\sqrt{8/3}a$, and $\sqrt{16/3}a$ can make up another optical switch, without interfering with other channels, even though all of the input light is irradiated in the same area.

Another situation in which an internally used frequency exists is a sum of products operation. A simplified example is shown in Figure 5.4(b). The QD *a* and QD 2*a* operate on two inputs, and their product appears in the (1,1,1)-level in QD $\sqrt{2}a$, which is further coupled to the sublevel (4,2,2) in QD 4*a*. The QD 4*a* is the output dot. Here, the QD $\sqrt{2}a$ is internally used; thus, any frequency that could couple to QD $\sqrt{2}a$ cannot be used for other input channels.

To verify the broadcasting method, the following experiments were performed using CuCl QDs inhomogeneously distributed in an NaCl matrix at a temperature of 22 K. To operate a 3-dot nanophotonic switch (2-input AND gate) in the device, at most two input light beams (IN1 and IN2) were irradiated. When both inputs exist, an output signal is obtained from the positions where the switches exist, as described earlier. In the experiment, IN1 and IN2 were assigned to 325 nm and 384.7 nm, respectively. They were irradiated over the entire sample (global irradiation) via far-field light. The spatial intensity distribution of the output, at 382.6 nm, was measured by scanning a near-field fiber probe within an area of approximately 1 $\mu$m × 1 $\mu$m. In Figure 5.5(a), only IN1 was applied to the sample, and so the output of the AND gate is ZERO (low-level), whereas in Figure 5.5(b) both inputs were irradiated, which means that the output is ONE (high-level). Note the regions marked by ■, ●, and ◆. In those regions, the output signal levels were respectively low and high in Figures 5.5(a) and (b), which indicates that multiple AND gates were integrated at densities beyond the scale of the globally irradiated input beam area. That is to say, broadcast interconnects to nanophotonic switch arrays are accomplished by diffraction-limited far-field light.

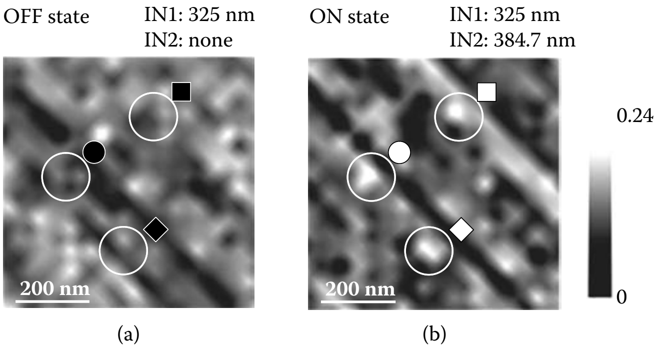

(a) (b)

**FIGURE 5.5**
Experimental results of broadcast interconnects: Spatial intensity distribution of the output of 3-dot AND gates. (a) Output level: low (1 AND 0 = 0), and (b) output level: high (1 AND 1 = 1).

Combining this broadcasting mechanism with the summation mechanism discussed in Section 5.2.2.2 will allow the development of nanoscale integration of optical parallel processing devices, which have conventionally resulted in bulky systems.

### 5.2.4 Signal Transfer and Environment: Tamper Resistance

In addition to breaking through the diffraction limit of light, such local interactions of optical near-fields also have important functional aspects, such as in security applications, particularly tamper resistance against attacks [32]. One of the most critical security issues in present electronic devices is so-called side-channel attacks, by which information is tampered with either invasively or noninvasively. This may be achieved, for instance, merely by monitoring their power consumption [33].

In this subsection, it is shown that devices based on optical excitation transfer via near-field interactions are physically more tamper-resistant than their conventional electronic counterparts. The key is that the flow of information in nanoscale devices cannot be completed unless they are appropriately coupled with their environment [34], which could possibly be the weakest link in terms of their tamper resistance. A theoretical approach is presented to investigate the tamper resistance of optical excitation transfer, including a comparison with electrical devices, for example, a single charge tunneling device [35], and numerical calculations based on a virtual photon model [36] will also be shown.

Here, tampering of information is defined as involving simple signal transfer processes, because the primary focus is on their fundamental physical properties.

In order to compare the tamper-resistance, an electronic system based on single charge tunneling is introduced here, in which a tunnel junction with capacitance $C$ and tunneling resistance $R_T$ is coupled to a voltage source $V$ via an external impedance $Z(\omega)$, as shown in Figure 5.6(b). In order to achieve single charge tunneling, besides the condition that the electrostatic energy $E_C = e^2/2C$ of a single excess electron be greater than the thermal energy $k_BT$, the environment must have appropriate conditions, as discussed in detail in Ref. [35]. For instance, with an inductance $L$ in the external impedance, the fluctuation of the charge is given by

$$<\delta Q^2> = \frac{e^2}{4\rho}\coth\left(\frac{\beta\hbar\omega_s}{2}\right), \tag{5.4}$$

where $\rho = E_C/\hbar\omega_S$, $\omega_S = (LC)^{-1/2}$, and $\beta = 1/k_BT$. Therefore, charge fluctuations cannot be small even at zero temperature unless $\rho \gg 1$. This means that a high-impedance environment is necessary, which makes tampering technically easy, for instance by adding another impedance circuit.

Here, let us define two scales to illustrate tamper resistance: (I) the scale associated with the key device size, and (II) the scale associated with the environment

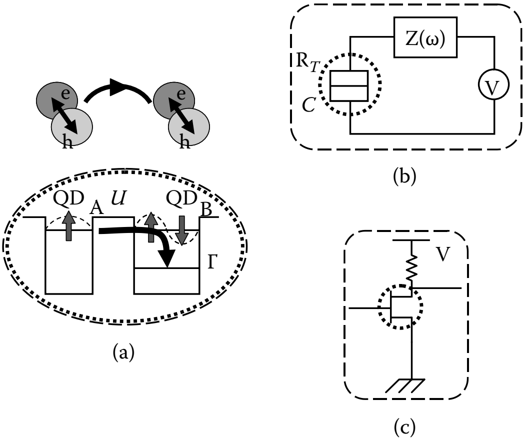

**FIGURE 5.6**
Model of tamper resistance in devices based on (a) optical excitation transfer, (b) single charge tunneling, and (c) a transistor. Dotted curves show the scale of a key device, and dashed curves show the scale of the environment required for the system to work.

required for operating the system, which are respectively indicated by the dotted and dashed curves in Figure 5.6. In the case of Figure 5.6(b), the scale I is the scale of a tunneling device, whereas the scale II covers all of the components. It turns out that the low tamper resistance of such wired devices is because scale II is typically the macro-scale, even though scale I is the nanometer scale.

As another example, the system in Figure 5.6(c) contains a field effect transistor (FET), which is the key device and is associated with the scale I. Because an FET needs connections to ground and power supply to function, the flow of information is determined by the energy dissipation occurring outside of scale I. Again, therefore, the scale II is defined so that it covers all of the components. Therefore, the scales I and II, as well as the tamper resistance, have the same properties as in the previous case.

In contrast, in the case of the optical excitation transfer shown in Figure 5.6(a), the two QDs and their surrounding environment are governed by scale I. It is also important to note that scale II is the same as scale I. More specifically, the transfer of an exciton from $QD_A$ to $QD_B$ is completed because of the nonradiative relaxation process occurring at $QD_B$, which is usually difficult to tamper with. Theoretically, the sublevel relaxation constant is given by

$$\Gamma = 2\pi\,|g(\omega)|^2\,D(\omega), \tag{5.5}$$

where $\hbar g(\omega)$ is the exciton-phonon coupling energy at frequency $\omega$, $\hbar$ is Planck's constant divided by $2\pi$, and $D(\omega)$ is the phonon density of states [37]. Therefore, tampering with the relaxation process requires somehow "stealing" the exciton-phonon coupling, which would be extremely difficult technically.

It should also be noted that the energy dissipation occurring in the optical excitation transfer, derived theoretically as $E_{(2,1,1)} - E_{(1,1,1)}$ in $\mathrm{QD_B}$ based on eq. (5.2), should be larger than the exciton-phonon coupling energy of $\hbar\Gamma$, otherwise the two levels in $\mathrm{QD_B}$ cannot be resolved. This is similar to the fact that the condition $\rho >> 1$ is necessary in the electron tunneling example, which means that the mode energy $\hbar\omega_S$ is smaller than the required charging energy $E_C$. By regarding $\hbar\Gamma$ as a kind of mode energy in the optical excitation transfer, the difference between the optical excitation transfer and a conventional wired device is the physical scale at which this mode energy is realized: nanoscale for the optical excitation transfer, and macro-scale for electric circuits.

Another possible method of attack is to use a probe, that is, an invasive attack, to tamper with the exciton flow. This is modeled by the system shown in Figure 5.7(a), where the original two QDs are depicted by A and B, and the attacker is represented by C. By using a virtual photon model [36], the solid curves shown in Figure 5.7(b) and (c) show the calculated evolution of the population of the lower level of B (= B1) in the absence of the attacker dot C. The interdot interaction is assumed to take 100 ps $(U^{-1})$, and the sublevel relaxation at B is assumed to take 5 ps $(\Gamma^{-1})$, as typical parameters. Now, in the presence of C, the dashed curve and the dotted curve in Figure 5.7(b) respectively show the evolution of the lower levels of B (B1) and C (C1). It is

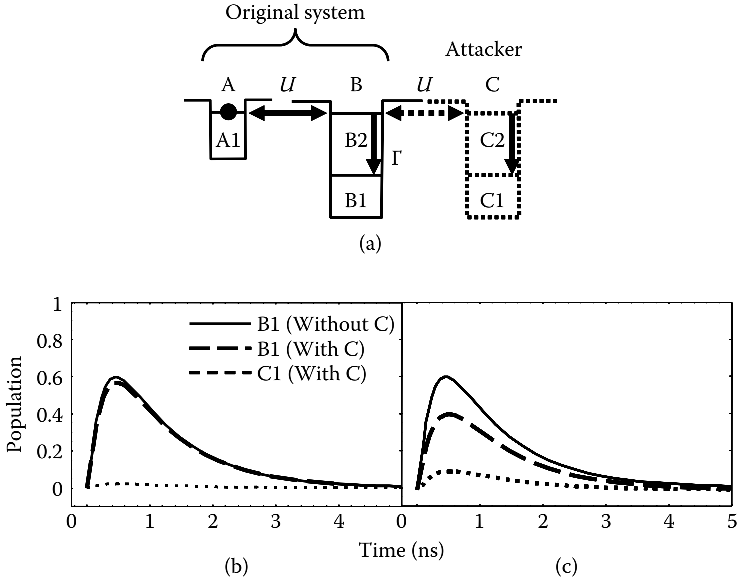

**FIGURE 5.7**
Tamper resistance in optical excitation transfer system. (a) Physical model based on virtual photon model. (b,c) Evolution of population of B1-level without QD C (solid curve), B1-level with QD C (dashed curve), and C1-level (dotted curve).

clear that there is little population in C1, meaning that tampering is difficult, because the sublevel relaxation at B is faster than the interaction between B2 and C2. Now, suppose that the interaction between B2 and C2 could be made faster (for example, 50 ps); then, the attacker could have a higher population, as shown by the dotted curve in Figure 5.7(c). However, at the same time, the population of B1 (dashed curve) is degraded accordingly, meaning that the attack is detectable from the performance degradation of the original system.

To summarize this subsection, the tamper resistance of optical excitation transfer via optical near-field interactions is analyzed by noticing the energy dissipation process or environmental factors for signal transfer. The tamper resistance is associated with the physical scale required for the environment, which is the nanoscale for optical excitation transfer and the macro-scale for conventional electrical circuits. As such, the physics of signal transfer in devices based on optical excitation transfer and conventional wired devices differ significantly.

## 5.3 Hierarchy in Nanophotonics and Its System Fundamentals

### 5.3.1 Physical Hierarchy in Nanophotonics and Functional Hierarchy

In this section, another feature of nanophotonics, the inherent hierarchy in optical near-field interactions, is exploited. As schematically shown in Figure 5.8(a), there are multiple layers associated with the physical scale between the macro-scale world and the atomic-scale world, which are primarily governed by propagating light and electron interactions, respectively. Between those two extremes, typically in scales ranging from a few nanometers to wavelength-size, optical near-field interactions play a crucial role. In this section, such hierarchical properties in this mesoscopic or subwavelength regime are exploited.

Such physical hierarchy in optical near-field interactions will be analyzed by a simple dipole-dipole interaction model, as discussed in Section 5.3.2, and based on an angular spectrum representation of optical near-fields, as shown in Section 5.3.3. Before going into details of the physical processes, functionalities required for system applications are first briefly reviewed in terms of hierarchy.

One of the problems for ultra-high-density nanophotonic systems is interconnection bottlenecks, which have been addressed previously in Section 5.2.3 regarding broadcast interconnects. In fact, a hierarchical structure can be found in these broadcast interconnects by relating far-field effects at a coarser scale and near-field effects at a finer scale.

In this regard, it should also be mentioned that such physical differences in optical near-field and far-field effects can be used for a wide range of applications. The behavior of usual optical elements, such as diffractive optical

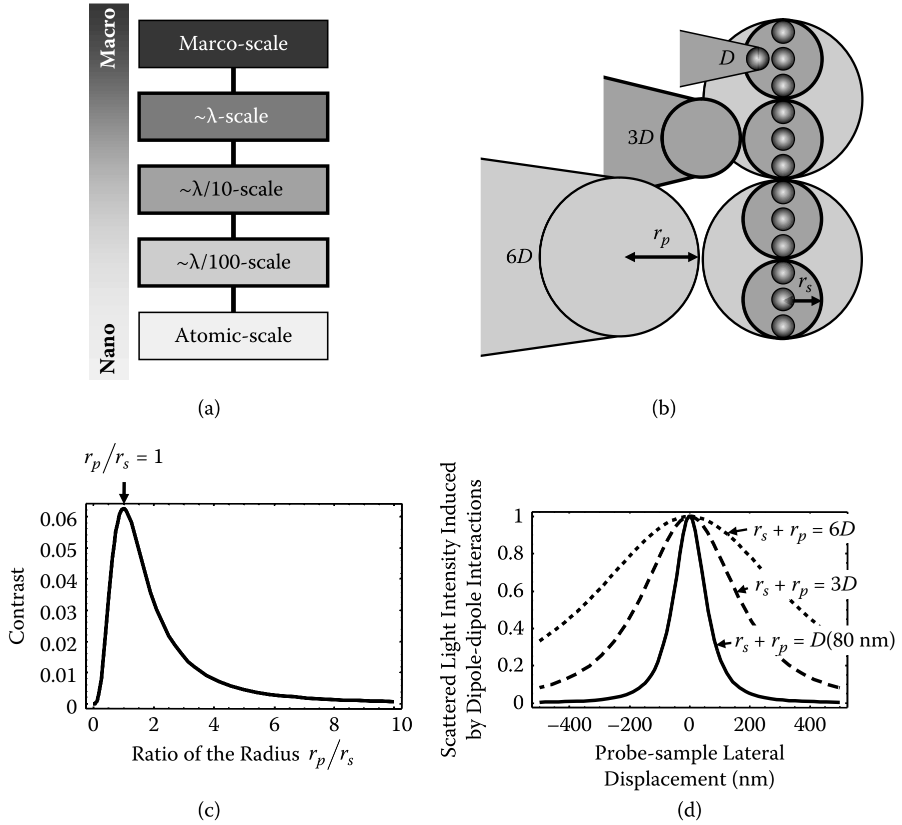

(a) (b)

(c) (d)

**FIGURE 5.8**
(a) Hierarchy in optical near-field interactions. (b) Dipole-dipole interaction. (c) Signal contrast as a function of the ratio of the radius of the sample and the probe. (d) Spatial resolution varies depending on the scale of the sample and the probe.

elements, holograms, or glass components, is associated with their optical responses in optical far-fields. In other words, nanostructures can exist in such optical elements as long as they do not affect the optical responses in far-fields. Designing nanostructures accessible only via optical near-fields provides additional, or hidden, information recorded in those optical elements while maintaining the original optical responses in far-fields. In fact, a "hierarchical hologram" or "hierarchical diffraction grating" has been experimentally demonstrated [38].

Because there is more hierarchy in the optical near-field regime, further applications should be possible; for example, it should be possible for nanometer-scale high-density systems to be gradually hierarchically connected to coarse layer systems.

Hierarchical functionalities are also important for several aspects of memory systems. One is related to recent high-density, huge-capacity memory systems, in which data retrieval or searching from entire memory archives is made even more difficult. Hierarchy is one approach for solving such a problem by making systems hierarchical, that is, by recording abstract data, meta data, or tag data in addition to the original raw data.

Hierarchy in nanophotonics provides a physical solution to achieve such functional hierarchy. As will be introduced later, in Figure 5.9(a), low-density, rough information is read-out at a coarser scale, whereas high-density, detailed information is read-out at a finer scale. Section 5.3.2 and 5.3.3 will show physical mechanisms for such hierarchical information retrieval.

Another issue in hierarchical functionalities will be security. High-security information is recorded at a finer scale, whereas less-critical security information is associated with a coarse layer. Also, in addition to associating different types of information with different physical scales, another kind of information could be also related to one or more layers of the physical hierarchy, for instance, traceability, history, or aging of information. Section 5.3.4 will demonstrate a *traceable* memory as an example.

### 5.3.2 Hierarchical Memory Retrieval

This section describes a physical model of optical near-field interactions based on dipole-dipole interactions [39]. Suppose that a probe, which is modeled by a sphere of radius $r_P$, is placed close to a sample to be observed, which is modeled as a sphere of radius $r_S$. Figure 5.8(b) shows three different sizes for the probe and the sample. When they are illuminated by incident light whose electric field is $\boldsymbol{E}_0$, electric dipole moments are induced in both the probe and the sample; these moments are respectively denoted by $\boldsymbol{p}_P = \alpha_P \boldsymbol{E}_0$ and $\boldsymbol{p}_S = \alpha_S \boldsymbol{E}_0$. The electric dipole moment induced in the sample, $\boldsymbol{p}_S$, then generates an electric field, which changes the electric dipole moment in the probe by an amount $\Delta \boldsymbol{p}_P = \Delta\alpha_P \boldsymbol{E}_0$. Similarly, $\boldsymbol{p}_P$ changes the electric dipole moment in the sample by $\Delta \boldsymbol{p}_S = \Delta\alpha_S \boldsymbol{E}_0$. These electromagnetic interactions are called dipole-dipole interactions. The scattering intensity induced by these electric dipole moments is given by

$$\begin{aligned} I &= |\boldsymbol{p_P} + \Delta\boldsymbol{p_P} + \boldsymbol{p_S} + \Delta\boldsymbol{p_S}|^2 \\ &\approx (\alpha_P + \alpha_S)^2 |E_0|^2 + 4\Delta\alpha(\alpha_P + \alpha_S)|E_0|^2 \end{aligned} \tag{5.6}$$

where $\Delta\alpha = \Delta\alpha_S = \Delta\alpha_P$ [39]. The second term in eq. (5.6) shows the intensity of the scattered light generated by the dipole-dipole interactions, containing the information of interest, which is the relative difference between the probe and the sample. The first term in eq. (5.6) is the background signal for the measurement. Therefore, the ratio of the second term to the first term of eq. (5.6) corresponds to a signal contrast, which will be maximized when the sizes of the probe and the sample are the same ($r_P = r_S$), as shown in Figure 5.8(c). (A detailed derivation is found in Ref. [39].) Accordingly, the spatial resolution varies depending on the sizes of the probe and the sample.

Figure 5.8(d) shows normalized signal intensity profiles corresponding to three cases where the sum $r_S + r_P$ is respectively $D$, $3D$, and $6D$ ($D = 80$ nm). Thus, one can see a scale-dependent physical hierarchy in this framework, where a small probe, say $r_P = D/2$, can nicely resolve objects with a comparable resolution, whereas a large probe, say $r_P = 3D/2$, cannot resolve detailed structure but it can resolve structure with a resolution comparable to the probe size. Therefore, although a large diameter probe cannot detect smaller-scale structure, it could detect certain features associated with its scale.

Based on this simple hierarchical mechanism, a hierarchical memory system is constructed. Consider, for example, a maximum of $N$ nanoparticles distributed in a region of subwavelength scale. Those nanoparticles can be nicely resolved by a scanning near-field microscope if the size of its fiber probe tip is comparable to the size of individual nanoparticles; in this way, the *first-layer* information associated with each distribution of nanoparticles is retrievable, corresponding to $2^N$-different codes. By using a larger-diameter fiber probe tip instead, the distribution of the particles cannot be resolved, but a mean-field feature with a resolution comparable to the size of the probe can be extracted, namely, the number of particles within an area comparable to the size of the fiber probe tip. Thus, the *second-layer* information associated with the number of particles, corresponding to $(N + 1)$-different level of signals, is retrievable. Therefore, one can access different set of signals, $2^N$ or $N + 1$, depending on the scale of observation. This leads to hierarchical memory retrieval by associating this information hierarchy with the distribution and the number of nanoparticles using an appropriate coding strategy.

For example, in encoding $N$-bit information, $(N\text{-}1)$-bit signals can be encoded by distributions of nanoparticles while associating the remaining 1-bit with the number of nanoparticles. Details of encoding/decoding strategies will be found in Ref. [40].

Simulations were performed assuming ideal isotropic metal particles to see how the second-layer signal varies depending on the number of particles using a finite-difference time-domain simulator (*Poynting for Optics*, a product of Fujitsu, Japan). Here, 80-nm-diameter particles are distributed over a 200-nm-radius circular grid at constant intervals. The solid circles in Figure 9(d) show calculated scattering cross-sections as a function of the number of particles. A linear correspondence to the number of particles was observed. This result supports the simple physical model described earlier.

In order to experimentally demonstrate such principles, an array of Au particles, each with a diameter around 80 nm, was distributed over a $SiO_2$ substrate in a 200-nm-radius circle. These particles were fabricated by a lift-off technique using electron-beam (EB) lithography with a Cr buffer layer. Each group of Au particles was spaced by 2 $\mu$m. A scanning electron microscope (SEM) image is shown in Figure 5.9(b) in which the values indicate the number of particles within each group. In order to illuminate all Au particles in each group and collect the scattered light from them, a near-field optical microscope (NOM) with a large-diameter-aperture (500 nm) metallized fiber

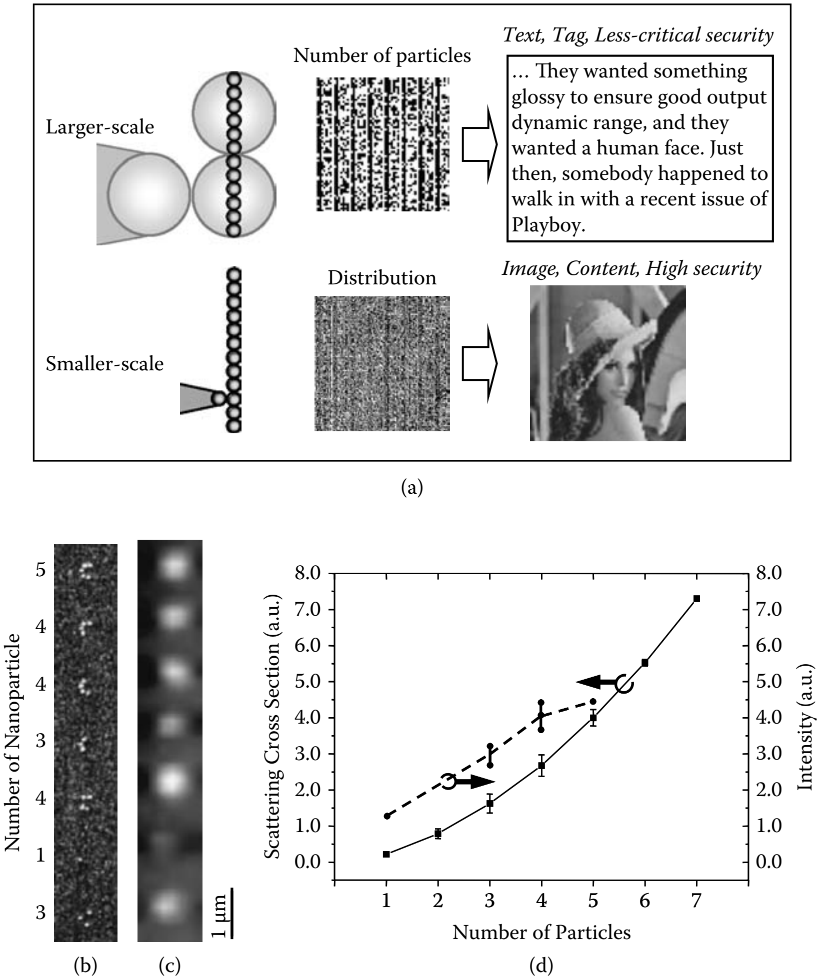

... They wanted something glossy to ensure good output dynamic range, and they wanted a human face. Just then, somebody happened to walk in with a recent issue of Playboy.

**FIGURE 5.9**
(a) Hierarchical memory retrieval from nanostructures. (b) SEM picture of an array of Au nanoparticles. Each section consists of up to seven nanoparticles. (c) Intensity pattern captured by a fiber probe tip whose diameter is comparable to the size of each section of nanoparticles. (d, square marks) Calculated scattering cross sections in each section. (b, circular marks) Peak-intensity of each section in intensity profile shown in (c).

probe was used in an illumination collection setup. The light source used was a laser diode with an operating wavelength of 680 nm. The distance between the substrate and the probe was maintained at 750 nm. Figure 5.9(c) shows an intensity profile captured by the probe, from which the second-layer information is retrieved. The solid squares in Figure 5.9(d) indicate the peak intensity of each section, which increased linearly. Those results show the validity of hierarchical memory retrieval from nanostructures, schematically shown in Figure 5.9(a).

### 5.3.3 Analysis and Synthesis of Hierarchy in Nanophotonics: Angular Spectrum-Based Approach

Hierarchical memory retrieval was demonstrated based on a simple interaction model in Section 5.3.2. Such an approach, however, demonstrates only part of the potential impact of the hierarchical nature of optical near-fields. In fact, there is a serious logical limitation in the mechanism based on the former discussion, as will be described later. In a logical sense, the signal obtained in the second layer depends on the summation of the signals obtained in the first layer. In other words, the signal obtained in the second layer is a mean-field approximation of the first layer signals; meaning that the upper layer signal exhibits a *scalable* feature with respect to the range of observation. Therefore, for example, it is impossible to have situations such as (i) retrieving a logical ONE in the first layer and, simultaneously, a logical ZERO in the second layer; and (ii) retrieving a logical ZERO in the first layer and, simultaneously, a logical ONE in the second layer. One of the motivations of this subsection is that such limitations are overcome in nanophotonics.

Here, the hierarchical nature of optical near-field interactions is analyzed based on an angular spectrum representation of the electromagnetic field [41, 42, 43]. This allows an analytical treatment and gives an intuitive picture of the localization of optical near-fields and represents relevance/irrelevance in optical near-field interactions at different scales of observation because it describes electromagnetic fields as a superposition of evanescent waves with different decay length and corresponding spatial frequency. Another merit of the angular spectrum representation in analyzing hierarchy in optical near-fields is that it explicitly contains the physical parameters associated with the positions and orientations of electric dipoles. It can also incorporate scatterers, such as nanoparticles, together with their positions and sizes [44].

As mentioned earlier, the coarse graining is conventionally a simple averaging process, meaning that the signal in the upper layer is obtained in terms of a mean-field approximation of the fine-grained, lower-layer signals. In contrast, here it is demonstrated that the optical near-field amplitude can be distributed independently at different scales of observation, by implementing subwavelength structures in dipole-source distributions because of the rapidly decaying nature of higher spatial-frequency terms in optical near-fields. In other words, the coarse graining of the optical near-fields provides an optical property independent of the lower-layer feature; such an *unscalable* hierarchical property of optical near-fields will be analyzed and attempts will be made towards engineering it.

#### 5.3.3.1 Analysis of Hierarchy Based on Angular Spectrum

This section theoretically analyzes the hierarchical coarse-grain process with the help of an angular spectrum representation [41, 42, 43].

Suppose, for example, that there is an oscillating electric dipole, $\boldsymbol{d}^{(k)} = d^{(k)}(\cos\phi^{(k)}, 0)$, on the $xz$ plane which is oriented parallel to the $x$ axis, as shown

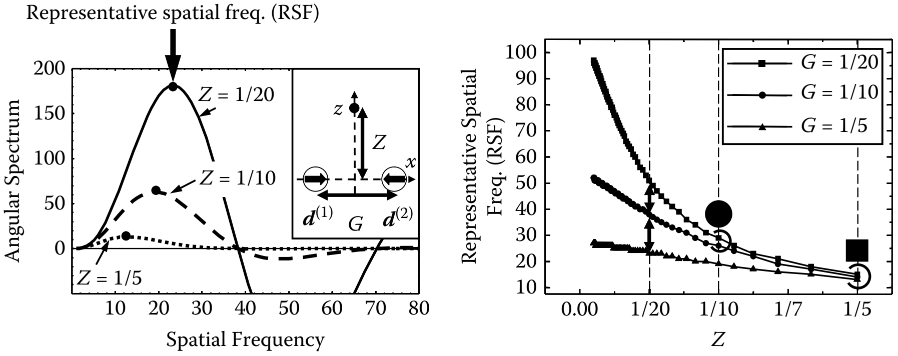

(a)

(b)

**FIGURE 5.10**

(a) Angular spectrum of two-dipole systems. Here the gap of the dipoles, G, is kept constant as 1/5. (b) Representative spatial frequencies (RSFs) are bifurcated as the scale (Z) gets smaller depending on the fine-structure of the optical excitations (G). This shows the hierarchy of optical near-fields.

in the inset of Figure 5.10(a). Now, consider the electric-field of radiation observed at a position displaced from the dipole by $\boldsymbol{R} = \left(r_{\|}^{(k)} \cos\varphi^{(k)}, z^{(k)}\right)$. The angular spectrum representation of the $z$-component of the optical near-field is given by

$$E_z(\boldsymbol{R}) = \left(\frac{iK^3}{4\pi\varepsilon_0}\right)\int_1^{\infty} ds_{\|}\frac{s_{\|}}{s_z} f_z(s_{\|}, \boldsymbol{d}^{(1)}, \cdots, \boldsymbol{d}^{(N)}) \tag{5.7}$$

where

$$f_z(s_{\|}, \boldsymbol{d}^{(1)}, \cdots, \boldsymbol{d}^{(N)}) = \sum_{k=1}^{N} d^{(k)} s_{\|}\sqrt{s_{\|}^2 - 1}\cos(\phi^{(k)} - \varphi^{(k)}) J_1\left(K r_{\|}^{(k)} s_{\|}\right)\exp\left(-K z^{(k)}\sqrt{s_{\|}^2 - 1}\right). \tag{5.8}$$

Here, $s_{\|}$ is the spatial frequency of an evanescent wave propagating parallel to the $x$ axis, and $J_n(x)$ represents Bessel functions of the first kind. Here the term $f_z(s_{\|}, \boldsymbol{d}^{(1)}, \cdots, \boldsymbol{d}^{(N)})$ is called the angular spectrum of the electric field.

Now, assume that there are two-dipoles whose phases differ from each other by $\pi$, and consider the electric field at a position equidistant to those dipoles and away from the $x$-axis by distance $Z$. The distance between the dipoles is $G$, which also represents the spatial fine/coarse structure of the original optical excitations. Here, $G$ and $Z$ indicate distances in units of wavelength. If the angular spectrum shown in Figure 5.10(a) contains higher spatial frequency components, it means that the electric field is localized at that position to the extent given by that spatial frequency. In order to evaluate localization at different scales (Z) and associate it with the spatial structure of the optical excitations ($G$), the spatial frequency that gives the maximum of the angular spectrum is noted; this is called the "representative spatial frequency" (RSF). Figure 5.10(b) shows RSF as a function of the distance $Z$, as well as its dependence on $G$; this diagram gives a quantitative, intuitive picture of the hierarchy in the subwavelength regime.

For instance, first note RSF when $Z$ is 1/5. The RSF exhibits nearly equal values for all cases $G = 1/5$, 1/10, and 1/20. This indicates that the degrees of localization of the electric field at this scale ($Z = 1/5$) are comparable and do not depend on the fine structure of the dipoles. Second, at $Z = 1/10$, the RSF values of $G = 1/10$ and 1/20 are nearly equal but that of $G = 1/5$ is small. This means that at this scale, $G = 1/10$ and 1/20 exhibit comparable degrees of localization but that of $G = 1/5$ deteriorates. Third, at $Z = 1/20$, these three cases exhibit different degrees of localization. As just described, the propagation of locality can be treated intuitively and explicitly by using the angular spectrum representation.

Numerical calculations were performed based on finite-difference time-domain methods to see how the calculation results compared with the predictions of the angular spectrum analysis. In order to simulate two dipoles, a virtual light source was assumed in Ag nanoparticles whose diameter was 10 nm. The operating wavelength used in the simulations was 488 nm. The gaps between the simulated dipoles were (i) 25 nm, (ii) 50 nm, and (iii) 100 nm, corresponding to $G$ values of 1/20, 1/10, and 1/5, respectively. In order to verify the localization of optical near-fields, intensity distributions were evaluated along the $x$-axis at positions (i) 25 nm, (ii) 50 nm, and (iii) 100 nm away from the dipoles. The distributions represented in Figure 5.11 agreed well with the theoretical predictions; for example in case (ii), the curves corresponding to $G = 1/10$ and 1/20 showed comparable responses, but the localization for

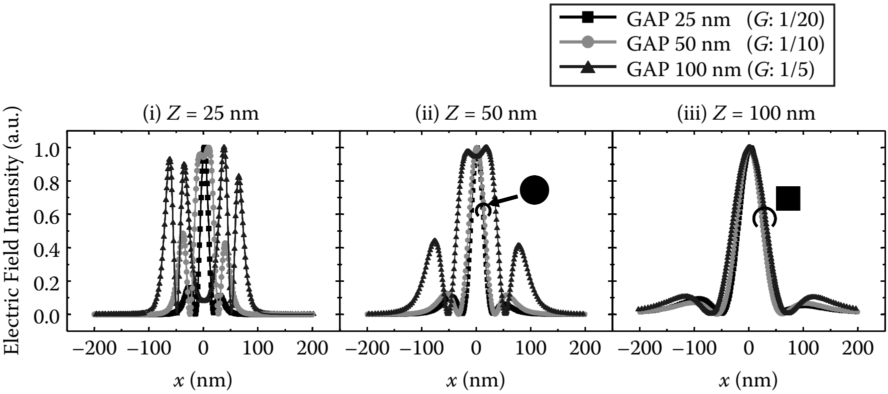

**FIGURE 5.11**
Calculated electric-field distributions in a two-dipole system. Localization of electric field is evaluated at positions (i) 25 nm, (ii) 50 nm, and (iii) 100 nm away from the dipoles. These results agree well with the theoretical predictions shown in Figure 5.10(b).

$G = 1/5$ deteriorated. As such, the angular spectrum representation helps in giving an analytical and intuitive understanding of the hierarchy in optical near-fields.

### *5.3.3.2 Synthesis of Hierarchy Based on Angular Spectrum*

The analysis shown in Section 5.3.3.1 leads to the possibility of designing a system in which the electric field exhibits a desired hierarchical response based on the fact that, as demonstrated, the orientations of the dipoles and their spatial arrangement are correlated with the localization of optical near-fields at each scale. Specifically, in the following, a two-layer system is introduced where (1) by observing very close to the dipoles, two items of first layer information are retrieved, and (2) by observing relatively far from the dipoles, one item of second layer information is retrieved.

Now, suppose that there are two closely spaced dipole pairs (so there are four dipoles in total). The dipoles $\boldsymbol{d}^{(1)}$ and $\boldsymbol{d}^{(2)}$ are oriented in the same direction, namely, $\phi^{(1)} = \phi^{(2)} = 0$, and another dipole pair, $\boldsymbol{d}^{(3)}$ and $\boldsymbol{d}^{(4)}$, are both oriented oppositely to $\boldsymbol{d}^{(1)}$ and $\boldsymbol{d}^{(2)}$, namely $\phi^{(3)} = \phi^{(4)} = \pi$. Those four dipoles are located at positions shown in Figure 5.12(a). Here, at a position close to the $x$ axis equidistant from $\boldsymbol{d}^{(1)}$ and $\boldsymbol{d}^{(2)}$, such as at the position $A_1$ in Figure 5.12(a), the electric field is weak (logical ZERO) because (i) the angular spectrum originating from $\boldsymbol{d}^{(1)}$ and $\boldsymbol{d}^{(2)}$ vanishes, and (ii) the electric field originating from $\boldsymbol{d}^{(3)}$ and $\boldsymbol{d}^{(4)}$ is small because $\boldsymbol{d}^{(3)}$ and $\boldsymbol{d}^{(4)}$ are far from the position $A_1$. In fact, as shown by the dashed curve in Figure 5.12(b), because the angular spectrum at position $A_1$ oscillates, the integral of the angular spectrum, which is correlated to the field intensity at that point will be low [43].

For the second layer retrieval, consider the observation at an intermediate position between the dipole pairs, such as the position $B$ in Figure 5.12(a). From this position, the four dipoles effectively appear to be two dipoles that are oriented in opposite directions to each other. Therefore, one can retrieve a logical ONE at one position following the analysis shown in Section 5.2.1 In fact, as shown by the solid curve in Figure 5.12(b), the angular spectrum involving relatively low spatial-frequency components shows a single peak, indicating that the electric field in the $xz$-plane is localized to the degree determined by its spectral width, so that a logical ONE is retrievable at position $B$. Meanwhile, the angular spectrum observed at position $A_2$ shown in Figure 5.12(a) is identical to that observed at position $A_1$, meaning that the electric field at $A_2$ is also at a low level.

To summarize these mechanisms, a logical level of ONE in the second layer can be retrieved even though the two items of information retrieved in the first layer are both ZEROs; therefore an unscalable hierarchy is achieved. The principle here is that the fine structure of the dipoles cannot have an effect at coarser layers, but the coarse structure does have an effect at coarser layers, which was the message of the results from Section 5.3.3.1.

As described earlier, one of the two first-layer signals, the electric field at $A_1$, primarily depends on the dipole pair $\boldsymbol{d}^{(1)}$ and $\boldsymbol{d}^{(2)}$, and the other,

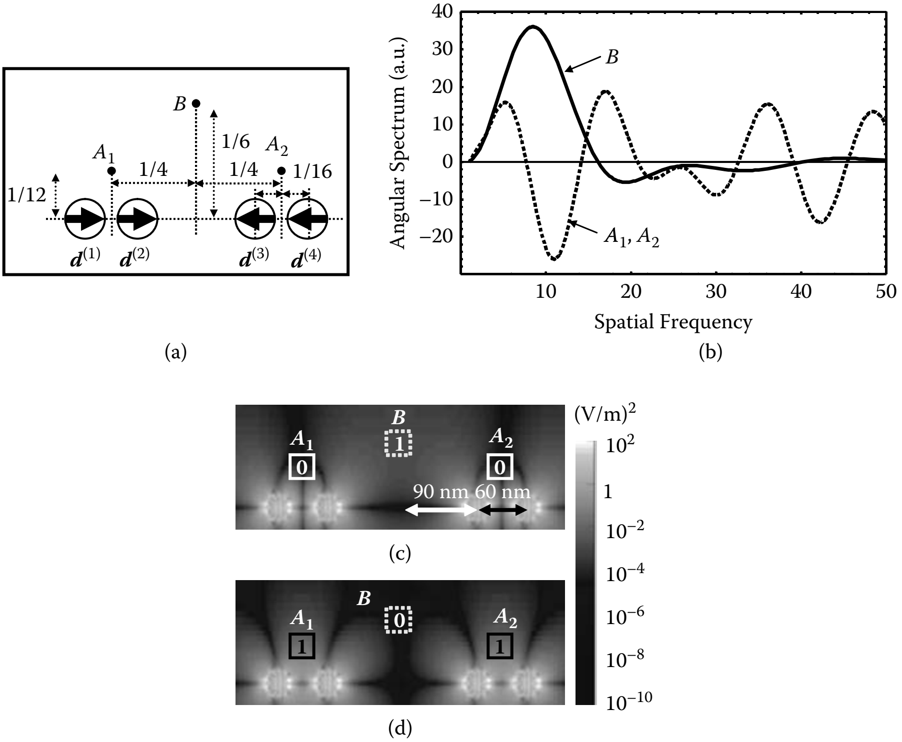

**FIGURE 5.12**

(a) The positions and orientations of four electric dipoles (b) and the corresponding angular spectrum observed at positions $A_1$, $A_2$, and $B$, indicating that the first-layer signals (obtained at $A_1$ and $A_2$) are logical ZERO, whereas the second-layer signal (obtained at $B$) is logical ONE. (c) Calculated electric field intensity distribution agreed with theoretical predictions shown in (b). (d) Another electric field distribution where logical ONEs are retrieved at the first layer ($A_1$ and $A_2$) and logical ZERO is retrieved at the second layer (B). These are examples of unscalable hierarchy.

the electric field at $A_2$, depends primarily on the dipole pair $\boldsymbol{d}^{(3)}$ and $\boldsymbol{d}(4)$. The second-layer signal is determined by all of those dipoles. Concerning such a hierarchical mechanism, it was shown that a total of eight different signal combinations were achieved by appropriately orienting the four dipoles [40].

Numerical simulations were performed based on finite-difference time-domain methods to see how they agree with the theoretical analysis based on the angular spectrum. Four silver nanoparticles (radius of 15 nm) containing a virtual oscillating light source were assumed in order to simulate dipole arrays. Their positions are shown in Figure 5.12(c). The first and the second layers were located 40 nm and 80 nm away from the dipole plane, respectively. The operating wavelength was 488 nm. The electric fields obtained at $A_1$, $A_2$ and $B$ agree with the combinations of the first and the second layer signals to be retrieved, as shown in Figure 5.12(c). As another unscalable hierarchy example, Figure 5.12(d) represents a situation where logical ONEs are obtained at the first-layer, whereas logical ZERO is obtained at the second layer.

To summarize this subsection, a theoretical analysis of the hierarchy in optical near-field interactions is represented based on an angular spectrum representation of electric fields. Based on the analysis, design, or synthesis of a hierarchy is also presented by appropriately orienting multiple electric dipoles. The hierarchical nature of optical near-fields is not simply an averaging process, but the optical near-field amplitudes in each scale could be independently configured.

One remark here is that an array of dipoles and nanoscale virtual light sources are assumed in discussing hierarchical properties in optical near-fields. Such models are well suited for demonstrating the fundamentals of the hierarchical nature. Experimentally, however, it is difficult, if not impossible, to directly manipulate the orientations in this way. Therefore, physically reasonable equivalents to an array of electric dipoles having designated orientations will be needed, for instance, by using QDs or engineering the shapes of metal nanostructures, as shown later in Section 5.3.4, so that they effectively act as an array of induced dipoles when illuminated with a plane wave.

### 5.3.4 Hierarchy Plus Localized Energy Dissipation: Traceable Memory

The hierarchical nature could be further exploited by combining other physical mechanisms in nanophotonics. As one of such example, one of the hierarchical layers can be associated with energy dissipation processes. Specifically, a two-layer system is analyzed in this subsection, where (i) at smaller scale, called *Layer 1*, the system should exhibit a unique response, and (ii) at a larger scale, called *Layer 2*, the system should output two different signals. Such a hierarchical response can be applied to functions like traceability of optical memory in combination with a localized energy dissipation process at Layer 1. Optical access to this memory will be automatically recorded because of energy dissipation occurring locally in Layer 1, while at the same time, information will be read out based on the Layer 2 behavior [45]. Therefore, such hierarchy enables *traceability* of optical memory, which will be important for the security (confidentiality is ensured) and management of digital content.

#### *5.3.4.1 Localized Energy Dissipation*

As one of the basic principles of the system, localized energy dissipation is applied to recording a memory access. There are several physical principles involved in achieving this function by using optical near-field interactions.

The first one is based on the generation of a strong electric-field because of excitation of a plasmon induced in a metal nanostructure [46, 47, 48, 49]. Here, assume that an electric-field-sensitive material is placed at a position where the strong electric-field will be generated. Now, if a beam of light is irradiated, that optical access excites a plasmon and the induced strong electric-field will cause a physical change in the material. In other words, optical access to the memory is recorded though a plasmon excitation. For example, it is well-known that irradiating a bow-tie-shaped metal nanostructure having a small gap between two wedge-shaped metallic plates generates an optical near-field between the two apexes because of the interaction of charges concentrated at those points. Therefore, by placing an electric-field-sensitive material near the gap, an optical access to this structure will be recorded as a physical change in the material. Possible materials include AgOx film, in which Ag particles are selectively decomposed at positions where the temperature is above the threshold level by optical accesses [50].

Other than engineered metal nanostructures, there is another physical system for localized energy dissipation: a QD system where optical excitations are transferred irreversibly via optical near-field interactions, which has been discussed in Section 5.2.2.2. In a system where a larger QD is surrounded by smaller QDs, a configuration known as a nanophotonic fountain [19, 20], excitons generated in the smaller QDs are transferred to the larger one. Therefore, by placing a material which absorbs the dissipated energy from the largest dot, a certain physical change occurs, and the system thus possesses the capability of recording the energy flow event.

Here, there are two points to note. The first is on the issue of how one would know if the memory was accessed or not. This should be discussed based on the detailed characteristics of the material used, for instance, the AgOx film mentioned earlier. Because it might not be needed to retrieve such trace information itself bit-by-bit, the physical change accompanying traces should be associated with macroscopically observable signals, such as transmission, reflection, and diffraction patterns, and so forth.

The second point is about the storage density. With metal nanostructures, a single bit occupies a rather large area, namely, about 400 nm × 100 nm in the example shown later, with a corresponding storage density comparable to actual optical storage technologies such as Blu-Ray [51]. By contrast, with QDs, significantly higher integration density will be obtained. Nevertheless, what should be emphasized are the unique physical attributes of optical near-fields, namely, hierarchy and localized energy dissipation, allowing qualitatively novel functions, rather than for quantitatively improving the storage density. Therefore, potential applications include, as mentioned in Section 5.3.1, security-related applications where qualitative metrics such as confidentiality are prioritized.

#### *5.3.4.2 Engineering Shape of Metal Nanostructures for Hierarchy*

We now focus on shape-engineering of metal nanostructures to achieve the hierarchy required for traceable memory [52]. Here, two types of shapes are assumed. The first one (*Shape I*) has two triangular metal plates aligned in the same direction; and the other one (*Shape II*) has them facing each other, as shown in Figure 5.13(a). The metal was gold, the gap between the two apexes was 50 nm, the horizontal length of one triangular plate was 173 nm, the angle at the apex was 30 degree, and the thickness was 30 nm. An incident

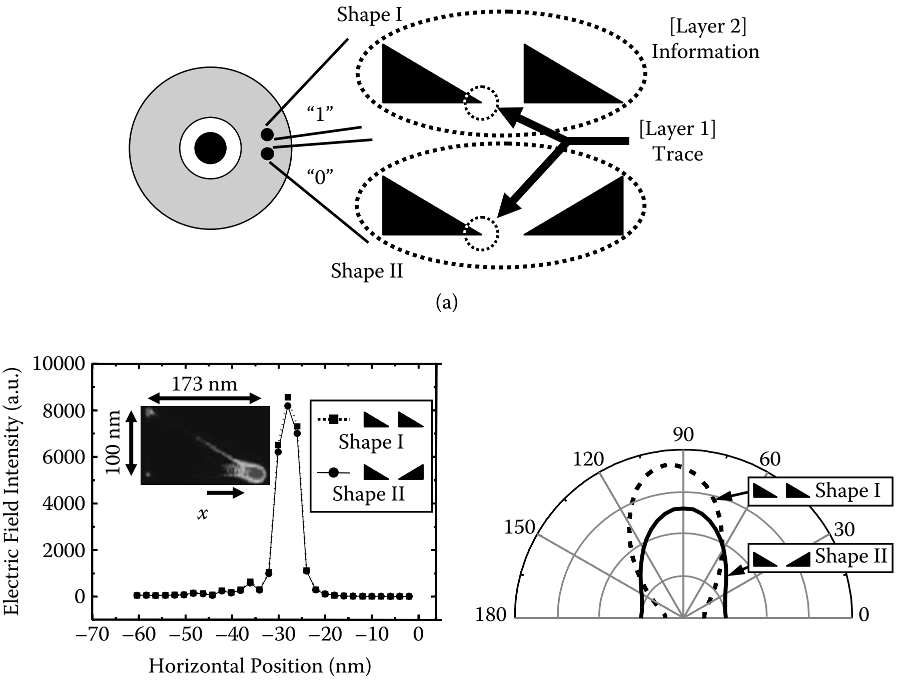

(a)

(b) [Layer 1] Electric field enhancement

(c) [Layer 2] Scattering cross-section

**FIGURE 5.13**
(a) Hierarchy in optical near-fields by engineering the shape of metal plates at nanometer scale. (b) In Layer 1, both shapes exhibit comparable electric-field enhancement, and (c) in Layer 2 they exhibit different system responses.

uniform plane wave with a wavelength of 680 nm was assumed for input light. The polarization was parallel to the $x$ axis in Figure 5.13(b).

Layer 1 is associated with the scale around the gap of the triangles, and Layer 2 is associated with the scale covering both of the triangles, as shown in Figure 5.13(a).

Regarding the optical response at Layer 1, as shown in Figure 5.13(b), the electric field near the surface (1 nm away from the metal surface) shows an intensity nearly five orders of magnitude higher than the surrounding area. It should also be noted that nearly comparable electric-field enhancements are observed near the apexes of Shapes I and II, which are respectively denoted by the squares and circles in Figure 5.13(b).

By contrast, Shapes I and II exhibit different responses at Layer 2. As shown in Figure 5.13(c), Shape I exhibits larger scattering cross-section compared to Shape II. This indicates that a digital output is retrievable by observing the scattering from the entire structure (Layer 2), where, for example, digital 1 and 0 are respectively associated with Shape I and Shape II.

In order to experimentally demonstrate the principle, Shapes I and II were fabricated in gold metal plates on a glass substrate by a liftoff technique using

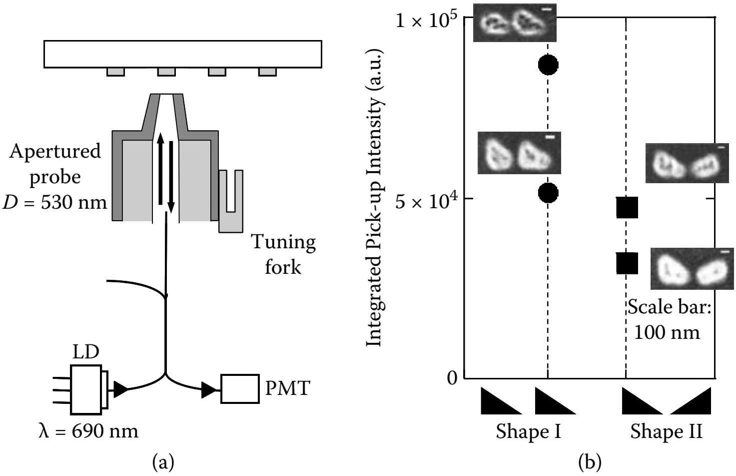

**FIGURE 5.14**
(a) Experimental setup for the Layer 2 signal retrieval. (b) Electric field intensity for Layer 2 signals for both Shapes I and II.

electron-beam lithography. A near-field optical microscope in an illumination collection setup was used with an apertured fiber probe having a diameter of 530 nm, as shown in Figure 5.14(a). The light source used was a laser diode with an operating wavelength of 690 nm. The distance between the substrate and the probe was maintained at 450 nm. Figure 5.14(b) shows the electric field intensity depending on the shape of the metal plates, where the Shape I series exhibited larger values compared to the Shape II series, as expected. The insets in Figure 5.14(b) are SEM pictures of each sample, where the horizontal length of a single triangle ranged from about 300 to 400 nm.

To summarize this subsection, hierarchical optical responses are discussed in association with localized energy dissipations to achieve traceability of information. Shape-engineering of metal nanostructures is also demonstrated for achieving such functionalities.

## 5.4 Summary and Discussion

In this chapter, fundamentals for nanophotonic systems are presented along with two principal physical features of nanophotonics: one is optical excitation transfer, and the other is hierarchy in optical near-field interactions. Both of these physical features originate from light-matter interactions on the nanometer scale.

Regarding optical excitation transfer, its implications to digital signal processing are shown from the viewpoint of its unique physical features. Computational architectures such as memory-based architectures are also discussed. Fundamental basic functionalities, such as global summation or interconnects, have been demonstrated. Also, concerning the environmental factors, signal transfer processes involving optical near-field interactions are significantly different in their associated physical scale for energy dissipation compared to conventional wired devices. In this regard, higher tamper resistance of nanophotonic devices is presented.

Hierarchy in optical near-field interactions is also discussed. Physical fundamentals are described using dipole-dipole interactions and angular spectrum representations of optical near-fields. Energy dissipation processes, which are also key processes in optical excitation transfer, can be combined with hierarchy for some applications. Hierarchical memory systems, including scalable and unscalable information retrieval, and traceable memory systems are presented.

The high spatial density of nanophotonics, thanks to the absence of the diffraction limit of light, is certainly one important aspect in nanophotonics; however, as discussed in this chapter, light-matter interactions on the nanometer scale can achieve qualitatively novel functions for system applications. In fact, the semiconductor technology roadmap raises the following five points for emerging research devices beyond CMOS information processing [53]: (1) Computational state variable(s) other than electron charge alone; (2) nonthermal equilibrium systems; (3) novel energy transfer interactions; (4) nanoscale thermal management, and (5) sublithographic manufacturing processes. It should be noted that all of those points are explicitly or potentially related to nanophotonics. Further exploration and attempts to exploit nanophotonics for future devices and systems will certainly be exciting.

## References

1. For example, 2006. *White Paper, Information and Communications in Japan,* Ministry of Internal Affairs and Communications, Japan.
2. Yao, S., Yoo S. J. B., Mukherjee, B., and Dixit, S. 2001. All-optical packet switching for metropolitan area networks:opportunities and challenges. *IEEE Commun. Mag.* 39:142–148.
3. Goodman, J. W., Dias, A. R., and Woody, L. M. 1978. Fully parallel, high-speed incoherent optical method for performing discrete Fourier transforms. *Opt. Lett.* 2:1–3.
4. Guilfoyle, P. S. and McCallum, D. S. 1996. High-speed low-energy digital optical processors. Opt. Eng. 35:436–442.
5. Ohtsu, M., Kobayashi, K., Kawazoe, T., Sangu, S., and Yatsui, T. 2002. Nanophotonics: design, fabrication, and operation of nanometric devices using optical near fields. *IEEE J. Sel. Top. Quantum Electron.* 8:839–862.
6. Pohl, D. W. and Courjon, D. eds. 1993. *Near Field Optics.* Dordrecht: Kluwer Academic.
7. Ohtsu, M. and Hori, H. 1999. *Near-Field Nano-Optics.* New York: Kluwer Academic/Plenum Publishers.

8. Naruse, M., Miyazaki, T., Kawazoe, T., Kobayashi, K., Sangu, S., Kubota, F., and Ohtsu, M. 2005. Nanophotonic computing based on optical near-field interactions between QDs. *IEICE Trans. Electron.* E88-C:1817–1823.
9. Maier, S. A., Kik, P. G., Atwater, H. A., Meltzer, S., Harel, E., Koel, B. E., and Requicha, A. A. G. 2003. Local detection of electromagnetic energy transport below the diffraction limit in metal nanoparticle plasmon waveguides, *Nature Materials.* 2:229–232.
10. Kawazoe, T., Kobayashi, K., Akahane, K., Naruse, M., Yamamoto, N., and Ohtsu, M. 2006. Demonstration of nanophotonic NOT gate using near-field optically coupled QDs. *Appl. Phys. B.* 84:243–246.
11. Tang, Z. K., Yanase, A., Yasui, T., Segawa, Y., and Cho, K. Optical selection rule and oscillator strength of confined exciton system in CuCl thin films. 1993. *Phys. Rev. Lett.* 71:1431–1434.
12. Akers, S. B. 1978. Binary decision diagrams. *IEEE Trans. Computers* C-27: 509–516.
13. Liu, H. 2002. Routing table compaction in ternary CAM, *IEEE Micro.* 22:58–64.
14. Grunnet-Jepsen, A., Johnson, A. E., Maniloff, E. S., Mossberg, T. W., Munroe, M. J., and Sweetser, J. N. 1999. Fibre Bragg grating based spectral encoder/decoder for lightwave CDMA. *Electron. Lett.* 35:1096–1097.
15. Naruse, M., Mitsu, H., Furuki, M., Iwasa, I., Sato, Y., Tatsuura, S., Tian, M., and Kubota, F. 2004. Terabit all-optical logic based on ultrafast two-dimensional transmission gating. *Opt. Lett.* 29:608–610.
16. Kitayama, K. and Murata, M. 2003. Versatile optical code-based MPLS for circuit, burst, and packet switchings. *IEEE J. Lightwave Technol.* 21:2753- 2764.
17. Kawazoe, T., Kobayashi, K., Sangu, S., and Ohtsu, M. 2003. Demonstration of a nanophotonic switching operation by optical near-field energy transfer. *Appl. Phys. Lett.* 82:2957–2959.
18. Sangu, S., Kobayashi, K., Shojiguchi, A., and Ohtsu, M. 2004. Logic and functional operations using a near-field optically coupled QD system. *Phys. Rev. B.* 69:115334 1–13.
19. Naruse, M., Miyazaki, T., Kubota, F., Kawazoe, T., Kobayashi, K., Sangu, S., and Ohtsu, M. 2005. Nanometric summation architecture using optical near-field interaction between QDs. *Opt. Lett.* 30:201–203.
20. Kawazoe, T., Kobayashi, K., and Ohtsu, M. 2005. Optical nanofountain: A biomimetic device that concentrates optical energy in a nanometric region. *Appl. Phys. Lett.* 86:103102 1–3.
21. Kawazoe, T., Kobayashi, K., Lim, J., Narita, Y., and Ohtsu, M. 2002. Direct Observation of Optically Forbidden Energy Transfer between CuCl Quantum Cubes via Near-Field Optical Spectroscopy *Phys. Rev. Lett.* 88:067404 1–4.
22. Arsovski, I., Chandler, T., and Sheikholeslami, A. 2003. A ternary content-addressable memory (TCAM) based on 4T static storage and including a current-race sensing scheme. *IEEE J. Solid-State Circuits.* 38:155–158.
23. Lin, P.-F. and Kuo, J. B. 2001. A 1-V 128-kb four-way set-associative CMOS cache memory usingwordline-oriented tag-compare (WLOTC) structure with the-content-addressable-memory (CAM) 10-transistor tag cell. *IEEE J. of Solid-State Circuits.* 36:666–675.
24. Saida, T., Okamoto, K., Uchiyama, K., Takiguchi, K., Shibata, T., and Sugita, A. 2001. Integrated optical digital-to-analogue converter and its application to pulse pattern recognition. *Electron. Lett.* 37:1237—1238.

25. Takahara, J., Yamagishi, S., Taki, H., Morimoto, A., and Kobayashi, T. 1997. Guiding of a one-dimensional optical beam with nanometer diameter. *Opt. Lett.* 22:475–477.
26. Brongersma, M. L., Hartman, J. W., and Atwater, H. A. 2000. Electromagnetic energy transfer and switching in nanoparticle chain arrays below the diffraction limit. *Phys. Rev. B.* 62:R16356-R16359.
27. Yatsui, T., Kourogi, M., and Ohtsu, M. 2001. Plasmon waveguide for optical far/near-field conversion. *Appl. Phys. Lett.* 79:4583–4585.
28. Nomura, W., Ohtsu, M., and Yatsui, T. 2005. Nanodot coupler with a surface plasmon polariton condenser for optical far/near-field conversion. *Appl. Phys. Lett.* 86:181108 1–3.
29. Naruse, M., Kawazoe, T., Sangu, S., Kobayashi, K., and Ohtsu, M. 2006. Optical interconnects based on optical far- and near-field interactions for high-density data broadcasting. *Opt. Express.* 14:306–313.
30. Li, B., Qin, Y., Cao, X., Sivalingam, K. M. 2001. Photonic Packet Switching: Architecture and Performance. *Optical Networking Mag.* 2:27–39.
31. De Souza, E. A., Nuss, M. C., Knox, W. H., and Miller, D. A. B. 1995. Wavelength-division multiplexing with femtosecond pulses. *Opt. Lett.* 20:1166–1168.
32. Naruse, M., Hori, H., Kobayashi, K., and Ohtsu, M. 2007. Tamper resistance in optical excitation transfer based on optical near-field interactions *Opt. Lett.* 32, 1761–1763.
33. Kocher, P., Jaffe, J., and Jun, B. Introduction to differential power analysis and related attacks. Cryptography Research. http://www.cryptography.com/resources/whitepapers/DPATechInfo.pdf
34. Hori, H. 2001. Electronic and Electromagnetic Properties in Nanometer Scales. In *Optical and Electronic Process of Nano-Matters,* ed. M. Ohtsu. 1–55. Tokyo: KTK Scientific/Dordrecht: Kluwer Academic.
35. Ingold, G.-L. and Nazarov, Y. V. 1992. Charge Tunneling Rates in Ultrasmall Junctions. In *Single Charge Tunneling,* eds. H. Grabert and M. H. Devoret, 21–107. New York: Plenum Press.
36. Kobayashi, K. and Ohtsu, M. 1999. Quantum theoretical approach to a near-field optical system. *J. Microscopy.* 194:249–254.
37. Carmichael, H. J. 1999. *Statistical Methods in Quantum Optics I* Berlin: Springer-Verlag.
38. Tate, N., Nomura, W., Yatsui, T., Naruse, M., Ohtsu, M. 2008. Hierarchical hologram based on optical near-and far-field responses *Optics Express* 16: 607–612.
39. Ohtsu, M. and Kobayashi, K. 2004. *Optical Near Fields.* Berlin: Springer-Verlag.
40. Naruse, M., Yatsui, T., Nomura, W., Hirose, N., and Ohtsu, M. 2005. Hierarchy in optical near-fields and its application to memory retrieval *Optics Express.* 13 9265–9271.
41. Naruse, M., Inoue, T., Hori, H. 2007. Analysis and synthesis of hierarchy in optical near-field interactions at the nanoscale based on Angular Spectrum. *Jpn. J. Appl. Phys.* Accepted.
42. Wolf, E. and Nieto-Vesperinas, M. 1985. Analyticity of the angular spectrum amplitude of scattered fields and some of its consequences *J. Opt. Soc. Am. A.* 2:886–890.
43. Inoue, T. and Hori, H., 2005. Quantum theory of radiation in optical near field based on quantization of evanescent electromagnetic waves using detector Mode. In *Progress in Nano-Electro-Optics IV,* ed. M. Ohtsu. 127–199. Berlin: Springer Verlag.

44. Naruse, M., Inoue, T. and Hori, H. Analysis of Modulation of Optical Near-Fields by Positioning Nanoparticles Based on Angular Spectrum Representation. In *Conference on Lasers and Electro-Optics/Quantum Electronics and Laser Science Conference and Photonic Applications Systems Technologies 2006 Technical Digest* (Optical Society of America, Washington, DC, 2006), JWB105.
45. Naruse, M., Yatsui, T., Kawazoe, T., Akao, Y., and Ohtsu, M. 2008. Design and simulation of a nanophotonic traceable memory using localized energy dissipation and hierarchy of optical near-field interactions. *IEEE Trans. Nanotechnol.* 7: 14–19.
46. Grober, R. D., Schoelkopf, R. J., and Prober, D. E. 1997. Optical antenna: towards a unity efficiency near-field optical probe. *Appl. Phys. Lett.* 70:1354–1336.
47. Crozier, K. B., Sundaramurthy, A., Kino, G. S., and Quate, C. F. 2003. Optical antennas: Resonators for local field enhancement. *J. Appl. Phys.* 94:4632–4642.
48. Matsumoto, T., Shimano, T., Saga, H., Sukeda, H., and Kiguchi, M. 2004. Highly efficient probe with a wedge-shaped metallic plate for high density near-field optical recording. *J. Appl. Phys.* 95:3901–3906.
49. Muhlschlegel, P., Eisler, H.–J., Martin, O. J. F., Hecht, B., and Pohl, D. W. 2005. Resonant optical antennas. *Science.* 308:1607–1609.
50. Fuji, H., Tominaga, J., Men, L., Nakano, T., Katayama H., and Atoda, N. 2000. A Near-Field Recording and Readout Technology Using a Metallic Probe in an Optical Disk. *Jpn. J. Appl. Phys.* 39:980–981.
51. For example, Blu-ray Disc Association. http://www.blu-raydisc.com/
52. Naruse, M., Yatsui, T., Kim, J. H., and Ohtsu, M. 2007. Hierarchy in Optical Near-Fields by Nano-Scale Shape Engineering and Its Application to Traceable Memory. In *Conference on Lasers and Electro-Optics/Quantum Electronics and Laser Science Conference and Photonic Applications Systems Technologies 2007 Technical Digest* (Optical Society of America, Washington, DC, 2007). CThV3.
53. Fundamental guiding principles—"Beyond CMOS" Information processing, Emerging Research Devices. 2005. In *International Technology Roadmap for Semiconductors 2005 Edition*. 56.

# Appendix A

## Projection Operator

We briefly outline what the projection operator is and what kind of properties it has. When one considers an interacting system such as a system consisting of an isolated quantum system and electromagnetic field, the Hamiltonian operator $\hat{H}$ for the total system is represented as a sum of $\hat{H}_0$ and $\hat{V}$ as

$$\hat{H} = \hat{H}_0 + \hat{V}, \tag{A1}$$

where $\hat{H}_0$ describes the isolated system while $\hat{V}$ represents the interaction. If eigenstates and eigenvalues of the Hamiltonian $\hat{H}$ are written as $|\psi_j\rangle$ and $E_j$, respectively, the following Schrödinger equation holds:

$$\hat{H}|\psi_j\rangle = E_j|\psi_j\rangle, \tag{A2}$$

where the suffix $j$ is used for specifying quantum number to distinguish each eigenstate. In a similar way let us denote eigenstates of the Hamiltonian $\hat{H}_0$ as $|\phi_j\rangle$. Then we define a projection operator $P$ as

$$P = \sum_{j=1}^{N} |\phi_j\rangle\langle\phi_j|, \tag{A3}$$

where $N$ is an arbitrary integer, but it is preferable to be a small number in practice. Acting the projection operator on an arbitrary state $|\psi\rangle$, we obtain

$$P|\psi\rangle = \sum_{j=1}^{N} |\phi_j\rangle\langle\phi_j|\psi\rangle. \tag{A4}$$

From this relation it follows that the projection operator transforms the arbitrary state $|\psi\rangle$ into the P space span by the eigenstate $|\phi_j\rangle$. We have defined the projection operator based on steady states of the Schrödinger equation. Readers who are interested in the time dependent approach of the projection operator method are referred to Refs. [14–19].

Using the projection operator $P$, we can derive an effective operator $\hat{O}_{\mathrm{eff}}$ of an arbitrary operator $\hat{O}$ that corresponds to a physical observable. In order to perform the calculation, let us begin with some elementary and useful properties of the projection operator. Becausee the eigenstate $|\phi_j\rangle$ is orthonormalized, the projection operator $P$ satisfies the following relation:

$$P = P^{\dagger}, \quad P^2 = P. \tag{A5}$$

The complimentary operator $Q$ given by

$$Q = 1 - P \tag{A6a}$$

reads

$$Q = Q^{\dagger}, \ \ Q^2 = Q. \tag{A6b}$$

Any state in the $P$ space is orthogonal to any state in the $Q$ space, and thus we have

$$PQ = QP = 0. \tag{A7}$$

Noticing that $|\phi_j\rangle$ is an eigenstate of $\hat{H}_0$, the commutation between the projection operator and $\hat{H}_0$ should be zero as follows:

$$[P, \hat{H}_0] = P\hat{H}_0 - \hat{H}_0 P = 0, \tag{A8a}$$

$$[Q, \hat{H}_0] = Q\hat{H}_0 - \hat{H}_0 Q = 0. \tag{A8b}$$

# Appendix B

## *Effective Operator and Effective Interaction*

Dividing the eigenstates $|\psi_j\rangle$ into two groups, we define $|\psi_j^{(1)}\rangle$ in the $P$ space and $|\psi_j^{(2)}\rangle$ in the $Q$ space as follows:

$$\begin{cases} \left|\psi_j^{(1)}\right\rangle = P\,|\psi_j\rangle, & \text{(B1a)} \\ \left|\psi_j^{(2)}\right\rangle = Q\,|\psi_j\rangle. & \text{(B1b)} \end{cases}$$

Then let us obtain a set of equations for $|\psi_j^{(1)}\rangle$ and $|\psi_j^{(2)}\rangle$. From Eq. (A6a) in Appendix A we have

$$|\psi_j\rangle = P\left|\psi_j^{(1)}\right\rangle + Q\left|\psi_j^{(2)}\right\rangle, \tag{B2}$$

and from Eqs. (A1) and (A2)

$$(E_j - \hat{H}_0)\,|\psi_j\rangle = \hat{V}\,|\psi_j\rangle, \tag{B3}$$

is derived. Inserting Eq. (B2) into Eq. (B3), it reads

$$(E_j - \hat{H}_0)P\left|\psi_j^{(1)}\right\rangle + (E_j - \hat{H}_0)Q\left|\psi_j^{(2)}\right\rangle = \hat{V}P\left|\psi_j^{(1)}\right\rangle + \hat{V}Q\left|\psi_j^{(2)}\right\rangle. \tag{B4}$$

Operating $P$ from the left side on Eq. (B4) and using Eqs. (A5), (A7), and (A8), one can obtain

$$(E_j - \hat{H}_0)P\left|\psi_j^{(1)}\right\rangle = P\hat{V}P\left|\psi_j^{(1)}\right\rangle + P\hat{V}Q\left|\psi_j^{(2)}\right\rangle. \tag{B5}$$

Similarly operating $Q$ from the left side on Eq. (B4), it can be rewritten as

$$(E_j - \hat{H}_0)Q\left|\psi_j^{(2)}\right\rangle = Q\hat{V}P\left|\psi_j^{(1)}\right\rangle + Q\hat{V}Q\left|\psi_j^{(2)}\right\rangle. \tag{B6}$$

From Eq. (B6), it is possible to formally express $Q|\psi_j^{(2)}\rangle$ by $P|\psi_j^{(1)}\rangle$ as

$$\begin{aligned} Q\left|\psi_j^{(2)}\right\rangle &= (E_j - \hat{H}_0 - Q\hat{V})^{-1}Q\hat{V}P\left|\psi_j^{(1)}\right\rangle \\ &= \{(E_j - \hat{H}_0)[1 - (E_j - \hat{H}_0)^{-1}Q\hat{V}]\}^{-1}Q\hat{V}P\left|\psi_j^{(1)}\right\rangle \\ &= \hat{J}(E_j - \hat{H}_0)^{-1}Q\hat{V}P\left|\psi_j^{(1)}\right\rangle, \end{aligned} \tag{B7}$$

where the operator $\hat{J}$ is defined by

$$\hat{J} = [1 - (E_j - \hat{H}_0)^{-1} Q \hat{V}]^{-1}. \tag{B8}$$

When one substitutes Eq. (B7) into the second term on the right-hand side in Eq. (B5), one obtains the equation for $P\,|\,\psi_j^{(1)}\rangle$ as follows:

$$\begin{aligned}(E_j - \hat{H}_0)P\left|\psi_j^{(1)}\right\rangle &= P\hat{V}P\left|\psi_j^{(1)}\right\rangle + P\hat{V}\hat{J}(E_j - \hat{H}_0)^{-1}Q\hat{V}P\left|\psi_j^{(1)}\right\rangle \\ &= P\hat{V}\hat{J}\{\hat{J}^{-1} + (E_j - \hat{H}_0)^{-1}Q\hat{V}\}P\left|\psi_j^{(1)}\right\rangle \\ &= P\hat{V}\hat{J}P\left|\psi_j^{(1)}\right\rangle.\end{aligned} \tag{B9}$$

By contrast, if Eq. (B7) is inserted into Eq. (B2), then we have the equation for $|\,\psi_j\rangle$ as

$$\begin{aligned}|\,\psi_j\rangle &= P\left|\psi_j^{(1)}\right\rangle + \hat{J}(E_j - \hat{H}_0)^{-1}Q\hat{V}P\left|\psi_j^{(1)}\right\rangle \\ &= \hat{J}\{\hat{J}^{-1} + (E_j - \hat{H}_0)^{-1}Q\hat{V}\}P\left|\psi_j^{(1)}\right\rangle \\ &= \hat{J}P\left|\psi_j^{(1)}\right\rangle.\end{aligned} \tag{B10}$$

Noticing the normalization condition for $|\,\psi_j\rangle$ and $|\,\psi_j^{(1)}\rangle$, it is possible to rewrite Eq. (B10):

$$|\,\psi_j\rangle = \hat{J}P(P\hat{J}^{\dagger}\hat{J}P)^{-1/2}\left|\psi_j^{(1)}\right\rangle. \tag{B11}$$

Because $|\,\psi_j\rangle$ has been expressed in terms of $|\,\psi_j^{(1)}\rangle$, one can obtain an effective operator $\hat{O}_{\text{eff}}$ from the following relation [5,6,20]:

$$\langle\psi_i\,|\,\hat{O}\,|\,\psi_j\rangle = \left\langle\psi_i^{(1)}\middle|\hat{O}_{\text{eff}}\middle|\psi_j^{(1)}\right\rangle. \tag{B12}$$

Substituting Eq. (B11) into the left-hand side of Eq. (B12) and comparing it with the right-hand side, we can get

$$\hat{O}_{\text{eff}} = (P\hat{J}^{\dagger}\hat{J}P)^{-1/2}(P\hat{J}^{\dagger}\hat{O}\hat{J}P)(P\hat{J}^{\dagger}\hat{J}P)^{-1/2}. \tag{B13}$$

If $\hat{V}$ is taken as $\hat{O}$, then an effective interaction operator $\hat{V}_{\text{eff}}$ is written as

$$\hat{V}_{\text{eff}} = (P\hat{J}^{\dagger}\hat{J}P)^{-1/2}(P\hat{J}^{\dagger}\hat{V}\hat{J}P)(P\hat{J}^{\dagger}\hat{J}P)^{-1/2}. \tag{B14}$$

This is what we are searching for. As is expected, $\hat{V}_{\text{eff}}$ operates only on any states in the P space. Once the bare interaction $\hat{V}$ is given, it only remains to obtain the unknown operator $\hat{J}$.

In order to obtain an explicit form of the operator $\hat{J}$ let us consider an operator relation $[\hat{J},\hat{H}_0]P$ and operate it on the state $|\psi_j\rangle$. This yields

$$\begin{aligned}[\hat{J},\hat{H}_0]P|\psi_j\rangle &= (\hat{J}\hat{H}_0 - \hat{H}_0\hat{J})P|\psi_j\rangle \\ &= \{(E_j - \hat{H}_0)\hat{J} - \hat{J}(E_j - \hat{H}_0)\}P|\psi_j\rangle.\end{aligned} \tag{B15}$$

We replace the first term $(E_j - \hat{H}_0)$ in Eq. (B15) by $\hat{V}$, which gives

$$[\hat{J},\hat{H}_0]P|\psi_j\rangle = \hat{V}\hat{J}P|\psi_j\rangle - \hat{J}(E_j - \hat{H}_0)P|\psi_j\rangle. \tag{B16}$$

By using Eqs. (B5) and (B7), the second term of Eq. (B16) can be rewritten as

$$\begin{aligned}\hat{J}(E_j - \hat{H}_0)P|\psi_j\rangle &= \hat{J}(E_j - \hat{H}_0)P\left|\psi_j^{(1)}\right\rangle \\ &= \hat{J}\left\{P\hat{V}P\left|\psi_j^{(1)}\right\rangle + P\hat{V}Q\left|\psi_j^{(2)}\right\rangle\right\} \\ &= \hat{J}P\hat{V}\left\{P\left|\psi_j^{(1)}\right\rangle + \hat{J}(E_j - \hat{H}_0)^{-1}Q\hat{V}P\left|\psi_j^{(1)}\right\rangle\right\} \\ &= \hat{J}P\hat{V}\hat{J}\left\{\hat{J}^{-1} + (E_j - \hat{H}_0)^{-1}Q\hat{V}\right\}P\left|\psi_j^{(1)}\right\rangle.\end{aligned} \tag{B17}$$

Making use of Eq. (B8) and noting that $P|\psi_j^{(1)}\rangle = P|\psi_j\rangle$, we can rewrite Eq. (B16) as

$$[\hat{J},\hat{H}_0]P|\psi_j\rangle = \hat{V}\hat{J}P|\psi_j\rangle - \hat{J}P\hat{V}\hat{J}P|\psi_j\rangle. \tag{B18}$$

Therefore, we have for the operator $\hat{J}$

$$[\hat{J},\hat{H}_0]P = \hat{V}\hat{J}P - \hat{J}P\hat{V}\hat{J}P, \tag{B19}$$

where all operators involved are known except $\hat{J}$.

In order to solve Eq. (B19) perturbatively, let us assume

$$\hat{J} = \sum_{n=0}^{\infty} g^n \hat{J}^{(n)}, \tag{B20}$$

where the $n$th term $\hat{J}^{(n)}$ contains $n$ $\hat{V}$s and $\hat{J}^{(0)} = P$. Substituting Eq. (B20) into Eq. (19) and equating terms of order $g^n$ on both sides, we successively obtain $\hat{J}^{(1)}, \hat{J}^{(2)}, \cdots, \hat{J}^{(n)}$. For example, noticing the identity

$$\begin{aligned} Q[\hat{J}^{(1)}, \hat{H}_0]P &= Q\hat{V}\hat{J}^{(0)}P - Q\hat{J}^{(0)}P\hat{V}\hat{J}^{(0)}P \\ &= Q\hat{V}P, \end{aligned} \tag{B21}$$

we take the matrix element of Eq. (B21) with $|\psi_j\rangle$;

$$\begin{aligned} \langle\psi_i | Q[\hat{J}^{(1)}, \hat{H}_0]P | \psi_j\rangle &= \left\langle\psi_i \middle| Q\hat{J}^{(1)}\left(E_P^0 - E_Q^0\right)P \middle| \psi_j\right\rangle \\ &= \langle\psi_i | Q\hat{V}P | \psi_j\rangle, \end{aligned} \tag{B22}$$

where we used the eigenvalues $E_P^0$ and $E_Q^0$ of the Hamiltonian $\hat{H}_0$ in the $P$ space and $Q$ space, respectively. From Eq. (B22), $\hat{J}^{(1)}$ is obtained as follows:

$$\hat{J}^{(1)} = Q\hat{V}\left(E_P^0 - E_Q^0\right)^{-1} P. \tag{B23}$$

Higher orders of $\hat{J}^{(n)}$ are successively given in a similar way. Whenever one improves the approximation of $\hat{J}$, one can examine the higher-order effects originating in the Q space. These procedures correspond to how to obtain many-body Green's functions for matter systems, or Green's functions for photons "dressed with matter excitations "[21].

# Appendix C

## *Elementary Excitation Mode and Electronic Polarization*

The concept of elementary excitations or quasi-particles has been discussed for a long time [22–27], and it is valuable for description of excited states, complex behavior, or dynamics of a many-body system. Excited states of a many-body system are considered as a collection of certain fundamental excited states that we call the elementary excitation. As a prerequisite, there must be a well-defined excitation energy whose value should be larger than the width of the relevant energy level. Then the relation between momentum $\vec{p}$ and energy $E$ of the elementary excitation, that is, $E = E(\vec{p})$, is referred to as the dispersion relation.

Phonons, as quanta of normal modes of crystal vibration, are well known as an example of the elementary excitation modes in a solid. The motion is collective, which means that the total number of phonons is independent of the number of crystal lattice. The momentum of the elementary excitation is $\vec{p} = \hbar\vec{k}$ in terms of the wave vector $\vec{k}$ of normal vibration, not the mechanical momentum of individual crystal lattice. The energy of the elementary excitation is also given by the angular frequency $\omega$ of the normal vibration as $E = \hbar\omega$.

As another example of the elementary excitations, we have plasmons, which correspond to collective motion of electron density in interacting electron gas; polarons are quasi-particles originated from the coupling between conduction electrons and optical phonons; and magnons corresponding to collective modes of spin density waves. Excitons are also well known, and describe the elementary excitation related to an electron-hole pair in a solid. As a limiting case, Frenkel excitons and Wannier excitons are frequently discussed. When the distance between the electron and hole in an exciton (Bohr radius of the exciton) is smaller than the atomic distance in the crystal, it is called a Frenkel exciton; Wannier excitons correspond to the opposite case, in which the Bohr radius of the exciton is relatively larger than the lattice constant of the crystal.

Let us consider the light-matter interaction, on the basis of the exciton concept. Incident photons interact with matter, and produce the successive creation and annihilation of excitons and photons in matter, that is, an electronic polarization field. This process indicates a new steady state with a new dispersion relation and energy because of the photon-exciton interaction.

Normal modes, or elementary excitation modes for this coupled oscillation are called polaritons. In particular, they are called exciton polaritons because of the occurrence of the mixed states of photons and excitons. The situation is analogous to the case in which two coupled oscillations with angular frequencies $\omega_1$ and $\omega_2$ produce new normal oscillations with angular frequencies $\Omega_1$ and $\Omega_2$. Dressed atom states in an atom-photon interacting system [28] are conceptually similar to the normal modes of the photon and electronic polarization field, or exciton polaritons as quasi-particles.

Rewriting the Hamiltonian for a photon-electron interacting system in terms of excitons, one can obtain the following Hamiltonian describing exciton polaritons:

$$\hat{H} = \sum_{\vec{k}} \hbar\omega_{\vec{k}} \hat{a}^{\dagger}_{\vec{k}} \hat{a}_{\vec{k}} + \sum_{\vec{k}} \hbar\varepsilon_{\vec{k}} \hat{b}^{\dagger}_{\vec{k}} \hat{b}_{\vec{k}} + \sum_{\vec{k}} \hbar D(\hat{a}_{\vec{k}} + \hat{a}^{\dagger}_{-\vec{k}})(\hat{b}^{\dagger}_{\vec{k}} + \hat{b}_{-k}). \tag{C1}$$

Here the first and second terms correspond to the Hamiltonians for free photons and free excitons, respectively, and the third term describes the photon-exciton interaction, whose coupling strength is $\hbar D$. The explicit expression for $\hbar D$ is given from Eqs. (9), (10), and (11) in Section 2.1. Energies caused by zero-point oscillation are suppressed in Eq. (C1). Creation and annihilation operators for photons are denoted by $\hat{a}^{\dagger}_{\vec{k}}$ and $\hat{a}_{\vec{k}}$, while those for excitons are designated by $\hat{b}^{\dagger}_{\vec{k}}$ and $\hat{b}_{\vec{k}}$. In the rewriting process, we define the creation and annihilation operators of excitons to be

$$\begin{cases} \hat{b}^{\dagger}_{\vec{l}} = \hat{c}^{\dagger}_{\vec{l},c} \hat{c}_{\vec{l},v}, \\ \hat{b}_{\vec{l}} = \hat{c}^{\dagger}_{\vec{l},v} \hat{c}_{\vec{l},c}, \end{cases} \tag{C2}$$

where we use the operator $\hat{c}_{\vec{l},v}$ that annihilates an electron in the valence band $v$ within an atom at the lattice site $\vec{l}$, and its Hermitian conjugate operator $\hat{c}^{\dagger}_{\vec{l},v}$ as well as the operator $\hat{c}^{\dagger}_{\vec{l},c}$ that creates an electron in the conduction band $c$ within an atom at the lattice site $\vec{l}$, and its Hermitian conjugate operator $\hat{c}_{\vec{l},c}$.

According to the conventional method, in addition, we introduce the operators

$$\begin{cases} \hat{b}_{\vec{k}} = \dfrac{1}{\sqrt{N}} \displaystyle\sum_{\vec{l}} e^{-i\vec{k}\cdot\vec{l}} \hat{b}_{\vec{l}}, \\ \hat{b}^{\dagger}_{\vec{k}} = \dfrac{1}{\sqrt{N}} \displaystyle\sum_{\vec{l}} e^{i\vec{k}\cdot\vec{l}} \hat{b}^{\dagger}_{\vec{l}}, \end{cases} \tag{C3}$$

in the momentum representation. Here the total number of lattice sites is assumed to be $N$ in the crystal considered.

Once the Hamiltonian for exciton polaritons is given by Eq. (C1), one can obtain eigenstates and eigenenergies of exciton polaritons, or the dispersion relation. For simplicity, we adopt the rotating wave approximation and neglect terms, $\hat{a}^{\dagger}_{-\vec{k}}\hat{b}^{\dagger}_{\vec{k}}$ and $\hat{a}_{\vec{k}}\hat{b}_{-\vec{k}}$, which create or annihilate both a photon and an exciton at the same time, and consider the following $\hat{H}_{\vec{k}}$:

$$\hat{H} = \sum_{\vec{k}} \hat{H}_{\vec{k}},$$

$$\hat{H}_{\vec{k}} = \hbar(\omega_{\vec{k}}\hat{a}^{\dagger}_{\vec{k}}\hat{a}_{\vec{k}} + \varepsilon_{\vec{k}}\hat{b}^{\dagger}_{\vec{k}}\hat{b}_{\vec{k}}) + \hbar D(\hat{b}^{\dagger}_{\vec{k}}\hat{a}_{\vec{k}} + \hat{a}^{\dagger}_{\vec{k}}\hat{b}_{\vec{k}}). \tag{C4}$$

We next introduce the creation and annihilation operators of exciton polaritons as $\hat{\xi}^{\dagger}_1$, $\hat{\xi}^{\dagger}_2$, and $\hat{\xi}_1$, $\hat{\xi}_2$, corresponding to new eigenfrequencies $\Omega_{\vec{k},1}$, $\Omega_{\vec{k},2}$, respectively. The Hamiltonian $\hat{H}_{\vec{k}}$ is assumed to be diagonalized in terms of $\hat{\xi}_1$, $\hat{\xi}_2$, and rewrite Eq. (C4) as

$$\begin{aligned}\hat{H}_{\vec{k}} &= \hbar(\Omega_{\vec{k},1}\hat{\xi}^{\dagger}_1\hat{\xi}_1 + \Omega_{\vec{k},2}\hat{\xi}^{\dagger}_2\hat{\xi}_2) = \hbar(\hat{b}^{\dagger}_{\vec{k}}, \hat{a}^{\dagger}_{\vec{k}})A\begin{pmatrix}\hat{b}_{\vec{k}}\\ \hat{a}_{\vec{k}}\end{pmatrix}\\ &= \hbar(a_{11}\hat{b}^{\dagger}_{\vec{k}}\hat{b}_{\vec{k}} + a_{12}\hat{b}^{\dagger}_{\vec{k}}\hat{a}_{\vec{k}} + a_{21}\hat{a}^{\dagger}_{\vec{k}}\hat{b}_{\vec{k}} + a_{22}\hat{a}^{\dagger}_{\vec{k}}\hat{a}_{\vec{k}}),\end{aligned} \tag{C5}$$

where $A$ is the 2 by 2 matrix whose elements are given by

$$A = \begin{pmatrix} a_{11} & a_{12}\\ a_{21} & a_{22}\end{pmatrix} = \begin{pmatrix}\varepsilon_{\vec{k}} & D\\ D & \omega_{\vec{k}}\end{pmatrix}. \tag{C6}$$

Applying unitary transformation $U$, (i.e., $U^{\dagger} = U^{-1}$)

$$\begin{pmatrix}\hat{b}_{\vec{k}}\\ \hat{a}_{\vec{k}}\end{pmatrix} = U\begin{pmatrix}\hat{\xi}_1\\ \hat{\xi}_2\end{pmatrix} \quad \text{with } U = \begin{pmatrix} u_{11} & u_{12}\\ u_{21} & u_{22}\end{pmatrix}, \tag{C7}$$

to Eq. (C5), we have

$$\hbar(\hat{b}^{\dagger}_{\vec{k}}, \hat{a}^{\dagger}_{\vec{k}})A\begin{pmatrix}\hat{b}_{\vec{k}}\\ \hat{a}_{\vec{k}}\end{pmatrix} = \hbar(\hat{\xi}^{\dagger}_1, \hat{\xi}^{\dagger}_2)U^{\dagger}AU\begin{pmatrix}\hat{\xi}_1\\ \hat{\xi}_2\end{pmatrix}. \tag{C8}$$

Since $U^{\dagger}AU = U^{-1}AU$ is diagonalized, we put

$$U^{-1}AU = \begin{pmatrix}\Omega_{\vec{k},1} & 0\\ 0 & \Omega_{\vec{k},2}\end{pmatrix} \equiv \Lambda, \tag{C9}$$

and obtain $AU = U\Lambda$, which reduces in terms of components $(j = 1,2)$ to

$$\begin{pmatrix}\varepsilon_{\vec{k}} - \Omega_{\vec{k},j} & D\\ D & \omega_{\vec{k}} - \Omega_{\vec{k},j}\end{pmatrix}\begin{pmatrix}u_{1j}\\ u_{2j}\end{pmatrix} = 0. \tag{C10}$$

This immediately gives the eigenvalue equation

$$(\Omega - \varepsilon_{\vec{k}})(\Omega - \omega_{\vec{k}}) - D^2 = 0, \tag{C11}$$

and the eigenenergies of exciton polaritons are

$$\hbar\Omega_{\vec{k},j} = \hbar\left[\frac{\varepsilon_{\vec{k}} + \omega_{\vec{k}}}{2} \pm \frac{\sqrt{(\varepsilon_{\vec{k}} - \omega_{\vec{k}})^2 + 4D^2}}{2}\right]. \tag{C12}$$

Equation (C12) provides the new dispersion relation that we are looking for. Using the dispersion relation of photons as $\omega_{\vec{k}} = ck$ with $k = |\vec{k}|$, we can plot the eigenenergies of exciton polariton as a function of $k$, as shown in Figure C.1. Here, for simplicity, we approximate the exciton dispersion as $\varepsilon_{\vec{k}} = \hbar\Omega$, independent of $k$.

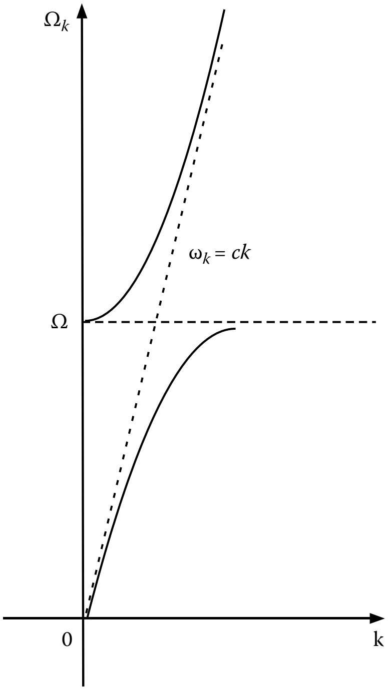

**FIGURE C.1**
Dispersion curve of an exciton polariton schematically drawn as a function of $k$. For simplicity, the exciton dispersion is approximated as $\varepsilon_k^r = h\Omega$, independent of $k$.

From Eq. (C10) and the unitarity of *U*, we have for the components of the eigenvectors

$$\begin{cases} u_{2j} = -\dfrac{\varepsilon_{\vec{k}} - \Omega_{\vec{k},j}}{D} u_{1j}, \\ u_{1j}^2 + u_{2j}^2 = 1, \qquad\qquad (j = 1, 2) \end{cases} \tag{C13}$$

and thus it reads

$$\left\{ 1 + \left( \frac{\varepsilon_{\vec{k}} - \Omega_{\vec{k},j}}{D} \right)^2 \right\} u_{1j}^2 = 1. \tag{C14}$$

Finally, the eigenvectors of exciton polaritons are given by

$$\begin{cases} u_{1j} = \left\{ 1 + \left( \dfrac{\varepsilon_{\vec{k}} - \Omega_{\vec{k},j}}{D} \right)^2 \right\}^{-1/2}, \\ u_{2j} = -\left( \dfrac{\varepsilon_{\vec{k}} - \Omega_{\vec{k},j}}{D} \right) \left\{ 1 + \left( \dfrac{\varepsilon_{\vec{k}} - \Omega_{\vec{k},j}}{D} \right)^2 \right\}^{-1/2}. \end{cases} \tag{C15}$$

New steady states for exciton polaritons can be described by Eqs. (C12) and (C15).

# Appendix D

## *Minimal Coupling and Multipolar Hamiltonians*

The "bare interaction" must be specified in order to obtain a more explicit expression of the effective interaction. There are two ways to describe the interaction between an electromagnetic field and a charged particle. One is to use the minimal coupling Hamiltonian, and the other is to employ the multipolar Hamiltonian. These two Hamiltonians are related to each other by a unitary transformation, and there are, in principle, no problems regardless of which is adopted [29–31]. However, it should be noted that the complexity of description depends on each problem: it may be easier for the minimal coupling Hamiltonian formalism to describe one problem, and more difficult to handle another. In this appendix, we briefly describe each Hamiltonian to show the equivalence of both Hamiltonians, as well as advantages and disadvantages of each Hamiltonian.

### Minimal Coupling Hamiltonian

We can derive the minimal coupling Hamiltonian for a charged particle, that is, the electromagnetic interaction with a charged particle, by imposing the local gauge invariance on the Hamiltonian describing free particle motion [14,29]. The minimal coupling Hamiltonian is defined such that the Schrödinger equation is not changed even if a wave function $\psi(\vec{r},t)$ is transformed by the phase transformation $\chi(\vec{r},t)$ as

$$\psi'(\vec{r},t) = \exp[i\chi(\vec{r},t)]\psi(\vec{r},t), \tag{D1}$$

and if vector potential $\vec{A}(\vec{r},t)$ and scalar potential $U(\vec{r},t)$ are transformed by the following gauge transformation

$$\begin{cases} \vec{A}'(\vec{r},t) = \vec{A}(\vec{r},t) + \dfrac{\hbar c}{e}\nabla\chi(\vec{r},t), \\ \\ U'(\vec{r},t) = U(\vec{r},t) - \dfrac{\hbar}{e}\dfrac{\partial}{\partial t}\chi(\vec{r},t). \end{cases} \tag{D2}$$

Here $\hbar$ and $e$ are the Planck constant divided by $2\pi$ and the electric charge of the particle. Let us simply assume the electromagnetic fields to be classical in this appendix. In order to satisfy this requirement, it follows that the Hamiltonian must be

$$H' = \frac{1}{2m}\left[\vec{p} - \frac{e}{c}\vec{A}'(\vec{r},t)\right]^2 + eU'(\vec{r},t), \tag{D3}$$

where the mass and the momentum of the particle are denoted by $m$ and $\vec{p}$ respectively. For confirmation, Eqs. (D1), (D2), and (D3) are substituted into the Schrödinger equation:

$$i\hbar\frac{\partial}{\partial t}\psi'(\vec{r},t) = H'\psi'(\vec{r},t). \tag{D4}$$

By noting that the momentum $\vec{p}$ should be an operator, $-i\hbar\nabla$ it follows that the left-hand side of Eq. (D4) reads

$$-\hbar\exp[i\chi(\vec{r},t)]\frac{\partial\chi(\vec{r},t)}{\partial t}\psi(\vec{r},t) + i\hbar\exp[i\chi(\vec{r},t)]\frac{\partial\psi(\vec{r},t)}{\partial t}. \tag{D5}$$

By contrast, the right-hand side of Eq. (D4) can be rewritten as

$$\begin{aligned}
&\frac{1}{2m}\left[-i\hbar\nabla - \frac{e}{c}\left\{\vec{A}(\vec{r},t) + \frac{\hbar c}{e}\nabla\chi(\vec{r},t)\right\}\right]^2 \exp\left[i\chi(\vec{r},t)\right]\psi(\vec{r},t)\\
&+e\left\{U(\vec{r},t) - \frac{\hbar}{e}\frac{\partial}{\partial t}\chi(\vec{r},t)\right\}\exp\left[i\chi(\vec{r},t)\right]\psi(\vec{r},t)\\
&= \frac{1}{2m}\left[-i\hbar\nabla - \frac{e}{c}\vec{A}(\vec{r},t) - \hbar\nabla\chi(\vec{r},t)\right]\cdot\exp[i\chi(\vec{r},t)]\left(-i\hbar\nabla - \frac{e}{c}\vec{A}(\vec{r},t)\right)\psi(\vec{r},t)\\
&+\exp[i\chi(\vec{r},t)]eU(\vec{r},t)\psi(\vec{r},t) - \hbar\exp\left[i\chi(\vec{r},t)\right]\frac{\partial\chi(\vec{r},t)}{\partial t}\psi(\vec{r},t)\\
&= \exp[i\chi(\vec{r},t)]\left\{\frac{1}{2m}\left[-i\hbar\nabla - \frac{e}{c}\vec{A}(\vec{r},t)\right]^2 + eU(\vec{r},t)\right\}\psi(\vec{r},t)\\
&-\hbar\exp\left[i\chi(\vec{r},t)\right]\frac{\partial\chi(\vec{r},t)}{\partial t}\psi(\vec{r},t).
\end{aligned} \tag{D6}$$

Here we used the following relation

$$-i\hbar\nabla\{\exp[i\chi(\vec{r},t)]\psi(\vec{r},t)\} = \exp[i\chi(\vec{r},t)](-i\hbar\nabla + \hbar\nabla\chi(\vec{r},t))\psi(\vec{r},t). \tag{D7}$$

Therefore, we can leave the Schrödinger equation unchanged as

$$\begin{aligned} &i\hbar\frac{\partial}{\partial t}\psi(\vec{r},t) = H\psi(\vec{r},t), \\ &H = \frac{1}{2m}\left[-i\hbar\nabla - \frac{e}{c}\vec{A}(\vec{r},t)\right]^2 + eU(\vec{r},t). \end{aligned} \tag{D8}$$

In other words, the relevant Hamiltonian is obtained by formally adding $eU(\vec{r},t)$ and replacing $\vec{p}$ by $\vec{p}-(e/c)\vec{A}(\vec{r},t)$ in the Hamiltonian for a free particle. From Eq. (D8), the interaction Hamiltonian for the electromagnetic field and the charged particle consists of two parts:

$$H_1 = -\frac{e}{mc}\vec{p}\cdot\vec{A}(\vec{r},t), \qquad H_2 = \frac{e^2}{2mc^2}\vec{A}^2(\vec{r},t). \tag{D9}$$

Advantages of this form of the Hamiltonian are that it can easily describe relativistic covariance and is firmly rooted in gauge theory [32,33]. However, it has the disadvantage that exact description including the retardation is cumbersome in the Coulomb gauge ($\nabla\cdot\vec{A}=0$), where the transversality of light is considered to be important in order to handle the interaction between light and matter as a many-body system.

## Multipolar Hamiltonian

Here we discuss another form of the light-matter interaction via a unitary transformation of the minimal coupling Hamiltonian, which removes the disadvantages mentioned ealier. The multipolar Hamiltonian has a simple form without the static Coulomb interaction, and can exactly describe the retardation effects by exchanging only transverse photons, up to the $\vec{A}^2$ term in the minimal coupling Hamiltonian [31].

Let us consider a charged-particle system confined in a microscopic area, and hereinafter call it a molecule. Electric neutrality of the molecule is assumed, and thus it may be an atom or a molecule as a physical entity. In the following, we choose a two-molecule system as an example, and look for an appropriate Hamiltonian. When the wavelength of electromagnetic waves is much greater than the molecular dimension, the vector potential $\vec{A}(\vec{R})$ at the center position $\vec{R}$ of a molecule is the same as $\vec{A}(\vec{q})$, independent of the position $\vec{q}$ of an electric charge in the molecule:

$$\vec{A}(\vec{q}) = \vec{A}(\vec{R}) \tag{D10}$$

From Eq. (D10), it follows that $\vec{B}=\nabla\times\vec{A}=0$, and thus we can neglect the interaction between the particle and the magnetic field. Moreover the electric dipole interaction, for simplicity, is taken into account, that is, the magnetic dipole and higher multipoles are neglected. We assume in addition that the electron exchange interaction is also negligible. Then the Lagrangian $L$ for the system, consisting of three parts $L_{\mathrm{mol}}$, $L_{\mathrm{rad}}$, and $L_{\mathrm{int}}$, can be written as

$$
\begin{aligned}
L &= L_{\mathrm{mol}} + L_{\mathrm{rad}} + L_{\mathrm{int}}, \\
L_{\mathrm{mol}} &= \sum_{\zeta=1}^{2}\left\{\sum_{\alpha}\frac{m_\alpha \dot{\vec{q}}_\alpha^{\,2}(\zeta)}{2} - V(\zeta)\right\}, \\
L_{\mathrm{rad}} &= \frac{1}{8\pi}\int\left\{\left(\frac{\dot{\vec{A}}}{c}\right)^2 - (\nabla\times\vec{A})^2\right\}d^3r, \qquad \text{(D11)} \\
L_{\mathrm{int}} &= \sum_{\zeta=1}^{2}\sum_{\alpha}\frac{e}{c}\dot{\vec{q}}_\alpha(\zeta)\cdot\vec{A}(\vec{R}_\zeta) - V_{\mathrm{inter}},
\end{aligned}
$$

where the index $\zeta$ is used for distinguishing the molecules 1 and 2, and $\alpha$ used to specify a charged particle in a molecule. The energy of the charged particles with mass $m_\alpha$ and velocity $\dot{\vec{q}}_\alpha$ in the Coulomb potential $V(\zeta)$ is denoted by $L_{\mathrm{mol}}$, while $L_{\mathrm{rad}}$ represents the energy of the electromagnetic field in free space. The third term in the Lagrangian shows the interaction between the charge and the electromagnetic field and the Coulomb interaction $V_{\mathrm{inter}}$ between molecules 1 and 2, which is given by

$$
V_{\mathrm{inter}} = \frac{1}{R^3}\{\vec{\mu}(1)\cdot\vec{\mu}(2) - 3(\vec{\mu}(1)\cdot\vec{e}_R)(\vec{\mu}(2)\cdot\vec{e}_R)\}. \qquad \text{(D12)}
$$

Here $R = |\vec{R}| = |\vec{R}_1 - \vec{R}_2|$ denotes the distance between the centers of molecules 1 and 2, and $\vec{e}_R$ is $\vec{R}/R$, the unit vector in the direction of $\vec{R}$. The electric dipole moments of molecules 1 and 2 are designated by $\vec{\mu}(1)$ and $\vec{\mu}(2)$ respectively.

In order to simplify the interaction Hamiltonian without changing the equations of motion, let us perform the Power-Zienau-Woolley transformation [29] on the original Lagrangian $L$:

$$
L_{\mathrm{mult}} = L - \frac{1}{c}\frac{d}{dt}\int\vec{P}^{\perp}(\vec{r})\cdot\vec{A}(\vec{r})d^3r, \qquad \text{(D13)}
$$

where $\vec{P}^{\perp}(\vec{r})$ is the transverse component of the polarization density $\vec{P}(\vec{r})$; this means that transverse photons can only contribute to the second term in Eq. (D13). The polarization density $\vec{P}(\vec{r})$ is

$$
\begin{aligned}
\vec{P}(\vec{r}) &= \sum_{\zeta,\alpha} e(\vec{q}_\alpha - \vec{R}_\zeta)\int_0^1 \delta(\vec{r} - \vec{R}_\zeta - \lambda(\vec{q}_\alpha - \vec{R}_\zeta))d\lambda \\
&= \sum_{\zeta,\alpha} e(\vec{q}_\alpha - \vec{R}_\zeta) \\
&\quad \left[1 - \frac{1}{2!}\{(\vec{q}_\alpha - \vec{R}_\zeta)\cdot\nabla\} + \frac{1}{3!}\{(\vec{q}_\alpha - \vec{R}_\zeta)\cdot\nabla\}^2 - \cdots\right]\delta(\vec{r} - \vec{R}_\zeta), \qquad \text{(D14)}
\end{aligned}
$$

and only the electric dipole term is retained:

$$\begin{aligned}\vec{P}(\vec{r}) &= \sum_{\zeta,\alpha} e(\vec{q}_\alpha - \vec{R}_\zeta)\delta(\vec{r}-\vec{R}_\zeta)\\ &= \vec{\mu}(1)\delta(\vec{r}-\vec{R}_1)+\vec{\mu}(2)\delta(\vec{r}-\vec{R}_2). \qquad \text{(D15)}\end{aligned}$$

Note that the current density $\vec{j}(\vec{r})$ is

$$\vec{j}(\vec{r}) = \sum_{\zeta,\alpha} e\dot{\vec{q}}_\alpha \delta(\vec{r}-\vec{R}_\zeta), \qquad \text{(D16)}$$

and the transverse component of the current density is related to the transverse component of the polarization density as follows:

$$\vec{j}^{\perp}(\vec{r}) = \frac{d\vec{P}^{\perp}(\vec{r})}{dt}. \qquad \text{(D17)}$$

Using Eqs. (D16) and (D17), we can rewrite the interaction Lagrangian $L_{\text{int}}$ as

$$L_{\text{int}} = \frac{1}{c}\int \vec{j}^{\perp}(\vec{r})\cdot\vec{A}(\vec{r})d^3r - V_{\text{inter}} = \frac{1}{c}\int \frac{d\vec{P}^{\perp}(\vec{r})}{dt}\cdot\vec{A}(\vec{r})d^3r - V_{\text{inter}}, \qquad \text{(D18)}$$

and thus $L_{\text{mult}}$ given by Eq. (D13) becomes

$$\begin{aligned}L_{\text{mult}} &= L - \frac{1}{c}\int \frac{d\vec{P}^{\perp}(\vec{r})}{dt}\cdot\vec{A}(\vec{r})d^3r - \frac{1}{c}\int \vec{P}^{\perp}(\vec{r})\cdot\dot{\vec{A}}(\vec{r})d^3r\\ &= L_{\text{mol}} + L_{\text{rad}} - \frac{1}{c}\int \vec{P}^{\perp}(\vec{r})\cdot\dot{\vec{A}}(\vec{r})d^3r - V_{\text{inter}}. \qquad \text{(D19)}\end{aligned}$$

Here recall the definition of the momentum $\vec{p}_\alpha$ conjugate to $\vec{q}_\alpha$, and $\vec{\Pi}(\vec{r})$ to $\vec{A}(\vec{r})$,

$$\begin{aligned}\vec{p}_\alpha &= \frac{\partial L_{\text{mult}}}{\partial\dot{\vec{q}}_\alpha} = \frac{\partial L_{\text{mol}}}{\partial\dot{\vec{q}}_\alpha} = m_\alpha\dot{\vec{q}}_\alpha,\\ \vec{\Pi}(\vec{r}) &= \frac{\partial L_{\text{mult}}}{\partial\dot{\vec{A}}(\vec{r})} = \frac{\partial L_{\text{rad}}}{\partial\dot{\vec{A}}(\vec{r})} - \frac{\partial}{\partial\dot{\vec{A}}(\vec{r})}\frac{1}{c}\int \vec{P}^{\perp}(\vec{r})\cdot\dot{\vec{A}}(\vec{r})d^3r\\ &= \frac{1}{4\pi c^2}\dot{\vec{A}}(\vec{r}) - \frac{1}{c}\vec{P}^{\perp}(\vec{r}) = -\frac{1}{4\pi c}\{\vec{E}^{\perp}(\vec{r})+4\pi\vec{P}^{\perp}(\vec{r})\}. \qquad \text{(D20)}\end{aligned}$$

Because we have the relation between the electric field $\vec{E}(\vec{r})$ and the electric displacement $\vec{D}(\vec{r})$, those transverse components also satisfy

$$\vec{D}^{\perp}(\vec{r}) = \vec{E}^{\perp}(\vec{r}) + 4\pi\vec{P}^{\perp}(\vec{r}), \qquad \text{(D21)}$$

and thus the momentum $\vec{\Pi}(\vec{r})$ can be rewritten as

$$\vec{\Pi}(\vec{r}) = -\frac{1}{4\pi c}\vec{D}^{\perp}(\vec{r}). \qquad \text{(D22)}$$

By putting them together, canonical transformation of the Lagrangian $L_{\text{mult}}$ gives a new Hamiltonian $H_{\text{mult}}$

$$H_{\text{mult}} = \sum_{\zeta,\alpha} \vec{p}_\alpha(\zeta)\cdot\dot{\vec{q}}_\alpha(\zeta) + \int \vec{\Pi}(\vec{r})\cdot\dot{\vec{A}}(\vec{r})d^3r - L_{\text{mult}}$$

$$= \sum_{\zeta}\left\{\sum_{\alpha}\frac{\vec{p}_\alpha^{\,2}(\zeta)}{2m_\alpha} + V(\zeta)\right\} + \left\{\frac{1}{8\pi}\int[(4\pi c\vec{\Pi}(\vec{r}))^2 + (\nabla\times\vec{A}(\vec{r}))^2]d^3r\right\}$$

$$+ 4\pi c\int \vec{P}^{\perp}(\vec{r})\cdot\vec{\Pi}(\vec{r})d^3r + 2\pi\int|\vec{P}^{\perp}(\vec{r})|^2\, d^3r + V_{\text{inter}}. \tag{D23}$$

It is possible to simplify Eq. (D23) by separating $2\pi\int|\vec{P}^{\perp}(\vec{r})|^2 d^3r$ into two parts: inter- and intramolecular. Let us consider the intermolecular part:

$$2\pi\int \vec{P}_1^{\perp}(\vec{r})\cdot\vec{P}_2^{\perp}(\vec{r})d^3r. \tag{D24}$$

Noting

$$\begin{aligned}\vec{P}_2(\vec{r}) &= \vec{P}_2^{\parallel}(\vec{r}) + \vec{P}_2^{\perp}(\vec{r}),\\ \vec{P}_1^{\perp}(\vec{r})\cdot\vec{P}_2^{\parallel}(\vec{r}) &= 0,\end{aligned} \tag{D25}$$

and

$$\vec{P}_1^{\perp}(\vec{r})\cdot\vec{P}_2^{\perp}(\vec{r}) = \vec{P}_1^{\perp}(\vec{r})\cdot\{\vec{P}_2^{\parallel}(\vec{r}) + \vec{P}_2^{\perp}(\vec{r})\} = \vec{P}_1^{\perp}(\vec{r})\cdot\vec{P}_2(\vec{r}), \tag{D26}$$

we rewrite Eq. (D24) as follows:

$$\begin{aligned}4\pi\int \vec{P}_1^{\perp}(\vec{r})\cdot\vec{P}_2^{\perp}(\vec{r})d^3r &= 4\pi\int \vec{P}_1^{\perp}(\vec{r})\cdot\vec{P}_2(\vec{r})d^3r\\ &= 4\pi\mu_i(1)\mu_j(2)\int \delta_{ij}^{\perp}(\vec{r}-\vec{R}_1)\delta(\vec{r}-\vec{R}_2)d^3r\\ &= 4\pi\mu_i(1)\mu_j(2)\delta_{ij}^{\perp}(\vec{R}_1-\vec{R}_2)\\ &= -\frac{\mu_i(1)\mu_j(2)}{R^3}(\delta_{ij} - 3\hat{e}_{Ri}\hat{e}_{Rj})\\ &= -\frac{1}{R^3}\{\vec{\mu}(1)\cdot\vec{\mu}(2) - 3(\vec{\mu}(1)\cdot\vec{e}_R)(\vec{\mu}(2)\cdot\vec{e}_R)\},\end{aligned} \tag{D27}$$

where we used Eq. (D15) in the first line, and the following identities for the Dirac $\delta$ function and the $\delta$-dyadics, $\delta_{ij}^{\parallel}(\vec{r})$ and $\delta_{ij}^{\perp}(\vec{r})$, in the third line:

$$\begin{aligned}\delta_{ij}\delta(\vec{r}) &= \delta_{ij}^{\parallel}(\vec{r}) + \delta_{ij}^{\perp}(\vec{r}),\\ \delta_{ij}^{\perp}(\vec{r}) = -\delta_{ij}^{\parallel}(\vec{r}) &= -\frac{1}{(2\pi)^3}\int \hat{e}_{ki}\hat{e}_{kj}\exp(i\vec{k}\cdot\vec{r})d^3r\\ &= \nabla_i\nabla_j\left(\frac{1}{4\pi r}\right) = -\frac{1}{4\pi r^3}(\delta_{ij} - 3\hat{e}_{ri}\hat{e}_{rj}).\end{aligned} \tag{D28}$$

Here the subscripts *i* and *j* refer to Cartesian components, as usual. Because the exchange of the subscripts 1 and 2 gives the same result as Eq. (D27), one can derive

$$2\pi\int \vec{P}_1^{\perp}(\vec{r})\cdot\vec{P}_2^{\perp}(\vec{r})d^3r + V_{\text{inter}} = 0. \tag{D29}$$

Therefore, we can only take care of the intramolecular part of $2\pi\int|\vec{P}^{\perp}(\vec{r})|^2 d^3r$ and have the simplified version of $H_{\text{mult}}$ as

$$\begin{aligned} H_{\text{mult}} = {} & \sum_{\zeta}\left\{\sum_{\alpha}\frac{\vec{p}_{\alpha}^{\,2}(\zeta)}{2m_{\alpha}} + V(\zeta) + 2\pi\int\left|\vec{P}_{\zeta}^{\perp}(\vec{r})\right|^2 d^3r\right\} \\ & + \left\{\frac{1}{8\pi}\int[(4\pi c\vec{\Pi}(\vec{r}))^2 + (\nabla\times\vec{A}(\vec{r}))^2]d^3r\right\} \\ & + 4\pi c\int \vec{P}^{\perp}(\vec{r})\cdot\vec{\Pi}(\vec{r})d^3r, \end{aligned} \tag{D30}$$

where each line represents the charged particle motion in each molecule, free electro- magnetic field, and the interaction, respectively. Because we can expand the polarization density in terms of $2^{\ell}$ multipoles ($l = 1,2,3,\cdots$), as shown in Eq. (D14), we call $H_{\text{mult}}$ the multipolar Hamiltonian. The interaction part can be more explicitly written as

$$\begin{aligned} 4\pi c\int \vec{P}^{\perp}(\vec{r})\cdot\vec{\Pi}(\vec{r})d^3r &= -\int \vec{P}^{\perp}(\vec{r})\cdot\vec{D}^{\perp}(\vec{r})d^3r = -\int \vec{P}(\vec{r})\cdot\vec{D}^{\perp}(\vec{r})d^3r \\ &= -\{\vec{\mu}(1)\cdot\vec{D}^{\perp}(\vec{R}_1) + \vec{\mu}(2)\cdot\vec{D}^{\perp}(\vec{R}_2)\}, \end{aligned} \tag{D31}$$

with the help of Eqs. (D15) and (D22). When the considered system is quantized, quantities such as $\vec{\mu}(i)$ and $\vec{D}^{\perp}(\vec{R}_i)$, $(i = 1,2)$ should be replaced by the corresponding operators,

$$-\left\{\hat{\vec{\mu}}(1)\cdot\hat{\vec{D}}^{\perp}(\vec{R}_1) + \hat{\vec{\mu}}(2)\cdot\hat{\vec{D}}^{\perp}(\vec{R}_2)\right\}, \tag{D32}$$

yielding the quantized multipolar Hamiltonian.

# Appendix E

## Transformation from Photon Base to Polariton Base

In this appendix, we derive Eqs. (10) and (11) in the text, diagonalizing an exciton-photon interacting system without the rotating wave approximation. Suppose that the Hamiltonian of the system as

$$\hat{H} \equiv \sum_k \hat{H}_k, \; \hat{H}_k = \hbar\omega_k \hat{a}_k^\dagger \hat{a}_k + \hbar\Omega \hat{b}_k^\dagger \hat{b}_k - \mathrm{i}\hbar C\left(\hat{b}_{-k} + \hat{b}_k^\dagger\right)\left(\hat{a}_k - \hat{a}_{-k}^\dagger\right) \tag{E1}$$

with creation and annihilation operators of a photon with energy of $\hbar\omega_k$, $\hat{a}_k^\dagger$ and $\hat{a}_{\vec{k}}^\dagger$, and those of an exciton with energy of $\hbar\Omega$, $\hat{b}_{\vec{k}}^\dagger$ and $\hat{b}_{\vec{k}}$. The exciton-photon coupling is denoted by $\mathrm{i}\hbar C$. We define an exciton-polariton operator $\hat{\xi}_k$ as

$$\hat{\xi}_k = W_k \hat{a}_k + y_k \hat{a}_{-k}^\dagger + X_k \hat{b}_k + Z_k \hat{b}_{-k}^\dagger \tag{E2}$$

and its hermitian conjugate $\hat{\xi}_k^\dagger$, and for simplicity assume that all the operators obey the boson commutation relation. Here $W_k, y_k, X_k$, and $Z_k$are the expansion coefficients. The Hamiltonian should be diagonalized in the form of $\hat{\xi}_k^\dagger \hat{\xi}_k$, and it follows that

$$H_k = \hbar\Omega_k \hat{\xi}_k^\dagger \hat{\xi}_k, \tag{E3}$$

and

$$\frac{1}{\mathrm{i}} \frac{d\hat{\xi}_k}{dt} = \frac{1}{\hbar}\left[\hat{H}, \hat{\xi}_k\right] = -\Omega_k \hat{\xi}_k. \tag{E4}$$

Substituting Eq. (E2) into Eq. (E4), the left-hand side is written as

$$\frac{W_k}{\mathrm{i}} \frac{d\hat{a}_k}{dt} + \frac{y_k}{\mathrm{i}} \frac{d\hat{a}_{-k}^\dagger}{dt} + \frac{X_k}{\mathrm{i}} \frac{d\hat{b}_k}{dt} + \frac{Z_k}{\mathrm{i}} \frac{d\hat{b}_{-k}^\dagger}{dt}, \tag{E5}$$

and the right-hand side reads

$$-\Omega_k\left(W_k \hat{a}_k + y_k \hat{a}_{-k}^\dagger + X_k \hat{b}_k + Z_k \hat{b}_{-k}^\dagger\right). \tag{E6}$$

Using the equations of motion as

$$\begin{cases} \dfrac{1}{\mathrm{i}}\dfrac{d\hat{a}_k}{dt} = \dfrac{1}{\hbar}\left[\hat{H},\, \hat{a}_k\right] = -\omega_k\hat{a}_k - \mathrm{i}C\left(\hat{b}_k + \hat{b}^\dagger_{-k}\right). \\ \dfrac{1}{\mathrm{i}}\dfrac{d\hat{a}^\dagger_{-k}}{dt} = \dfrac{1}{\hbar}\left[\hat{H},\, \hat{a}^\dagger_{-k}\right] = \omega_k\hat{a}^\dagger_{-k} - \mathrm{i}C\left(\hat{b}_k + \hat{b}^\dagger_{-k}\right). \\ \dfrac{1}{\mathrm{i}}\dfrac{d\hat{b}_k}{dt} = \dfrac{1}{\hbar}\left[\hat{H},\, \hat{b}_k\right] = -\Omega\hat{b}_k + \mathrm{i}C\left(\hat{a}_k - \hat{a}^\dagger_{-k}\right). \\ \dfrac{1}{\mathrm{i}}\dfrac{d\hat{b}^\dagger_{-k}}{dt} = \dfrac{1}{\hbar}\left[\hat{H},\, \hat{b}^\dagger_{-k}\right] = \Omega\hat{b}^\dagger_{-k} - \mathrm{i}C\left(\hat{a}_k - \hat{a}^\dagger_{-k}\right). \end{cases} \tag{E7}$$

we can rewrite Eq. (E5) as follows:

$$\begin{aligned} &\left[-\omega_k\hat{a}_k - \mathrm{i}C\left(\hat{b}_k + \hat{b}^\dagger_{-k}\right)\right]W_k + \left[\omega_k\hat{a}^\dagger_{-k} - \mathrm{i}C\left(\hat{b}_k + \hat{b}^\dagger_{-k}\right)\right]y_k \\ &\quad + \left[-\Omega\hat{b}_k + \mathrm{i}C\left(\hat{a}_k - \hat{a}^\dagger_{-k}\right)\right]X_k + \left[\Omega\hat{b}^\dagger_{-k} - \mathrm{i}C\left(\hat{a}_k - \hat{a}^\dagger_{-k}\right)\right]Z_k \end{aligned} \tag{E8}$$

Because the operators are linearly independent, it follows from Eqs. (E6) and (E8) that we have

$$\mathbf{M}\begin{pmatrix} W_k \\ X_k \\ y_k \\ Z_k \end{pmatrix} \equiv \begin{pmatrix} \Omega_k - \omega_k & \mathrm{i}C & 0 & -\mathrm{i}C \\ -\mathrm{i}C & \Omega_k - \Omega & -\mathrm{i}C & 0 \\ 0 & -\mathrm{i}C & \Omega_k + \omega_k & \mathrm{i}C \\ -\mathrm{i}C & 0 & -\mathrm{i}C & \Omega_k + \Omega \end{pmatrix}\begin{pmatrix} W_k \\ X_k \\ y_k \\ Z_k \end{pmatrix} = 0. \tag{E9}$$

The conditions that the coefficients $W_k$, $X_k$, $y_k$, and $Z$ are not zero, lead us to have

$$\det(\mathbf{M}) = 0, \text{ or } \left(\Omega_k^2 - \omega_k^2\right)\left(\Omega_k^2 - \Omega^2\right) = 4C^2\Omega\omega_k, \tag{E10}$$

as an eigenvalue equation. By setting $E(k) = \hbar\Omega_k$, and $E_m = \hbar\Omega$ Eq. (E10) can be rewritten as

$$(E^2(k) - (\hbar\omega_k)^2)\left(E^2(k) - E_m^2\right) = 4\hbar\omega_k C^2 E_m. \tag{E11}$$

In order to determine the coefficients $W_k$, $X_k$, $y_k$, and $Z_k$, we then express $X_k$, $y_k$, and $Z_k$ in terms of $W_k$ from Eq. (E9).

$$y_k = -\frac{E(k) - \hbar\omega_k}{E(k) + \hbar\omega_k} W_k, \quad X_k = -\frac{(E(k) + E_m)(E(k) - \hbar\omega_k)}{2i\hbar C E_m} W_k, \quad Z_k = \frac{E(k) - E_m}{E(k) + E_m} X_k. \tag{E12}$$

The boson commutation relation, $[\hat{\xi}_k, \hat{\xi}_k^{\vee}] = 1$ gives the following constraint

$$|W_k|^2 + |X_k|^2 - |y_k|^2 - |Z_k|^2 = 1. \tag{E13}$$

Using Eqs. (E11), (E12), and (E13), we finally obtain

$$W_k = \frac{E(k) + \hbar\omega_k}{2\sqrt{E(k) \cdot \hbar\omega_k}} \sqrt{\frac{E^2(k) - E_m^2}{2E^2(k) - E_m^2 - (\hbar\omega_k)^2}} = \frac{\Omega_k + \omega_k}{2\sqrt{\Omega_k \omega_k}} \sqrt{\frac{\Omega_k^2 - \Omega^2}{2\Omega_k^2 - \Omega^2 - \omega_k^2}}. \tag{E14}$$

Corresponding to two eigenvalues of Eq. (E11), $E^{(\pm)}(k)$, we classify exciton-polariton operator and expansion coefficients by superscripts $(\pm)$ such as $\hat{\xi}_k^{(\pm)}$, $\hat{\xi}_k^{(\pm)}$, and $W_k^{(\pm)}$. Then Eq. (E2) are rewritten as follows:

$$\begin{pmatrix} \hat{\xi}_k^{(+)} \\ \hat{\xi}_k^{(-)} \\ \hat{\xi}_{-k}^{(+)\dagger} \\ \hat{\xi}_k^{(-)\dagger} \end{pmatrix} \equiv \begin{pmatrix} W_k^{(+)} & X_k^{(+)} & y_k^{(+)} & Z_k^{(+)} \\ W_k^{(-)} & X_k^{(-)} & y_k^{(-)} & Z_k^{(-)} \\ y_k^{(+)*} & Z_k^{(+)*} & W_k^{(+)*} & X_k^{(+)*} \\ y_k^{(-)*} & Z_k^{(-)*} & W_k^{(-)*} & X_k^{(-)*} \end{pmatrix} \begin{pmatrix} \hat{a}_k \\ \hat{b}_k \\ \hat{a}_{-k}^{\dagger} \\ \hat{b}_{-k}^{\dagger} \end{pmatrix}, \tag{E15}$$

which can be inversely transformed as

$$\begin{pmatrix} \hat{a}_k \\ \hat{b}_k \\ \hat{a}_{-k}^{\dagger} \\ \hat{b}_{-k}^{\dagger} \end{pmatrix} \equiv \begin{pmatrix} W_k^{(+)*} & W_k^{(-)*} & -y_k^{(+)} & -y_k^{(-)} \\ X_k^{(+)*} & X_k^{(-)*} & -Z_k^{(+)} & -Z_k^{(-)} \\ -y_k^{(+)*} & -y_k^{(-)*} & W_k^{(+)} & W_k^{(-)} \\ -Z_k^{(+)*} & -Z_k^{(-)*} & X_k^{(+)} & X_k^{(-)} \end{pmatrix} \begin{pmatrix} \hat{\xi}_k^{(+)} \\ \hat{\xi}_k^{(-)} \\ \hat{\xi}_{-k}^{(+)\dagger} \\ \hat{\xi}_k^{(-)\dagger} \end{pmatrix}. \tag{E16}$$

After the superscripts $(\pm)$ are abbreviated, then we have

$$\begin{cases} \hat{a}_k = W_k^* \hat{\xi}_k - y_k \hat{\xi}_{-k}^{\dagger}, \\ -\hat{a}_{-k}^{\dagger} = y_k^* \hat{\xi}_k - W_k \hat{\xi}_{-k}^{\dagger}, \end{cases} \tag{E17}$$

which are substituted into the photon operators in $\hat{\vec{D}}^{\perp}(\vec{r})$. Using Eqs. (E12) and (E14), we finally obtain

$$K_\alpha(\vec{k}) = \sum_{\lambda=1}^{2} (\vec{\mu}_\alpha \cdot \vec{e}_\lambda(\vec{k})) f(k) e^{i\vec{k}\cdot\vec{r}_\alpha} \tag{E18}$$

with

$$f(k) = \frac{ck}{\sqrt{\Omega(k)}} \sqrt{\frac{\Omega^2(k) - \Omega^2}{2\Omega^2(k) - \Omega^2 - (ck)^2}}\ , \tag{E19}$$

which are Eqs. (10) and (11) to be derived.